SEISMIC RETROFIT OF PRECAST RC WALLS BY EXTERNALLY BONDED CFRP COMPOSITES

Teză destinată obţinerii
titlului ştiinţific de doctor inginer
la
Universitatea "Politehnica" din Timişoara
în domeniul INGINERIE CIVILĂ
de către

ing. István DEMETER

Conducător ştiinţific:	prof.univ.dr.ing. Valeriu STOIAN
Referenţi ştiinţifici:	prof.univ.dr.ing. Radomir FOLIĆ
	prof.univ.dr.ing. Zoltán KISS
	conf.univ.dr.ing. Daniel DAN

Ziua susţinerii tezei: October 17, 2011

Seriile Teze de doctorat ale UPT sunt:

1. Automatică
2. Chimie
3. Energetică
4. Ingineria Chimică
5. Inginerie Civilă
6. Inginerie Electrică
7. Inginerie Electronică şi Telecomunicaţii
8. Inginerie Industrială
9. Inginerie Mecanică
10. Ştiinţa Calculatoarelor
11. Ştiinţa şi Ingineria Materialelor

Universitatea „Politehnica” din Timişoara a iniţiat seriile de mai sus în scopul diseminării expertizei, cunoştinţelor şi rezultatelor cercetărilor întreprinse în cadrul şcolii doctorale a universităţii. Seriile conţin, potrivit H.B.Ex.S Nr. 14 / 14.07.2006, tezele de doctorat susţinute în universitate începând cu 1 octombrie 2006.

România, 300159 Timişoara, Bd. Republicii 9,
tel. 0256 403823, fax. 0256 403221
e-mail: editura@edipol.upt.ro

Preface

The preparatory works of this thesis commenced in October 2006, when the author enrolled to the Department of Civil and Industrial Buildings, Faculty of Civil Engineering, Politehnica University of Timişoara, Romania as PhD Student under the supervision of Prof. Valeriu Stoian. At that time an extensive research project was already running on the retrofitting of reinforced concrete members by Fiber Reinforced Polymer composites under the coordination of Dr. Tamás Nagy-György. The author received the task to carry out an experimental investigation on the seismic response of precast reinforced concrete wall panels weakened by cut-out openings and retrofitted by externally bonded FRP composites.

During the first year of doctoral studies the author was acquainted with the experimental procedures in the Laboratory of Reinforced Concrete Structures by Dr. Nagy-György, Mr. Mircea Marity Sr. and PhD Student colleagues Cosmin Dăescu and Dan Diaconu. In the same time the author was eager to accumulate theoretical knowledge regarding the precast large panel buildings, Fibre Reinforced Polymer composites and similar experimental works on RC walls. The student membership to professional organizations such as ACI, *fib* and EERI was very instrumental in conducting the literature survey. The initially coarse experimental program was gradually shaped through fertile discussions with Prof. Stoian, Dr. Nagy-György, Dr. Daniel Dan and Mr. Marity from Politehnica University of Timisoara, and Dr. Anders Carolin and PhD Student Gabriel Sas from Lulea University of Technology, Sweden.

The construction of the experimental specimens and of the test rig commenced in the late summer of 2007, the first test was carried out in June 2008 while the last one in December 2009. During this time the author was mainly involved physically in every operation from the construction of the specimens to the laboratory testing. Building site manager Mr. Jar and project manager Mrs. Cuc of SC Constructim SA were helpful in the technical, logistic and administrative aspects of the specimen construction. Dr. Nagy-György, PhD Student Gabriel Sas and other colleagues from the Department were also involved in the logistics. Technical staff member Mr. Ionel Mihalache was the workmanship fellow of the author during the construction, set-up and strengthening of the specimens. The test rig and the hydraulic equipments were installed by Mr. Marity and Mr. Nicolae Albu while SC Klitehnima SRL provided the steel sections and workmanship for the reaction frames and loading beams. The experimental tests were performed in collaboration with Dr. Nagy-György, PhD Students Cosmin Dăescu, Dan Diaconu, Codruţ Floruţ, Alexandru Fabian and other colleagues and students from the Department.

After the completion of the tests it followed a nearly two year period of data processing, further literature survey and the elaboration of the thesis. During this time the author received valuable guiding from Prof. Stoian, Dr. Nagy-György and Dr. Daniel Dan. The final draft of the thesis was reviewed by Prof. Radomir Folić from University of Novi Sad, Serbia, Prof. Zoltán Kiss and Dr. Ferdinánd-Zsongor Gobesz from Technical University of Cluj-Napoca, and Prof. Stoian, Dr. Daniel Dan and Dr. Nagy-György.

The author expresses his grateful acknowledgement for all who were involved in this work.

Timişoara, September 2011 István Demeter

DEMETER, István

Seismic retrofit of precast RC walls by externally bonded CFRP composites

Teze de doctorat ale UPT, Seria 5, Nr. 80, Editura Politehnica, 2011, 251 pagini, 274 figuri, 38 tabele.

ISSN: 1842-581X

ISBN: 978-606-554-338-6;

Keywords: reinforced concrete, precast wall, seismic retrofit, FRP, cut-out opening, cyclic test, seismic performance

Abstract:
This work pertains to the field of earthquake engineering and addresses the seismic behaviour of the reinforced concrete walls. The objectives of the thesis are to investigate the seismic performance of the precast reinforced concrete walls, assess the weakening effects caused by doorway cut-outs and reveal the effects of the seismic retrofit by externally bonded carbon fibre reinforced polymers. The experimental program consisted in seven quasi-static cyclic tests on near-full scale precast reinforced concrete wall specimens. Particular care was paid to the design of the test set-up and loading procedure in order to model the outrigger effect which stimulates shear behaviour instead of the flexural one. The experimental variables referred to the opening and the strengthening condition. The influence of the cut-out opening size on the shear strength, stiffness and energy dissipation rate was considerable. The retrofitting technique by means of CFRP-EBR yielded improved behaviour characteristics, primarily in terms of energy dissipation; however, certain limitations were identified on the use of this strengthening system in reversed cyclic applications. In addition, the test results showed that by considering the outrigger effect the cyclic response and the failure mode of the shear walls is governed by diagonal compression. This imply a different look on the seismic design and analysis of the reinforced concrete wall structures.

TABLE OF CONTENTS

Symbols and abbreviations

SYMBOLS

Latin lower case letters

a	opening-to-web panel upper left corner horizontal distance
b	opening-to-web panel upper left corner vertical distance
b	thickness
b_w	thickness of the web
f_c	concrete strength
$f_{c,web}$	measured (on cube samples) concrete strength of the web-panel
$f_{c,wing}$	measured (on cube samples) concrete strength of the boundary-wing
f_{ck}	characteristic cylinder strength of concrete
f_{cm}	mean concrete cylinder strength of concrete
$f_{cm}(t_1)$	mean concrete cylinder strength of concrete at t_1 age
$f_{cm,cube}$	mean concrete cube strength of concrete
$f_{cm,cube}(t_1)$	mean concrete cube strength
f_y	yield strength of steel reinforcement
f_{yk}	characteristic yield strength of steel reinforcement
f_t	tensile strength of steel reinforcement
f_{tk}	characteristic tensile strength of steel reinforcement
h	height
h_o	opening height
h_w	wall height
l	length
l_o	opening
l_w	web-panel length
n	number of cycles on a displacement level
n	normalised axial load
n	number of the horizontal re-bars
n_S	normalised axial load considering the gross section of the wall
t	age of concrete (time)
t_1	age of the concrete samples at testing
t_2	age of the concrete at the time of the wall testing
x	opening centreline position from the left edge of the web panel

Latin upper case letters

A	in-plane area
A_c	area of cross-section
A_{co}	cross-section area of the opening
A_{cw}	gross cross-section area of the web-panel
A_f	fibre area in the cross section of the FRP laminate
A_{FRP}	area of the FRP laminate's cross section
A_o	in-plane area of the opening
A_m	resin matrix area in the cross section of the FRP laminate
A_s	area of the horizontal reinforcement
A_w	in-plane area of the web-panel
C	class of concrete
CD_j	Cumulative Drift corresponding to a point "j" on the load-displacement curve
CED_j	Cumulative Energy Dissipated corresponding to a point "j" on the response

CED_{max}	maximum cumulative energy which could be theoretically dissipated during the load-displacement response
CR_j	cumulative drif ratio corresponding to a point "j" on the load-displacement curve
E_f	tensile modulus of elasticity of dry fibre parallel with the fibre direction
E_{FRP}	tensile modulus of elasticity of the FRP laminate parallel with the fibre direction
E_m	tensile modulus of elasticity of the resin matrix
E_s	modulus of elasticity of steel reinforcement
ED_{max}	the maximum energy which could be theoretically dissipated during a load-displacement cycle
F_{DC}	diagonal compression force in the concrete strut
I1	wall area-to-floor area structural index
I2	total weight-to-wall area structural index
K	stiffness
K1, K2, K3	secant stiffness corresponding to cracking point, peak load and failure, respectively, on the backbone envelope
K_{sec}	secant stiffness
$K_{sec,Ri}$	denotes the secant stiffness corresponding to the δi displacement amplitude (Ri drift ratio) on the monotonic load-displacement envelope
K_{tan}	tangent stiffness
K_0	initial stiffness (at 0.1% drift ratio)
$K_{0,Ri}$	reloading (tangent) stiffness at the i-th displacement level with target drift ratio amplitude of Ri
$K_{0,P2}$	reloading stiffness in the load cycle corresponding to the peak load point
$K_{0,1\text{-}T}$	initial stiffness of the solid reference wall PRCWP 1-S-T
M	bending moment
M_R	moment of resistance
N	axial load; initial axial load
N1, N2	axial loads acting above pier#1 and pier#2, respectively
ΔN	additional variable axial load
R	drift angle (drift ratio)
R1, R2, R3	drift ratios corresponding to cracking point, peak load and failure, respectively, on the backbone envelope
R_i	target drift ratio at the i-th displacement level
ΔR	drift ratio increment from one displacement level to the other
$(R)_{sound}$	response characteristic of the sound (solid, as-built) member in terms of shear resistance, initial stiffness or energy dissipation rate
$(R)_{weak}$	response characteristic of the weakened member in terms of shear resistance, initial stiffness or energy dissipation rate
V	lateral load; shear force
V1, V2, V3	lateral loads corresponding to cracking point, peak load and failure, respectively on the backbone envelope
V_{DC}	shear carried by the concrete strut
V_{DT}	shear carried by the diagonal tension load transfer mechanism
V_{fl}	shear force corresponding to the flexural capacity
V_j	lateral load corresponding to a point "j" on the load-displacement curve
V_{Ri}	shear force corresponding to Ri drift ratio
$V_{Rd,c}$	design shear resistance of the member without shear reinforcement
$V_{Rd,max}$	design value of the maximum shear force, which can be sustained by the member, limited by crushing of the compression struts
$V_{Rd,s}$	design value of the shear force which can be sustained by the yielding shear reinforcement
$V_{R,sh}$	shear force at shear failure

S	steel grade

Greek lower case letters

α_p	performance ratio
α_s	aspect ratio
β_{cc}	time coefficient in relation to the strength of concrete
δ	displacement
δ_i	drift at the i-th displacement level
δ_j	drift corresponding to a point "j" on the load-displacement curve
δ_u	ultimate displacement
δ_y	yield displacement
ε	unit strain
η	normalised length of the compression strut
η	opening ratio
θ	inclination angle of the concrete strut to the vertical direction
μ	ductility factor
$\mu_{0.85}$	ductility measured from at 0.85 pre- and post-peak shear strength
σ	unit stress
σ_c	compressive stress in the concrete strut
σ_0	initial compressive stress on the wall cross-section
σ_s	tensile stress in the reinforcement
ϕ	diameter of reinforcing bar

ABBREVIATIONS

A	type A test set-up
A-CL	type A test set-up with cantilever boundary condition
AM	additional moment (boundary condition)
B	former Romanian designation of concrete quality
B	type B test set-up
B-RR	type B test set-up with restrained rotation boundary condition
C	Cyclic; Cycle
C1, C2	first and the second load-displacement cycle on a displacement level
C	type C test set-up
C-AM	type C test set-up with additional moment boundary condition
CD	Cumulative Drift
CCD	Cyclic Cumulative Drift
CED	Cumulative Energy Dissipated
CF	carbon fibre
CFRP	Carbon FRP
CL	cantilever (boundary condition)
CR	Cumulative drift ratio
D	Displacement; displacement transducer
E	Energy
E	opening
E1	narrow door opening
E3	wide door opening
EBR	Externally Bonded Reinforcement
ED	Energy Dissipated
EMS	European Macroseismic Scale
FRP	Fibre Reinforced Polymer

G	Strain Gauge
M	Monotonic
M	average (mean)
M	modular unit
M1	monotonic envelope
M2	average cyclic envelope
OB	Romanian smooth (plain) reinforcing bar (otel beton)
PRCLP	Precast Reinforced Concrete Large Panel
PRCWP	Precast Reinforced Concrete Wall Panel
PC	Romanian ribbed reinforcing bar (profil periodic laminat la cald)
PSD	pseudo-dynamic loading
P/M	Predicted/Measured ratio
QSC	quasi-static cyclic loading
QSM	quasi-static monotonic loading
R	retrofit
R/T	prior-to-damage strengthening (Retrofitted and Tested)
RC	Reinforced Concrete
RR	restrained rotation (boundary condition)
S	solid wall
S	carbon fibre fabric (Sheet)
S/E	solid wall with cut-out opening
STNB	Romanian smooth wire reinforcement (sarma trasa neteda pentru beton)
T	test
T/R	post-damage strengthening (Tested and Retrofitted)

List of Figures

List of Tables

Rezumat

Cuvinte cheie: beton armat, perete prefabricat, consolidare seismică, FRP, gol tăiat ulterior, test ciclic, performanță seismică.

Lucrarea aparține domeniului ingineriei seismice și se referă la studiul comportarea la acțiuni seismice a pereților de beton armat în varianta de panouri mari prefabricate. Obiectivele principale a tezei au fost: investigarea performanțelor seismice ale panourilor mari de perete, evaluarea efectelor tăierii golurilor de ușă asupra răspunsului seismic și evaluarea efectelor consolidării folosind materiale compozite polimerice armate cu fibre (FRP). Programul experimental a constat în șapte teste alternant ciclice cvasi-statice pe elemente de panouri din beton armat realizate la scară aproape-reală. O atenție deosebită a fost acordată proiectării standului experimental și modului de încărcare pentru a modela efectul de stabilizare laterală care favorizează forfecarea în loc de încovoiere. Variabilele experimentale s-au referit la lățimea golurilor și la starea de consolidare. Influența lățimii golurilor asupra capacității portante la forță tăietoare, rigidității și vitezei de disipare a energiei a fost însemnată. Tehnica de consolidare prin armare exterioară cu compozite polimerice a rezultat în caracteristici de comportare îmbunătățite, în primul rând în termeni de disipare de energie, însă au fost identificate și câteva limitări în legătură cu folosirea acestui sistem de consolidare în aplicații ciclice. Adițional, rezultatele experimentale au arătat, că luând în considerare efectele de stabilizare laterală, răspunsul ciclic și modul de cedare a pereților de forfecare este guvernat de compresiune pe diagonală. Acest lucru implică o viziune diferită asupra analizării și proiectării structurilor cu pereți din beton armat.

1 INTRODUCTION

1.1 Frame of reference

This work pertains to the field of earthquake engineering and addresses the seismic behaviour of the reinforced concrete walls. The main principle the author kept in mind is that the as-built boundary conditions should be modelled faithfully in the experimental research. In the subsequent sections some of the issues under scientific or engineering debate are highlighted.

The load resisting structural systems evolved considerably in the past one hundred years from masonry and timber to reinforced concrete (RC) and structural steel. The analysis and design of materials and structures was one step behind of the technology and consequently the process of learning from faults prevailed. These faults were evidenced most strikingly by earthquakes, when life and economic losses were put in the balance. The structural engineers are required to devise lateral load resisting systems and the lateral load demand must be evaluated. There is a 100 year old debate on this subject involving explanatory theories and design philosophies, thousands of experimental tests and a series of earthquake reports. However, almost each significant earthquake reveals unaccounted issues.

The seismic performance of reinforced concrete wall structural systems was reportedly satisfactory as opposed to the performance of frame systems. This can be attributed to the wide diagonal load path (see Figure 1.1) available to transfer the lateral loads from one level to the other with sufficient stiffness to avoid large deformations which would cause eccentric gravity loads and non-structural damage. The degree of engineering of a shear wall improves its lateral load response, but even plain concrete walls were effective in avoiding catastrophic collapses. There is an ongoing scientific debate regarding the shear transfer mechanism in RC walls and whether design assumptions of ductility and the extent of energy dissipation are correctly accounted for with respect to the as-built response.

Despite this excellent seismic performance, the general use of RC wall structural systems is hindered by a series of factors such as functional space requirements and some professional and social antagonism. Instead, structural systems that combine RC frames and walls are preferred more widely. Nevertheless, in some regions of the world like Eastern Europe, Russian Federation and Chile a considerable many residential buildings were constructed of wall structural systems of either monolithic or precast reinforced concrete. Romania is a typical example, with tens of thousands of mid-rise apartment blocks built using the precast large panel system. The seismic performance of these structural systems was tested by several Romanian earthquakes (1977, 1986 and 1990) and responded satisfactorily. On the other hand, the large panel structural system features very limited space flexibility and this constitutes a drawback from a functional standpoint. For instance, an occupancy change from residential to commercial, which is quiet frequently the case of the ground floor apartments, imply a functional vs. structural controversy. The functional side requires more open space and therefore proposes to remove some wall portions while the structural side protects the integrity or performance of the walls.

1.2 Objectives

Structural alterations by doorway cut-outs impair the seismic performance of a reinforced concrete wall member. According to the common sense of structural engineering the weakening effect (see Figure 1.1) should be proportional to the size of the cut-out opening, although this assumption needs further data regarding the shape and position of the opening. Moreover, the weakening should be specified in terms of strength, stiffness, ductility and energy dissipation. Even the assumption of weakening may be subject of investigation with respect to the structure's overall response given that slitted walls were adopted as seismic rehabilitation method.

In order to enhance the seismic performance of the cut-out weakened walls retrofitting should be carried out. The strengthening technique of FRP-EBR (Externally Bonded Fibre Reinforced Polymers) was introduced in the past twenty years and gained widespread application for its advantages with respect to conventional/traditional methods primarily for RC beams and column members and masonry elements. As with many other novel techniques, the structural engineering research and design regarding the FRP-EBR strengthening is one step behind technology and application, consequently a series of unaddressed issues are expected. As externally bonded reinforcement (EBR) this technique can be used similarly (emulating) to conventional steel reinforcement, bearing in mind the differences between them in terms of material and geometric properties. In the case of an RC shear wall the reinforcement, either steel or FRP, should be flexural, shear or confinement and should have corresponding directions at specific locations: vertical concentrated at the extremities, horizontal or diagonal in the web, and transversal, respectively. Furthermore the strengthening should address the behaviour aspects as strength, stiffness, ductility and energy dissipation.

The objectives of the thesis are to investigate the seismic performance of the precast reinforced concrete walls, assess the weakening effects caused by doorway cut-outs and reveal the effects of the seismic retrofit by externally bonded carbon FRPs, see Figure 1.1.

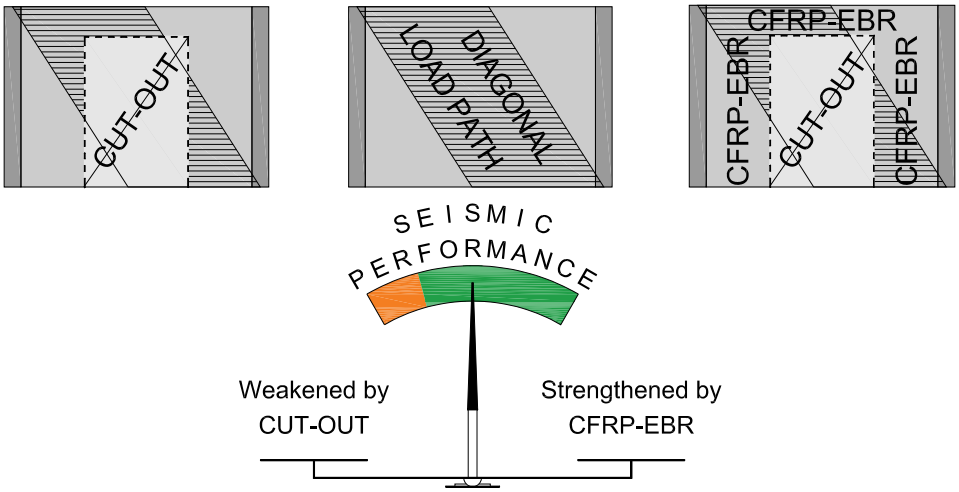

Figure 1.1 The *weight* of the cut-out weakening against the FRP-strengthening

1.3 Overview of the thesis

The thesis is composed of six chapters and appendices totalising over 200 pages. The core of this work is constituted of seven quasi-static cyclic tests on near-full scale precast wall panels. Essentially, the thesis has three parts, namely the experimental program including a series of preliminary studies; the laboratory tests containing the recorded and observed response; and the analysis of the results.

The first chapter outlines the frame of reference the work is set into, states the objectives and contains a short overview of the thesis.

In Chapter 2 a general presentation of earthquake engineering is provided highlighting some of the historical aspects of this field and pointing out the importance of the laboratory investigations and of the post-earthquake reports. Furthermore, the structural system of the precast large panel buildings widely used in Romania is described in view of identifying the prototype for the experimental campaign. Afterwards, an extensive review of the literature on RC wall tests is presented in the form of a database with strong emphasis on the test set-up loading and boundary conditions.

Chapter 3 contains a detailed description of the experimental program and a complete account of the recorded and observed response. The chapter commences with the presentation of the test matrix indicating the experimental variables and the comparison lines. It follows the characterisation of the experimental specimens in terms of concrete outlines, steel reinforcing details and CFRP-EBR layout. Subsequently, the properties of the three structural material types are presented. Special attention was paid to the description of the test set-up, and of the loading and boundary conditions in order to highlight the novelties. The experimental program is concluded by the instrumentation of the specimens. In the followings the results obtained by the seven cyclic wall tests are rendered in two ways, namely primary results and detailed test logs. The primary results consists in the load-displacement response, the loading and displacement histories, the final cracking pattern, a brief description of the observed behaviour and failure mode, and a limited number of photographs on failure details. The test logs contain all the recorded responses and an expanded cyclic account of the load-drift response, of the loading and drift history, and of the observed behaviour and failure mode.

In Chapter 4 the author's objective was to characterize the responses and exhibit the effects of the experimental variables on the response characteristics. These tasks are referred to as analysis of the results. In accordance to the general seismic performance characteristics of the lateral load resisting members the following analysis types were undertaken: strength analysis, displacement and strain analysis, stiffness analysis, and energy dissipation analysis. In addition to the measured response analyses, the observed behaviour aspects peculiar to concrete members were also addressed through cracking analysis.

Chapter 5 provides the analytical modelling of the response based on the load transfer mechanism. Diagonal tension and diagonal compression shear mechanisms are modelled and the predictions are compared with the measured response. The Eurocode 2 and Eurocode 8 provisions regarding the shear resistance of the large lightly reinforced walls are applied and the code predictions are compared with the experimental records.

In Chapter 6 the conclusions are drawn with respect to the weakening effect of the doorway cut-outs and the strengthening effect of the FRP-EBR retrofitting on

the cyclic response of the precast reinforced concrete wall panels. Recommendations are formulated for the engineering practice and an outlook is provided for future research directions. The chapter is concluded by an account of the author's publications and his personal contribution to this work.

The Appendices contain supplementary descriptive information consisting primarily in charts and photographs which would have been disruptive if presented in the main body of the thesis: in Appendix A are tabulated the main characteristics of the RC wall seismic test programs available in the literature; Appendix B furnishes detailed description of the FRP-layout for the strengthened specimens; in Appendix C the complete instrumentation of each specimen is presented; Appendix D provides an account of the measurement errors; Appendix E contains the detailed test logs; and in Appendix F are presented the cyclic energy dissipation histograms.

2 PREPARATORY INVESTIGATIONS

2.1 Earthquake Engineering

2.1.1 Observation of the earthquake phenomenon

The author recollects his personal experience of a moderate earthquake in a small town situated in the Eastern Carpathian Mountains, back in the early 1990s. The earthquake occurred about noon. The tremor of the 2-storey block of flats building was felt on the 2nd floor as being very quick with considerable rattling of the windows. The inhabitants, including the author's family, rushed out of the building and stayed there for a while. The duration of the earthquake was of about 30 seconds. No damage was observed and the memory of it is obscure.

In hindsight, it was most probably the magnitude 7.0 Vrancea, Romania event of May 30, 1990 felt at about 150 km off the source. According to the EMS-98 [1] scale the author's judgement is that it was an intensity V earthquake at that location. The 2-storey building was of reinforced concrete frame structure with masonry infill walls and the author's judgement is that the period of vibration of the building was about 0.5 s or less.

In the past 20 years, several devastating earthquakes occurred throughout the world, among them the following: 1994 Northridge-California, USA, magnitude 6.8, causing 60 deaths, partial or total collapse of parking garages of precast concrete structure [2]; 1995 Hyogo-ken Nanbu (Kobe), Japan, magnitude 6.9, death toll of 5420, significant damage to engineered building structures and bridges of all types [3]; 1999, Kocaeli, Turkey, magnitude 7.4, more than 17000 casualties, 60000+ buildings collapsed or sustained heavy damage, see Figure 2.1 [4]; 2003, Bam, Iran, magnitude 6.6, over 31000 fatalities, large number of traditional adobe houses collapsed [5];

Figure 2.1 Buildings damaged by the 1999 Kocaeli, Turkey earthquake (EERI, [4])

2008 Wenchuan, China, magnitude 7.9, 69226 were killed, 216000 buildings destroyed [6]; 2009 L'Aquila, Italy, magnitude 6.3, 305 people lost their lives, 10000+ buildings, including historic centres, were severely damaged [7]; 2010 Port au Prince, Haiti, magnitude 7.0, over 220000 fatalities, 105000+ constructions collapsed, including educational, medical and governmental buildings [8]; 2010 Chile, magnitude 8.8 eqk. and tsunami, 521 casualties, 81000+ buildings sustained heavy damage [9]; 2010/2011 Darfield/Christchurch, New-Zealand, magnitude 7.1/6.3, causing 184 deaths, several engineered buildings collapsed [10, 11]; and 2011, Tohoku, Japan, magnitude 9.0 eqk. and tsunami, 22626 persons killed or missing, 107000 buildings collapsed and many others damaged, including nuclear power plants, by the tsunami [12].

2.1.2 Earthquake science: Seismology

The scientific approach to earthquakes is the objective of a specialized field of geology. The origin of this field is strongly related to the development of a measuring instrument that is able to quantify the earthquake in terms of displacements in a time scale. This device, called seismograph was invented in the late 1800s [13] and facilitated the outset of a new science called seismology with the objective of measuring the earthquake motions, analysing it and devising explanatory theories.

Seismographs are sensitive devices that can precisely measure even the ground motions imperceptible to common human senses. These records are instructive from scientific standpoint, but are not useful in engineering; on the other hand the seismographs are not suitable to measure the strong motions, which can be destructive to the built environment and are instrumental in engineering. Employing the ground motion records obtained by seismographs, seismologists devised methods to determine the exact location of the earthquake (epicentre and depth), the energy released (magnitude) and other characteristics of the earthquakes (e.g. rupture mechanism). The establishment, development and maintenance of seismographic networks constitute the basement of seismology. This effort is carried out by national institutes and by international collaboration between them; some of the networks are listed in Table 2.1.

Table 2.1 – Networks of seismographs (partial list)

Host	**Name**	**Area**	**Stations**
USGS	Global Seismographic Network [14]	global	150
USGS	Advanced National Seismic System [15]	USA	590+
EMSC-CSEM	n/a (collaborative network) [16]	Euro-Mediterranean	2400+
INFP	National Seismic Network of Romania [17]	Romania	n/a

Note: USGS – United States Geological Survey; EMSC – European-Mediterranean Seismological Centre; INFP – National Institute for Earth Physics of Romania.

Table 2.2 – Databases on historical earthquakes (partial list)

Host Institute	**Name**	**Area of ref.**	**Time reference**
IISEE	Catalog of Damaging Earthquakes in the World (Utsu Catalog) [18]	global	-2009
NGDC	Global Significant Earthquake Database [19]	global	2150 B.C. – present
EMSC-CSEM	European Archive of Historical Earthquake Data [20]	Europe	1000-1963
USGS-NEIC	Earthquake Lists and Maps [21]	USA+	856 – present
NIEP	ROMPLUS [22]	Romania	984 – present

Note: IISEE – International Institute of Seismology and Earthquake Engineering; NGDC – National Geophysical Data Centre; NEIC – National Earthquake Information Centre.

Beside the instrumental characteristics of the earthquakes, there is another approach that quantifies the intensity of earthquakes based on the effects on the built environment. The intensity scales were the only measures of earthquakes before the development of the seismograph and they exist continually today due to the different information they furnish. Several intensity scales were developed, e.g. the EMS-98 in Europe, the MMI-scale in the Americas and Japan also have its own.

The prediction (estimate) of the earthquakes, mostly of that ones which are capable to cause human and economic loss, is the foremost practical outcome of seismology. In this effort are of significant importance the historical references on damaging earthquakes, the collection of which constitute the catalogues [23] and databases, see Table 2.2.

2.1.3 Earthquake engineering in general

Generally speaking, the profession of engineering, as the term of applied science reflects it very instructively, is composed of theoretical background and practical experience. In the case of civil engineering the practical side of the profession has its origins traced back thousands of years, with the vast experience accumulated over the time working with traditional materials as wood, stone and brick masonry. Even today a considerable many of dwellings are represented worldwide by the so called non-engineered buildings, which are built by craftsman based on the local traditions. The scientific bases of the profession of civil engineering are closely related to the invention of concrete in the mid-1800s and later of the reinforced concrete. Design, detailing and specification of reinforced concrete structures required special knowledge, which was held only by the civil engineers. The first design codes were introduced in the inception of the twentieth century in Japan, USA and Italy [13]. The principal issue of the scientific side of civil engineering deals with the prediction of the load carrying capacity of structural members and systems, that is, the members are designed to withstand a specific load. Note that a craftsman would say that a member will or will not endure a specific load, whereas an engineer will tend to predict the precise value of the load that can be endured by the member, that is, its load carrying capacity. Another issue, of comparable importance, that civil engineers must deal with is that they must evaluate the loads that act on the structural member in order to be able to design the respective member to withstand it.

The civil engineering community was humiliated several times at the turn of the nineteenth and twentieth century, when destructive earthquakes in Japan (1891, 1896), California (1906) and Italy (1908) caused damage and collapse of many newly designed buildings, many life and extensive economic losses. Alongside the engineered buildings, the traditional buildings suffered even more causing losses of the same or even higher extent. The community realised that they must deal with the earthquakes in their design. This was the inception of a field in civil engineering called earthquake engineering. One hundred years later, at the turn of the twentieth and twenty-first centuries, the fatality toll and economic loss caused by damaging earthquakes is even more. However, there are significant achievements too, predominantly in the developed economies, where it was observed that the life loss reduced and the economical loss increased. Efforts are continuously invested to reduce both life and economic losses caused by earthquakes.

Due to the fact that civil engineering is divided in a series of branches which deals with specific structures, whereas the built environment is unanimously affected in an earthquake-hit area, the earthquake engineering is ubiquitous in civil engineering: in *civil* earthquake engineering, the term *civil* can be replaced by the

specific branch, such as geotechnical, structural, bridge, lifeline, etc. Interdisciplinary fields that involve earthquake engineering and another topic are engineering seismology (toward seismology), seismic risk analysis and management (toward politics, emergency response agencies and insurance agencies).

2.1.4 Engineering seismology

As stated previously one of the principal issues civil engineering is dealing with is the evaluation of loads that acts on structures. In earthquake engineering this objective is a very complex one and partly is addressed by the sub-field referred to as engineering seismology. This is a hybrid field between engineering and seismology and addresses the earthquake related effects that can be harmful to built environment or society [24]. Primary effects: fault rupture, strong ground motion and tsunami. Secondary effects: liquefaction, landslides, rock-falls, building damage/collapse, earthquake triggered fire and flooding. The primary objective is related to the strong ground motions.

Instruments that can record strong ground motions were invented in the 1930s in the USA [13] and are referred to as accelerographs, as opposed to seismographs that are used to the measurement of weak motions in seismology. The main engineering characteristics of the accelerograms (strong ground motion records) are: Peak Ground Acceleration/Velocity/Displacement (PGA, PGV, PGD), duration, Aries intensity and response spectra. In order to record the strong motions of damaging earthquakes a large number of accelerograph is strategically placed in earthquake-prone regions. Some of the strong motion networks are listed in Table 2.3. Generally the institutes that maintain these networks developed a database of their own and of other records indicated in Table 2.4.

Another important topic addressed by engineering seismology is to furnish information on the seismic activity of a certain location that is to assess the seismic hazard. Seismic hazard assessment must deal with earthquake occurrence and ground motion prediction (propagation). Occurrence prediction: location (source) and magnitude in time. Ground motion prediction for a defined earthquake deals with (1) attenuation with distance, (2) amplification (scaling) due to magnitude and (3) site geology (shear wave velocity). The results of this effort are the probabilistic and deterministic seismic hazard maps indicating the seismicity of the reference area in terms of PGA for a certain recurrence of a certain type of earthquake.

Table 2.3 – Strong-motion networks (partial list)

Host	Name	Area	Stations
BRI	BRI strong motion network [25]	Japan	74
NIED	Kyoshin-net [26]	Japan	~1000
USGS	National Strong Motion Network [27]	USA	1000+
ISC-INCERC-CNRRS	ISC-INCERC Seismic Network [28]	Romania	100+

Table 2.4 – Databases on strong-motion earthquakes (partial list)

Host	Name	Area	First record / #eqk
BRI	BRI strong motion database [29]	Japan	1957/?
COSMOS	Cosmos Virtual Center [30]	global	1933/515
USGS-CGS-ANSS	Center for Engineering Strong Motion Data [31]	USA/Global	1933
PEER	PEER Strong Motion Database [32]	global	?1935/143
PEER	NGA Database [33]		
NIED	K-net [26]	Japan	1996
INGV	Italian Accelerometric Archive [34]	Italy	1972
ISC-INCERC	Accelerograms (examples) [35]	Romania	1977

2.1.5 Structural earthquake engineering

Structural earthquake engineering deals with the earthquake-resistant design of buildings and other structures. This objective is achieved by addressing both sides of the demand-capacity equation. In his work [13] on the history of earthquake engineering in Japan, Reitherman provides a very instructive account of the structural analysis methods and design philosophies. Beattie et al. [36] overviewed the major contributions to earthquake engineering achieved in New-Zealand. Some of the methods and principles in seismic design are the followings: equivalent static lateral force elastic method (seismic coefficient); lateral force distribution among the structural elements as a function of their rigidity; inverted triangle static loading method; response spectrum method; inter-storey drift as design criterion; earthquake resistant design details; capacity design approach; adequate ductility, energy absorption, plastic deformation; displacement-based seismic design; and seismic structural control.

In the seismic design of RC shear walls the capacity design approach stipulates that the shear force corresponding to the flexural capacity (V_{fl}) should be less than the shear force at shear failure ($V_{R,sh}$), see Figure 2.2. This design requirement is based on laboratory experiments carried out on RC walls which indicated that the shear failure is brittle, occurs at low ductility level and implies limited amount of energy absorption, whereas the flexural failure is more ductile and much larger amount of energy is dissipated. Consequently, the foregoing regulation is meant to avoid shear failure and promote flexural failure. For a given shear span (refer to Figure 2.2) and moment demand this objective is a matter of adequate proportioning of the concrete section and reinforcement.

As in many other fields of engineering and science, the experimental investigations are of paramount importance in earthquake engineering. The laboratory tests are very useful to compare the theoretical predictions with experimental measurements or simply assess the seismic performance of materials, components, elements, building systems and structures, analyse the behaviour, and devise explanatory theories. The experimental elements can be derived from a theoretical model or from the as-built conditions (prototype). Note that if a theoretical assumption is confirmed in laboratory conditions or vice-versa, that is, an explanatory theory is based exclusively on laboratory results, it doesn't mean necessarily that the assumption or theory is correct and corresponds to the in-situ real earthquake conditions. Many researchers are deceived by the good correlation obtained between theory and laboratory, but this is only a half-success.

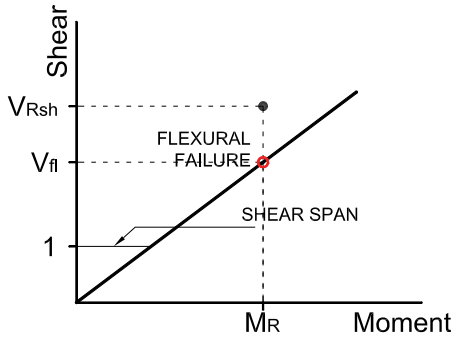

Figure 2.2 Capacity design approach for RC shear wall design

Table 2.5 – English-language publications (partial list)

Organisation	Publication	First issue
ACI	ACI Structural Journal	1929
EERI	Earthquake Spectra	1984
IAEE	Earthquake Engineering & Structural Dynamics	1972
NZSEE	The Bulletin of NZSEE	1968
EAEE	Bulletin of Earthquake Engineering	2003
ASCE	Journal of Structural Engineering	1956
IAEE	World Conference on Earthquake Engineering	1956
EAEE	European Conference on Earthquake Engineering	1964
PCA	Research and Development Bulletin	1939

In the past 60 years a considerable many tests were carried out to assess the seismic behaviour of structural elements. However, a significant part of the results is published only in national languages and probably is not available online. English language publications related to this field date back approximately to the 1950s, including journals, conference proceedings, research reports and doctoral theses. Some of these publications are listed in Table 2.5. As the number of experimental research projects augments in time it becomes more difficult to be updated with all the new information, and respectively the possibility to redo what was already done elsewhere increase. Recognizing the drawbacks of this situation a collection of the earthquake engineering experimental projects carried out on reinforced concrete members was published by Abrams [37].

2.1.6 Earthquake reports

The aim of the post-earthquake reports is to make a documented inventory of the damage (or non-damage) sustained by the buildings and other structures and record any other effects of the earthquake on the built or natural environment. These reports are extremely important and instructive to assess the actual behaviour and compare it with the performance expected per design. Parties interested in the reconnaissance activity include academia, research institutions, governmental or private agencies. Field observations are generally published in short preliminary reports, such as the EERI's "Learning from earthquakes" series. More detailed investigations are conducted after destructive earthquakes, including the analysis of the performance of instrumented buildings and structures if any, in order to explain the causes of the damage and make revisions to the seismic regulations.

2.1.7 Seismic risk analysis and management

The seismic risk of a specific location or area is the result of the convolution of seismic hazard, exposure and vulnerability [24]. The seismic hazard indicates the earthquake type that is considered to occur in a certain time interval; the exposure takes into account the population and the buildings and other structures, as well as the other tangible assets on that area; and the vulnerability shows the damage that a building would incur if subjected to a specific earthquake. The evaluation, analysis and reduction of the seismic risk is a very complex process marked by interdisciplinary collaboration.

In the case of a destructive earthquake the relief operations are generally coordinated by governmental agencies. Civil engineers are involved primarily in the safety assessment (inspection) of the damaged buildings.

2.2 Precast RC Large Panel Buildings

2.2.1 Building inventory

Likewise other Eastern European countries, Romanian urban areas underwent significant transformation during the second half of the 20th century, regarding the housing conditions. A considerable 28% of the total room area of residential buildings, as of 2002 according to [38] was represented by flat blocks of reinforced concrete construction realised in the period of 1950-2000, totalizing more than 57000 buildings. Over 40000 of these blocks are low-rise 5-storey Precast Reinforced Concrete Large Panel (PRCLP) buildings, see Figure 2.3, more than 3500 are 9-storey (P+8) and more than 4500 are 11-storey (P+10) mid-rises. The Romanian terminology used the large-panel residential building or large-panel block.

A short overview of the history of large-panel structures in Romania was published by the author in [39]. The construction period of the large panel started in the early 1960-ies and gained wide application starting from 1970, see Figure 2.3. A landmark event was the Vrancea earthquake of March 4, 1977. This event marked the decline of 11-storey (P+10) but didn't affect the ascent of 5-storey (P+4) and induced the emerging of 9-storey (P+8). Post-1977 large-panel reinforcement was modified, see later in this. The 1970 to 1990 period can be referred to as the decades of P+4 large-panel low-rises, with more than 36000 buildings constructed. The 1989-1990 marked the end of large-panel in Romania.

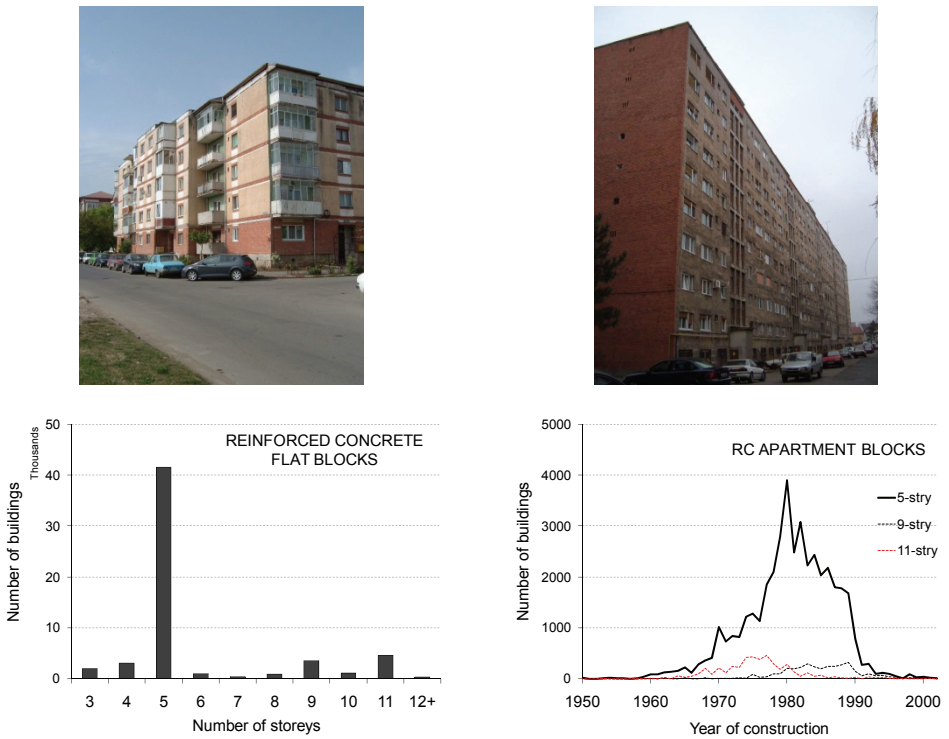

Figure 2.3 Inventory and construction period of RC flat blocks in Romania

2.2.2 Structural characteristics

The architectural floor plan of a 5-storey large-panel block consists generally in four flat units and a staircase, without elevator shaft. The ground floor is at about 1 meter above street level and the utility (uninhabitable) basement level is about 2 meters below ground level. Terrace roofs are the prevailing roof types.

The structural system of the 5-storey PRCLP buildings is composed of the cast-in-place RC infrastructure and the entirely precast superstructure. The infrastructure consists in strip foundations and 200 mm thick RC walls. The superstructure was made of room-size (2÷5 m in their plane) precast slab and wall panels, assembled on-site through vertical and horizontal joints along their edges by lap welding of steel reinforcement and casting in-place concrete, emulating the conventionally formed cast-in-place RC structures. Modular construction was employed using M300 mm as unit.

In Figures 2.4 and 2.5 are shown the plan layouts for the 1615/X large-panel building dated from 1973 (pre-1977) [40] and for the 770-81 building from 1982 (post-1977) [41, 42], respectively. The structural characteristics for the 770-81 building are presented in Table 2.6. The ground floor area represents the area inside the perimeter of the exterior walls' centreline, i.e. exclusive balconies, while the building area accounts for the total floor area on all five levels. The wall area represents the horizontal sectional area at a level 1.25 m above grade crossing through door and window openings (gross interior/exterior). One can observe that the distribution of the wall area amongst the two principal directions is slightly higher in the transverse direction. The total dead weight was ciphered considering the weight of structural panels plus 300 kg/m^2 on the floors above each level, as dead load. The unit weight of the bare structure of the PRCLP is about 800 kg/m^2. Wall-to-floor area ratio is I1 structural index, while weight-to-wall area is I2 structural index, as reported in [43].

Table 2.6 – Structural characteristics

Typical plan		**770-81**
Year		1982
Stories		5
Ground floor area (m^2)		242
Building area (m^2)		1210
Wall area (m^2)	total	14.62
	longitudinal	5.93
	transverse	8.69
Weight (1000 kg)	total	1370
	structural	972
Unit weight (kg/m^2)	total	1130
	structural	800
Wall area-to-floor area I1 %	total	6.04
	longit	2.45
	transverse	3.59
Total weight-to-wall area I2 (MPa)	total	0.9
	longit	2.22
	transverse	1.52

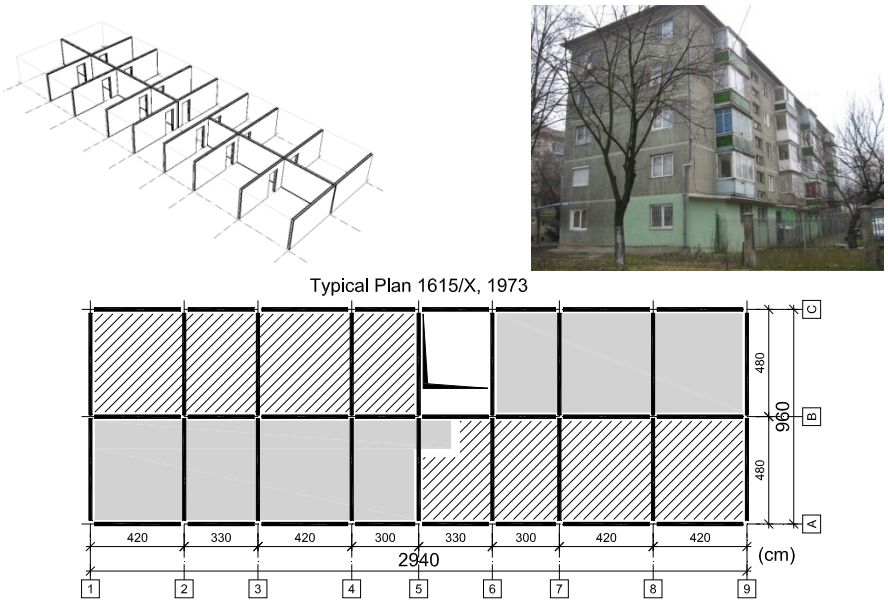

Figure 2.4 Plan-layout of the 1615/X large-panel building

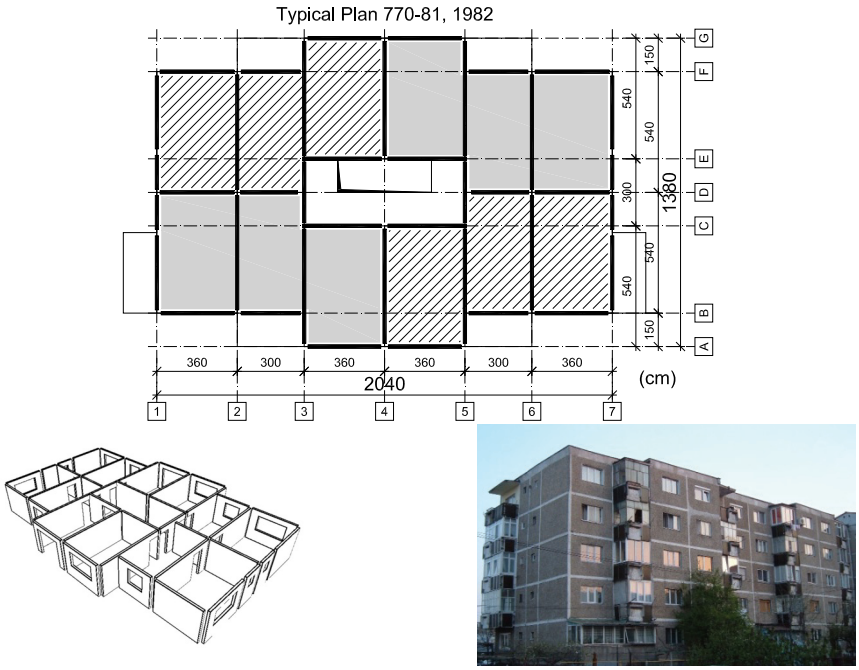

Figure 2.5 Plan-layout of the 770-81 large-panel building

2.2.3 Large-panel element characteristics

The precast large panels were of three types: exterior wall, interior wall and slab; other precast elements were the stairways, bathroom cabins, terrace attics, ventilation shafts, terrace egress element and additional thermal insulation walls. The exterior wall panels comprise two layers: a load-bearing (120 mm) and the other for thermal insulation (150 mm), slab panels were of 130 mm. Solid exterior wall, window opening and combined door-window opening for balcony access.

The concrete outlines and reinforcement patterns for a pre-1977 engineered solid interior wall panel and a post-1977 solid interior wall are presented in Figure 2.6, and the characteristics for these two are given in Table 2.7. The in-plane dimensions of the walls were modular dimensions, hence the nominal values were multiples of the M300 mm, like height of 2700 mm and length of 4200 or 3300 mm. However, the real dimensions were reduced considering the joints between the panels. Wall thickness is 140 mm concrete for all interior walls. The edges were key-formed to prevent sliding shear between adjacent walls. In general the wall panels were reinforced by a single curtain of reinforcement, except the coupling beams, which were reinforced by spatial cage. Post-1977 panels had the narrow piers also reinforced by spatial cage. The reinforcement pattern of the pre-1977 I 42-1 panel is characterised by plain concrete web and single-curtain reinforcement composed of four plane-cages along the wall edges made of plain rebars. The only reinforcements that cross the web are the vertical panel to-panel connection deformed bars. The post-1977 I36-1 wall panel's horizontal reinforcement was increased by three times by the addition of a welded wire mesh and by continuous horizontal bars crossing through the web. Vertical reinforcement consists in through-panel deformed bars and in-panel wire mesh. Panel-to-panel connection was realised by splicing the horizontal bars by lap welding. Note that horizontal connection is much more than vertical. Also note that vertical connection is realised by through-wall bars, while the horizontal connection is in the case of 1615/X, of short anchored bars, except the three through-wall bars.

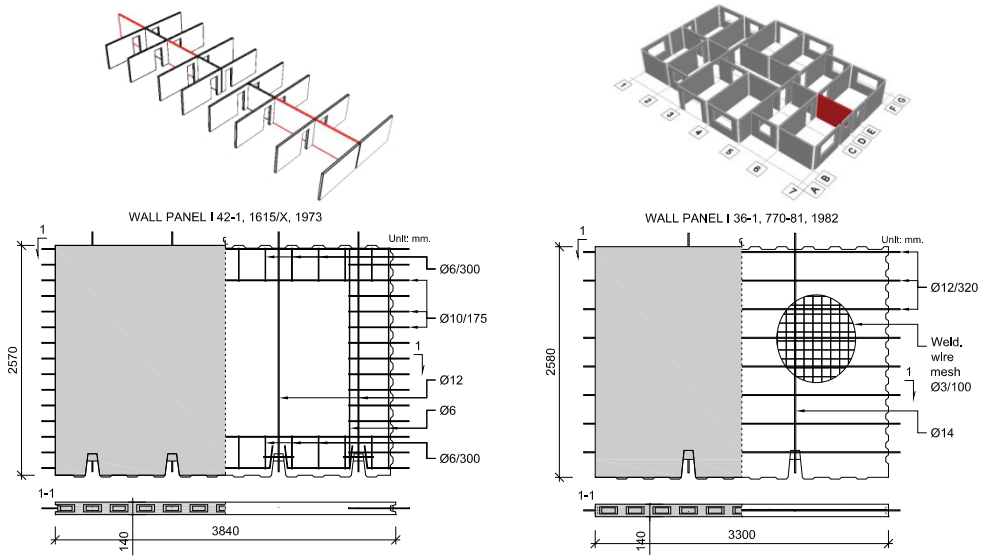

Figure 2.6 Concrete outlines and reinforcement of the I 42-1 and I 36-1 walls

Table 2.7 – Wall panel element characteristics

Typical plan		**1615/X**	**770-81**
Year		1973	1982
Wall panel designation		I 42-1	I 36-1
Location		interior	interior
Dimension (mm)	Nominal length	4200	3600
	length	3840	3300
	height	2570	2580
	thickness	140	140
Weight (kg)			2900
Web steel reinforcement ratio (%)	horizontal	0.09	0.3
	vertical	0.11	0.12
Panel-to-panel connection steel reinforcement ratio (%)	horizontal	0.33	0.25
	vertical	0.084	0.067

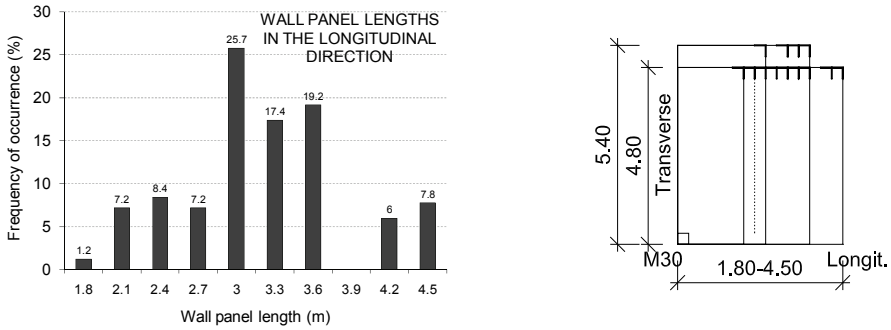

Figure 2.7 Wall panel lengths (in metres)

An analysis regarding the occurrence of the nominal wall lengths is presented in Figure 2.7. Principal (transverse) direction are only two dimensions, while the orthogonal (longitudinal) walls' length range from 1.8 to 4.5 m. The most frequent dimensions are the 3, 3.3 and 3.6 m. Note that the interior longitudinal walls are mostly solid walls.

2.2.4 Properties of the materials used for the large-panels

The properties of concrete and steel used for the fabrication of the large panels are presented in Table 2.8. The wall panels were made of B250 concrete, where 250 refers to the mean cube strength in daN/cm^2, on 141 mm edge samples, which corresponds to C16/20 class concrete. B200 (C12/15) concrete was used for the interior walls in seismic zones 6 and 7. The cast-in-place joints were made of B300 (C18/22.5) concrete. Accordingly to the investigated typical plans, the specified concrete quality was maintained, irrespective of the 1977 seismic event. The steel reinforcement was made initially of OB38 steel, corresponding to S235, and of PC52, corresponding to S355. After the 1977 seismic event, the steel was changed to PC60 (S405) and STNB (S490), while OB37 was used only for hoops. Note that the OB-type reinforcement bars were plain, the PC-type steels were deformed (ribbed) and the STNB was welded wire mesh, made of cold formed plain wire rods.

Table 2.8 – Properties of the material used for the large panels

Typical plan	**1615/X**			**770-81**		
Year	1973			1982		
CONCRETE						
Designation	B200	B250	B300	B200	B250	B300
Equivalent class	C12/15	C16/20	C18/22.5	C12/15	C16/20	C18/22.5
Mean cube strength (MPa)	20	25	30	20	25	30
Characteristic cylinder strength (MPa)	12	16	18	12	16	18
STEEL REINFORCEMENT						
Designation	OB38	PC52		OB37	PC60	STNB
Equivalent	S255	S355		S255	S405	S490
Type	Plain	Def		plain	def	WWM
Characteristic yield strength (MPa)	255	355		255	405	490
Characteristic tensile strength (MPa)	360	510		360	590	600

2.3 Database of RC Wall Seismic Laboratory Tests

2.3.1 Existing test databases

As the number of experimental investigations increases continuously the need for the data to be ordered emerged also. Laboratory tests on structural members are aimed to reproduce the as-built loading and boundary conditions and observe the behaviour mode and measure the response. The experiments are excellent for checking the accuracy of theoretical predictions and/or to assess the behaviour for devising explanatory theories. These two philosophies of conducting experimental research are blended in varying proportions and it seems a rule that as the first component gains priority the set of assumptions is introduced that not necessarily is in accordance with the as-built conditions. Contrary, the second component is biased to the accuracy of the assumptions that is the as-built boundary and loading conditions, and tends to postpone the theoretical part.

Three types of ordered information on lab tests was identified: reference list, catalogue and database. Reference list documents are the most widespread, in fact, each experimental investigation report includes a review of the literature regarding previous works in the field. Extended reference list documents are works dedicated especially to the review of the literature on a specific field. In the field of RC members subjected to seismic loading tests extended reference lists were published by Abrams [37] and Farrar et al. [44]. Catalogue type documents furnishes more detailed tabulated information on the experiments, mostly on specimen basis. Several authors included catalogued information on previous seismic wall tests and results in their papers as Greifenhagen and Lestuzzi [45], Farvashany et al. [46], and Orakcal et al. [47]. The data columns refers to specimen identification, dimensions, reinforcement ratios, material properties, loading characteristics and results obtained in terms of experimental vs. predicted shear strength. Extensive catalogues on reinforced concrete wall seismic tests were published by Hirosawa [48], Wood [49], and Gulec [50]. As the number of data lines increases in a catalogue, it can be used for statistical evaluations employing specialised computer programs featuring filtering, sorting and searching functions, and it can be referred to as database. RC wall cyclic test databases were assembled by Wood [51], Stanic et al. [52], and Gulec and Whittaker [53]. General RC member

cyclic test databases, including beams, columns and walls, were published by Panagiotakos and Fardis [54] and Biskinis et al. [55]. Online databases are the most easily accessible sources of test information and there is an increasing number of projects in this direction, for example PEER Structural Performance Database on RC column cyclic tests [56], Kawashima Lab's database on RC columns [57], shear wall database by Palermo [58], University of Minho's DABASUM on FRP-based shear strengthening of RC beams [59], and RILEM's MSC Data warehouse on masonry strengthening with FRP composites [60].

It is important to note that a significant portion of the test data is not available, for language barrier reasons, proprietary issues or not in mainstream publications. Some of the most important data sources are listed in Table 2.5, including conference proceedings, journals and research reports.

2.3.2 Database characteristics

The database described in the following sections was assembled with the aim of general overview of the cyclic tests carried out on RC walls, with particular attention paid to the boundary conditions. As mentioned in the foregoing section, the unit of a catalogue is commonly a specimen, see Table 2.9. In order to reduce the data collection time and bearing in mind the scope of focusing on the boundary conditions, which are in most cases invariables for a program, the unit of the present database is a test program. In general a database has two major clusters of data columns: specimen data and results. In the present phase the database contains information pertaining only to the first cluster of program data. In these conditions it can be referred to as a condensed program database, see Table 2.10.

A sample of the database is shown in Table 2.11. The data columns were grouped in three sets: program identification, specimen data and boundary conditions. The first set of data columns contains information regarding the laboratory the tests were performed at, year of reference and country name. As a convention, the year of reference was assumed to be the one corresponding to the earliest publication that contains detailed information on the program. Specimen data columns refers to designation, construction, specimen type, concrete technology, opening condition, strengthening condition, number of specimens, scale and web thickness. The third set of data columns includes information on the test-set-up, loading and boundary conditions.

Table 2.9 Structure of a specimen database

PROGRAM ID	**SPECIMEN ID**	**SPECIMEN DATA**			**RESULTS DATA**		
		data column	data column	data column	data column	data column	data column
Program 1	Specimen 1						
	Specimen i						
	Specimen n						
Program i	Specimen 1						
	Specimen i	DATA LINE for Specimen "i" in Program "i"					
	Specimen n						
Program n	Specimen 1						
	Specimen i						
	Specimen n						

Table 2.10 Structure of a condensed Program database

PROGRAM ID	**SPECIMEN DATA**				**BOUNDARY CONDITIONS**		
	data column	data column	data column	data column	data column	data column	data column
Program 1							
Program i	DATA LINE for Program "i"						
Program n							

Table 2.11 Sample of the database

PROGRAM ID		SPECIMEN					
Laboratory-Year	Country	Designation	Construction	Type	Concrete techn	Opening	Strengthening
AUTH-2003	Greece	MSW; LSW; FRPM	civil	wall element	monolithic	solid	non; FRP EBR
BFRL-1996	USA	GSS; PTT	civil	wall element	precast	solid	non
BHRC-2000	Iran	SHW	civil	wall system	monolithic	solid	non
BRI-1980	Japan	W	civil	wall-frame syster	monolithic	solid	non
CARLT-2000	Canada	wall	civil	wall element	monolithic	solid	non; FRP EBR
CBRI-1988	India	A; B; C; D; E; F	civil	wall component	precast	n/a	non
CEBTP-1989	France	KV	nuclear	wall element	monolithic	solid	non
CEBTP-1992	France	PH	nuclear	wall element	monolithic	solid; door; wind	non
CEBTP-2004	France	wall	nuclear	wall element	monolithic	solid	non
CHUG-1984	Japan	C; IS; B; E; O	civil	wall-frame syster	monolithic	solid; window	non
CHULA-2001	Thailand	W	civil	wall element	monolithic	solid	non
CISMID-2009	Peru	MQE; MFIEN	civil	wall element	monolithic	solid	non
CLARK-1996	USA	RW; BW; TW	civil	wall system	monolithic	solid; door	non

It is noteworthy that most of the data columns represented a constant parameter for a specific program. A few exceptions were represented by the wall thickness and specimen type, par example, which in many cases were variable inside a program, causing an effect of multiplication of the program. This was resolved by dividing the program in smaller units in order to have unique values for the data columns. This explains why other, more detailed information was excluded from the database.

As of March 2011, the database contains 151 data lines and 222 reference lines. The discrepancy is owing to the fact that a certain test program commonly is published more than once at different stages of data processing. The complete database is presented in Appendix A.

2.3.3 Overview of the database

Early laboratory investigations on RC walls subjected to in-plane lateral loads were conducted starting from the 1950s in USA, Japan, Canada and New-Zealand. This early period can be considered until the end of the 1970s, see Figure 2.8. A significant increase in the number of tested specimens in the 1980s and onward can be observed. It is important to stress again that the actual content of the database is limited to the available literature in English language and consequently is not exhaustive. It would be of great importance to obtain country-level reports on this topic by resident researchers who have more in-depth view of the situation in their own country. The geographic distribution of the actual content indicates an approximately one-quarter share of the experimental work between USA, Japan, Europe and other countries. The tested walls were representative of prototypes pertaining to civil constructions and to Nuclear Power Plants (NPP), the first case being more common. In the following discussions the NPP-walls were not considered.

According to the present content of the database the Romanian contribution to the RC wall experimental investigations is represented by 7 programs conducted at 4 laboratories, the earliest being dated from 1992, see Table 2.12. This should be also reviewed by researchers from each university centre in order obtain a more accurate view of the situation.

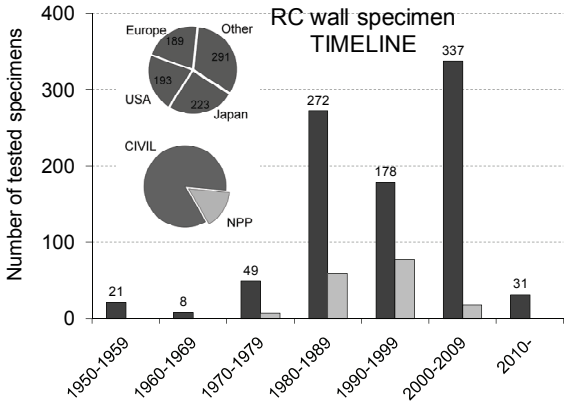

Figure 2.8 RC wall test timeline

Table 2.12 RC wall tests in Romania

PROGRAM ID		SPECIMEN					
Laboratory-Year	Country	Designation	Type	Concrete techn	Opening	Strengthening	No. of spec.
INCC-1992	Romania	Unit	wall-frame-slab s	precast	solid	non	1
UPT-1992	Romania		wall system	monolithic	door	non	9
INCT-1998	Romania	M; F	wall system	precast	solid	non	6
UPT-2005	Romania	SW; RW	wall system	monolithic	solid; door	non; FRP-EBR	5
UTCB-2007	Romania	W	wall system	monolithic	solid	non	5
UPT-2010	Romania	PRCWP	wall element	precast	solid; door cut-ou	non; FRP-EBR	5
UPT-2011	Romania	CSRCW	wall system	monolithic	solid	non; FRP-EBR	6

2.3.4 Specimen characteristics in the database

The experimental specimens modelling prototype walls of civil structures were classified in component, element and building system types, see Figure 2.9. Components are web-isolated panels or joints of precast elements. Wall elements are 1-storey, 1-plane and 1-bay structural members not framed by columns and beams. The components of a typical wall element and cross-sectional shapes are presented in Figure 2.10. Wall building systems are multi-storey, multi-plane or multi-bay or frame-wall assemblages. Note that there may be a need for judgement to make difference between a wall element with barbell cross section and a 1-storey frame-wall system. It can be seen in Figure 2.9 that the wall element and building system tests share a 45% and 40%, respectively, while the wall component tests represent 15% of the total civil wall specimens. A generic loading type data column was also introduced at this stage in order to separate quasi-static tests from dynamic ones. Complex programs featuring both loading types were divided in two uniform groups so as to comply with this criterion. Subsequent discussions are restricted to wall elements and building systems (components excluded) tested in quasi-static manner (dynamic tests excluded). The distribution of storey numbers amongst the wall building system specimens is also indicated in Figure 2.9.

Two further data columns referring to model-to-prototype scale and web thickness of the specimens were considered, see Figure 2.11. These parameters exhibited different distribution according to the type of the specimens: the scale of the wall elements was concentrated in the 0.25÷0.4 or 0.8÷1 ranges, while for the wall building systems the 0.2÷0.33 scale factor range was preferred; as for the web thickness, the 50, 80 and 100 mm values were representative for both the wall elements and wall building systems.

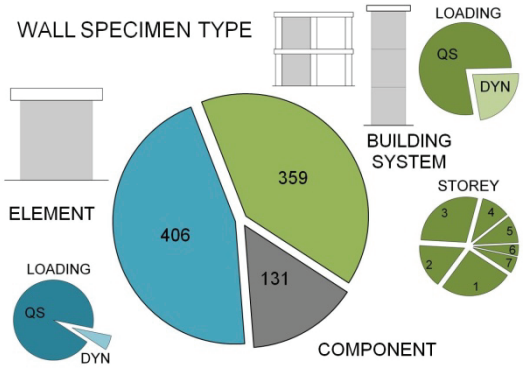

Figure 2.9 RC wall specimen types

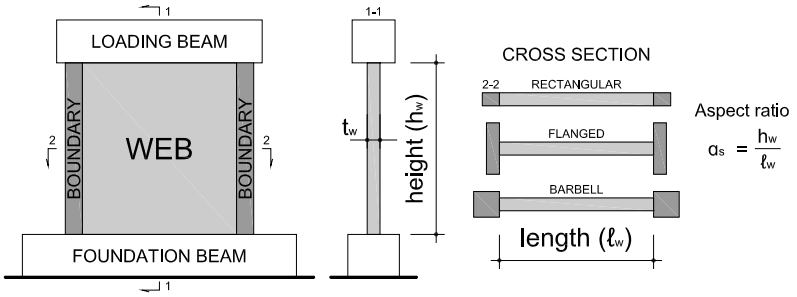

Figure 2.10 Components of a generic wall element

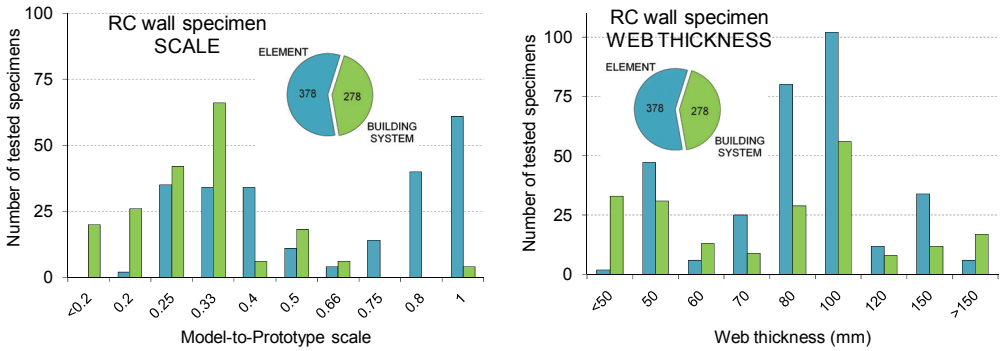

Figure 2.11 Scale and web thickness distribution

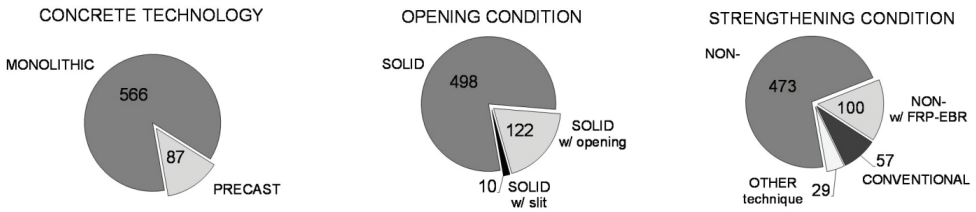

Figure 2.12 Distribution by concrete technology, opening and strengthening

Table 2.13 RC wall test programs that included FRP-EBR strengthening

PROGRAM ID		SPECIMEN					
Laboratory-Year	Country	Designation	Type	Concrete techn	Opening	Strengthening	No. of spec.
CARLT-2000	Canada	wall	wall element	monolithic	solid	non; FRP-EBR	7
TOKYU-2000	Japan	T; U; RC; CF; CFR; A	column wing-wal	monolithic	n/a	non; FRP-EBR	15
TUSJ-2000	Japan	Specimen	wall-frame syster	monolithic	solid; door; windo	non; FRP-EBR	10
AUTH-2003	Greece	MSW; LSW; FRPM	wall element	monolithic	solid	non; FRP-EBR	11
MGILL-2003	Canada	W	wall system	monolithic	solid	non; FRP-EBR; RC;	4
UUTAH-2003	USA	Specimen; wall as	wall system	precast	solid	FRP-EBR connecti	9
HOKU-2004	Japan	WA	wall-frame syster	monolithic	door; window	non; FRP-EBR	3
MMCAN-2004	Canada	CW; RW	wall element	monolithic	solid	non; FRP-EBR	3
NCREE-2004b	Taiwan	PF; WF	wall-frame syster	monolithic	solid; frame	non; FRP-EBR	6
UFUK-2005	Japan	W; specimen	wall-frame syster	monolithic	solid	non; FRP-EBR	6
UPT-2005	Romania	SW; RW	wall system	monolithic	solid; door	non; FRP-EBR	5
NTUSG-2010	Singapore		wall element	monolithic		FRP-EBR	4
UPT-2010	Romania	PRCWP	wall element	precast	solid; door cut-ou	non; FRP-EBR	5
UPT-2011	Romania	CSRCW	wall system	monolithic	solid	non; FRP-EBR	6

A series of three data columns were taken referring to concrete technology, opening condition and strengthening condition. As it can be seen in Figure 2.12, monolithic, solid and non-strengthened specimens prevailed over test programs including precast, solid with opening or slitted and strengthened specimens, respectively. Amongst the latter category three groups were identified according to the employed strengthening technique: conventional, FRP-EBR and other. Conventional techniques mean repair of the damaged walls by replacing of the crushed concrete and fractured reinforcements; FRP-EBR means Fiber Reinforced Polymers Externally Bonded on concrete surface; while other techniques included Steel Plates bonded, selective weakening, frame infill or wing walls. The restricted database contains 16 programs that included precast walls, 14 programs that involved walls with openings and 16 programs with walls strengthened by FRP-EBR technique. A detailed review of the tests on FRP-EBR strengthened RC walls was published by Demeter et al. [61].

2.3.5 Test set-up, loading and boundary condition database

The arrangement of the tested specimen relative to the laboratory floor, reaction frames, the number and position of the loading devices, and the beam used to convey the loads to the specimen is generically referred to as test set-up or test rig or mock-up. The majority of the tested walls were fixed to the laboratory's strong floor through a heavily reinforced foundation (base beam, lower beam, pedestal) and were loaded at the top through a loading beam, see also Figure 2.10. This arrangement was referred to as type-A test set-up, see Figure 2.13. As for the number and position of loading devices the term loading degree was defined in each principal direction, i.e. in-plane axial and lateral, and out-of-plane. Each degree represents a loading device acting in a specific direction at a specific location in one sense. The axial loading degree was zero (without axial load), one for simple control (constant axial load), or two or greater to realise complex control (rotation and variable axial loads). The lateral loading degree was one for monotonic loading and two for in-plane cyclic loading. Note that in many test programs the lateral loads were applied by double acting actuators, which integrate push and pull force capabilities in a single device. In those cases the lateral loading degree is two, according to the definition adopted previously. The position of the lateral load relative to the wall height was used to define the test set-up types, see Figure 2.13. As described above, in the case of the type-A set-up the lateral load is applied at the level of wall height. The type-B set-up has an L-shaped loading beam and the

load is applied lower than the wall height while in the case of type-C set-up the lateral load is applied higher than the wall through the stud of an inverted T-shaped loading beam. Note that in the case of type B and C set-up the lateral load generates a restraining and an additional moment, respectively, when the reference is made to the wall height. These moments are proportional to the lateral load and therefore can be referred to as load controlled rotation. Another way to apply rotation control at the top of the specimens is by means of the pantograph device, see Figure 2.13, which restrains rotation but the vertical and lateral displacements are free.

One of the major concerns of laboratory investigations on structural members is to reproduce the as-built real life conditions. Besides prototype-model correlation, the loading and boundary conditions are important issues to account for. The loading conditions regards the fashion the loads are applied and it can be depicted by the load history diagram that indicates the variation of loads in time. Because the loads are generally applied in displacement control, the displacement history plot may be of interest too. The greater the loading degree of a test set-up, the more complex loading history is possible to be employed. A review of the loading strategies for quasi-static cyclic tests on RC walls was published by Demeter et al. [62, 63].

The boundary conditions represent the degrees of freedom at the extremities of a structural member. In the case of RC wall seismic tests these conditions refer to the supporting conditions at the base, the structural components along the vertical edges, and the displacement and rotation control at the top loaded part of the wall. As for the supporting conditions, except a few cases, the wall specimens were fixed to the laboratory's strong floor. Structural components (as the boundary elements of the walls, see Figure 2.10) or structural members (like columns or orthogonal walls) along the vertical edges or in the vicinity of the vertical edges (in the case of multi-bay wall-frames or wall-systems) can have significant effects on the behaviour of walls, for example by the outrigger effect [37].

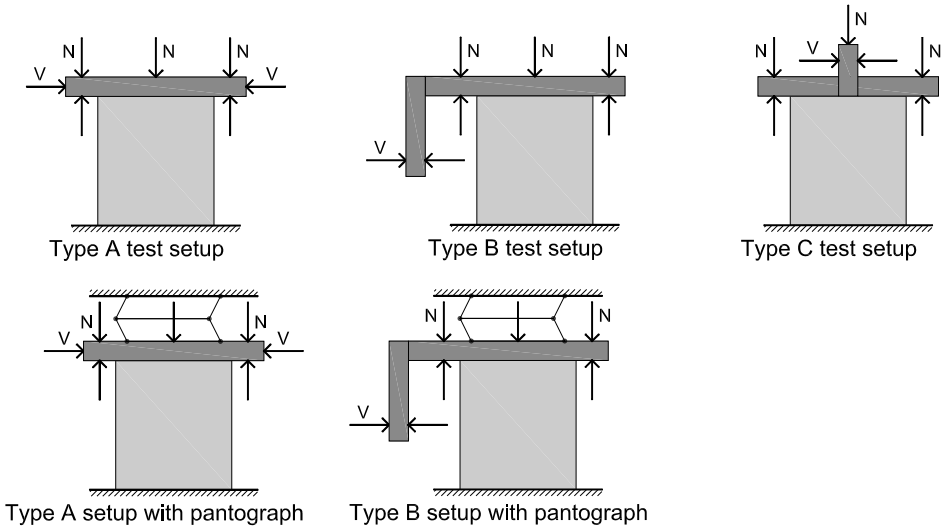

Figure 2.13 Test set-up types

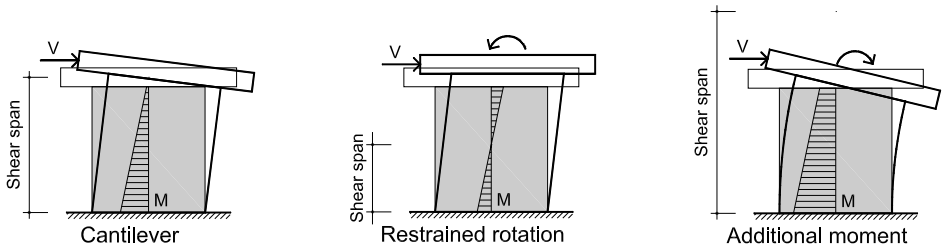

Figure 2.14 Boundary conditions

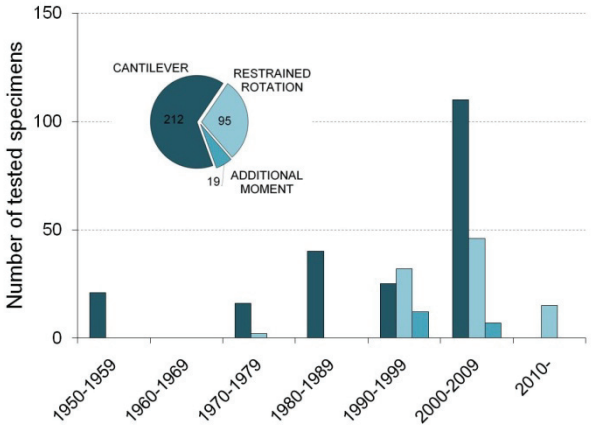

Figure 2.15 Timeline and distribution of the boundary conditions

The most important boundary conditions are imposed at the top by the displacement and rotation control of the loaded beam. These conditions can be characterised by the comparison of the shear span (moment to shear ratio) and the wall height, or by the relative values of the shear span to depth (i.e. length) ratio and aspect ratio (height to length ratio), refer to Figure 2.14 and Figure 2.10. The most widely used boundary condition is the cantilever, where the wall is fixed to the base and free at the top, that is, the shear span is approximately equal to the wall height and correspondingly the shear span to depth ratio equals the aspect ratio. In this case the failure mode is controlled by the internal strength ratios, i.e. the shear at flexural strength to shear strength ratio, see also Figure 2.2. In the second case, the rotation of the top beam is restrained by a moment acting inversely as the lateral load and therefore this case was referred to as restrained rotation. The shear span is significantly less than wall height and the shear span to depth ratio is less than the aspect ratio. Consequently shear failure is favoured. The third situation is when the rotation of the loaded beam is further increased by a moment acting in the same sense as the lateral load; this situation can be referred to as additional moment. The shear span is greater than the wall height and the shear span to depth ratio is more than the aspect ratio. In this case flexural failure is favoured. Note that multi-storey wall systems loaded at the top as cantilevers have additional moment condition if the reference is made to the first storey.

An analysis of the boundary conditions of the wall element tests in the database indicates, see Figure 2.15, that the cantilever test prevails overall, but it is

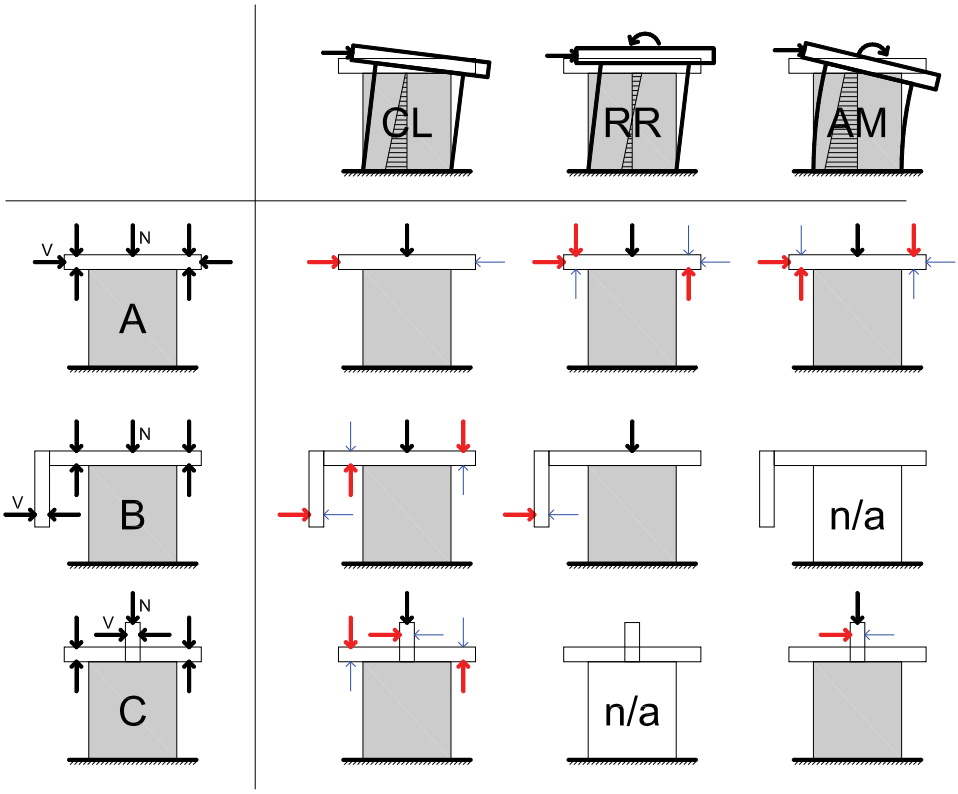

Figure 2.16 Loading configurations for different boundary conditions

also clear the increasing number of restrained rotation tests starting from the 1990s.

Finally, it can be stated that a specific boundary condition can be achieved by adequate set-up and loading. The matrix shown in Figure 2.16, gives some examples of loading configurations for each test set-up that result in different boundary condition. Each set-up has its initial boundary condition (A-CL, B-RR and C-AM), which can be modified by multiple axial load control.

3 QUASI-STATIC CYCLIC TESTS

3.1 Experimental program

The objectives of the experimental research were to record the seismic performance of the precast large wall panels considering the outrigger effect of adjacent structural members, to assess the weakening of doorway cut-outs and to investigate the performance of the CFRP-EBR strengthening method. The tests were carried out in the Reinforced Concrete Structures Laboratory of the Department of Civil and Industrial Buildings, Faculty of Civil Engineering, Politehnica University of Timisoara, Romania during March, 2008 through December, 2009. A general (condensed) overview of the program is given in Table 3.1. In the following sections a detailed description of the experimental program is presented.

3.1.1 Test matrix

An outline of the test program can be structured in three levels, see Figure 3.1 and Table 3.2. The first level is represented by a bare solid wall, which was the reference specimen. The second level comprises two bare walls with cut-out openings, which were identical in all aspects with the solid reference, except the presence of the cut-outs. The difference between the elements of this level was the width of the door opening. The third level is composed by two pairs of strengthened specimens, which corresponded in all regards to the second level walls and were additionally retrofitted. Besides the opening size, the difference between the specimens of the third level consisted in the state of the walls at the time of retrofitting: after sustaining a number of damaging load reversals, the specimens of the second level were upgraded to the third one by repair and post-damage strengthening, whereas their counterparts were prior-to-damage strengthened.

Table 3.1 – Overview of the experimental program

Program ID	Laboratory	Reinforced Concrete Structures Dep. of Civil and Industrial Bldgs Faculty of Civil Engineering Politehnica Univ.of Timisoara
	Country	Romania
	Year	2008-2009
Specimen	Designation	PRCWP
	Construction type	civil
	Specimen type	wall element
	Concrete technology	precast
	Opening	solid; door cut-out
	Strengthening	non; FRP-EBR
	No. of specimens	5 (2 double, 3 simple)
	Scale	0.83
	Web thickness (mm)	100
Boundary conditions	Set-up	A-type
	Loading	QSC
	Boundary condition	restrained rotation

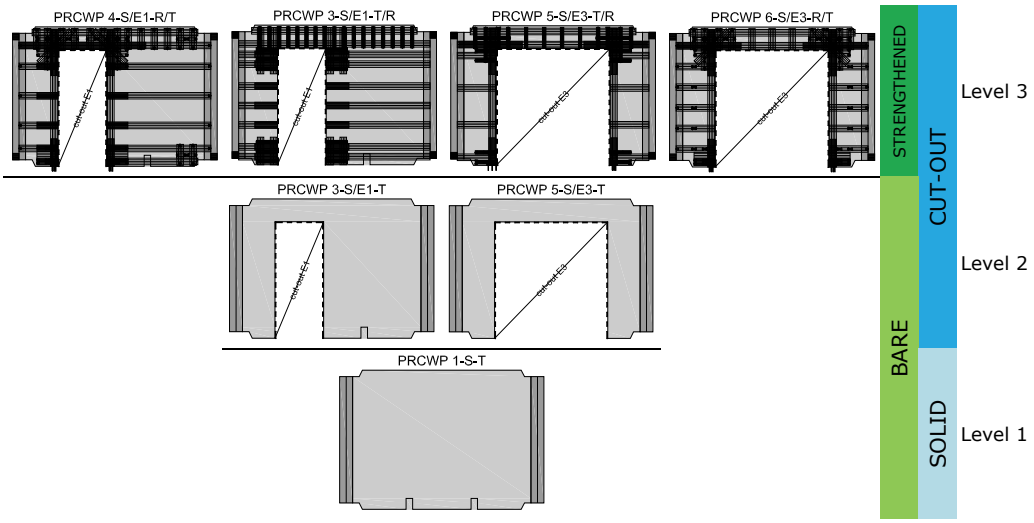

Figure 3.1 Test matrix

Table 3.2 Variables of the experimental program

Level	Element designation	As-built/ cut-out opening type	Strengthening condition
1	PRCWP 1-S-T	Solid (S)	Bare (T)
2	PRCWP 3-S/E1-T	Solid/narrow door (S/E1)	
	PRCWP 5-S/E3-T	Solid/wide door (S/E3)	
3	PRCWP 3-S/E1-T/R	Solid/narrow door (S/E1)	Post-damage strengthened (T/R)
	PRCWP 4-S/E1-R/T		Prior-to-damage strengthened (R/T)
	PRCWP 5-S/E3-T/R	Solid/wide door (S/E3)	Post-damage strengthened (T/R)
	PRCWP 6-S/E3-R/T		Prior-to-damage strengthened (R/T)

Note: PRCWP – Precast Reinforced Concrete Wall Panel

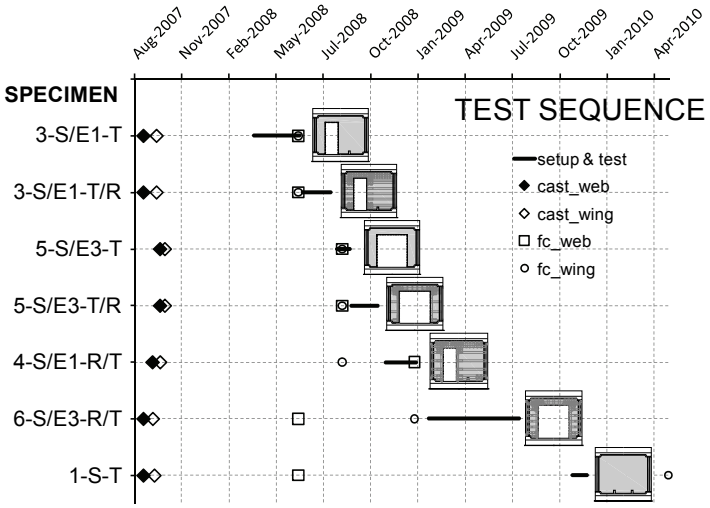

Figure 3.2 Fabrication and testing time-line

A comparison line is defined as a series of at least two specimens or tests that are identical in all regards except one parameter (variable). These lines are set up in order to assess the effect of the investigated variable on the behaviour of the specimens. The present program contains three comparison lines, each of them comprising of three tests, see Figure 3.3. The first comparison line was set to assess the weakening effect of doorway cut-out. The reference specimen of this line is the solid specimen while the variable is the cut-out width. The second and third comparison lines are referred to as strengthening effect of CFRP-EBR, with reference specimens being the bare walls with narrow and wide door cut-out, respectively and the variable being the strengthening condition.

The fabrication and testing time-line of the specimens is shown in Figure 3.2. The construction of the specimens was performed during August-October 2007, while the testing started in June 2008. The sequence of testing was chose so as to identify the behaviour mode and critical shear transfer regions for the bare specimens with cut-out, in order to rely on the subsequent strengthening. The first tested specimen was the PRCWP 3-S/E1-T bare wall with narrow cut-out. The second test was performed on the same specimen, but after repair and strengthening was undertaken. The third and fourth tests were similarly carried out on the bare and thereafter on the repaired/strengthened specimen PRCWP 5-S/E3-T and PRCWP 5-S/E3-T/R, respectively. In the fifth and sixth tests the prior-to-damage strengthened companions of the foregoing specimens were tested. The seventh (last) test was performed on the solid bare specimen PRCWP 1-S-T.

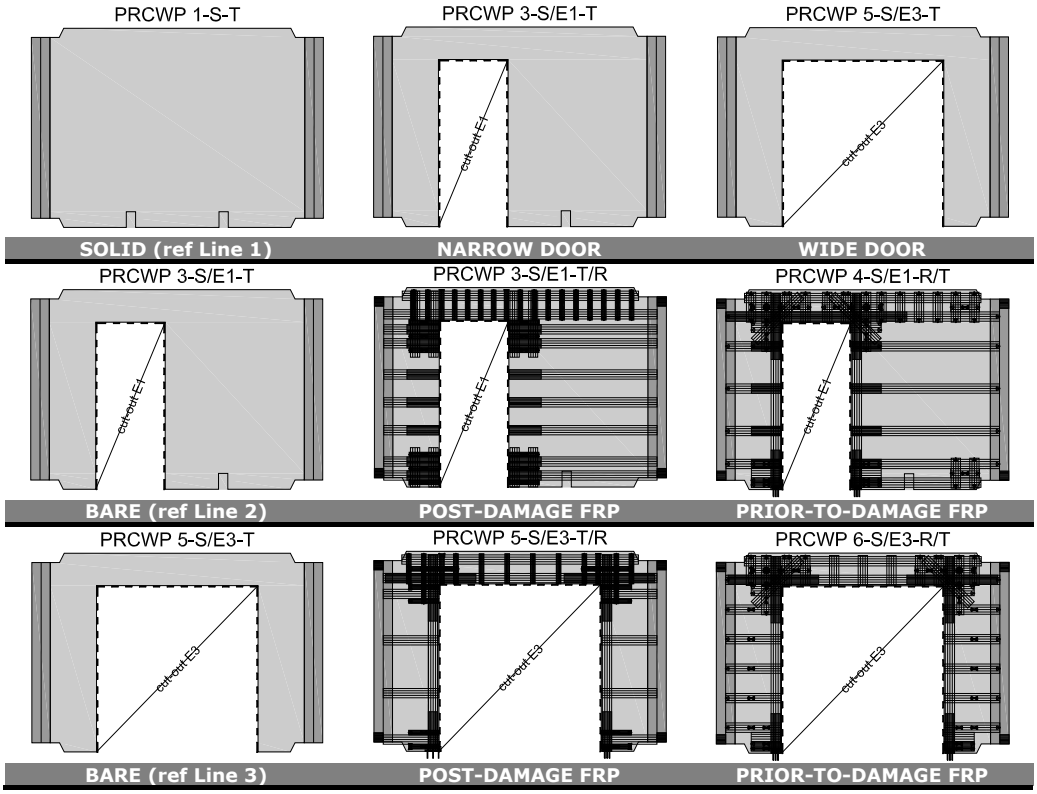

Figure 3.3 Comparison lines

3.1.2 Wall specimen characteristics

The experimental walls were constructed according to the 1980 Romanian large panel manufacturing practice described previously in section 2.2. Although there are no available statistics regarding the structural details of wall panels used in the large panel buildings, it was assumed that the post-1977 reinforcing pattern prevails. The prototype wall panel for the experimental program was the interior longitudinal panel labelled I36-1 of the typical plan 770-81, see Figure 2.6. This type of wall panel can be found in several other typical plans of the 770-series and can be considered as representative for the post-1977 large panel buildings. The dimensions of the prototype are 3300 mm length, 2580 mm height and 140 mm thickness, and it weighs 2900 kg. Taking into account the load capacity of the testing facility and the lifting capacity of the bridge crane available in the laboratory, a geometric reduction factor of 0.83 was adopted, which corresponds to 1:1.2 model to prototype scale, see Figure 3.4a. Regarding the specimen type discussed in section 2.3.4, the experimental specimen can be referred to as wall element, because it represents a 1-storey, 1-bay and 1-plane member. Each specimen was composed of a web-panel and two T-shaped boundary elements referred to as wings, see Figure 3.4b. The purpose of the wing elements was to prevent the out-of-plane displacements during in-plane lateral loading and to reproduce the vertical connection joints toward the adjacent panels of the as-built conditions.

The specimens were fabricated at a construction site in Timisoara using the reinforcement and concrete provided by the constructor firm. The process of wall element construction is presented in Figure 3.5. Likewise the original large panels the experimental walls were cast in horizontal position. Modular formwork panels available at the building site were used to create a plane surface 100 mm above the support level in order to have space for the out-of-plane wings. The experimental specimens were poured in two phases. First the web-panel reinforcement was mounted in timber formwork, this was placed and secured to the modular panels and the web concrete was poured. Note in Figure 3.5 the protruding connection re-bars along the edges of the web-panel. After a few days of curing, refer to Figure 3.2, the timber formwork was removed, wing reinforcement cages were mounted in the wing formwork and the wings were poured. The completed specimens were stacked on the building site and then transported to the laboratory where they were deposited in horizontal position one over the other.

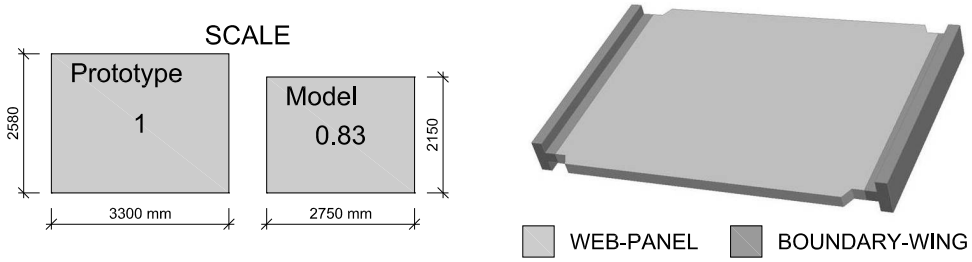

Figure 3.4 Specimen scale and components

Figure 3.5 Construction of the specimens

The concrete outlines and reinforcing details of the solid reference specimen are depicted in Figure 3.6. The proportions of the solid wall and its components (web and wing) are listed in Table 3.3. The dimensions of the web-panel were 2750 mm length, 2150 mm height and 100 mm thickness. One can observe that the web thickness is slightly less than the one corresponding to the general model-to-prototype scale factor (116.7 mm), which was adopted to reduce the capacity and simplify the construction. However, the average thickness measured on the specimens was greater than the nominal value, consequently it was somewhere in the midway. The cross sectional area of the solid web-panel was 2750 cm^2 and its aspect (height-to-length) ratio was 0.8. The in-plane area of the web-panel was 5.9 m^2. Similarly to the original large panels, shear keys were formed along the edges of the web-panel to improve the sliding shear resistance, see details in Figure 3.6c. For the same reason larger set-backs were provided at the panel corners. The wings were composed of a short in-plane connection zone and a flange perpendicular to the wall plane. Flange dimensions were 300 mm width and 100 mm thickness. Each wing added 200 mm to the length and 400 cm^2 to the section area of the web-panel. The nominal weight of the solid wall specimen was 1900 kg.

Steel reinforcing details of the solid reference wall are presented in Figure 3.6. Web-panel reinforcement consisted in single curtain composed of a welded wire mesh of ϕ4 mm diameter cold drawn wires at 100 mm centres, horizontal deformed bars of 10 mm diameter at 265 mm centres and 2 ϕ14 mm diameter vertical continuity bars. The flanges of the end-wings were reinforced by spatial cages made of 4ϕ14 mm longitudinal deformed bars and ϕ8 mm plain transverse hoops at 85 mm centres and a ϕ16 mm vertical continuity bar, see Figure 3.6d.

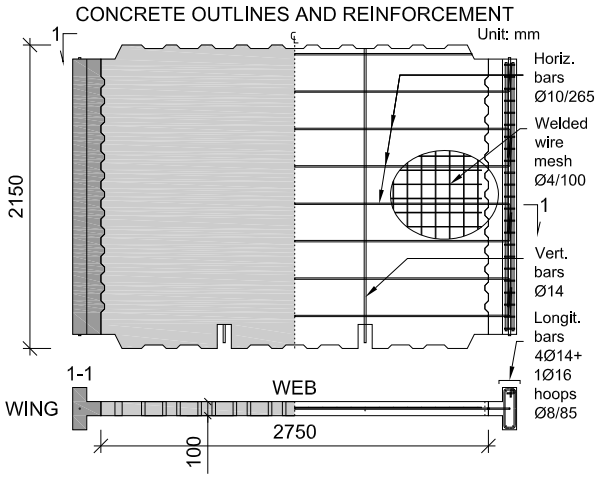

(a)

(b)

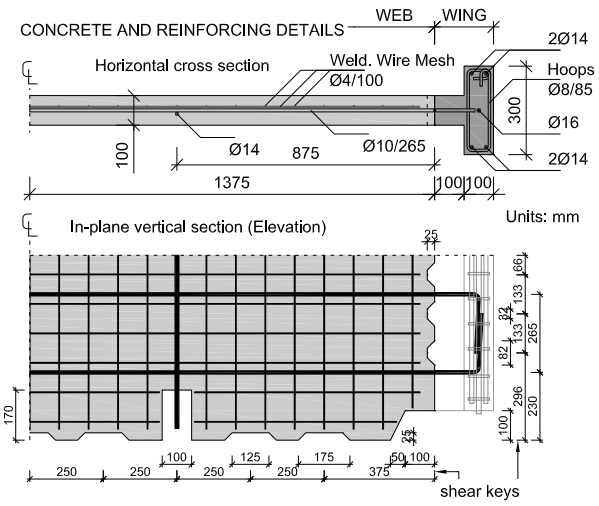

(c)

(d)

Figure 3.6 Concrete outlines and reinforcement details

Table 3.3 – Wall specimen proportions

COMPONENT	ℓ (mm)	h (mm)	b (mm)	A_c (cm²)	A (m²)	α_s
Web-panel	2750	2150	100	2750	5.91	0.78
Boundary wing	200	1950	100	400	0.39	n/a
Wall specimen	3150	2150	100	3550	6.69	0.68
Cut-out E1	750	1800	100	750	1.35	2.4
Cut-out E3	1750	1800	100	1750	3.15	1.03
Pier #1	500	2150	100	500	1.08	4.3
Pier #2 E1	1500	2150	100	1500	3.23	1.43
Spandrel E1	750	350	100	350	0.26	2.14
Spandrel E3	1750	350	100	350	0.61	5

Note: ℓ - length; h – height; b – thickness; A_c – area of cross-section; A – in-plane area; α_s – aspect ratio.

Table 3.4 Steel ratios of the wall specimen

COMPONENT	Horiz steel ratio	Vertic steel ratio	Transv steel ratio
Web-panel	0.42%	0.24%	Plain
Boundary flange	0.79%	2.72%	2.38%
Web-to-wing	0.28%	plain	Plain
Wall-to-foundation	n/a	0.17%	n/a

The web-to-wing connection was realised through anchoring the horizontal ϕ10 mm panel-bars into the confined core of the flange. Note that the approx. 150 mm wide short in-plane connection regions between the web and the flanges the only reinforcement were these horizontal protruding bars, that is no vertical re-bars due to welded wire cut-off and no transverse steel. The wall-to-foundation anchorage was realised by lap-welding of the 4 vertical continuity re-bars to the starter bars of the foundation. The steel reinforcement ratios are presented in Table 3.4. One can observe that the web-panel horizontal steel ratio (0.42%) is larger than the corresponding value of the prototype wall (0.3%, see Table 2.7); in fact the steel ratio should remain the same if the geometric scale is rigorously applied. The difference can be attributed to the smaller-than-scale wall thickness, the larger than scale welded wire mesh diameter (ϕ4 instead of ϕ3) and steel quality (PC52 instead of PC60). Note the reduction of the steel ratios at the connection regions.

All four specimens with openings represented an initially solid wall which was affected by a doorway cut-out. Consequently the reinforcing details were the same for all specimens, irrespective of the cut-out conditions, as for the solid specimen. By removing a door-shaped portion from a solid wall the rectangular outline of the web-panel changes and it becomes a frame-like element composed of two piers and a spandrel beam at the sides and above the opening, respectively. In order to ease the fabrication process the specimens were cast with openings instead of literally cutting out the door-sized portions, see Figure 3.5. The outlines of the specimens with cut-out opening and the designation of the web-panel components are presented in Figure 3.7. It can be observed that the left and right side piers were designated as pier #1 and #2, respectively. The proportions of the piers and spandrel beam are defined by the size and location of the opening. Two opening sizes were considered, namely narrow (small) door referred to as E1 and wide (large) door referred to as E3. The E1-door was 750 mm wide by 1800 mm high and the E3-type wide door was of the same height, but 1750 mm wide. Table 3.3 contains the proportions of the openings, piers and spandrels in the same order as for the solid reference so as to facilitate comparison. It is instructive to note the differences between the solid web-panel and the piers in terms of length, cross sectional area, in-plane area and aspect ratio. Taking into account that the web-panel's and piers' height is the same, the increase of the aspect ratio indicates an inversely proportional change in the cross section. Note that in the case of the spandrel beams the shear span is parallel to its length and consequently the aspect ratio was ciphered accordingly as length-to-height ratio and not vice versa as for the other components. With regard to the location of the openings the E1-door was eccentric while the E3 opening was centred. Quantitatively, this can be indicated in two ways, see Table 3.5: by the position of the upper left corner of the opening with respect to the corresponding corner of the solid wall (a and b values, as in [64]) and by the ratio of the left wall edge to opening centreline distance and the wall length (x/l, as in [65]), refer also to Figure 3.7. Note that "a" and "b" represents in fact the length and height of pier #1 and the spandrel beam, respectively which are the same for both openings.

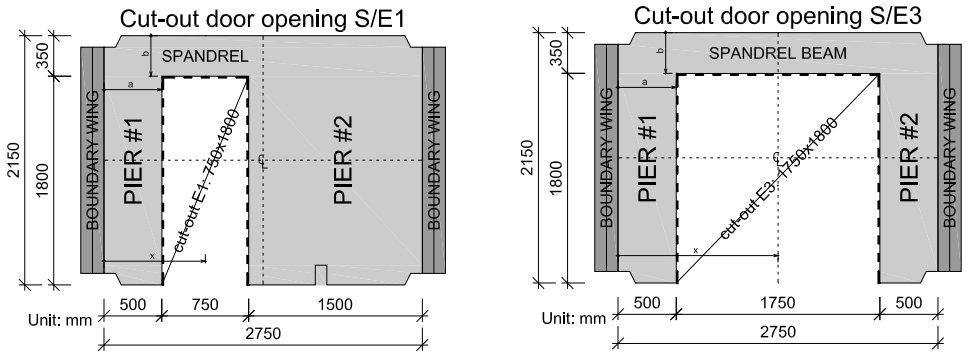

Figure 3.7 Cut-out openings

Table 3.5 – Opening location and ratio

Opening type		**Narrow door (E1)**	**Wide door (E3)**
Location	Location	eccentric	centred
	a (mm)	500	500
	b (mm)	350	350
	x/l	0.32	0.50
Opening ratio	Length ratio l_o/l_w	0.27	0.64
	Height ratio h_o/h_w	0.84	0.84
	Diagonal ratio $\sqrt{\frac{{l_o}^2+{h_o}^2}{{l_w}^2+{h_w}^2}}$	0.56	0.72
	Cross section ratio A_{co}/A_{cw}	0.27	0.64
	In-plane area ratio A_o/A_w (%)	23	53
	Peripheral ratio $\sqrt{A_o/A_w}$	0.48	0.73

Note: a – opening-to-web panel upper left corner horizontal distance; b - opening-to-web panel upper left corner vertical distance; x – opening centreline position from the left edge of the web panel; l_o - opening length; h_o - opening height; l_w – web-panel length; h_w - wall height; b_w – thickness of the web; $A_{co} = l_o b_w$ – cross-section area of the opening; $A_{cw} = l_w b_w$ – gross cross-section area of the web-panel; $A_o = l_o h_o$ in-plane area of the opening; $A_w = l_w h_w$ in-plane area of the web-panel.

The x/l ratio yields 0.5 for the centred E3 opening and 0.32 for the left-ward eccentric E1 door. A third method that defines the location could be the distance between the centrelines of the opening and the web-panel. The most comprehensive geometric trait that characterises a pierced (perforated) wall is the opening ratio that indicates the relative proportions of the opening and the solid wall. In Table 3.5 are listed a series of various opening ratios, namely length-(as in [65, 66]), height-(as in [66]), diagonal-, sectional-, areal-[67] and peripheral ratios. Each of these ratios relates the corresponding dimensions of the opening and the solid web-panel consequently are non-dimensional numbers less than unity or percents. Thus, one can say for example that the E1 opening represents 0.27 (or 27%) of the solid web-panel's cross section or the reduction (weakening) of the in-plane area of the solid wall caused by the E3 cut-out was 0.53 (or 53%). The peripheral ratio is the square root of the in-plane area ratio, as reported in [66, 68]. It is noteworthy that if the dimensions of the solid wall are taken as the centre-to-centre distances of the boundaries this would yield slightly smaller opening ratios. This was not the case in the present study because the precast web-panel is a clearly distinguished component of the wall element.

3.1.3 Strengthening

The strengthening was performed by means of Carbon Fiber Reinforced Polymers (CFRP) using the Externally Bonded Reinforcement (EBR) technique. In the followings a general overview of the strengthening is presented, while more explicit details are given in Appendix B. The overall objectives of the strengthening were to counterbalance the weakening incurred by a solid wall as a result of a door cut-out. The conventional goal to fully re-establish all the seismic performance characteristics seems to be difficult to be achieved. The approach of selective strengthening, that is addressing each of the response properties separately, could be more appropriate; however, it was impracticable in the case of the present experimental program due to the uncertainties regarding the behaviour of the wall specimens and of the CFRP-strengthening system under the applied loading and boundary conditions. Hence, a conservative empirical approach was adopted, which aims to enhance the seismic performance by retrofitting the critical regions.

The CFRP-layout of the four strengthened specimens is depicted in Figure 3.8. Two of the specimens namely PRCWP 3-S/E1-T/R and PRCWP 5-S/E3-T/R were post-damage strengthened, while the other two specimens PRCWP 4-S/E1-R/T and PRCWP 6-S/E3-R/T were retrofitted prior-to-damage. Note that the end group of letters in the specimens' designation refers to the strengthening condition, T/R meaning Tested and Retrofitted while R/T stands for Retrofitted and Tested. The post-damage strengthening was preceded by the repair of the specimens which comprised the replacement of the crushed and spalled concrete with high-strength mortar. Details on the repair are provided later, in Appendix B. Two types of unidirectional Carbon Fiber (CF) sheets, denoted by S1 and S2, were applied by wet layup method. The properties of the CF sheets and of the corresponding epoxy resins are presented in a subsequent section. The S1 and S2 CF-sheets were utilized mostly in form of strips with 100 mm and 50 mm width, respectively. The strengthening was carried out symmetrically on both faces of the wall. The substrate preparation consisted in grinding the concrete surface, rounding the edges (20÷30 mm radius), drilling ϕ10 mm holes through the wall and vacuum-cleaning.

The strengthening strategy was based on the behaviour and failure mode observed during the tests performed on the bare specimens (3T and 5T). The identified behaviour aspects were as follows: (1) flexural cracking at the joints of the spandrel beams and wall piers, (2) shear cracking of the piers, and (3) concrete spalling and crushing at the beam-pier joints and at the piers' bottom corners near the cut-out opening. Consequently, the strengthening strategy was divided into three directions: (1) to offer flexural capacity along the vertical and horizontal edges of the cut-out opening, (2) to increase the shear capacity of the wall piers, and (3) to provide confinement effect at the cut-out opening corners. The CFRP-strips intended to address these aims were designated as flexural (f), shear (sh) and confinement (c) sheets. For comparison reasons Figure 3.9 shows separately the assigned components of the strengthening layout for each of the retrofitted specimens. As a general rule, the unidirectional CFRP-strips were oriented parallel to the tension forces for flexural strengthening, parallel to the shears for shear strengthening and perpendicular to the compressions for confinement. The flexural strips (f) were placed alongside the opening outline and along the upper edge of the spandrel beam. Except specimen 3-T/R, the openings were continuously bounded by long strips and a second series of shorter bands were overlaid at the corners, and vertical anchorage was provided to the base beam. Additionally for specimens 4 and 6, inclined strips were disposed at the upper corners of the openings and horizontal

anchorage was provided to the wing walls. The layout altering was an evolutionary process based on the experience gained after the previous tests.

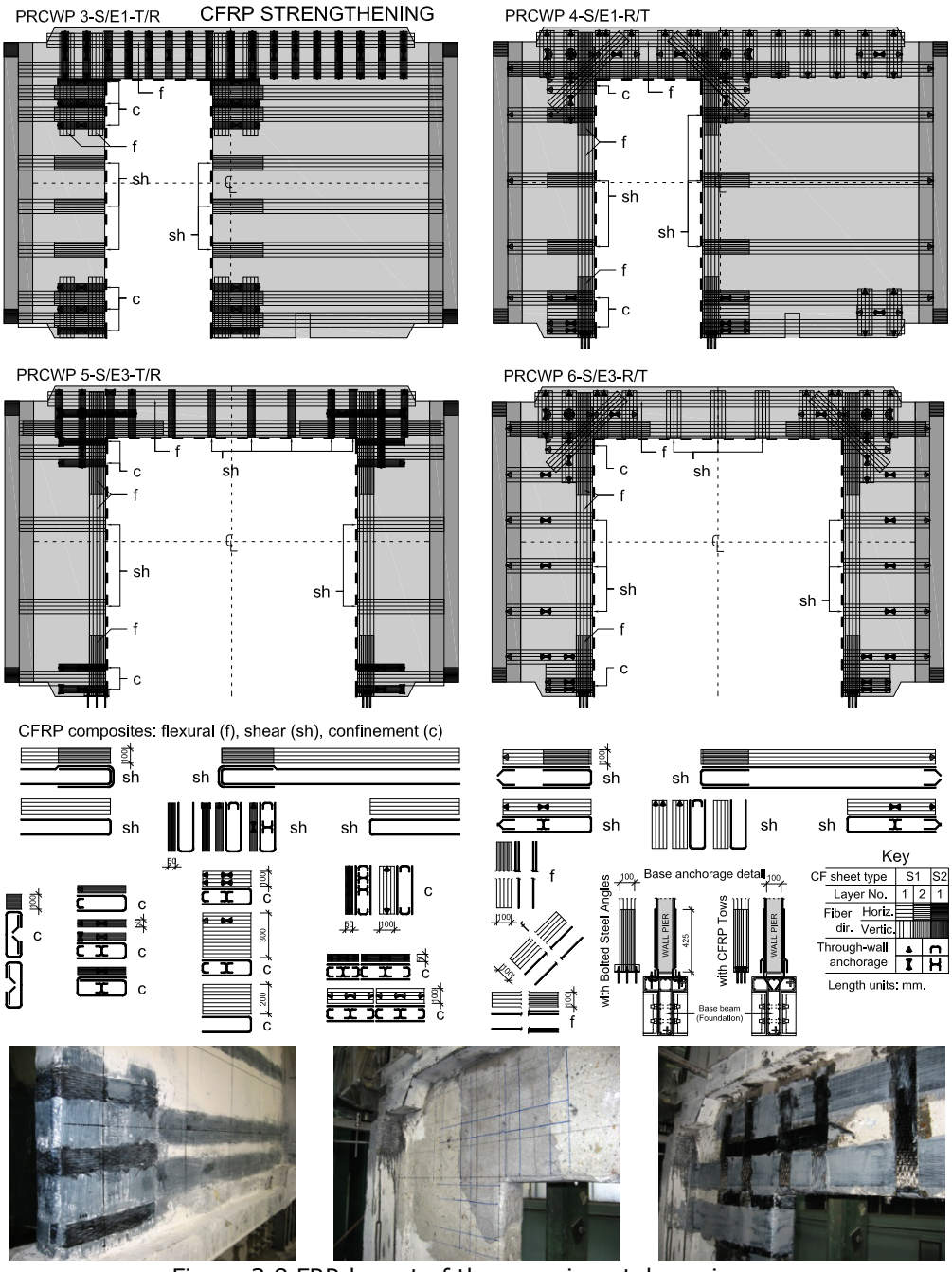

Figure 3.8 FRP-layout of the experimental specimens

The author is aware that the flexural strips fail to fully comply with the rules regarding the fibre orientation that is the CFRP-strips subjected to tension in a loading direction will be subjected to compression in the opposite loading direction. Consequently there are concerns regarding the effectiveness of the flexural strips. The shear strips (sh) were disposed horizontally on the piers and vertically on the spandrel beam so as to be parallel with the local shear forces. The CFRP-bands on the piers were 100 mm wide S1-type strips at 300÷500 mm centres. A shear-line was composed either of a single U-shaped strip or of more strips overlapping at the opening-side edges. The wing-side ends were anchored to the flanges (confined cores) in the case of specimens 4 and 6, the latter being provided with additional cross-ties. The spandrels of the 3-TR and 5-TR specimens were retrofitted by 50 mm wide S2-type CFRPs while for the other two specimens S1-CFRPs were used. The strips were shaped similarly to the conventional steel stirrups either with open legs or closed by cross-ties.

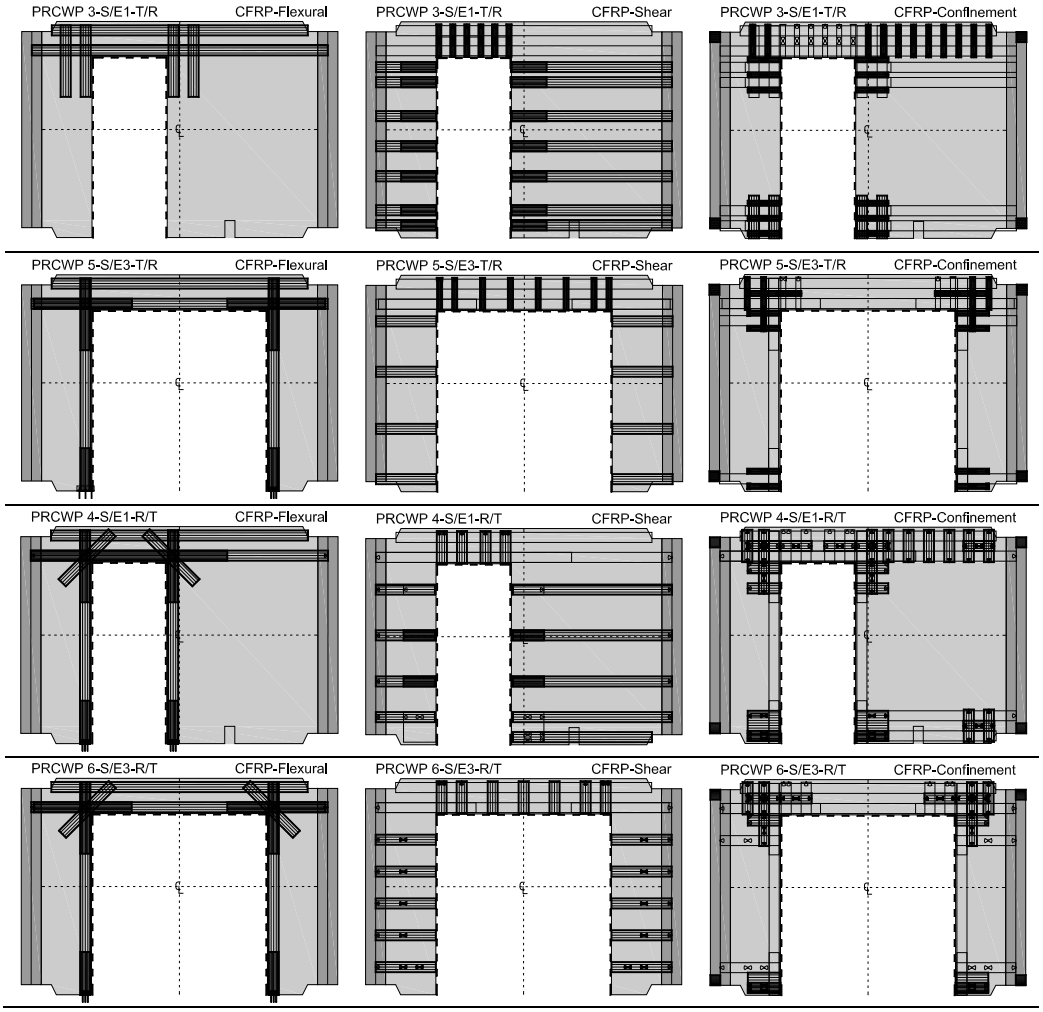

Figure 3.9 Flexural, shear and confinement FRP strengthening

Table 3.6 FRP consumption

Specimen	**3-S/E1-T/R**	**4-S/E1-R/T**	**5-S/E3-T/R**	**6-S/E3-R/T**
S1 CF (m^2)	6.35	7.83	3.87	6.15
S2 CF (m^2)	2.10	1.00	1.52	1.14
S1 resin (kg)	10.50	10.00	7.30	9.40
S2 resin (kg)	3.93	2.55	4.10	3.04
Wall area (m^2)	10.42	10.42	6.92	6.92
CF S1+S2 (m^2)	8.45	8.83	5.39	7.29
CF S1+S2 (g)	2758	2419	1830	2119
Resin S1+S2 (kg)	14.43	12.55	11.40	12.44
Specific CF (m^2/m^2)	0.81	0.85	0.78	1.05
Specific CF (g/m^2)	265	232	264	306
Specific resin (kg/m^2)	1.38	1.20	1.65	1.80
No. of CFRP cross-ties	75	48	80	72

Note: CF – Carbon Fibre fabric.

The confinement (c) strengthening of the specimens consisted in CFRP-hoops with cross-ties at the piers' inside toes, at the pier-to-beam connection regions, along the upper edge of the wide piers and at the wing ends. In the case of specimens 3 and 5 the confinement was exclusively made of S2-CFRPs while for specimens 4 and 6 S1-type hoops and S2-cross-ties were used. In the case of specimen 4 the outside toe of the wide pier was also confined.

The material consumption for the strengthening of each wall is shown in Table 3.6. The specific usages were ciphered with reference to the gross wall area composed of two times the in-plane areas (inclusive the in-plane parts of the wings) and the transverse area of the pier edges at the openings. The specific CF-usage ranged between 0.8÷1 m^2CF/m^2wall or 230÷300 g CF/m^2wall while the resin amount was 1.2÷1.8 kg/m^2wall. The number of cross-ties was 50 to 80 per wall.

Strengthening details are provided for the base anchorages and pier-to-beam connection in Figure 3.10. At the inside toes of the piers the anchorage of the vertical flexural strips was resolved by two methods: with bolted steel angles and with CFRP *fingers*. In the first case in the base beam a channel was made with approx. 20 mm depth 150 mm length and 50 mm width. In the next step three vertical ϕ10 mm holes were drilled. The channel and the holes were vacuum cleaned. Prior to the application of the CFRPs the holes were filled with resin. The CFRPs were laid on the bottom of the channel which was subsequently filled to the level of the beam with resin. A previously drilled 50 mm equal wing steel angle was then placed over the resin-filled channel which was gripped to the foundation through three fi8 mm threaded bolts pushed to the vertical holes. After curing the bolts were tightened by nuts. In the second case preparing phase consisted in drilling three ϕ10 mm inclined holes 100 mm deep in the base beam at the edge of the pier toes after which the holes were vacuum-cleaned. Preceding the application of the flexural strips the holes were filled with resin and 50 mm wide by 250 mm long S1-type CFRPs were squeezed inside the holes the other end of these being laid and spread on the toe of the pier overlapping the flexural strips. The former anchorage was used only for pier #1 of specimen 5-S/E3-T/R, all the other being the latter type. The strengthening details of the pier-to-spandrel connection regions were the most difficult due to the congestion of the flexural, shear and confinement strips. During the preparatory works a series of ϕ10 mm holes were drilled through the wall typically in a grid-like pattern at 150 mm centres. The ingress and egress portions of the holes were rounded by shallow drilling with larger diameter. The holes were cleaned from dust by vacuum and air blasting.

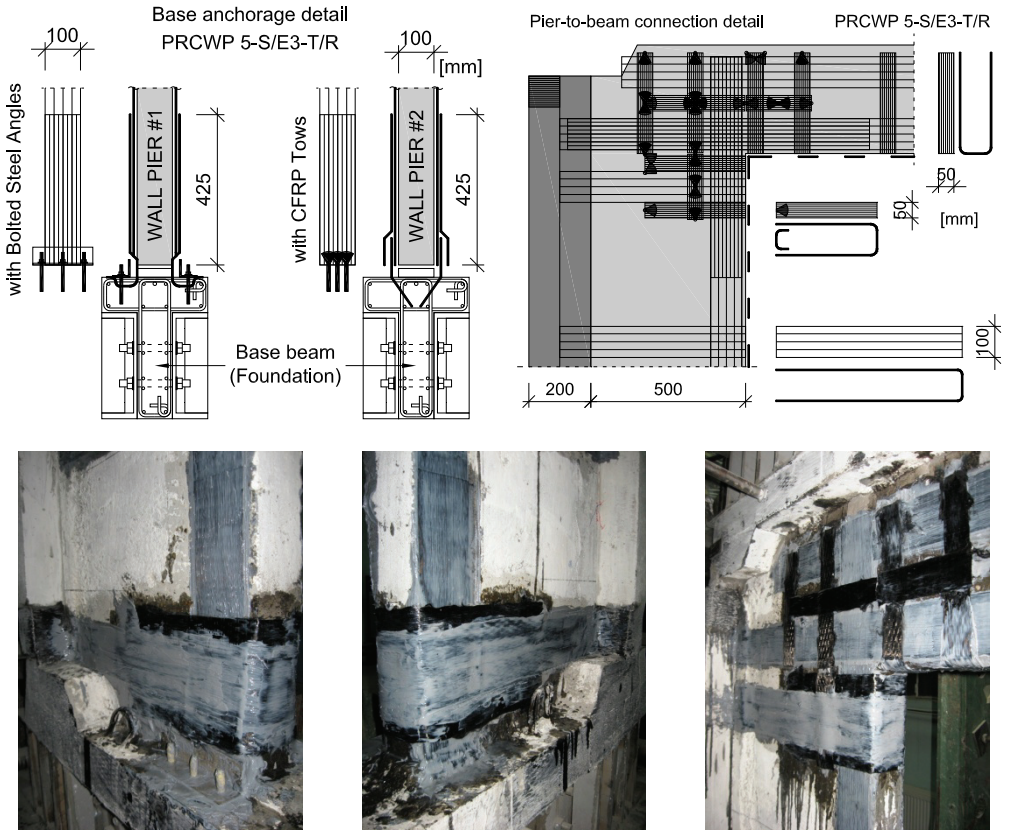

Figure 3.10 FRP strengthening details

After the layup of the flexural strips the CFRP cross-ties were mounted by pulling the previously impregnated S2-type 50x250 mm strips through the holes and laying and spreading the ends in one direction (C-shape) or aside (H-shape) on the opposite wall faces. The remaining pits were sealed by S1 resin and the CFRP-hoops were overlaid in a pattern that the cross-ties closed (connected) hoop legs.

3.1.4 Material properties

The structural materials used in the experimental program were as follows: concrete, steel reinforcement, CFRP reinforcement and repair mortar. Material tests were carried out on concrete (according to [98]) and steel (in compliance with [99, 100]) samples while the properties of the CFRP and the repair mortar were specified by the producer.

The normal-weight concrete was provided by the construction firm to the site the elements were fabricated at. From each batch three 150 mm edged cube samples were obtained. Additionally from one batch three 100x100x300 mm prisms and three 150x300 mm cylinders were fabricated, see Figure 3.11a. After concrete setting and hardening initiation (one or two days) the samples were removed from the moulds and were placed into a water basin and maintained there during strength development. The compression tests were carried out using a Universal Testing Machine of 2000 kN capacity, see Figure 3.11b. The material tests were planned to be carried out on the day of the testing of the corresponding wall elements, refer to Figure 3.2, although this was not possible in all the cases due to double tests and casting more elements from one concrete batch.

The results of the compression tests obtained on cube samples are shown in Figure 3.12 and in Table 3.7. Concrete batches of web-panel and boundary wings were numbered sequentially in the order of casting. There was a considerable scatter in the compressive strength of the concrete which is indicated more clearly by normalising the results to the strengths of the reference solid specimen, see Figure 3.12.b. In part this can be attributed to the differences in the ages of the concrete samples at testing (t_1) which varied from 294 to 979 days, see Table 3.7. As per Eurocode 2 [69] the variation of the concrete strength by time is given by the coefficient $\beta_{cc}(t)$. In order to arrive at the characteristic strengths of the concrete, that is the cylinder strength at 28 days, the measured cube strengths were transformed in cylinder values $f_{cm}(t_1)$, than the coefficient beta was employed to roll back the time to 28 day and finally mean to characteristic transformation was performed as per $f_{ck} = (1 - 1.64 \cdot 0.15) f_{cm}$ reported in [70]. The concrete classes of the web-panel concrete are indicated in Table 3.8. It is clear that the concrete classes differ from the intended C16/20 of the prototype, but this was a compromise to be accepted.

(a) (b) (c)

Figure 3.11 Concrete testing: (a) samples; (b) universal testing machine; (c) compression test on concrete cube

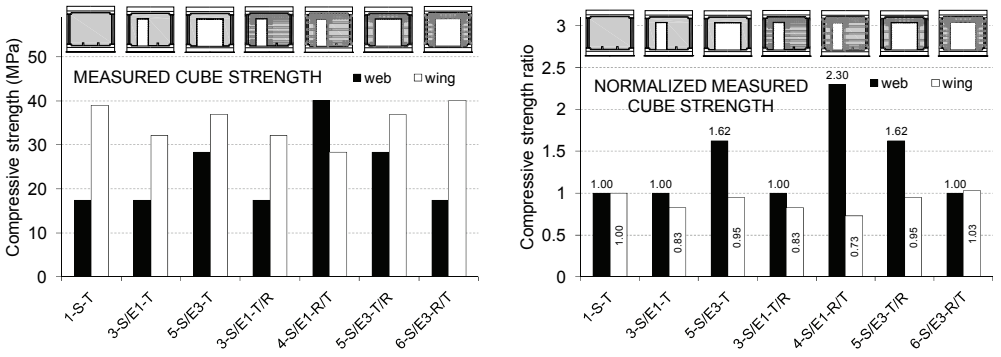

(a) (b)

Figure 3.12 Compressive strength of concrete

Table 3.7 Concrete sample ages and compression test results

Element / Component		Batch #	Age t_1 (day)	Age t_2 (day)	$f_{cm,cube}(t_1)$ (MPa)
1-S-T	web	B#1	294	841	17.5
	wing	B#6	979	821	39.0
3-S/E1-T	web	B#1	294	294	17.5
	wing	B#7	270	270	32.2
5-S/E3-T	web	B#8	347	361	28.4
	wing	B#10	338	352	36.9
3-S/E1-T/R	web	B#1	294	354	17.5
	wing	B#7	270	330	32.2
4-S/E1-R/T	web	B#5	498	500	40.2
	wing	B#8	347	486	28.4
5-S/E3-T/R	web	B#8	347	407	28.4
	wing	B#10	338	398	36.9
6-S/E3-R/T	web	B#1	294	714	17.5
	wing	B#5	498	697	40.2

Note: t_1 – at material test; t_2 – at element test; $f_{cm,cube}(t_1)$ – mean concrete cube strength.

Table 3.8 Concrete class of the web-panel

Element	$f_{cm}(t_1)$ (MPa)	$\beta_{cc}(t_1)$	f_{cm} (MPa)	f_{ck} (MPa)	Class
1-S-T	14.0	1.19	11.8	8.9	C8/10
3-S/E1-T	14.0	1.19	11.8	8.9	C8/10
5-S/E3-T	22.7	1.20	19.0	14.3	C12/15
3-S/E1-T/R	14.0	1.19	11.8	8.9	C8/10
4-S/E1-R/T	32.1	1.21	26.5	20.0	C20/25
5-S/E3-T/R	22.7	1.20	19.0	14.3	C12/15
6-S/E3-R/T	14.0	1.19	11.8	8.9	C8/10

Note: f_{cm} – mean concrete cylinder strength; β_{cc} – time coefficient; f_{ck} – characteristic cylinder strength of concrete.

Samples of steel re-bars were collected from each reinforcement type and diameter used in the experimental program, namely smooth (OB37) and ribbed (PC52) hot-rolled bars and cold-drawn ribbed welded fabric (STPB), see Figure 3.13. The tensile tests were performed using the Universal Testing Machine of the Steel Structures Laboratory, Politehnica University of Timisoara. The results of the test series are indicated in Figure 3.13b and Table 3.9. The hot-rolled OB- and PC-type reinforcement stress-strain relationship is a ductile response whereas the cold-drawn wires are brittle.

Specified properties of typical Romanian reinforcements are indicated in Table 3.10. As the primary reinforcement was the ϕ10 mm PC-type deformed bars and the ϕ4 mm STPB-type welded wire fabric in the web-panel the yield strains were figured out by dividing the measured yield stress by the specified modulus of 210 GPa, resulting in 0.2% and 0.3%, respectively.

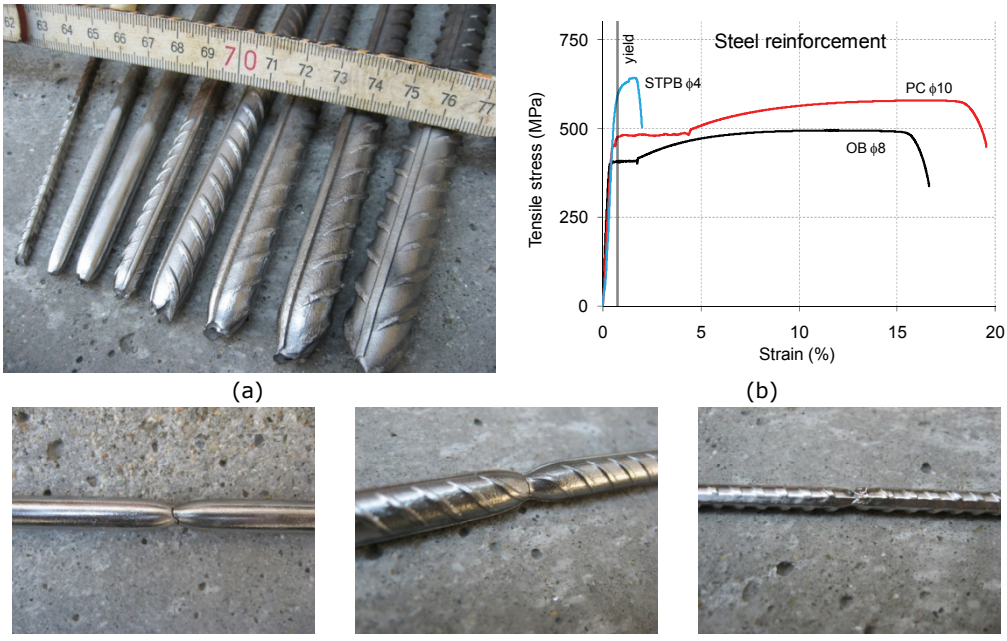

Figure 3.13 Steel reinforcement testing: (a) range of steel reinforcements; (b) measured stress-strain relationship; (c) OB re-bar; (d) PC re-bar; (e) STPB wire

Table 3.9 Measured steel strengths

Re-bar type	**Production / surface**	**ϕ (mm)**	**f_y (MPa)**	**f_t (MPa)**	**f_t/f_y**
OB	Hot-rolled / smooth bar	6	400	550	1.38
		8	425	507	1.19
PC	Hot-rolled / ribbed bar	8	424	553	1.30
		10	**450**	**564**	**1.25**
		12	446	642	1.44
		14	395	584	1.48
		16	385	613	1.59
STPB	Cold-drawn / ribbed wire	**4**	**618**	**667**	**1.08**

Note: f_y – yield strength of reinforcement; f_t – tensile strength of reinforcement.

Table 3.10 Specified steel strengths [70]

Type	**Grade**	**ϕ (mm)**	**f_{yk} (MPa)**	**f_{tk} (MPa)**	**f_t/f_y**	**E_s (GPa)**
OB37	S255	6÷12	255	360	1.41	210
PC52	S355	6÷14	355	510	1.44	210
PC60	S420	6÷12	420	590	1.40	210
STPB	S490	3÷4	490	590	1.20	210

Note: f_{yk} – characteristic yield strength of reinforcement; f_{tk} – characteristic tensile strength of reinforcement; E_s – modulus of elasticity of steel reinforcement

The Externally Bonded Fiber Reinforced Polymer Reinforcements (FRP-EBR) used in the present experimental program were of the manually impregnated fabric composite system type. Two types of FRP systems were used in the experimental program and for the sake of reference these were designated as S1 and S2. The carbon fibre (CF) unidirectional fabrics of the two systems are presented in Figure 3.14. The properties of the CF-fabrics, resin matrices and the laminated FRP materials were taken as per the product data sheets, brochures and design manuals, see Tables 3.11, 3.12 and 3.13. There was a slight variation in the properties of the same product depending on the country and type of data source; therefore, it was considered adequate to present the results of a single source. It is noteworthy that the properties of the FRP laminates are referred to as nominal values and are strongly related to the thickness of the components of the composite by the rule of mixtures [71], see Figure 3.15. The US specifications [72, 73] indicates 60÷70 GPa modulus for a 30% fiber content while the European counterpart product [74] has 25 GPa modulus for a laminate with 13% fiber. The average specified tensile strengths are 850÷900 MPa and 350 MPa for the corresponding fiber contents. If the same fiber content is considered the properties would be approximately the same. There is also important to look at the tensile elongations at failure which explains the result obtained by the rule of mixtures applied to the strength values and the one ciphered from the modulus of elasticity.

Concrete repair was carried out using a high-strength mortar (product name Sika Repair 13). It has a compressive strength of 48÷52 MPa at 7 days according to the product data sheet [75].

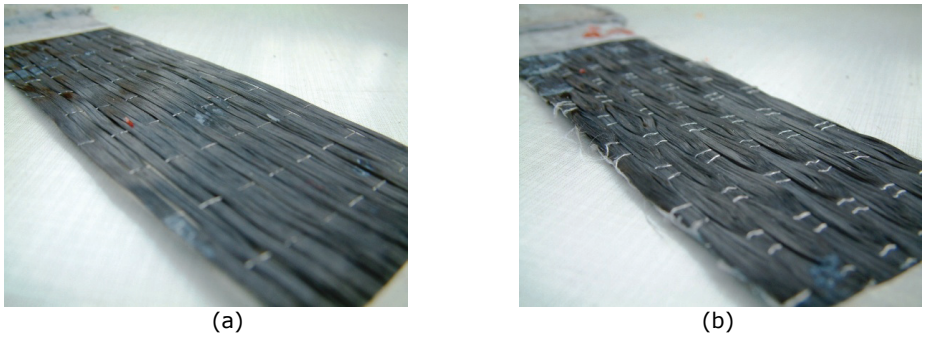

(a) (b)

Figure 3.14 Carbon Fibre (CF) sheets: (a) CF of the S1 FRP; (b) CF of the S2 FRP; 50 mm wide strips

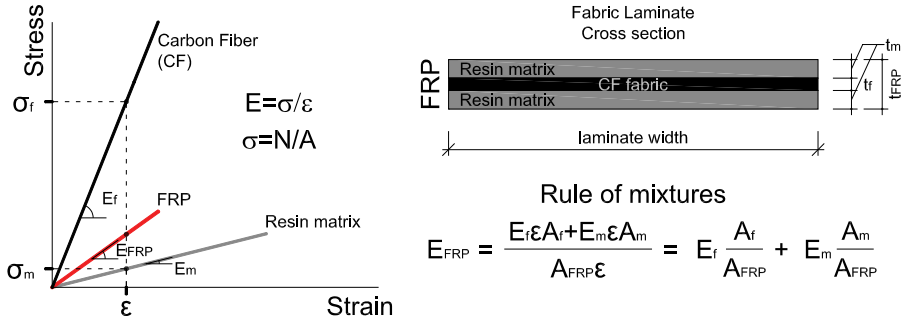

Figure 3.15 FRP stress-strain relationship and the rule of mixtures

Table 3.11 Properties of S1 FRP system – Germany [74a, 74b]

Component / system	**CF fabric**	**Resin matrix**	**CFRP Laminate**
Product name	SikaWrap 230C C/45	SikaDur-330	SikaWrap Composite
Thickness (mm)	0.131	n/a	1
Areal weight (g/m^2)	230	n/a	n/a
Tensile strength (MPa)	4300	30	350
Tensile modulus (GPa)	234	4.5	25
Elongation at break (%)	1.8	0.9	n/a

Table 3.12 Properties of S1 FRP system – USA [72a, 72b]

Component / system	**CF fabric**	**Resin matrix**	**CFRP Laminate**
Product name	SikaWrap Hex 230C	SikaDur-330US	SikaWrap Composite
Thickness (mm)	n/a	n/a	0.381
Areal weight (g/m^2)	230	n/a	n/a
Tensile strength (MPa)	3450	33.8	894
Tensile modulus (GPa)	230	n/a	65.4
Elongation at break (%)	1.5	1.9	1.33
Compressive strength (MPa)	n/a	77.2	779
Compressive modulus (GPa)	n/a	n/a	67

Table 3.13 Properties of S2 FRP system – USA [73a, 73b]

Component / system	**CF fabric**	**Resin matrix**	**CFRP Laminate**
Product name	SikaWrap Hex 103C	SikaDur 300	SikaWrap Composite
Thickness (mm)	n/a	n/a	1.016
Areal weight (g/m^2)	618	n/a	n/a
Tensile strength (MPa)	3793	55	849
Tensile modulus (GPa)	234.5	1.72	70.55
Elongation at break (%)	1.5	3	1.12
Compressive strength (MPa)	n/a	n/a	779
Compressive modulus (GPa)	n/a	n/a	67

3.1.5 Test set-up

The main testing facilities of the Reinforced Concrete Structures Laboratory consists in a 20 m long strong floor with two parallel, continuous, 1350 mm centred anchoring channels; 4 modular vertical steel reaction frames of 1000 kN capacity; and two truss type horizontal load steel reaction frames of 1000 kN capacity at approx 3 m height. The hydraulic loading apparatus (device) is composed of electric pumps (200 bar maximum pressure), hand pumps (700 bar), a series of jacks and cylinders (200 and 400 bar) from 100 to 2000 kN and hoses of 375 bar working pressure. The laboratory is provided with a bridge crane of 3200 kg lifting capacity. It is to mention that the laboratory housed previously a large variety of experimental programs conducted on RC and masonry structural members, including RC walls, and a recently completed upgrade of the full hydraulic loading equipment and reaction elements will further improve its testing capabilities.

A general view of the test set-up assembled for the current experimental program is presented in Figure 3.16. Besides the wall specimen, the test set-up comprises two beams, four vertical reaction frames, two lateral reaction frames and the hydraulic equipment. According to the classifications described in section 2.3.5, this test set-up is an A-type with 4 loading degrees, suitable to achieve advanced cyclic loading for restrained rotation boundary conditions. Its singularity relies in the load transfer mechanism to model the outrigger effect deemed to be of primary importance in the real site seismic conditions. The performance characteristics of

the test set-up are 1000 kN cyclic horizontal loading at approx. 3 m height with ±80 mm displacement that corresponds to approx. 4% drift ratio and two independently actuated (driven) vertical loads of 1000 kN each.

The specimens were set between two heavily reinforced steel concrete composite beams at the top and bottom parts referred to as cap and base beams, respectively. The cap beam served as load conveyor at the top of the specimen while its counterpart at the bottom served as foundation. These beams were especially designed and constructed for the experimental program and the same, except some minor modifications, pair of beams was used throughout the 7 tests. The concrete outlines and reinforcement arrangement for the loading beams are presented in Figure 3.17. In cross section, the loading beams were composed of two U300 steel channels and a reinforced concrete T-beam, connected by a series (42) of ϕ20 mm threaded tie rods. The concrete and reinforcing details were the same for both beams, except the presence of the starter bars in the base beam. Shear keys were formed according to the ones presented for the web panel horizontal edges and at the beam ends shear steps (outset) were provided.

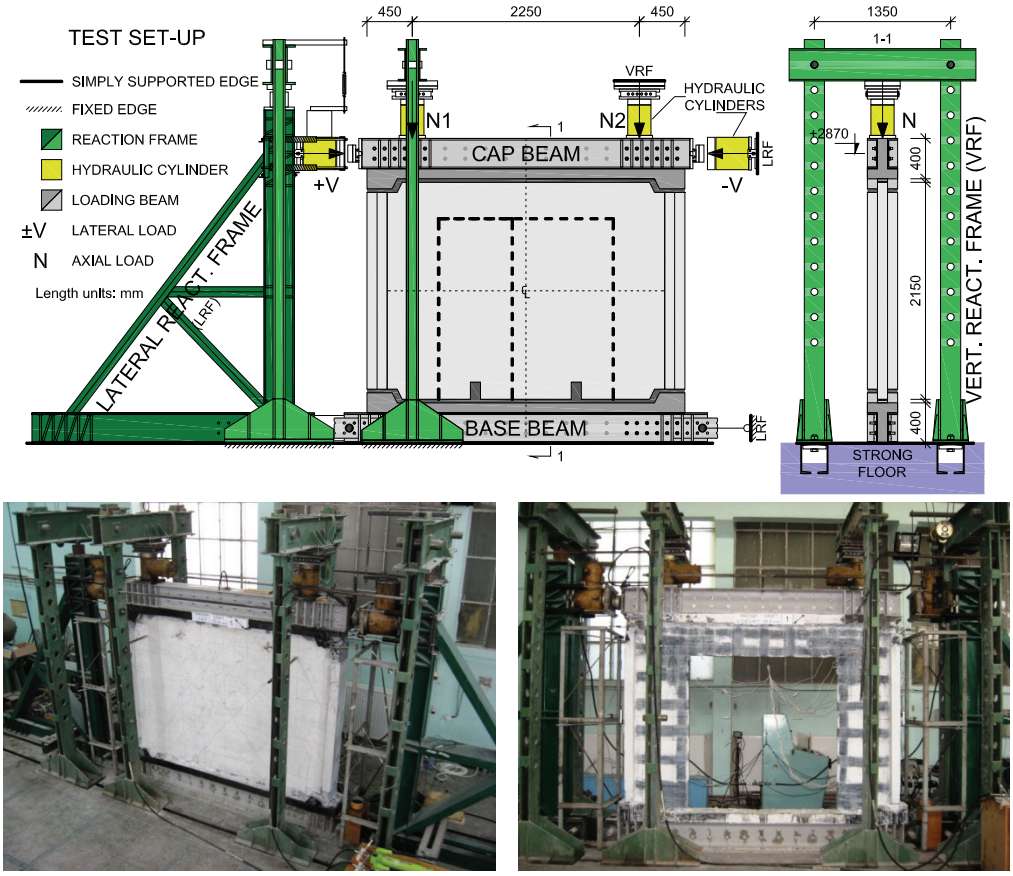

Figure 3.16 Test set-up

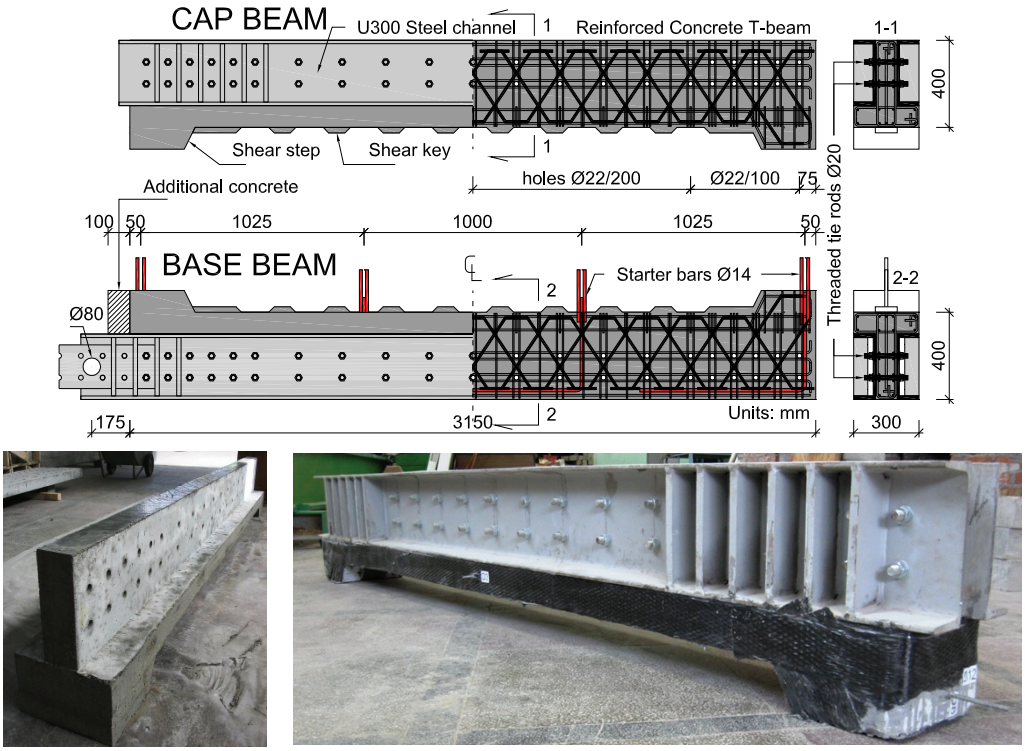

Figure 3.17 Loading beams

The holes for the tie rods were placed in two rows and were centred at 100 mm at the end and at 200 mm in the middle. The concrete used for the beams was in-house prepared with 600 kg/m^3 cement content, maximum aggregate size of ϕ7 mm and low w/c ratio with water-reducing admixtures. The resulting measured concrete cube strength was $f_{cm,cube}$=47÷60 MPa, corresponding to concrete class of C30/37. The reinforcement bars used were the OB (ϕ6) and PC (ϕ8,10,14) types presented in Table 3.9. Bar congestion was significant. The base beam was provided with ϕ14 starter bars to accommodate the connection to the wall elements' vertical continuity bars by lap welding. The gap between the loading beams and the wall element was grouted (filled) with high-strength repair mortar, the same as the one presented in the previous section. At the extremities of the loading beams special connection details were provided, namely ϕ70 mm steel bolt hinge at the base (see Figure 3.18c) and ball bearings at the top. After the first test the cover concrete spalled from the base beam's ends, therefore it was repaired and strengthened by FRP-wrapping and an additional 100 mm concrete was added to the ends of the base beam. The performance of the loading beams was good. Before the test of the solid wall (the last test in the series) the beams were repaired by recasting the shear keys and FRP-strengthening along the entire circumference of the T-beam.

The configuration of the loading devices acting on the cap beam and the support conditions of the base beam are presented in Figure 3.18. Four hydraulic cylinders were used to impose the seismic loadings, two horizontal for the lateral loads acting on the ends of the cap beam and two vertical for axial loads. The

devices were referred after the loading type, namely ±V for the horizontal ones as these generated the shear forces and N1 and N2 for the vertical ones as these were generating the axial loads and were positioned on the centrelines of the narrow pier#1 and #2, respectively.

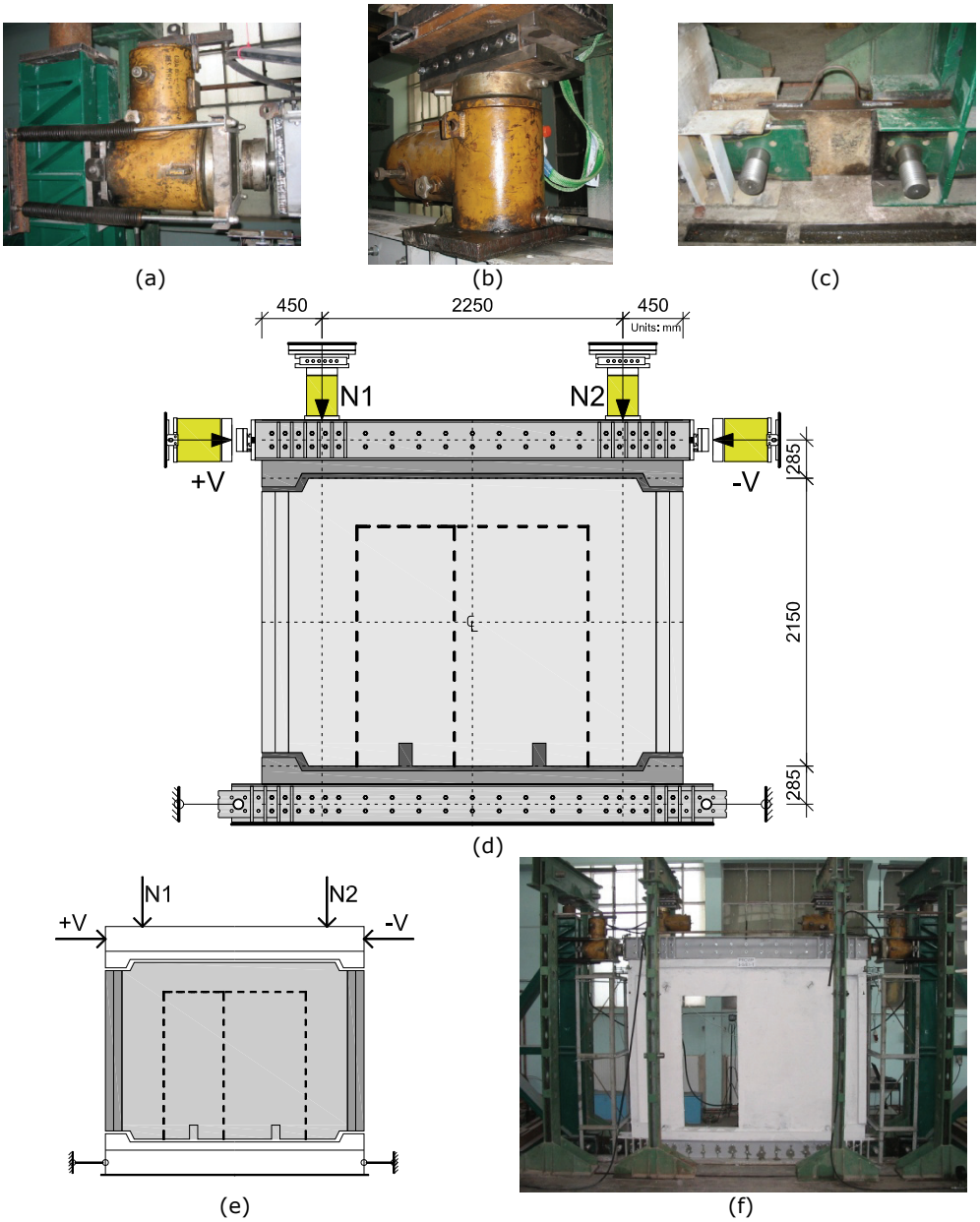

Figure 3.18 Arrangement of the loading devices: (a) horizontal loading hydraulic cylinder; (b) vertical loading hydraulic cylinder; (c) hinged connection at the base; (d) loading configuration; (e) schematic loading; (f) specimen 3-S/E1-T.

The position of the loading devices is shown in Figure 3.18. This configuration was maintained the same throughout the entire program for each specimen. The two axial loads were had independent hydraulic lines connected to hand pumps, while the lateral devices were actuated by a single electric pump as only one of them was in service at the same time. Each loading device was capable two generate a nominal 1000 kN force. The base beam was positioned in the middle axis of the strong-floor, refer also to Figure 3.16, between the two anchoring channels. It was placed on a thin mortar bed and no vertical tension anchoring was provided, hence it can be considered simply supported. This support condition is rather unusual in the wall tests performed by other researchers where the foundation is most often fixed to the strong floor. The reason for this is that in order to model the outrigger effect the flexural tension reaction forces must be limited or completely eliminated. It must be noted that the wall to base beam anchorage was in accordance to the construction practice of the large panel buildings. Horizontally the base beam was connected to the lateral reaction frame footing through a double hinged 60 mm thick steel plate, refer to Figure 3.18c. It is to note that the lateral reaction frames were also positioned in the middle of the strong floor, a condition imposed primarily by several factors, the most important being the one that large tension forces of the order of 1000 kN would be not possible to be transmitted as tension by the frame itself, only by the transversely placed portal frames that were fixed to the anchoring channels and provided a vertical restraint atop the column of the lateral truss.

3.1.6 Loading procedure

The experimental specimens were subjected to quasi-static in-plane reversed cyclic lateral and alternating axial loadings. These two are discussed separately in the following sections. The adopted procedure was based on a literature survey on this topic published by Demeter et al. in [62, 63].

For lateral loading a reversed cyclic, displacement controlled, increasing displacement amplitude load/displacement history (protocol) was adopted, see Figure 3.19. The control displacement was the horizontal drift calculated as the difference between the horizontal displacements measured at the top and bottom edge of the experimental specimens. The distance between the top and bottom measurements was approximately equal to the height of the wall, that is, 2150 mm.

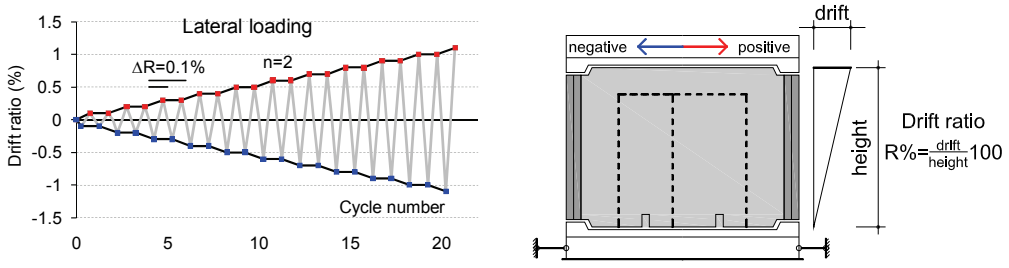

Figure 3.19 Lateral loading procedure

Table 3.14 Cycle drift amplitudes

Cycle #	**1;2**	**3;4**	**5;6**	**7;8**	**9;10**	**etc.**
Drift (mm)	2.15	4.30	6.45	8.60	10.75	+2.15
Drift ratio (%)	0.1	0.2	0.3	0.4	0.5	+0.1

The drift ratio (R%) is the drift to height ratio as presented in Figure 3.19. One can cipher that 21.5 mm drift corresponds to 1% drift ratio. The positive and negative loading directions are also indicated in Figure 3.19. The displacement history has its unit a drift ratio of 0.1%. The displacement amplitudes were multiples of this base value, that is, a constant drift increment (ΔR%) of 0.1% was applied. On each displacement level two cycles were performed (n=2). In these conditions the subsequent displacement levels were 0.1, 0.2, 0.3, etc. %, or in terms of drift 2.15, 4.3, 6.45, etc., mm (see Table 3.14). This loading history was a conservative one. In order to assess the behaviour under more gentle conditions the elements were subjected to a series of initial load controlled cycles prior to the 0.1% level, that is one cycle was imposed at 10, 50, 100, 150, etc., kN lateral loads until the drift reached 1 mm. The failure criterion was 20% lateral load carrying capacity drop with respect to the maximum value in each direction.

The axial loads were composed of two parts, namely a constant and an alternating (variable) part. The constant level was set so as to reproduce the gravity loading conditions at the base of a 5-storey large panel building. For this, a mean compressive stress of 0.9 MPa was considered based on Demeter et al. [62]; also refer to the I2 structural index in section 2.2.2. In order to account for the differences in the concrete properties, the normalised axial load (n) concept was employed, see Figure 3.20. This value yielded 5.1% for the nominally C16/20 as-built concrete. In the experimental program a 6% n-value was taken for the reference solid wall. The difference is caused by the overlook of the β_{cc} time factor in ciphering the characteristic concrete strengths, which was included later, when the tests were already performed. The axial loads for the experimental specimens, the compressive stress levels and the normalised axial loads are indicated in Figure 3.21 and Table 3.15. One can observe that the specimens with cut-out openings had normalised axial loads greater than 6%, namely 7.7% for the E1-cutout and 12% for the E3-cutout openings. The reason for this is that the axial loads correspond to the solid reference and the cross sectional loss caused by the cut-out implies the increase of the compressive stress, see also Figure 3.20. The initial compressive stress was in the 0.5÷1.7 MPa range, depending on the cut-out condition and the concrete compressive strength. In Figure 3.21 the normalised axial load values are indicated considering both the web-panel and boundary wing concrete properties. In the last column of Table 3.15 the normalised axial loads were ciphered with the gross cross sectional area of the solid wall, yielding values close to the 6% reference.

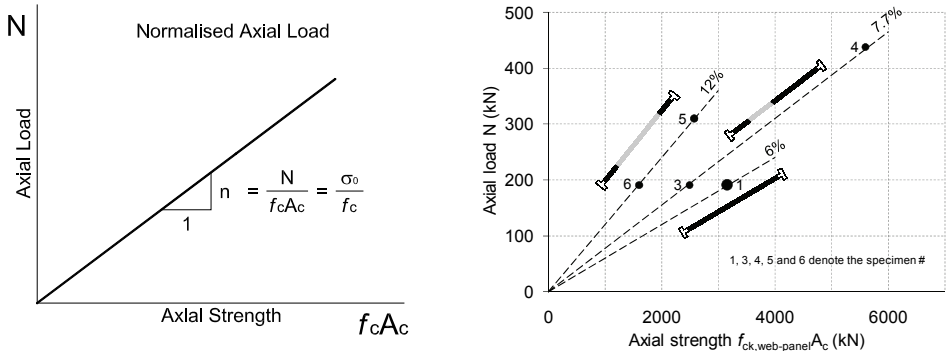

Figure 3.20 Normalised axial load

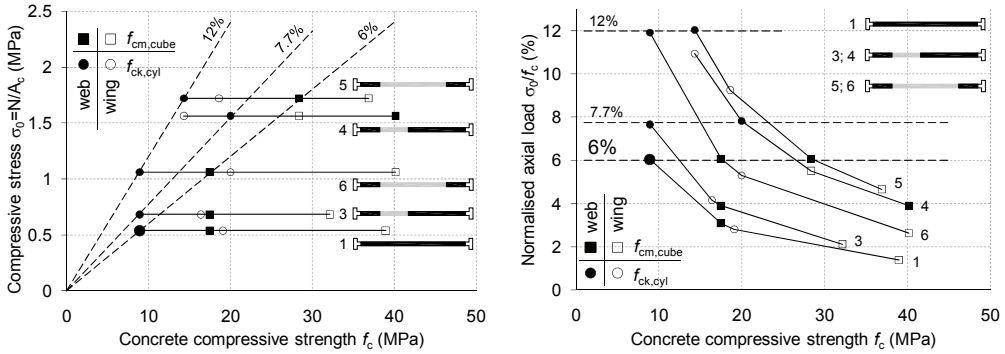

Figure 3.21 Axial compressive stress

Table 3.15 Initially applied axial loads

Element	N (kN)	A_c (cm^2)	f_{ck} (MPa)	σ_0 (MPa)	n (%)	n_S (%)
1-S-T	191	3550	8.9	0.54	6.0	6.0
3-S/E1-T	191	2800	8.9	0.68	7.7	6.0
5-S/E3-T	310	1800	14.3	1.72	12.0	6.1
3-S/E1-T/R	191	2800	8.9	0.68	7.7	6.0
4-S/E1-R/T	438	2800	20.0	1.56	7.8	6.2
5-S/E3-T/R	310	1800	14.3	1.72	12.0	6.1
6-S/E3-R/T	191	1800	8.9	1.06	11.9	6.0

Note: N – initial axial load; A_c – area of concrete cross-section; f_{ck} – characteristic cylinder strength of concrete; σ_0 – compressive stress $\sigma_0 = N/A_c$; n – normalised axial load $n = N/(f_{ck}A_c)$; n_S – normalised axial load considering the gross section of the wall.

In addition to the constant level, alternating axial loads were imposed in order to restrain the rocking (rigid body) rotation of the laterally loaded walls. These additional axial loads were applied through the vertical hydraulic jacks closer to the loaded end of the cap beam, that is through N1 for positive lateral loading and through N2 for negative lateral loading, see Figure 3.22. The increase of the axial loads was controlled by the uplift displacements measured at the ends of the cap beam through two vertically oriented displacement transducers, D8 and D7, at a rate of 100 kN/mm, see Figure 3.22. Hence, the axial loads applied by each of the vertical hydraulic cylinders were of the following magnitude: $N_1 = N/2 + 100 \cdot D8$ and $N_2 = N/2 + 100 \cdot D7$, with units of kN and mm. Note that in the lateral unloading phase the axial loads were decreased too but not below the constant level.

The author acknowledges that the foregoing axial loading procedure is quiet uncommon in the literature and maybe it seems inadequate to some of his critics. The reader is gently remembered that the base beam's support conditions don't allow for vertical tension reaction forces, given that it was not fixed to the strong floor. Consequently, the only forces resisting against the overturning moment generated by the lateral loads were provided by the vertical axial loads. If the axial loads were kept constant the specimen would rock at a lateral load corresponding to an overturning moment that exceeds the resisting moment, which in turn is much less than the moment corresponding to the shear strength of the solid wall. Thus, the additional axial loads were necessary to provide an increasing resisting moment in order to restrain the rigid body rotation.

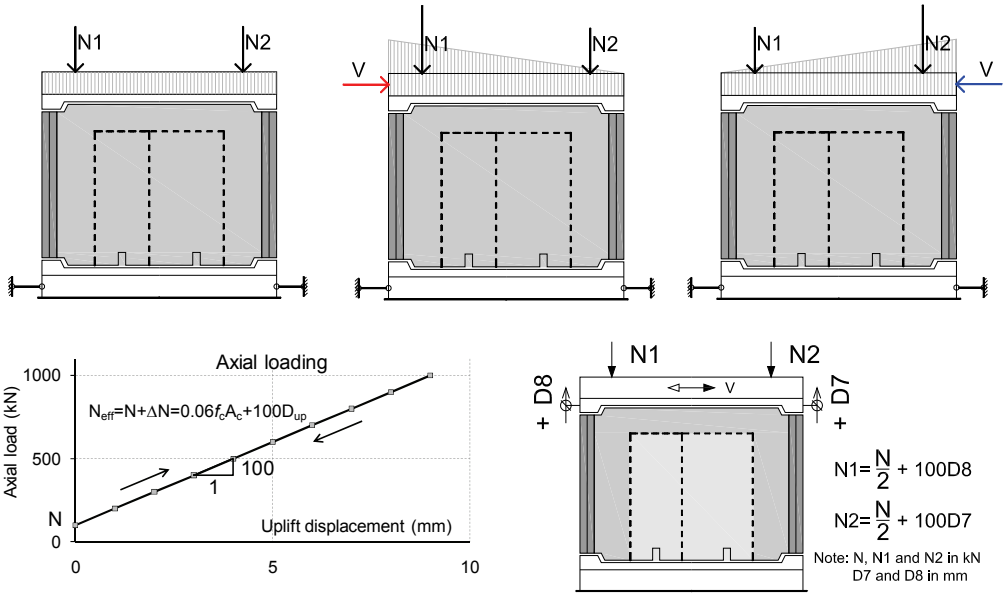

Figure 3.22 Additional alternating axial loading procedure

In fact the additional alternating axial loads works similarly to the external post-tensioned rods used for axial loading in several experimental programs like in [45, 76], although in these references it was stated by the authors that the increase of the tensile forces was unwanted and therefore spring connections were provided. With regard to the rate of 100 kN/mm, it was dictated by the 1000 kN capacity of both the reaction frame and the hydraulic equipment, divided by 10 mm, considered appropriate after the first test, when a higher axial loading rate was temporarily (accidentally) applied in a few cycles and resulted in very stiff response, whereas a lower rate would imply too big rotations. A rough calculation indicates that the 100 kN/mm load rate is equivalent to the tensile stiffness of a 2100 mm long and 1000 mm^2 sectional area steel bar (e.g. 2ϕ25) when its elongation is 1 mm and that is elastic up to 1000 MPa tensile stress corresponding to the 1000 kN tensile force.

3.1.7 Boundary conditions

As presented in section 2.3.5, there are three types of boundary conditions, namely cantilever, restrained rotation and additional moment. These are the concerted effect of the test set-up, the loading procedure and the elements adjacent to the wall ends. The present experimental program is featuring a restrained rotation type boundary condition for the wall specimens, with a series of special traits inside this category. Also it was discussed in section 2.3.5 that the restrained rotation boundary condition is promoting the shear behaviour as opposed to the flexural one, through reducing the shear span, that is, the base moment corresponding to the base shear. The test set-up adopted in the experimental program is featuring a zero overall base moment trait by the hinged end connections, although in the case of the specimens with openings there are interior moments possible to develop through the wall to base beam interface. The development of the moments is limited in both cases by the increasing axial loads, which acts against the vertical tensile forces. Therefore it can be stated that the shear span and the shear span ratio is negligible in the case of the solid wall, while

it is slightly greater for the wall piers. The exact value is quiet difficult to evaluate, due to the variable axial loads, differences in the anchored vertical reinforcement in the two loading directions and the coupling effect of the spandrel beam. Consequently, shear behaviour is extensively stimulated.

There are two principal shear transfer mechanisms, namely diagonal compression and diagonal tension. The third one would be the dowel effect of the kinking vertical reinforcement associated to the sliding shear failure. The boundary conditions of the present program eliminates the sliding-dowel mode by the construction of the two loading beams through the shear steps and the diagonal tension mechanism by the lack of vertical reinforcement anchored to the cap beam and by the variable but always in compression axial loads. Consequently, the only mechanism that is permitted is the diagonal compression shear transfer. In these conditions the present boundary conditions can be referred to as a subtype of the restrained rotation, namely diagonal compression dominated shear transfer.

Besides the model-to-prototype issue, the question remains to be addressed is the adequacy of the adopted boundary conditions to reproduce the as-built real situation during a seismic event. The experimental elements are modelling a prototype ground floor wall, part of a large panel building. In general the free behaviour of an element may be significantly altered with respect to the condition when it is restrained/constrained to interact with other structural members connected to it. The boundary conditions adopted in the experimental program were aimed to reproduce the outrigger effect, deemed to be of high importance in the behaviour of lateral load resisting structural systems. This effect was mentioned by Abrams [37], but it was abandoned and only recently is gaining wider attention. The core idea is that the either of the extremities of a vertical structural member is restrained from rotation by the counterbalance exerted by the structural members on the uplifting side. This effect can be conveyed by a rigid diaphragm floor or directly through the vertical edges from orthogonal walls, the latter being the case for the large panels. The uplifting end attracts additional axial loads from the nearby elements to the extent which these axial loads are available, for the total amount is finite. It is interesting to note that the dynamic condition may increase the available axial loads due to a vertical uplifting acceleration that may be added or subtracted from the vertical acceleration of the ground motion. The amount of additional axial load available for a specific lateral load resisting element is a matter of structural system configuration and relative stiffness.

3.1.8 Instrumentation

The behaviour of the specimens during the experimental tests was monitored by measuring three quantities, namely displacements, unit strains and forces. The main characteristics of the measuring devices (sensors) used are indicated in Table 3.16. The average number of measured values in each test was 10 displacements, 15 unit strains and 3 pressures. For data acquisition an Almemo 5990 system was used with 29 measuring inputs, see Figure 3.23. The generic layout of the displacement transducers and of the strain gauges is presented in Figure 3.23. A rear view of one of the specimens (6RT) shows the cable congestion (trajectories) conveying the recorded data to the acquisition system. The specific layout and detailed list of instrumentation for each test is given in Appendix C.

The displacement measurement was realised through linear potentiometers fixed either on independent steel frames or directly on the specimens. Only the two out-of-plane deflections for the first tested specimen (3T) were measured by mechanical dial gauges. The displacement transducers fixed on the independent

measuring frame and interconnected with the specimen by thin steel wires were referred to as external devices, given that the measurements was made with reference to an external independent system, while the transducers attached directly to the specimen were referred to as internal devices for measured the total strains between two points of the specimen. Four displacement measurements were used to control the loading of the specimens, these were referred to as control displacements. The difference between the top and bottom horizontal displacements (D1 and D2) resulted in the drift used for lateral load control while the vertical uplift measured by the two transducers at the two ends of the loading beam (D7 and D8) controlled the variable component of the axial loading.

Table 3.16 Characteristics of the measuring devices

Measurement	**Sensor**	**Product**	**Range**	**Resolution**
Displacement	Linear potentiometer	Almemo FWA100TR	(0÷100) mm	0.01 mm
		Almemo FWA150T	(0÷150) mm	0.01 mm
	Mechanical dial gauge	n/a		0.1 mm
Strain	Electric resistance strain gauge	HBM 1-LY18-6/120	(-5...+5)%	0.01 Ohm 0.004%
Pressure	Piezo-resistive	Almemo FD8214 21U	(0÷600) bar	0.1 bar

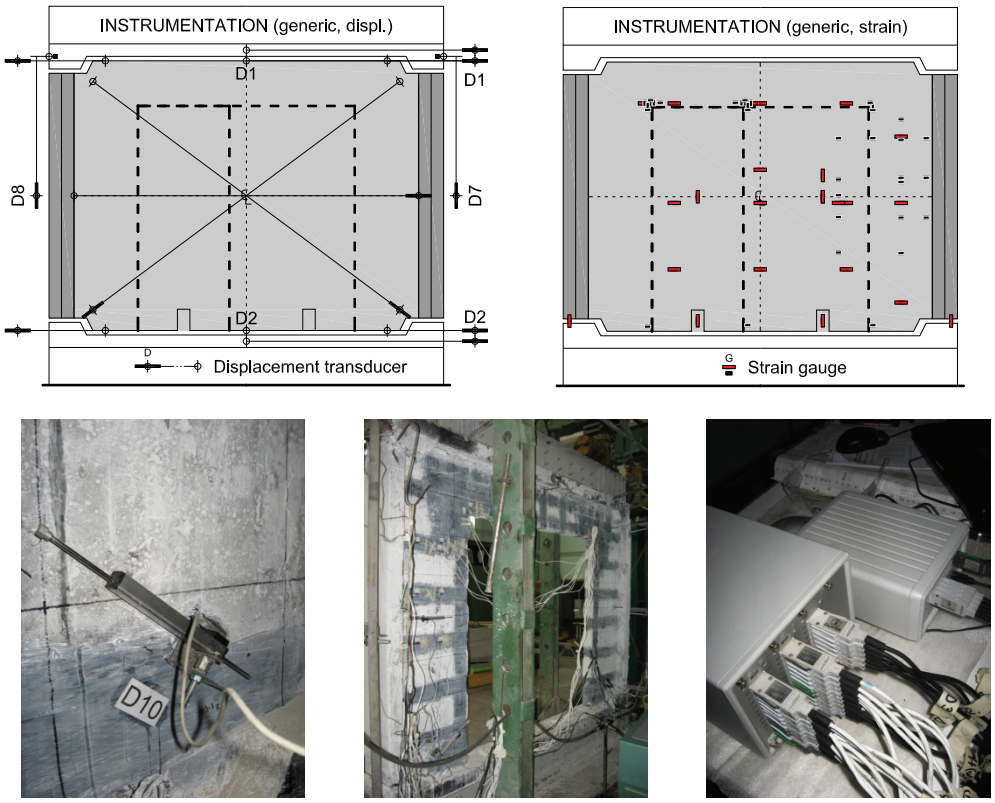

Figure 3.23 Instrumentation of the specimens

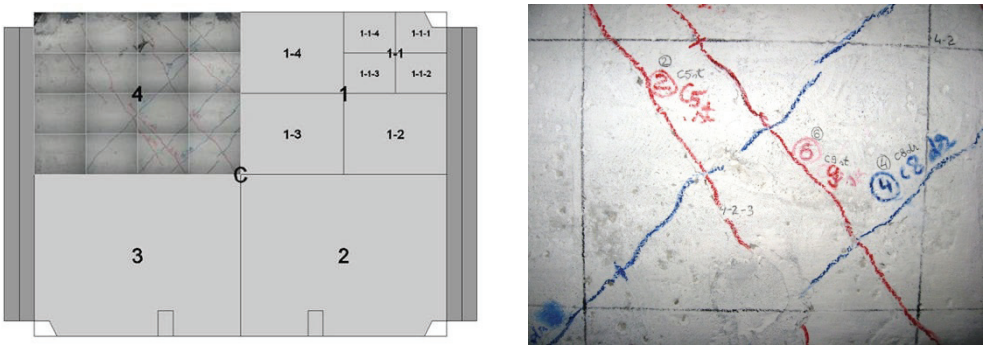

Figure 3.24 Observation grid

Other external devices measured the horizontal displacements at different locations (D3 through D6) these being slightly modified after the third test, that is D3 was moved to the cap beam and D5 and D6 was eliminated. Instead, an internal horizontal displacement was introduced starting with the fourth test (5TR) that measured the horizontal elongation at the mid-height of the specimen (D4). The D2 transducer was alternatively fixed on the base beam when the wide cut-out opening removed the concrete at the bottom of the wall. Two internal measurements were used to monitor the total diagonal strains between the opposite corners (D9 and D10). The out-of-plane horizontal displacements were measured by two external devices at each end of the cap beam (D11 and D12).

The unit strains were measured by electric resistance strain gauges attached on the internal steel and on the external CFRP reinforcements. The steel strains were monitored in the vertical continuity bars at the wall base and mid-height and in the horizontal ϕ10 bars at various locations, including the corners of the cut-out openings. The CFRP-strains were recorded in the flexural strips around the opening corners, in the shear strips of the piers and for the confinement strips at the base of the piers. A total of 100 strain gauges were mounted in the experimental program.

The pressure measurements were made by piezo-resistive transducers mounted on the three hydraulic lines, namely one for the lateral loads and two for the axial loads. The only exception was the N2 axial load during the first test (3T) which was monitored by dial pressure gauge (manometer). The loads were figured out by multiplying the recorded pressure with the piston area of the hydraulic cylinders.

In addition to the measured quantities presented above, an important behavioural aspect of the reinforced concrete elements to be recorded is the cracking pattern. The front face of the wall-panels was surveyed for crack occurrence and propagation at each cycle peak and the newly appeared cracks were marked on the wall. In order to accurately localise and then assess the cracks, an orthogonal reference grid (observation grid) was initially marked on the wall face, see Figure 3.24. The observation gridlines divided the web-panel area in quarters which were numbered clockwise starting with the upper right. Each of the four quarters was further subdivided using the same principle resulting in 4x4=16 second level rectangles, which in turn were also divided resulting in 4x4x4=64 third level rectangles. After each test the third level rectangles were photographed, see a close-up in Figure 3.24, and a photo-map was assembled which was used to obtain

the final cracking pattern. The dimensions of the observation grid are also indicated in Appendix C. The tests were also recorded by a commercial digital video-camera.

The accuracy of the measurements is an important concern in each experimental program. Deviations from the nominally intended values (errors) were evaluated by a series of auxiliary measurements regarding the rigidity of the independent steel frame used as support of the external devices, the elongation of the thin wires used for interconnecting the displacement transducers to the measuring point, the relative accuracy of the displacement transducers, the flexibility of the threaded rods used to fix the displacement transducers and the additional force ensued by the elongation of the springs used to retract the pistons of the horizontal hydraulic cylinders. The results of these measurements are presented in Appendix D. It was concluded that the average displacement measurement error was about 0.5% and the additional spring load varied between 5 to 10 kN. This latter load was subtracted from the measured value according to $V_{cor} = V_{rec} - \Delta V$, where $\Delta V = 10 + 0.2 \cdot D1$ and the V=(-10...+10) kN lateral load range was eliminated from the measured (recorded) data.

3.2 Test results

3.2.1 General commentary on the results

In the followings the results obtained by the seven cyclic wall tests are presented. Owing to the large amount of data to be dealt with, the results are rendered in two ways, namely primary results and detailed test logs. The primary results consists in the load-displacement response, the loading and displacement histories, the final cracking pattern, a brief description of the observed behaviour and failure mode, and a limited number of photographs on failure details. The test logs contains all the recorded responses and the observed behaviour and failure mode in the following order: load versus displacement diagrams, load versus strain diagrams, expanded cyclic load and displacement histories, cracking history, expanded cyclic lateral load versus drift hysteresis loops, commentary on the behaviour mode and test events, and failure details. Each test log is composed in average of 65 graphs and around 20 images which would disrupt the readability of the thesis. Thus, the detailed test logs are presented separately in Appendix E.

If not specified otherwise, the term "the load-displacement response" denotes the lateral load vs. drift (or drift ratio) diagram, as the most representative response characteristic; likewise, the displacement history regards the drift history.

The load-displacement graphs presented in the primary results section underwent a certain "facelift" consisting in removal of the data acquisition "bugs", elimination of the unsuccessful cycle attempts and of the data recorded during the change of the loading direction. Practically this operation, referred to as smoothing, was carried out by deletion of a number of data lines from the recorded data file. In the case of specimen 6-S/E3-R/T the load-displacement diagram comprised a huge number of bugs, thus an alternative smoothing method was employed, referred to as averaging, which consisted in recalculating each of the lateral load data as being the arithmetic mean of the records in a measuring interval defined by an equal distance above and below in the data column. Supplementary to the foregoing facelift the load-displacement diagrams presented in this section sustained a second processing phase, referred to as lateral load adjustment, so as to account for the additional loads ensued by the tensioned piston springs. The reader is reminded that the adjustment was necessary due to the indirect measurement of the forces by

pressure transducers. These additional loads were evaluated experimentally (refer to Appendix D) to be in the range of 5 to 10 kN, depending on the position of the piston. However, the adjustment was operated by subtracting from the recorded lateral loads a spring contribution of 10 to 20 kN, based on the nominal spring coefficient (conservative approach). The lateral load adjustment implied that the data lines with measured lateral loads in the range of -10 to 10 kN (change of the loading direction) were deleted from the data file. For the load-displacement responses without any facelift or adjustment the reader is referred to the expanded cyclic diagrams presented in the detailed test logs in Appendix E.

The load and displacement histories presented in the primary results section are the originally recorded "virgin" responses, except the "condensation" of the time by eliminating the major gaps when the test was halted for more hours or days.

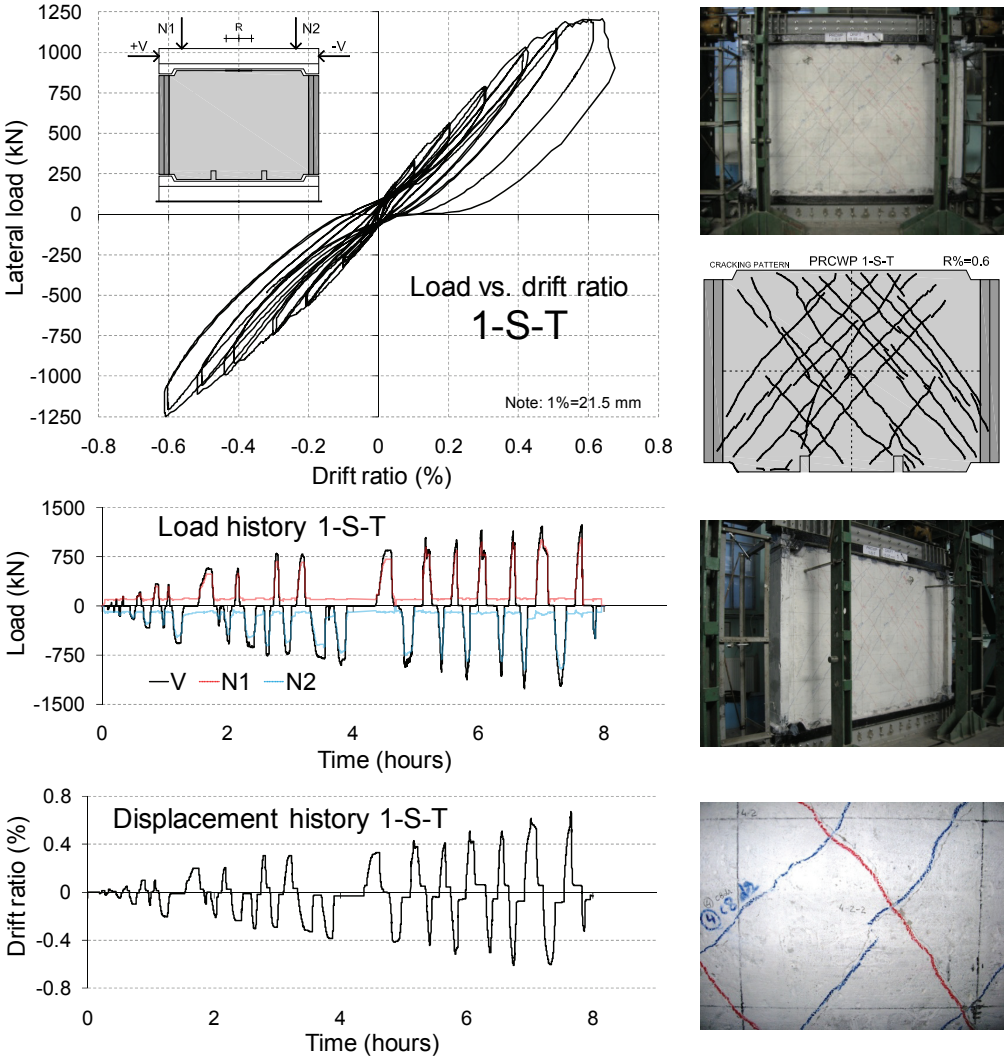

Figure 3.25 Primary results for specimen PRCWP 1-S-T

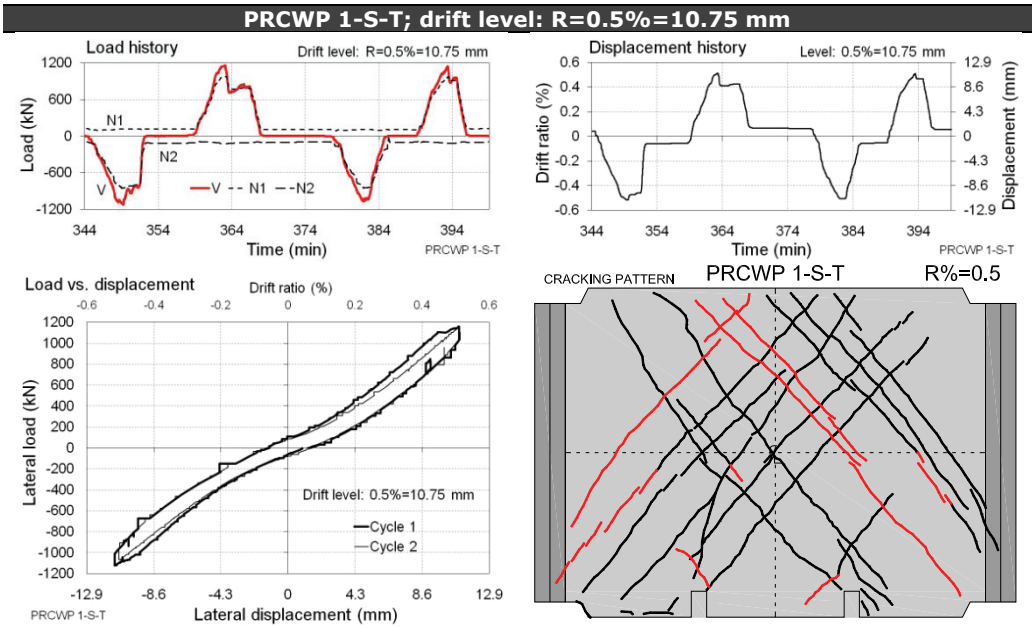

Figure 3.26 Expanded cyclic response of PRCWP 1-S-T at 0.5% drift ratio

In the subsequent description of the behaviour and failure modes the author attempted deliberately to avoid comments regarding the flexural or shear aspects of the responses. The principle kept in mind was that to report what was observed without any room for misinterpretation. Discussion on the behaviour and analysis of the response characteristics is provided later in this chapter.

Each test commenced with the application of the axial loads. Note that in the load history diagrams the N1 and N2 loads are plotted on the opposite sides of the horizontal axes. Nevertheless, the N2 load was acting in the same direction as the N1 and its negative value serve only representation purposes. The initial cycles were carried out in load control with increasing load amplitudes until the 1 mm drift level was attained. Afterwards the loading shifted into displacement control.

3.2.2 Primary results of specimen PRCWP 1-S-T

The primary results for the bare solid wall panel PRCWP 1-S-T are depicted in Figure 3.25. The first inclined cracks developed on the R=0.2% (2.15 mm) drift level running at approximately 50 deg angles, extending from the top to the bottom edges. Thereafter the cracking pattern was marked by straight cross-inclined cracks in both loading directions. The cracks in the same direction were parallel and formed eventually a cracked strut width of approximately 1.1 m, measured perpendicular to the cracks. Due to the unexpectedly high lateral load resistance that exceeded the capacity of the hydraulic equipment, the solid wall was not loaded beyond 1210 kN and 0.6% drift ratio. The most striking characteristic of the load-displacement response is the extremely pinched shape of the hysteresis loops with parallel loading and unloading branches. This is more clearly visible in the expanded cyclic response diagrams presented in the detailed test logs (refer to Appendix E), wherefrom the one corresponding to the R=0.5% drift level is shown in Figure 3.26. It is

noteworthy in the same time the alternate waving of the axial loads in the load history diagrams. One can observe that the strength degradation by cycling on the same drift level was negligible, whereas significant reloading stiffness degradation occurred by cycling to increasing drift amplitudes (kinking of the hysteresis loops).

3.2.3 Primary results of specimen PRCWP 3-S/E1-T

The primary results are depicted in Figure3.27. The cracking initiated at the base and top corners of the opening. At 0.4÷0.5% drift ratio (8.6÷10.75 mm) diagonal cracks, extending at 50÷60 deg angles, developed through pier#2 in both loading directions, while concrete spalling initiation was observed at the inside toe (near the opening) of pier#2. The expanded cyclic responses and the cracking propagation at R=0.5% (10.75 mm) are shown in Figure 3.28. One can remark the considerable waving of the axial load. The missing N2 load from the load history

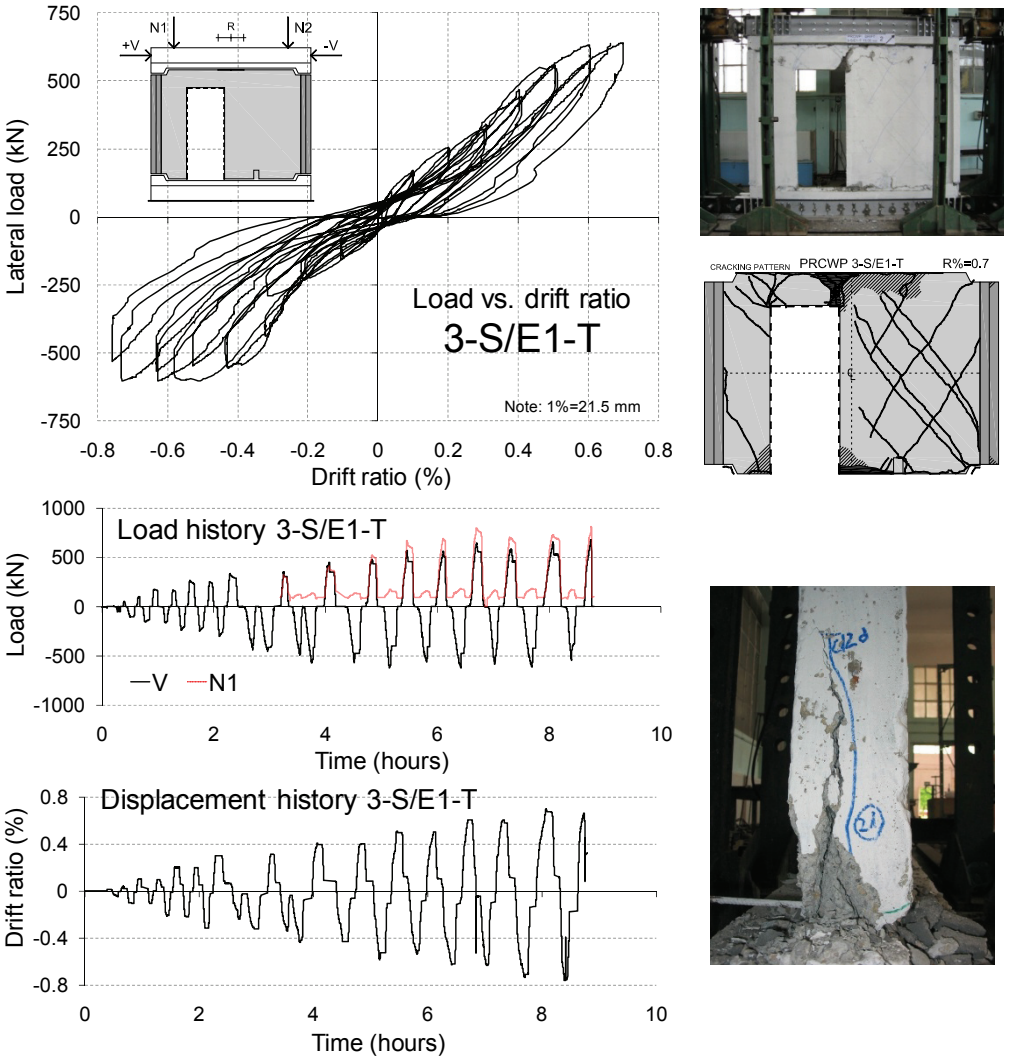

Figure 3.27 Primary results for specimen PRCWP 3-S/E1-T

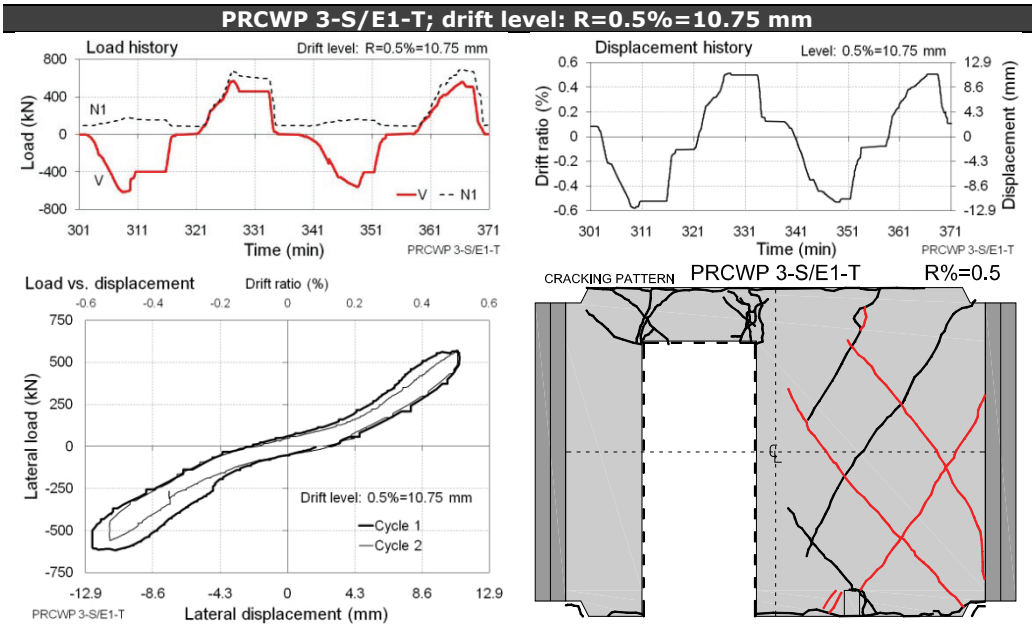

Figure 3.28 Expanded cyclic response of PRCWP 3-S/E1-T at 0.5% drift ratio

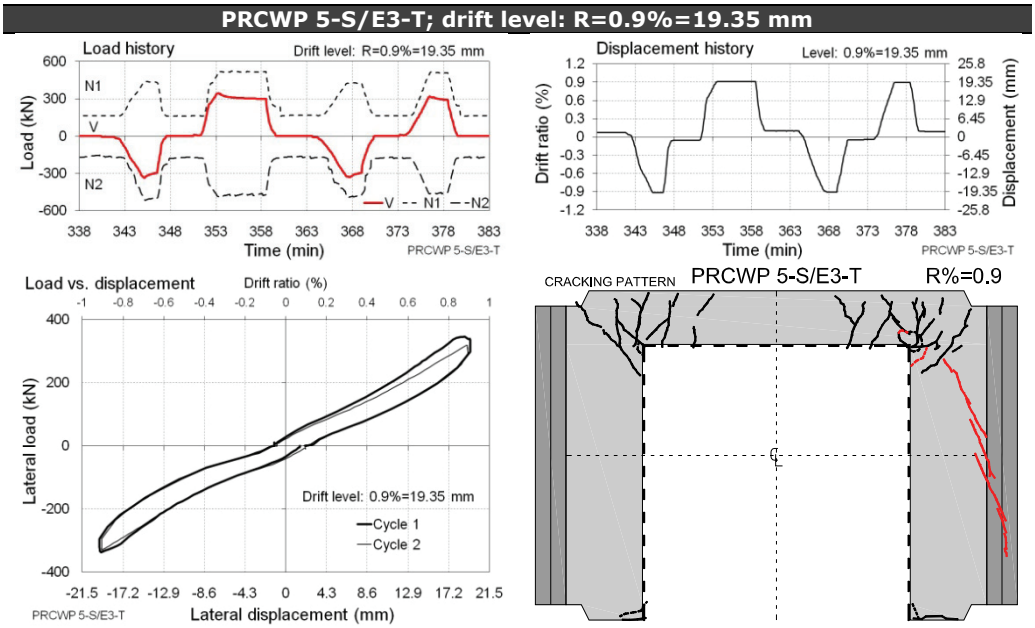

Figure 3.29 Expanded cyclic response of PRCWP 5-S/E3-T at 0.9% drift ratio

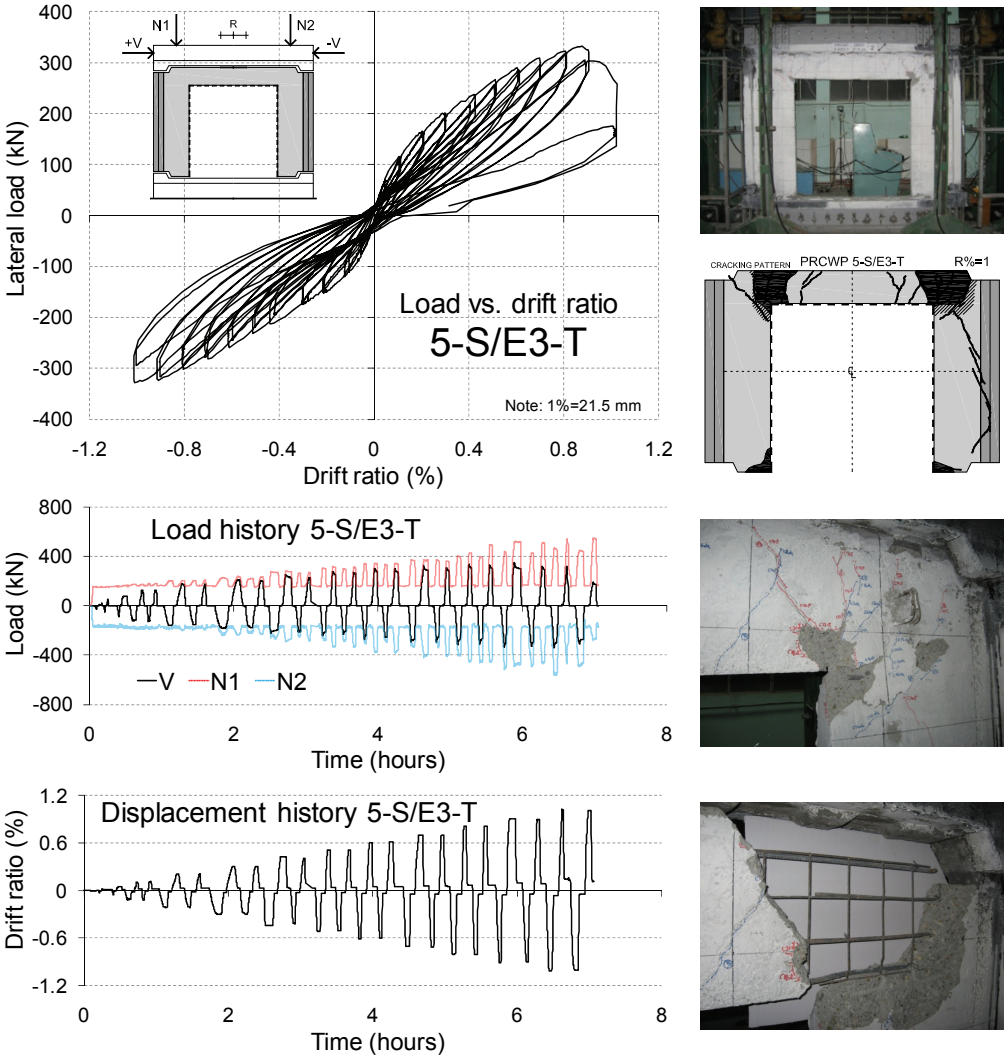

Figure 3.30 Primary results for specimen PRCWP 5-S/E3-T

was actually acting on the wall, but it was not recorded digitally, though monitored with a dial manometer. The hysteresis loops are remarkably pinched exhibiting parallel ascending and descending branches with slight decline (kinking) of the curve at reloading. The failure occurred at R=0.7% in the positive loading direction of cycle #2 by severe crushing and spalling of the concrete at the spandrel-to-pier#2 connection and along the top of pier#2. It was noted that the wall slanted backward in the out-of-plane direction.

3.2.4 Primary results of specimen PRCWP 5-S/E3-T

The primary results of the bare PRCWP 5-S/E3-T specimen are shown in Figure 3.30. The cracking was confined mainly to the pier-to-spandrel connection zones and to the opening-side toes of piers. At R=0.9% (19.35 mm) 65 deg inclined cracks appeared across pier#2. The expanded cyclic responses and the cracking

pattern at this drift level are shown in Figure 3.29. It is notable the concurrent waving of the axial loads and the remarkably pinched shape of the hysteresis loops. However, the kinking of the loops (decline at reloading) was negligible, i.e. the loading and unloading branches were quasi-linear. The failure occurred at R=1% (21.5 mm) in the positive loading direction by severe concrete crushing at the spandrel-to-pier#2 connection. The examination of the wall specimen after the test revealed that the damage extension was much larger than it seemed at first glance: at both pier-to-beam connection regions the concrete was crushed in the full depth of the spandrel.

3.2.5 Primary results of specimen PRCWP 3-S/E1-T/R

The primary results of the post-damage strengthened PRCWP 3-S/E1-T/R specimen are presented in Figure 3.31. The cracking of the specimen was initially

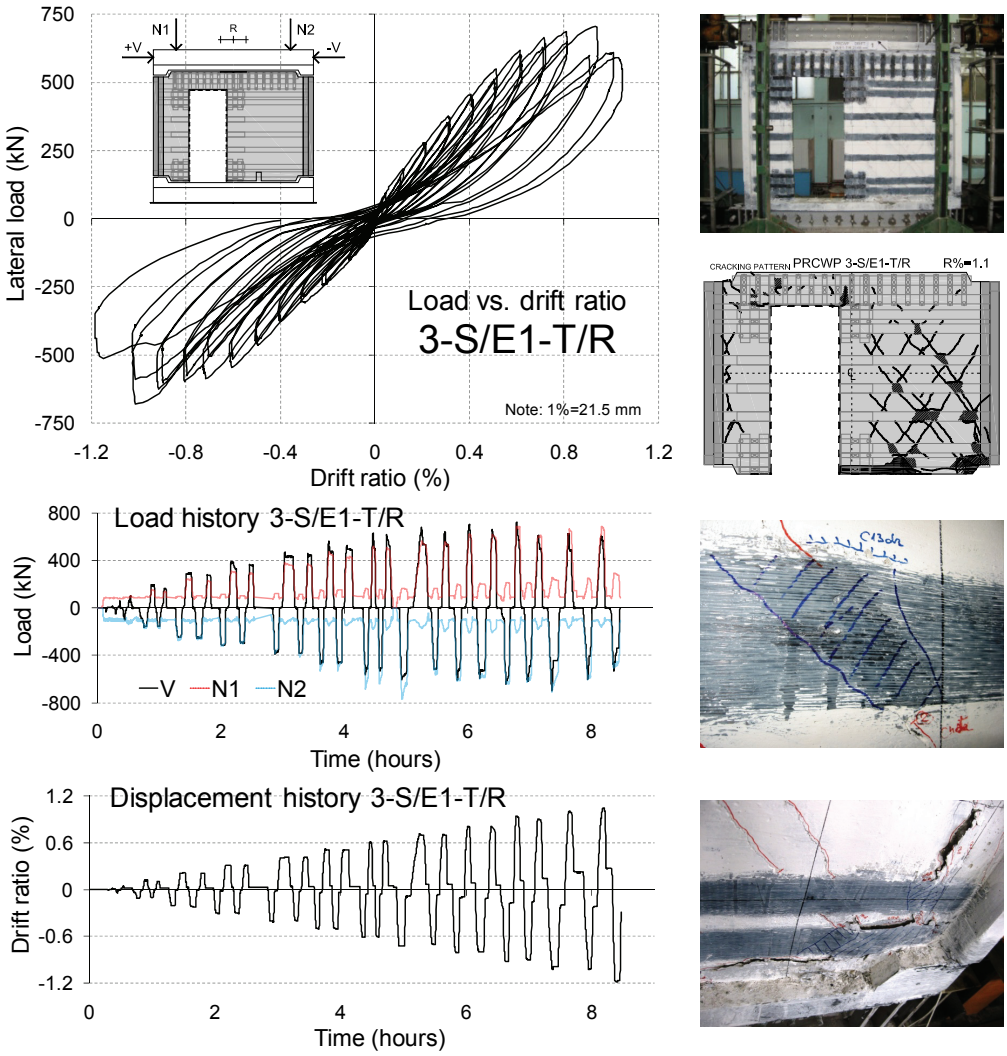

Figure 3.31 Primary results for specimen PRCWP 3-S/E1-T/R

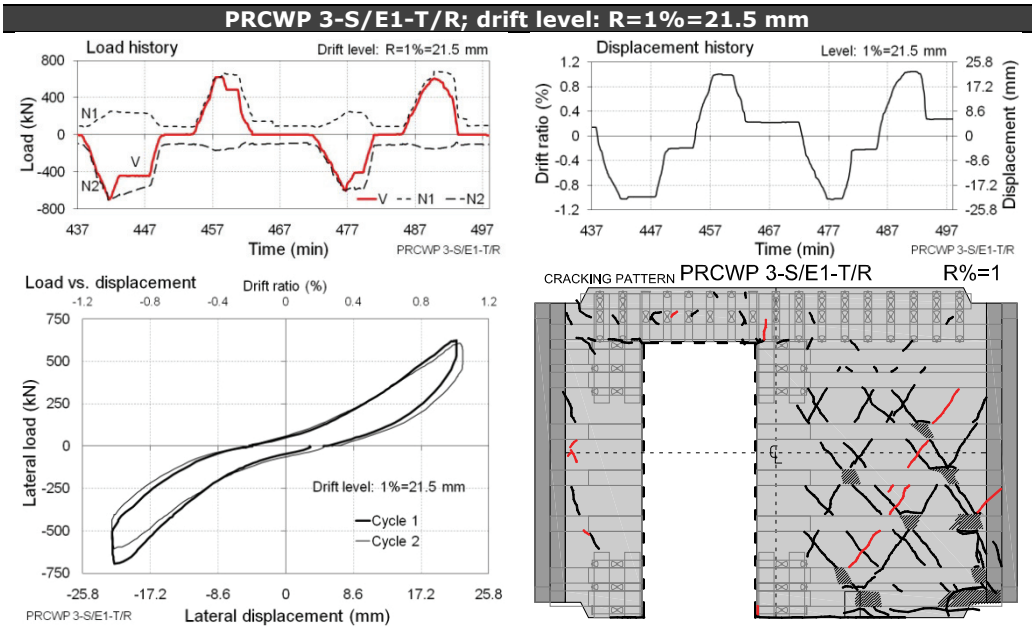

Figure 3.32 Expanded cyclic response of PRCWP 3-S/E1-T/R at 1% drift ratio

(from R=0.2% onward) characterised by existing crack opening in pier#2, while at larger load-displacement amplitudes (from R=0.7% onward) new inclined cracks appeared parallel to the old ones and a vertical string of short inclined cracks developed along the pier#1-to-wing connection line. The crack tracking at the spandrel-to-pier connection regions was impeded by the FRP strip congestion. FRP debonding initiation was noticed (at R=0.5% and onward) along the edge-line of several horizontal strips at crack crossing on pier#2. Specific snapping sounds were heard as the FRPs deformed and debonded. At R=0.8% a tapping inspection of the FRPs indicated that several horizontal strips on pier#2 were debonded at the intersections with inclined cracks. Certain flexural FRPs around the top corners of the opening fractured at R=0.4% and 0.8% drift ratio, whereas at the inside toe of pier#2 compression bulging of the vertical FRP strips was observed between the horizontal confinement strips. The specimen failed at R=0.9÷1% (19.35÷21.5 mm) by concrete crushing and FRP confinement fracture at the compression toes of the wide pier. The expanded cyclic responses and the cracking propagation corresponding to the R=1% (21.5 mm) drift level are shown in Figure 3.32. One can remark the waving of the axial loads, the pinched form of the hysteresis loops and the kinking (decline) of the curves at reloading.

3.2.6 Primary results of specimen PRCWP 4-S/E1-R/T

The primary results of the prior-to-damage strengthened PRCWP 4-S/E1-R/T specimen are presented in Figure 3.33. The specimen's behaviour was marked by initial cracking (from R=0.1÷0.2% onward) at the pier-to-spandrel connections and at the pier-to-foundation joint, and by inclined cracking (from R=0.4% onward) in both piers, extending at 68 deg in pier#1 and at 40 to 60 deg in pier#2. Crack tracking at the pier-to-spandrel connection regions was impeded by FRP congestion. FRP debonding was detected (from R=0.3% onward) on the spandrel and at the

pier-to-spandrel connections accompanied by FRP-snapping sounds. Pull-out distress of the FRP-anchorage at the inside toe of pier#2 was exhibited (R≥0.4%) by spalling of the surrounding cover concrete of the foundation beam. Further FRP debonding was noticed (from R=0.8% onward) on pier#2 along the edge of the horizontal strips at the crossing of diagonal cracks and along the base joint. The expanded cyclic responses and the cracking propagation corresponding to the R=0.9% (19.35 mm) drift level are shown in Figure 3.34. It is noteworthy the waving of the axial loads, the moderately pinched shape of the hysteresis loops and the slight decline (kinking) at reloading. The failure occurred at R=1÷1.1% (21.5÷23.65 mm) by concrete crushing at the outer toe of pier#2 and at the base of the wing element.

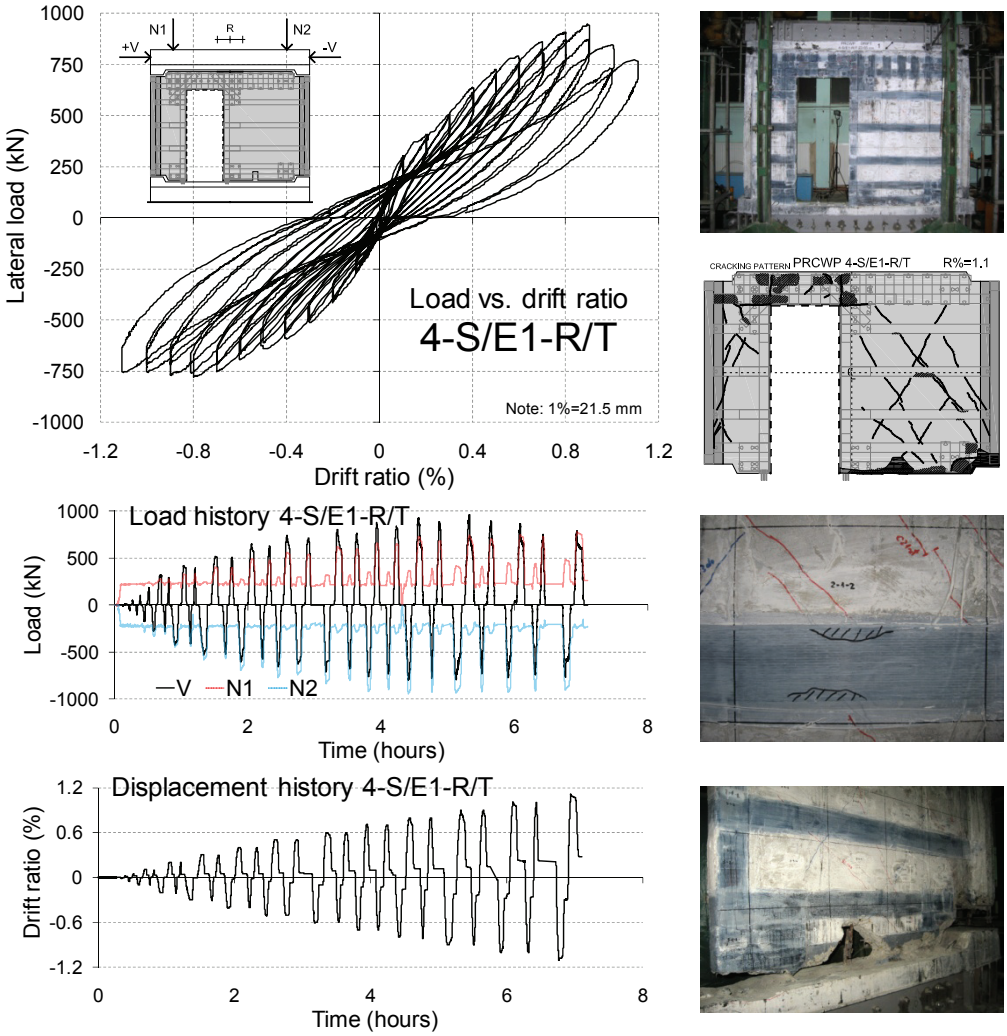

Figure 3.33 Primary results for specimen PRCWP 4-S/E1-R/T

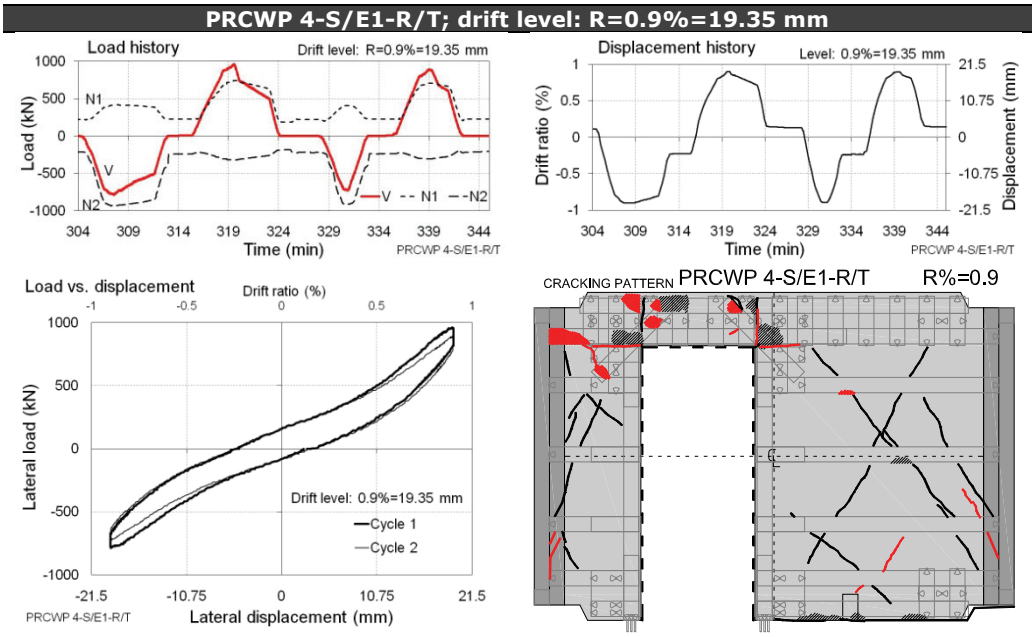

Figure 3.34 Expanded cyclic response of PRCWP 4-S/E1-R/T at 0.9% drift ratio

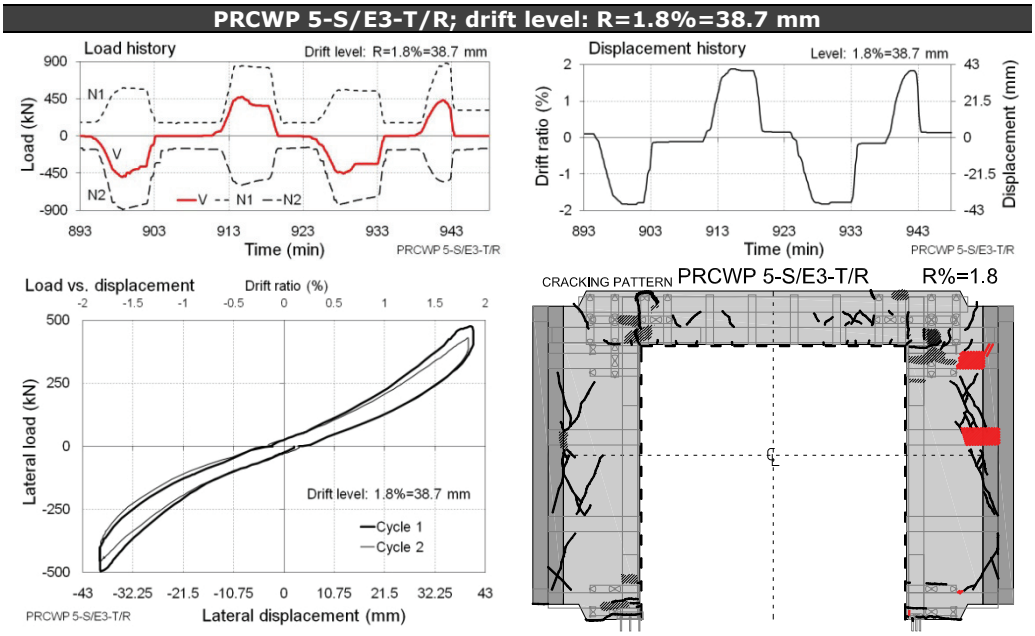

Figure 3.35 Expanded cyclic response of PRCWP 5-S/E3-T/R at 0.5% drift ratio

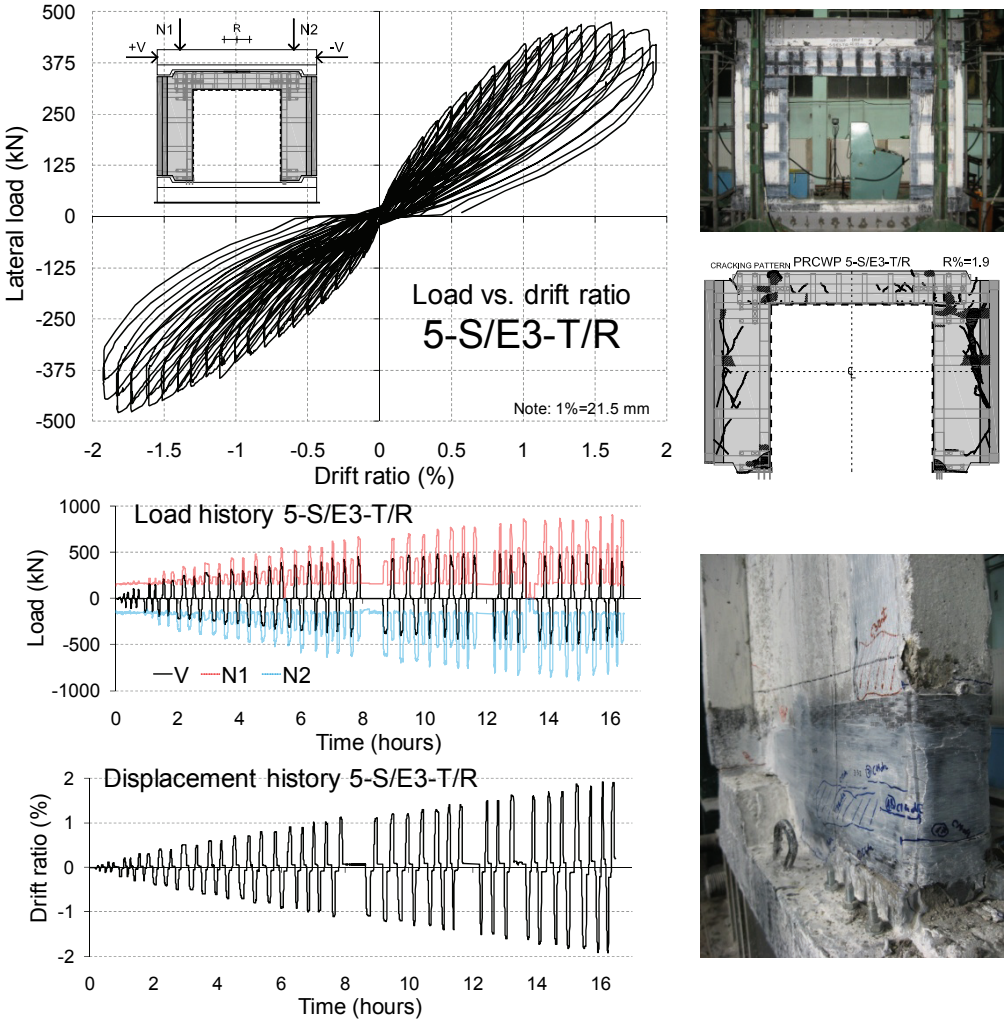

Figure 3.36 Primary results for specimen PRCWP 5-S/E3-T/R

3.2.7 Primary results of specimen PRCWP 5-S/E3-T/R

The primary results of the post-damage strengthened PRCWP 5-S/E3-T/R wall panel are presented in Figure 3.36. The specimen presented distributed cracking throughout the wall's components in the following order: horizontal cracks at the base and orthogonal (vertical and horizontal) cracks extending from the opening corners at the pier-to-spandrel connections (R≥0.2%), 65 to 70 deg inclined cracks across the piers (R≥0.5% existing and R≥0.8% new cracks) and 45 deg inclined cracks in the spandrel (R≥0.6%). Crack-tracking at the pier-to-spandrel connections was impeded by FRP congestion. The local FRP deterioration process comprised: fracture of the flexural strips at the pier-to-spandrel connections and at the base anchorages (R≥0.7%); debonding at the pier-to-spandrel connections (R≥0.7%); bulging above and underneath the confined portions of the pier toes and of the connections (R≥1.2%), respectively; and confinement fracture at the inside toe of pier#2 (R=1.8%). The final failure occurred at R=1.8÷1.9% (38.7÷40.85 mm)

along the pier#2-to-wing connection zone by concrete crushing and vertical sliding, simultaneously with FRP peeling-off at the end-anchorages of the horizontal strips. The expanded cyclic responses and the cracking propagation corresponding to the R=1.8% (38.7 mm) drift level are shown in Figure 3.35. One can observe the waving of the axial loads, the pinched shape of the hysteresis loops and the peeling-off failure of the horizontal FRP strips on pier#2. The inspection of the wall after the test revealed extensive concrete crushing along the pier-to-wing joint; fracture of the flexural FRP strips at the base anchorages and at the pier-to-spandrel connections next to the corners of the opening; and crushed concrete inside the FRP confinement at the pier toes.

3.2.8 Primary results of specimen PRCWP 6-S/E3-R/T

The primary results of the prior-to-damage strengthened PRCWP 6-S/E3-R/T wall panel are presented in Figure 3.37. The cracking development initiated at the

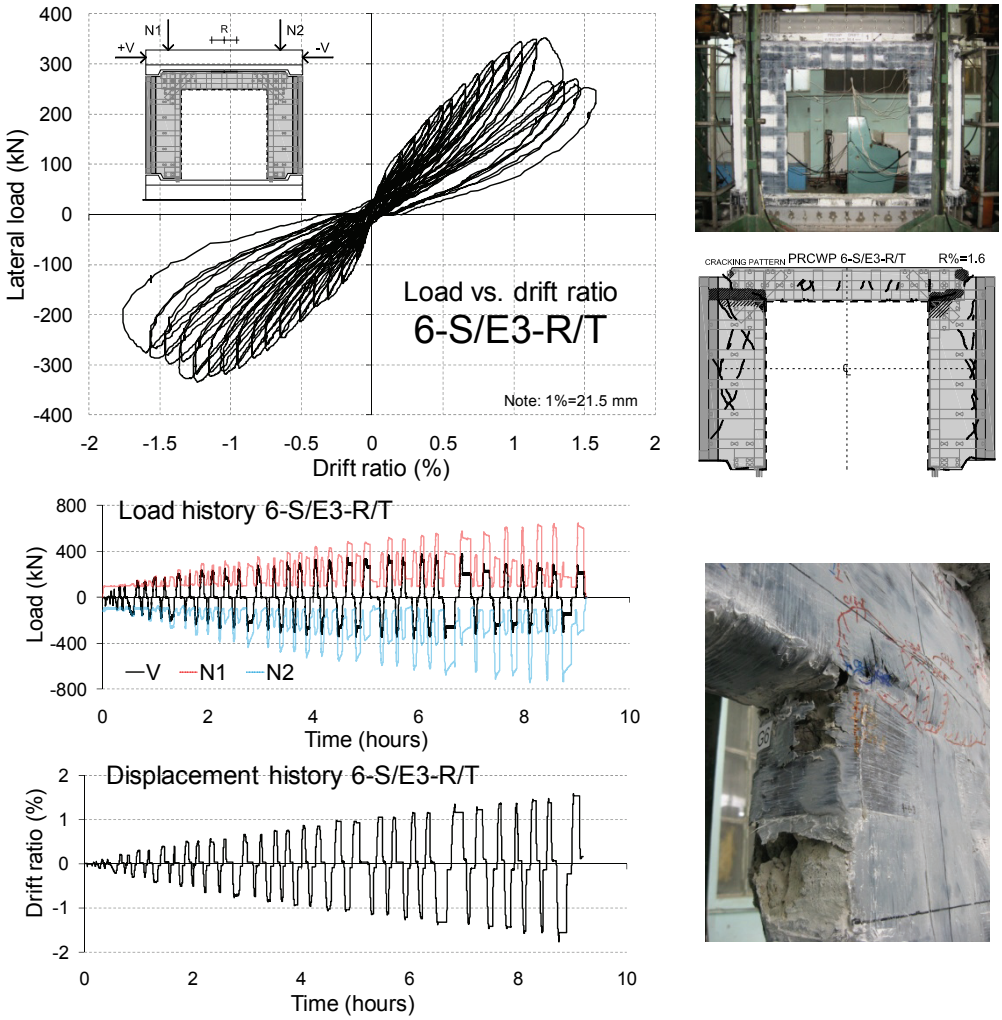

Figure 3.37 Primary results for specimen PRCWP 6-S/E3-R/T

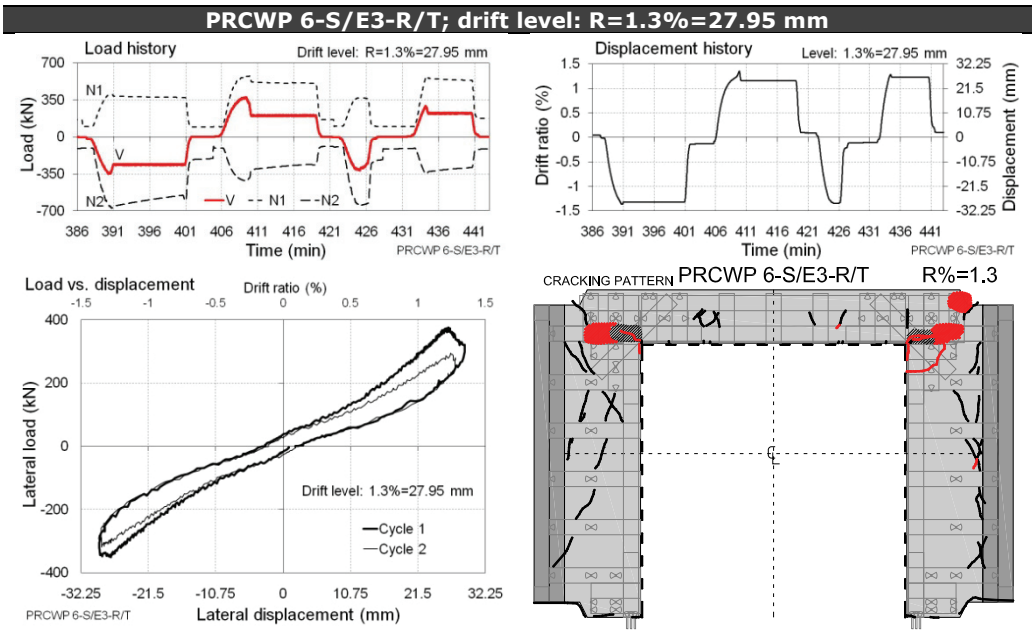

Figure 3.38 Expanded cyclic response of PRCWP 6-S/E3-R/T at 1.3% drift ratio

piers' base and at the pier-to-spandrel connections (R≥0.2%) while at larger displacement levels (R≥0.6%) inclined cracks occurred running at 57÷68 deg angle across the piers and crack propagation was observed along the spandrel (R≥0.7%). The congestion of FRP strips at the pier-to-spandrel connections impeded the tracking of the cracks at these locations. The local deterioration of the FRP reinforcements consisted in debonding at the spandrel-to-pier connections (R≥0.7%), pull-out distress at the base anchorages (R≥0.7%), and bulging (R≥0.9%) and fracture (R≥1%) of the flexural strips at the pier-to-spandrel connections. The failure occurred at R=1.3% (27.95 mm) by severe concrete crushing, FRP debonding, bulging and fracture at the spandrel-to-pier connections around the opening corners. The FRP confinement strips under the opening corners fractured at the edges and the flexural FRPs bulged and fractured in compression. The expanded cyclic responses and the cracking propagation corresponding to the R=1.3% drift level are shown in Figure 3.38. It is noteworthy the simultaneous waving of the axial loads, the pinched shape of the hysteresis loops and the lateral load drop at failure.

3.2.9 Comparison of the primary results

The load-displacement graphs presented in the foregoing figures were plotted to the particular load and drift limits of each specimen so as to display accurately the response. However, the drawback of this representation technique is that it is inappropriate to exhibit the differences between the individual responses. In order to facilitate comparison, in Figure 3.39 the responses were plotted to commensurate load and drift limits along the three comparison lines of the experimental program. As presented earlier (refer to section 3.1.1) the first comparison line was aimed to assess the weakening effect of the doorway cut-outs.

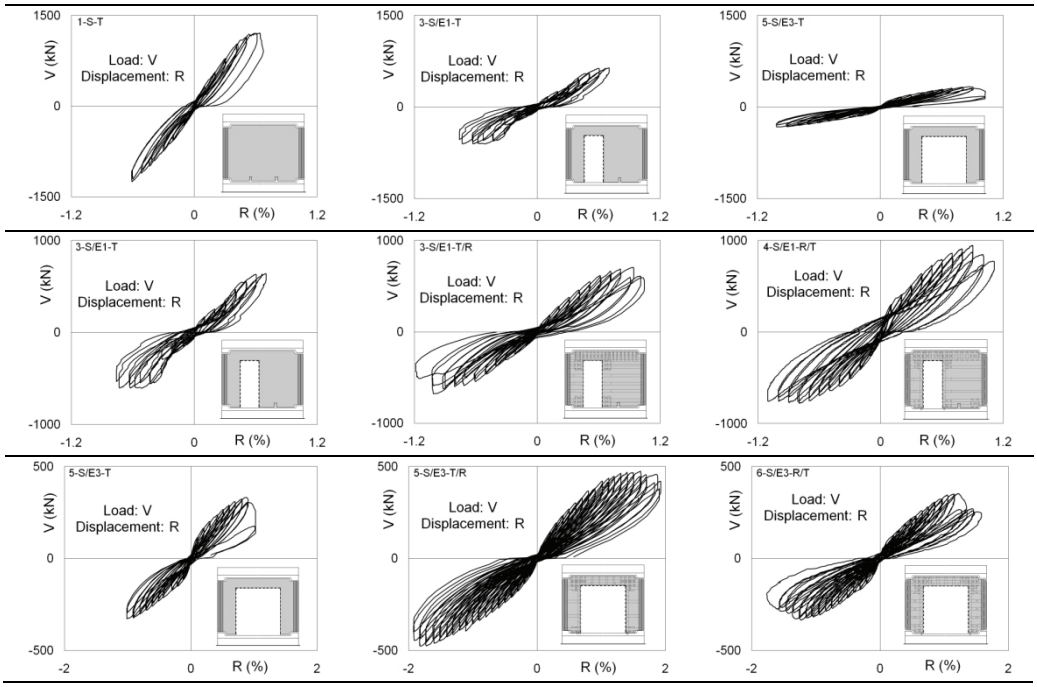

Figure 3.39 Comparison of the load-displacement responses

It is impressive the loss of load resistance of the specimens with cut-out door with respect to the solid reference. Comparison lines 2 and 3 were meant to assess the performance improvement achieved by CFRP-EBR strengthening for the narrow and wide door cut-out conditions, respectively. Both lines comprised a bare, a post-damage strengthened and a prior-to-damage strengthened wall test of the same opening condition. One can remark the increased load and displacement capacity and the enlarged hysteresis loops of the strengthened specimens with respect to the bare references.

4 ANALYSIS OF THE RESULTS

4.1 Data processing

The measured cyclic response along with the observed behaviour and failure modes represent the engineering outcome of the experimental tests. From this point onward, the objective of the research was to characterize the responses and exhibit the effects of the experimental variables on the response characteristics. These tasks are referred to as analysis of the results. In accordance to the general seismic performance characteristics of the lateral load resisting members the following analysis types were undertaken: strength analysis, displacement and strain analysis, stiffness analysis, and energy dissipation analysis. In addition to the measured response analyses, the observed behaviour aspects peculiar to concrete members were also addressed through cracking analysis.

In order to arrive at the response characteristics the recorded data was processed by extracting the significant information and performing simple mathematical operations. The data processing commenced with the denomination of the hysteresis loops' specific portions. In Figure 4.1 are presented the loading points and branches of the hysteresis loops at the i-th displacement level (R_i) of a generic load-displacement response featuring two reversed cycles. Each hysteresis loop (i.e. cycle) is composed of four branches in the following order: loading, unloading, opposite direction loading, and opposite direction unloading. Each branch is delimited by two consecutive points: curve-to-horizontal axis crossing point (reloading point) and the point at the target displacement (peak loading point). Note that the numbering begins in the negative loading direction.

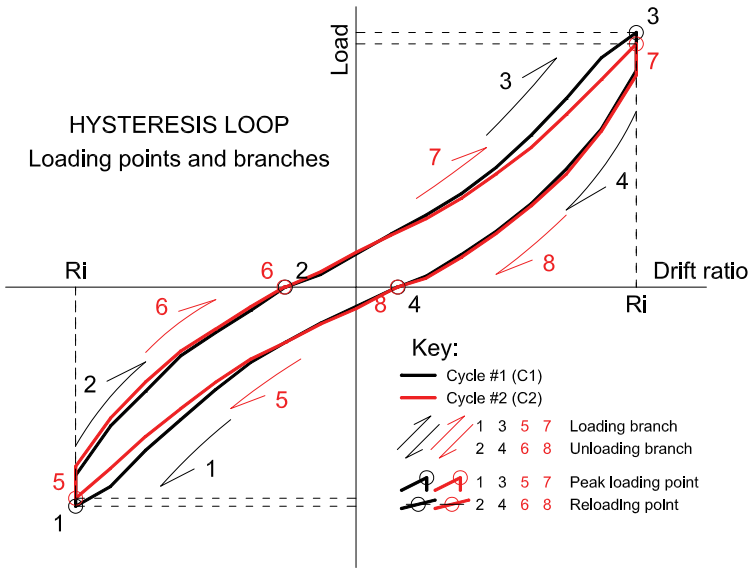

Figure 4.1 Denomination of the loading points and branches

4.2 Envelope Curves

4.2.1 Envelope types

In this thesis the envelope curves were obtained by interconnecting the peak loading points through the consecutive displacement levels. However, other definitions of the envelopes were reported in the literature like in [77, 78]. In general the principle of envelope curves can be applied to any of the cyclic response diagrams: load-displacement, load history, displacement history, load-strain, etc. Moreover, for a given cyclic response there are several envelope types that can be obtained through data processing, e.g. cyclic envelopes, average cyclic envelopes, average monotonic envelopes and backbone envelopes. Bearing in mind that the tests were displacement (drift) controlled the following envelope types are addressed in the subsequent sections: cyclic load-drift, cyclic displacement-drift, cyclic strain-drift, monotonic lateral load-drift and backbone lateral load-drift.

4.2.2 Cyclic envelopes

In Figure 4.1 one can observe that there are four peak loading points on a displacement level, namely: #1, #3, #5 and #7. Accordingly, the cycle #1 envelope curves, referred to as ENVELOPE C1, were obtained by connecting the points #1 and #3 through the increasing displacement levels, while the cycle #2 envelopes, referred to as ENVELOPE C2, were obtained by connecting the peak loading points #5 and #7 through the consecutive drift levels. The average cyclic envelopes, referred to as ENVELOPE M2, were obtained by calculating the arithmetic means between the C1 and C2 envelopes, i.e. by connecting the average peak loading points #(1-5) and #(3-7) through each drift level. In Figure 4.2 is presented the construction method of the M2 envelopes.

In order to exhibit the variation of the axial loads in relation with the lateral loading the N1-drift, N2-drift and V-drift envelopes were plotted on the same graph resulting in a general load-drift envelope, see Figure 4.3. Note that the axial loads at negative deflections were plotted on the negative load axis so as to facilitate comparison with the lateral loads. The bubbles along the lateral load envelope represent the peak loading points at each drift level.

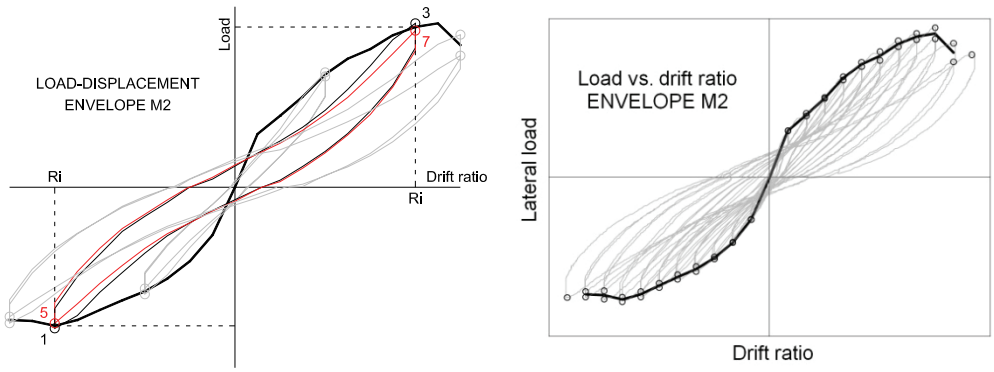

Figure 4.2 Construction of the average cyclic envelopes

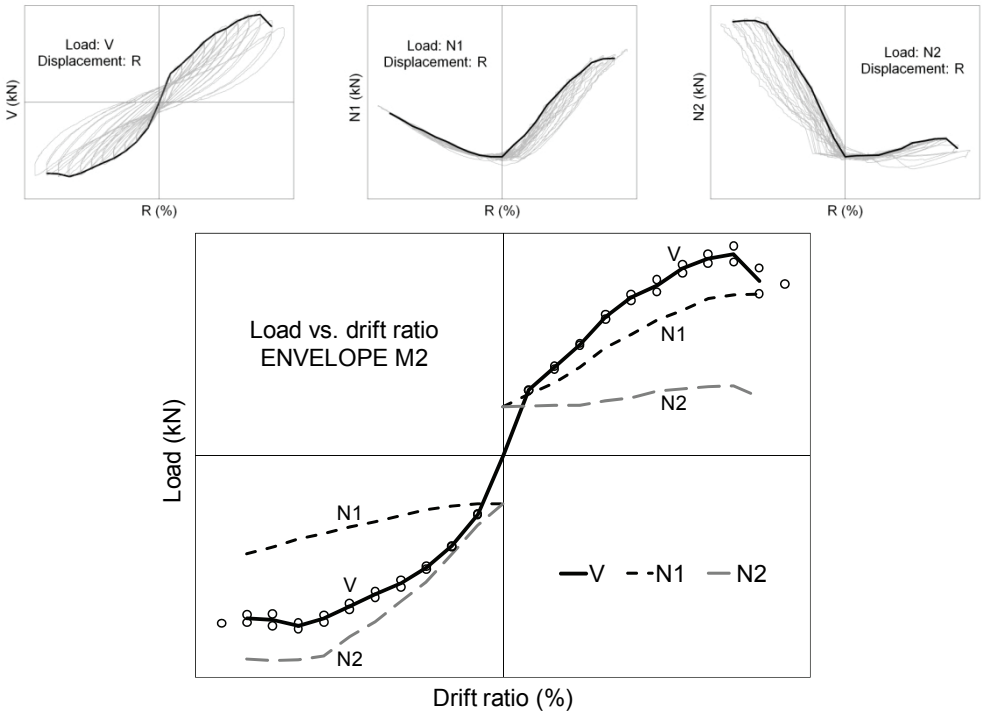

Figure 4.3 Components of the general load-drift envelope

In Figure 4.4 are shown the cyclic load envelopes for each specimen. One can remark in these plots the main characteristic of the loading conditions: the differential increase of the two axial loads during the lateral loading. Because the axial loads acted so as to counterbalance the overturning moment generated by the cyclic lateral loading, this phenomenon is referred to as outrigger effect. It is noteworthy that the increase rate of the axial loads is strongly affected by the lateral loading direction and by the opening conditions. In the case of the solid wall the axial load closer to the laterally loaded end (i.e. N1 in the positive direction and N2 in the negative direction) increased commensurately with the lateral load, while the farther axial load (i.e. N2 in positive and N1 in the negative direction) remained nearly constant. In the case of the specimens with narrow cut-out door opening (S/E1) the windward axial loads increased still commensurately with the lateral loads, but exhibiting also a directivity effect: in the positive direction the N1 envelopes run slightly below the lateral load curve, while in the opposite direction the N2 values exceed the corresponding lateral loads; the leeward axial load curves show a slight ascending tendency. The directivity effect can be correlated with the eccentric location of the opening. On the 3-S/E1-T plot the abrupt ascent of the N2-envelope in the (-0.2÷-0.4)% drift range denotes excessive axial loading, refer also to the detailed test log of this specimen in Appendix E.2. As for the wall panels with wide cut-out doors (S/E3) both axial load envelopes are above the lateral load curve in either loading direction. This loading condition can be regarded as local outrigger effect, because it is attributed to the limited coupling between the two piers.

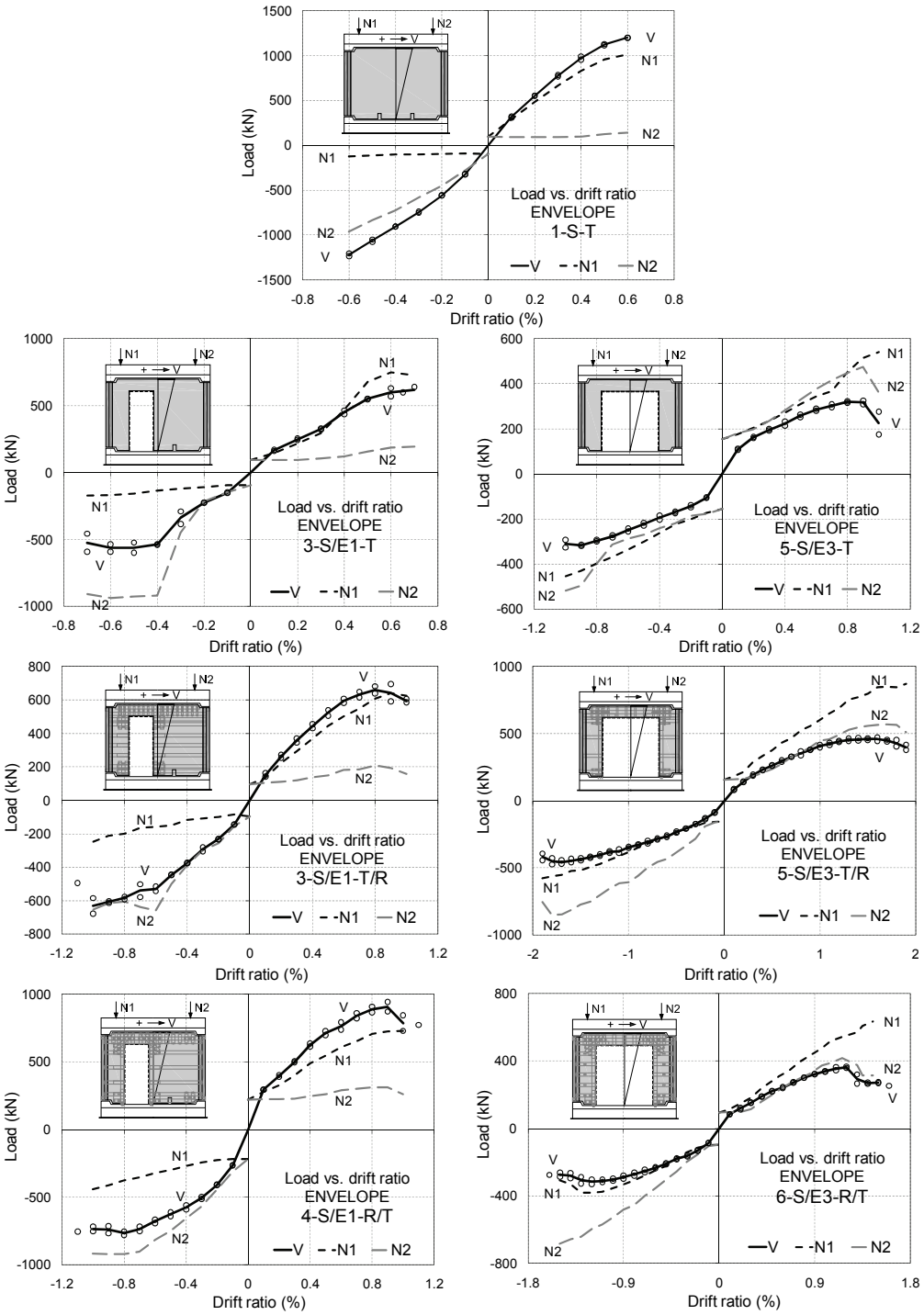

Figure 4.4 Cyclic load envelopes of the specimens

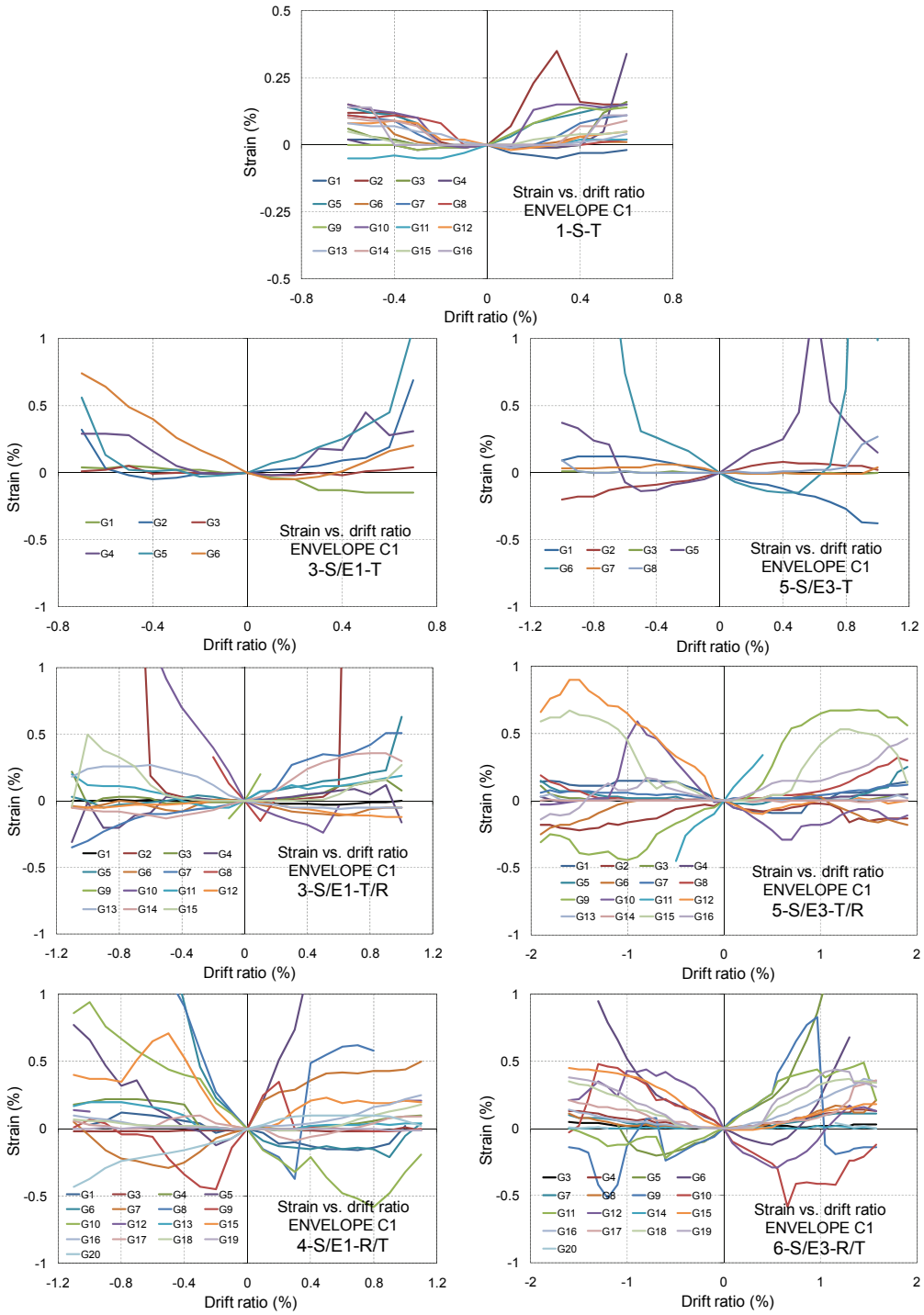

Figure 4.5 Strain-drift envelopes

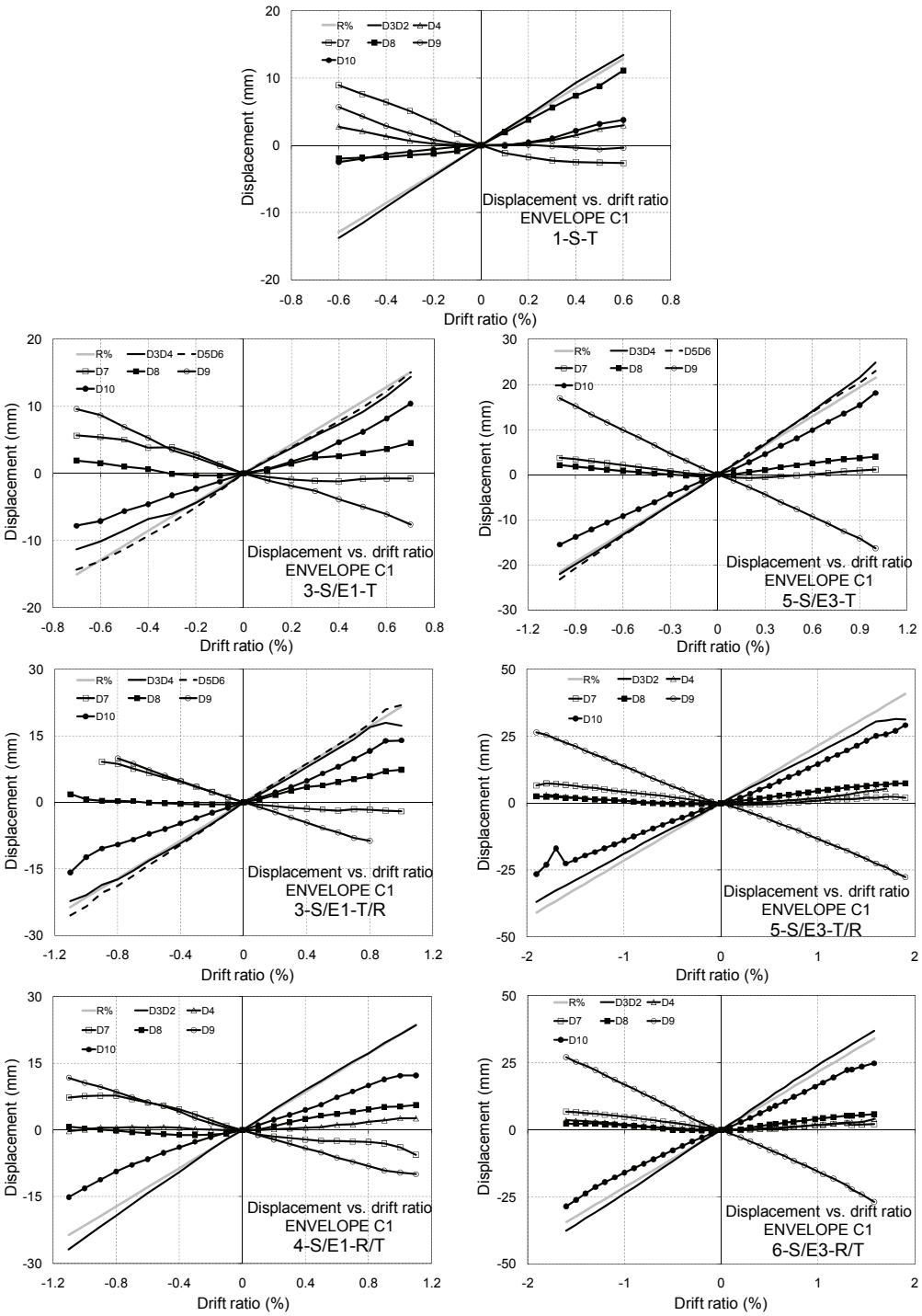

Figure 4.6 Displacement-drift envelopes

After the construction of the load-drift envelopes it was desirable to represent the other measured responses in a similar way. Hence, the strain and displacement envelopes were also drawn employing the pattern used for the loads. The strain-drift and displacement-drift envelopes are presented in Figure 4.5 and Figure 4.6, respectively. Owing to the large amount of data to be handled it was deemed satisfactory to process only the C1 (cycle #1) envelopes. Looking at the strain envelopes one can easily assess the strain activity at each drift level. It is remarkable that most of the recorded strains were in the (-0.5÷0.5)% range and only a few exceeded 1%. As regards the displacement envelopes one can observe that the drifts were the largest among the displacement records. A detailed analysis of the strains and displacements is provided later in this chapter.

4.2.3 Monotonic envelopes

The monotonic envelope curves, referred to as ENVELOPE M1, were processed only for the lateral load-drift responses, refer to Figure 4.7. The M1 envelopes were obtained from the average cyclic envelopes (M2) by ciphering the mean ordinates between the positive and negative direction branches, taken as absolute values. In other words the monotonic envelopes were drawn by connecting the average peak loading points #(1;3;5;7), taken as absolute values, through each drift amplitude.

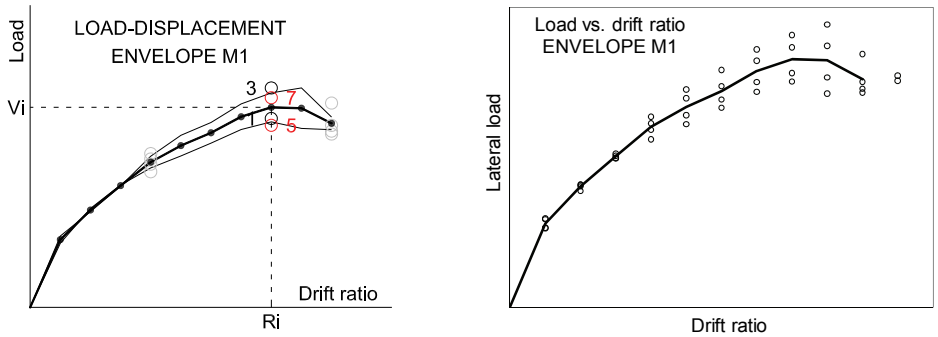

Figure 4.7 Construction of the monotonic load-drift envelopes

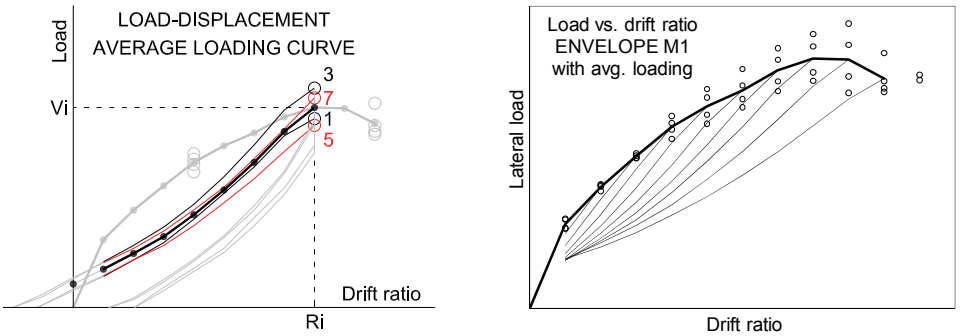

Figure 4.8 Construction of the envelopes with average loading branches

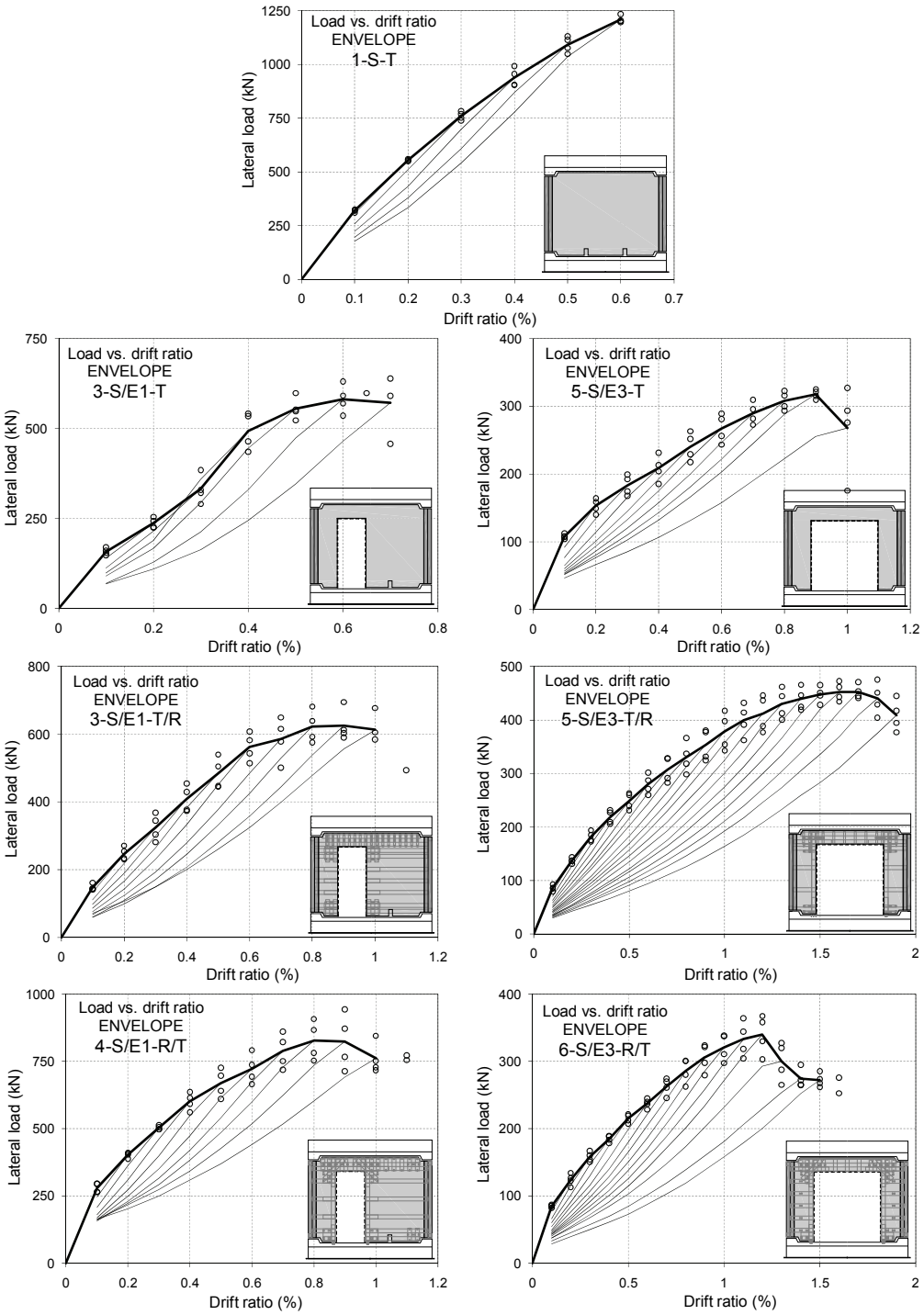

Figure 4.9 Monotonic load-drift envelopes with average loading branches

A more complex version of the monotonic envelope is the one where in addition to the peak loading points also the average loading branches are plotted. The construction method of the average loading branch at the i-th drift amplitude of a cyclic load-displacement response is depicted in Figure 4.8: the four loading branches (refer to Figure 4.1) were plotted to the positive axes and the mean ordinates were ciphered at each drift level up to the target drift amplitude; note that the average loading curve and the monotonic envelope meet at the average peak loading point. The complete diagram is obtained by plotting all the average loading branches corresponding to the consecutive drift amplitudes. These graphs are extremely helpful to assess the strength and stiffness degradation. In Figure 4.9 are presented the monotonic load-drift envelopes with average loading for the seven wall tests. Because the 1-S-T test was incomplete (refer to the test log in Appendix E.1) the envelope does not show any descending part. The sagging of the 3-S/E1-T envelope in the (0.1÷0.4)% drift range is the result of the change in the axial load control (refer to the test log in Appendix E.2). As a general remark it is noteworthy the drooping (sagging) of the average loading branches at increasing drift amplitudes. The individual peak loading points represented by the small circles along the envelope curves show the strength variation by loading direction and by repeated cycling.

4.2.4 Backbone envelopes

The backbone envelope is a schematic poly-linear representation of the monotonic envelope. Several recommendations were reported in the literature regarding the construction method of the bi-, tri-, or tetra-linear schematic envelopes for cyclic load-displacement responses.

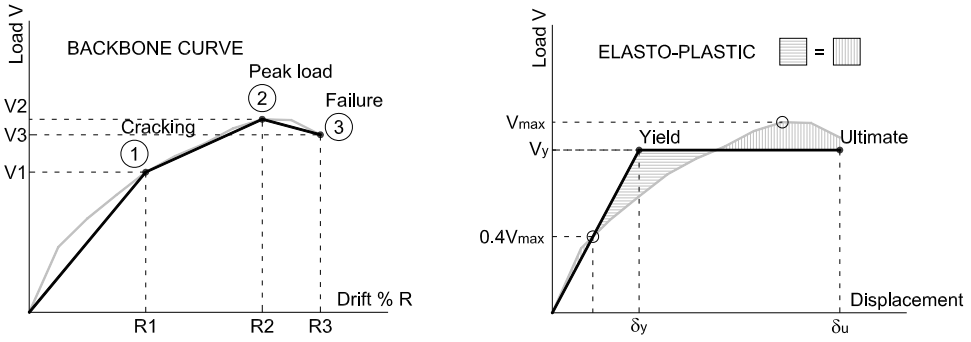

Figure 4.10 Construction of the schematic envelopes: (a) tri-linear backbone; (b) bi-linear elasto-plastic

Table 4.1 Cracking drift levels and selection criteria

Element	**Cracking drift R1%**	**Selection criteria**
1-S-T	0.2	diagonal cracking
3-S/E1-T	0.4	diagonal cracking
5-S/E3-T	0.3	significant cracking development
3-S/E1-T/R	0.4	significant cracking development
4-S/E1-R/T	0.4	diagonal cracking
5-S/E3-T/R	0.5	significant cracking development
6-S/E3-R/T	0.6	diagonal cracking

The bi-linear envelopes are idealised elasto-plastic force-displacement relationships involving the definition of the yield load, yield displacement and ultimate displacement as e.g. in [79]; one of the various construction methods of the elasto-plastic envelope, namely the equal energy method, is presented in Figure 4.10b. The tri-linear backbone envelopes are much closer to the real response and involve the definition of three load-displacement points: elastic limit, peak load and failure. Different approaches were found in the literature regarding the definition of the elastic limit: analytical [65], based on experimental steel strain measurements [80], peak load-based [81] and cracking-based [82]. The position of the peak load point is quiet obvious, while the failure load is generally defined as (75÷85)% of the peak load. The tetra-linear backbones are similarly constructed as the tri-linear ones, but additionally contain a fourth point, referred to as residual strength [65].

In this thesis the author adopted basically the tri-linear backbone concept presented in Figure 4.10a. In order to construct the backbones the following three load-displacement points were selected from the monotonic envelopes: (1) cracking point, (2) peak load and (3) failure. The designation of the first point was based on the observed cracking history by using the criteria of either diagonal cracking across the piers or significant cracking development. In Table 4.1 are listed the cracking drift levels along with the selection criteria for each wall specimen. The author admits that the foregoing definition of the elastic limit relies partly on the engineering judgement. However, it should be noted that the other approaches mentioned above were developed for flexural responses, thus their application to shear dominated responses, which is the case in the present experimental program, is not always suitable. The second load-displacement point (peak load) of the backbone corresponded to the maximum load on the monotonic envelope, while the third point (failure) was defined on a 20% post-peak load drop basis.

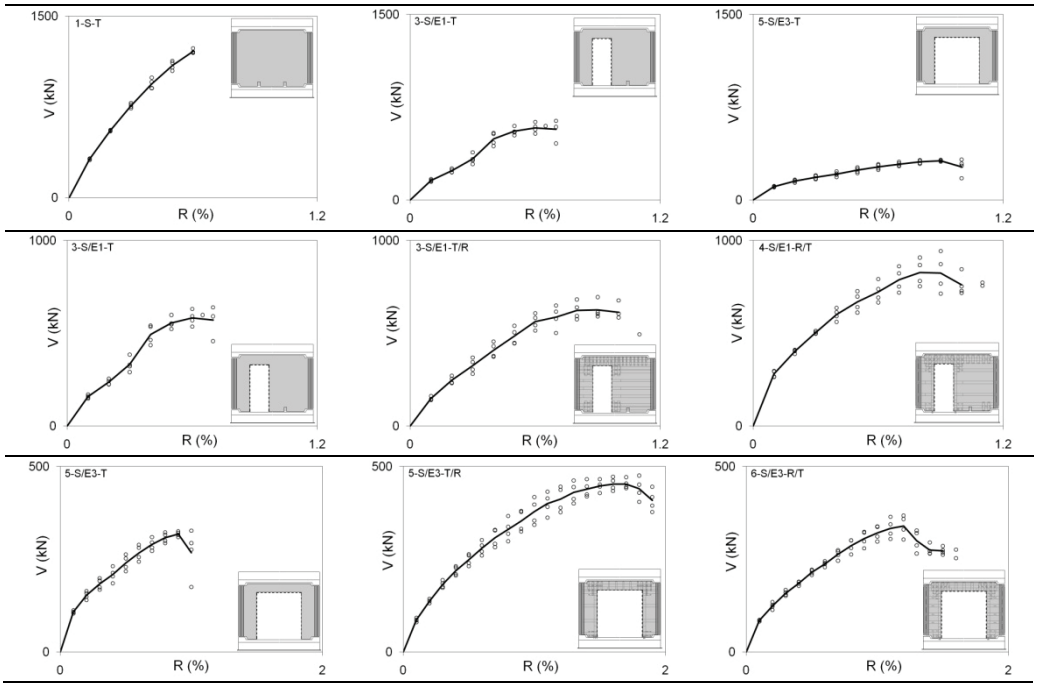

Figure 4.11 Monotonic load-drift envelope comparison lines

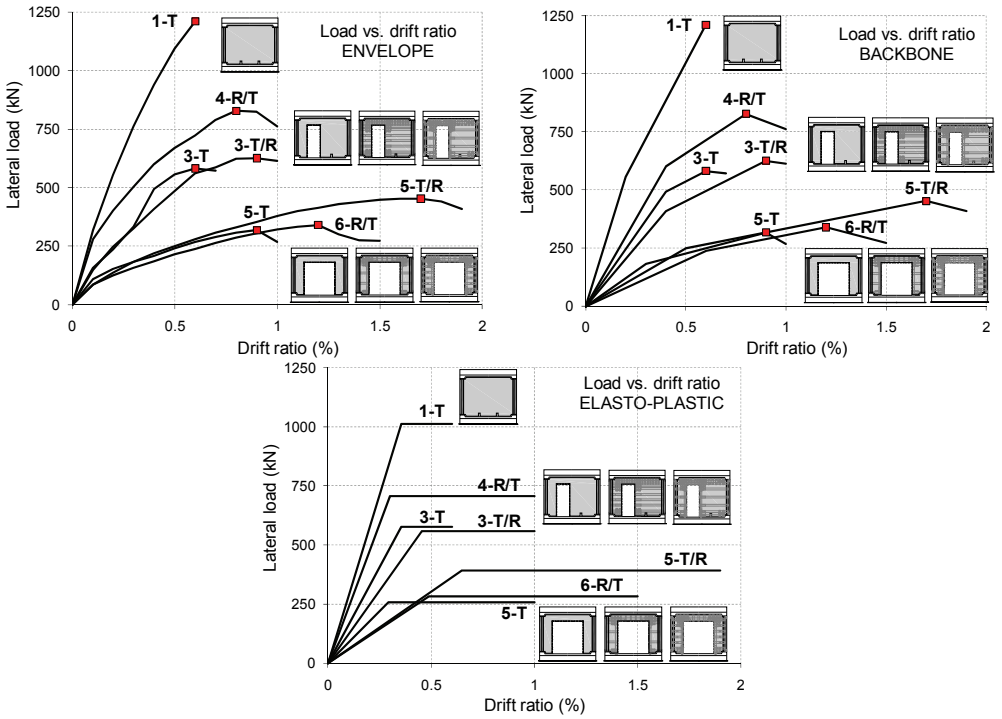

Figure 4.12 Comparison of the load-drift envelopes

It is noteworthy the degree data reduction from the recorded cyclic responses to the backbone envelopes: in average the recorded data files comprised about 20000 lines for each test; after the "facelift" (refer to section 3.2.1) remained 11000 data lines per test in average; the significant hysteretic responses comprised 2025 lines per test; the cyclic envelopes (C1+C2) contained 46 lines per specimen; the average cyclic envelopes (M2) were composed of 23 data lines per element; the monotonic envelopes (M1) consisted in 12 data lines per curve; and finally the backbones were constructed of only 3 pairs of data.

4.2.5 Comparison of the envelopes

In Figure 4.11 are presented the monotonic envelopes plotted to commensurate load-drift limits along the three comparison lines. One can observe the drooping of the envelopes along Line 1, which exhibits the weakening effect of the doorway cut-outs on the response of the solid wall. The comparison Line 2 and 3 show the effects of repair and FRP-EBR strengthening on the behaviour of the bare references with cut-outs. It is remarkable the stretching of the FRP-curves in terms of load and displacement.

Finally, a concise comparison of the monotonic, backbone and elasto-plastic envelopes is shown in Figure 4.12. One can observe that there are three curve clusters according to the cut-out condition. These plots are very useful to rapidly assess also the main response characteristics, except the energy dissipation, of each specimen and hence are regarded as principal results.

4.3 Strength analysis

The shear strength was defined as the maximum load on the monotonic envelope curve or in other words as the peak load point on the backbone envelope, denoted by V2. Accordingly, the shear strength is slightly less than the maximum recorded lateral load, because it regards an average value (refer to Figure 4.7 monotonic envelopes). The shear strength for the seven wall specimens are shown in Figure 4.13, both as absolute values and as normalized to the strength of the solid reference. Looking at the shear strength histogram one can observe that the strength ranged from 318 to 1210 kN. Taking into account the lightly reinforced web panels, the poor concrete quality and the cut-out conditions the bare specimens' shear strength was surprisingly high. The quantitative analysis of the shear strength in correlation with the load transfer mechanism will be provided later in this thesis. As regards the contribution of the repair and FRP-strengthening it is obvious that the shear strengths increased after the retrofit, although the strength of the solid reference wall couldn't be restored. The normalized shear strength histogram indicates the loss of lateral load resistance of each specimen with respect to the solid wall.

Henceforth the shear strength analysis is continued along the comparison lines. The first comparison line exhibits the weakening effect of the doorway cut-outs. In Figure 4.14 are presented the monotonic envelopes of the three bare specimens along with the performance ratio histogram. On the envelopes the peak load points are highlighted with red spots. Generally speaking, the term performance ratio may refer to any response characteristic normalized to the corresponding characteristic of a reference specimen. Here it was preferred because in addition to the normalized shear strength the histogram indicates also the normalized concrete strength of the web and wing for each specimen. This was deemed necessary because differences in concrete strength may have significant influence on the variation of the addressed response characteristic along the comparison line. It is quite obvious the progressive decrease of the strength by the increase of the cut-out size, even though the higher concrete strength of specimen 5-S/E3-T. In order to correlate strength loss with the size of the cut-out door, in Figure 4.14 the shear strength performance ratio was plotted against the cut-out ratio.

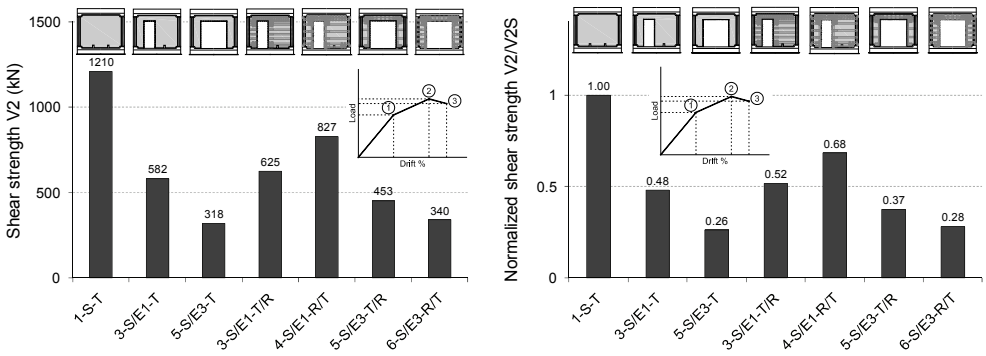

Figure 4.13 The shear strength of the wall specimens

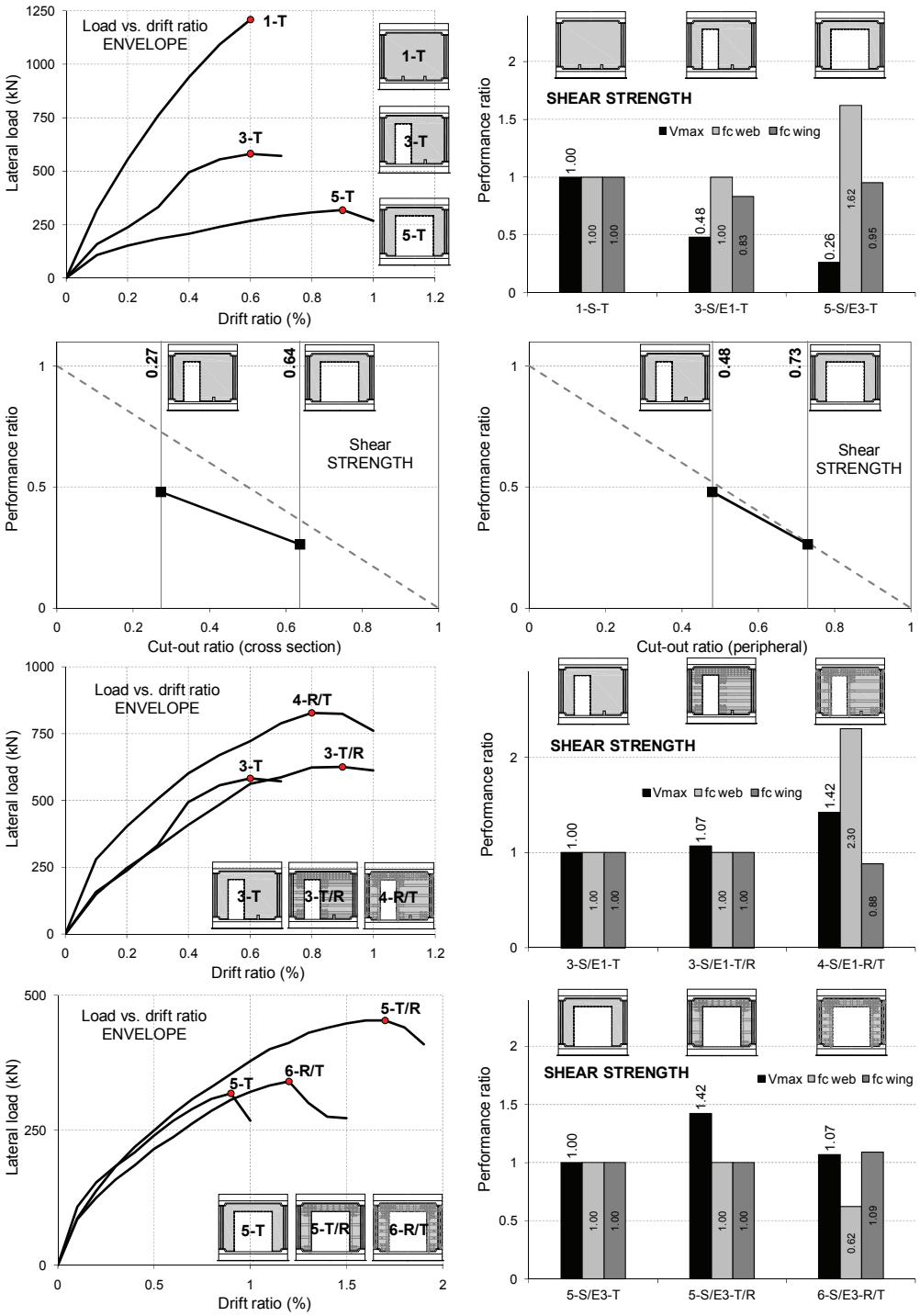

Figure 4.14 The effect of the experimental variables on the shear strength

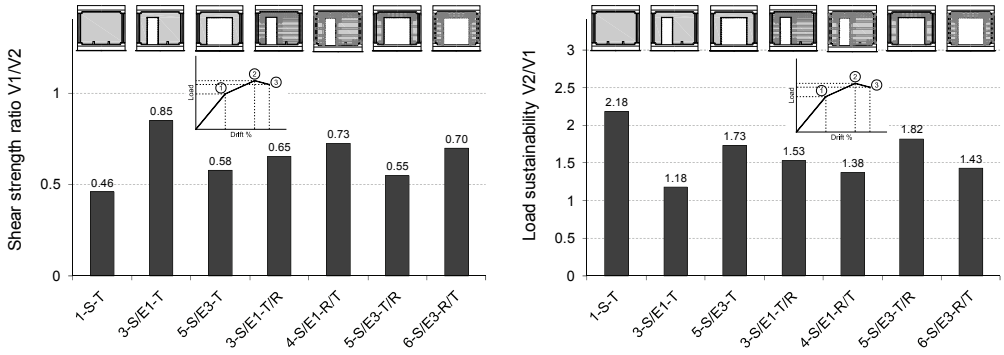

Figure 4.15 Shear strength ratios

The various opening ratios were defined in section 3.1.2 (refer to Table 3.5); here the cut-out ratio stands for the cross section ratio. As reference, the situation of complementarity between the performance ratio and the cut-out ratio is represented by the dashed line joining the unities of the two axes. It can be seen in Figure 4.14 that the performance ratios are below the reference (complementarity) line, that is the loss of strength was greater than the cut-out ratio in both cases. In-between the two experimentally obtained points one can assume linear performance-to-cutout relationship.

The second and third comparison lines exhibit the strengthening effect of the FRP-EBR for the specimens with narrow (S/E1) and wide (S/E3) cut-out doors, respectively. It is important to recall that the references of Lines 2 and 3 were the bare specimens with the corresponding cut-out conditions and not the solid wall. The monotonic envelopes and the performance ratio histogram for Line 2 are presented in Figure 4.14. It is remarkable that shear strength increased much more in the case of the prior-to-damage strengthened 4-S/E1/R/T specimen than for the post-damage repaired and strengthened 3-S/E1-T/R. However, this can be attributed, at least partly, also to the significant difference in the concrete strengths. The envelopes and the histogram for Line 3 are show in Figure 4.14. The deviation from the common sense, that is, the shear strength of the post-damage strengthened wall 5-S/E3-T/R was considerably higher in comparison to that of the prior-to-damage strengthened 6-S/E3-R/T specimen, can be explained by the significant difference in the web concrete strengths and by the large amount of concrete replaced by high-strength mortar during the repair of the former, refer to Appendix B.

Besides the shear strength (V2), the backbone envelope outlines also the cracking strength (V1). The ratio between these strengths, given either as cracking-to-shear strength (V1/V2) or as shear-to-cracking strength (V2/V1), is an important response characteristic. The latter form is referred to as load sustainability ratio (overstrength). As can be seen in Figure 4.15 the highest load sustainability (or inversely the lowest cracking strength ratio) was exhibited by the solid wall. However, there is no clear correlation between the cut-out size or strengthening condition and the variation of the load sustainability.

4.4 Displacement and Strain analysis

4.4.1 Displacement analysis

The principal displacement characteristics of the seismic response are defined on the backbone envelope, namely cracking drift (R1), peak drift (R2) and failure drift (R3). As can be seen from the drift ratio histogram in Figure 4.16, the cracking drift ratio varied in the range of (0.2÷0.6)%, exhibiting a slight increasing tendency with the cut-out size and strengthening condition. However, one should bear in mind that the assignment of the cracking limit was based partly on engineering judgement upon the damage state (refer to section 4.2.4); thus it was deemed inappropriate to construe the variation of the cracking drift as the effect of either of the experimental variables. The peak (R2) and failure drifts (R3) varied in the ranges of (0.6÷1.7)% and (0.7÷1.9)%, respectively. It is clearly visible that by FRP-strengthening the displacement capacities increased with respect to the bare references, particularly in the case of the specimens with wide cut-out openings.

In seismic analysis and design one of the paramount response characteristic is the displacement ductility, defined as the ratio between the ultimate displacement and the elastic limit displacement. Despite the importance of the ductility, its practical determination is quiet ambiguous owing to the different definitions of the component displacements (refer to section 4.2.4).

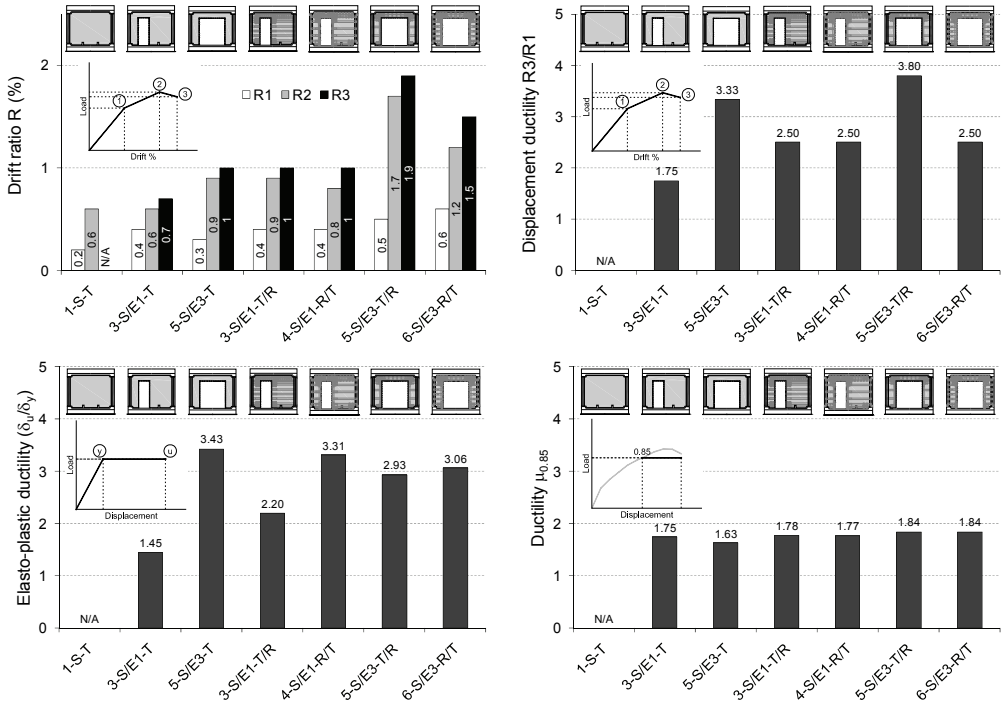

Figure 4.16 Backbone drift ratios and ductility

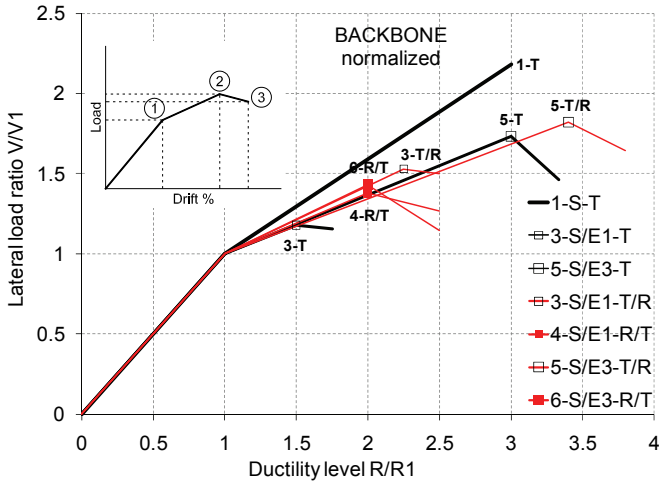

Figure 4.17 Normalised backbone envelopes

In this thesis the definition of the ductility was adapted to the shear dominated load transfer conditions, that is, it was calculated as the ratio between the failure drift (R3) and the cracking drift (R1). The displacement ductility histogram is shown in Figure 4.16. Note that the ductility ranged from 1.75 to 3.8 showing a slight increasing tendency by strengthening. However, this should be viewed in the light of the uncertainties regarding the cracking limit. For reference purposes the displacement ductility was calculated also according to the idealized elasto-plastic response and to the $\mu_{0.85}$ method. The elasto-plastic ductility is defined on the bi-linear response (refer to Figure 4.10) as the ratio of the ultimate displacement to the yield displacement. The $\mu_{0.85}$ method defines the ductility as the ratio of the ultimate displacement to the displacement corresponding to 0.85 of the maximum load on the ascending branch of the monotonic envelope [65]. As can be seen in Figure 4.16, the elasto-plastic ductility values were similar to the calculations carried out on the backbone, while the m0.85 method yielded considerably lower results. The correlation between the ductility level and the post-cracking load level is illustrated by the normalized backbone envelopes shown in Figure 4.17. Note that this is a dimensionless plot where the unity represents the cracking load and displacement for each specimen. It is noteworthy that, despite the incomplete test, the solid wall attained a ductility level of 3, one of the highest values amongst the specimens.

Besides the drift displacement there were a number of deformation and deflection measurements, which convey significant evidence regarding the shear transfer mechanism and the effects of the experimental variables on the behaviour mode. In Figure 4.18 are shown the comparative plots of the following cyclic displacement envelopes: horizontal bulging deformation (D4), cross-diagonal deformation (D9, D10) and vertical uplift displacement (D7, D8). It is clearly visible that the specimens with openings exhibited lower bulging and uplift, and higher diagonal strains than the solid reference.

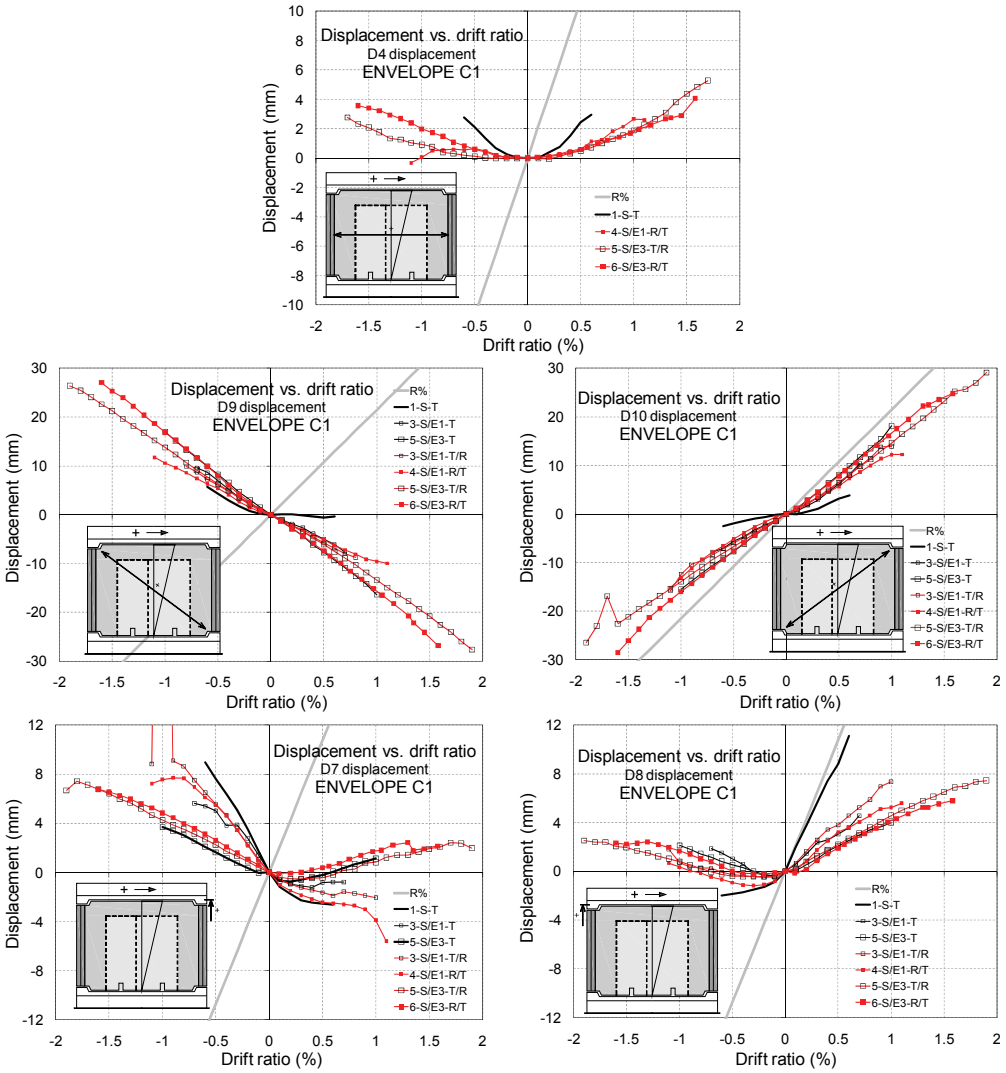

Figure 4.18 Displacement envelope comparison

4.4.2 Strain analysis

The strain measurements are fundamental in any experimental structural response analysis because it indicates precisely the local behaviour. When addressing a strain record one should bear in mind the substrate material, location and direction of the gauge. In the present experimental program two material types were monitored by strain gauges, namely internal steel reinforcements and externally bonded CFRP reinforcements. In the subsequent sections the steel and FRP strains are discussed separately.

In Figure 4.19 are shown the cyclic envelopes (C1) of the steel strain-drift responses arranged along the three comparison lines. On these plots the conventional yield strains (±0.2%) are marked with horizontal dashed lines.

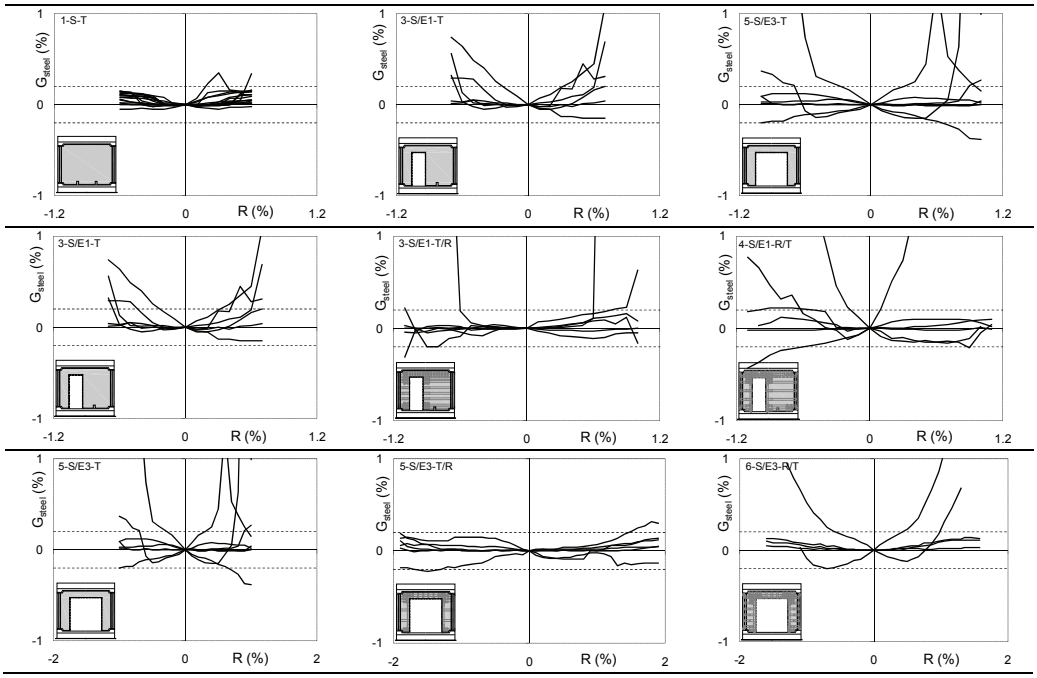

Figure 4.19 Steel-strain envelope comparison lines

Looking at the first comparison line one can notice the differences in the strain activity caused by the door cut-outs. In the case of the solid wall (1-S-T) the strain measurements indicated extension barely exceeding 0.2%, except in the extreme vertical bars. According to the strain records of the bare specimens with cut-outs (3-S/E1-T and 5-S/E3-T), the most active steel reinforcements were the horizontal bars atop the opening corners, with strains over 0.2% at 0.3% drift ratio and beyond, while the pier re-bars were much less active. With regard to the second and third comparison lines it is remarkable the low activity of the steel reinforcements in the post-damage strengthened specimens (3-S/E1-T/R and 5-S/E3-T/R), whereas their prior-to-damage strengthened counterparts (4-S/E1-R/T and 6-S/E3-R/T) exhibited steel strain responses similar to the bare walls with cut-out doors. Based on the steel strain measurements two wall regions can be distinguished: one exhibiting high and adverse strain activity at the pier-to spandrel and pier-to-foundation connections, and the other with low to moderate strains at the piers' inner parts.

The FRP-strain envelopes are presented in Figure 4.20. It can be observed that all but two gauges recorded strains in the (-1÷+1)% range, most of the records not even exceeding the ±0.5% limits. Some of the measurements indicated very early FRP failure (refer to the highlighted curves G9 and G11) at (0.1÷0.6)% drift amplitudes and at (0.2÷0.35)% strain levels, which was substantiated by the visual observations made during the tests (refer to the test logs in Appendix E). In Figure 4.20 are depicted some of the fractured FRPs at the end of the tests. These premature FRP failures were attributed to the adverse strain activity at the pier-to-spandrel connection regions already mentioned above. At these locations the FRP strips were subjected to repeated increasing compression-tension reversals parallel to the fibre direction, a loading condition to which the extremely thin FRP-EBR

sheets responded unsatisfactorily. Although not monitored by strain gauges, similar FRP failure was detected at the pier-to-foundation anchorages of specimen 5-S/E3-T/R (refer to the test log in Appendix E.6).

The foregoing experimental evidences and the explanation given to them raise a more general question with respect to the suitability of FRP-EBR for flexural strengthening in reversed cyclic applications. The principle of flexural strengthening requires that the FRPs to be oriented parallel to the tensile forces; however, in cyclic loading conditions the flexural tension changes into commensurate compression forces when the element is loaded in the opposite direction; hence, the flexural FRPs are subjected to alternating compression-tension forces which cannot be withstood by the thin FRP overlays.

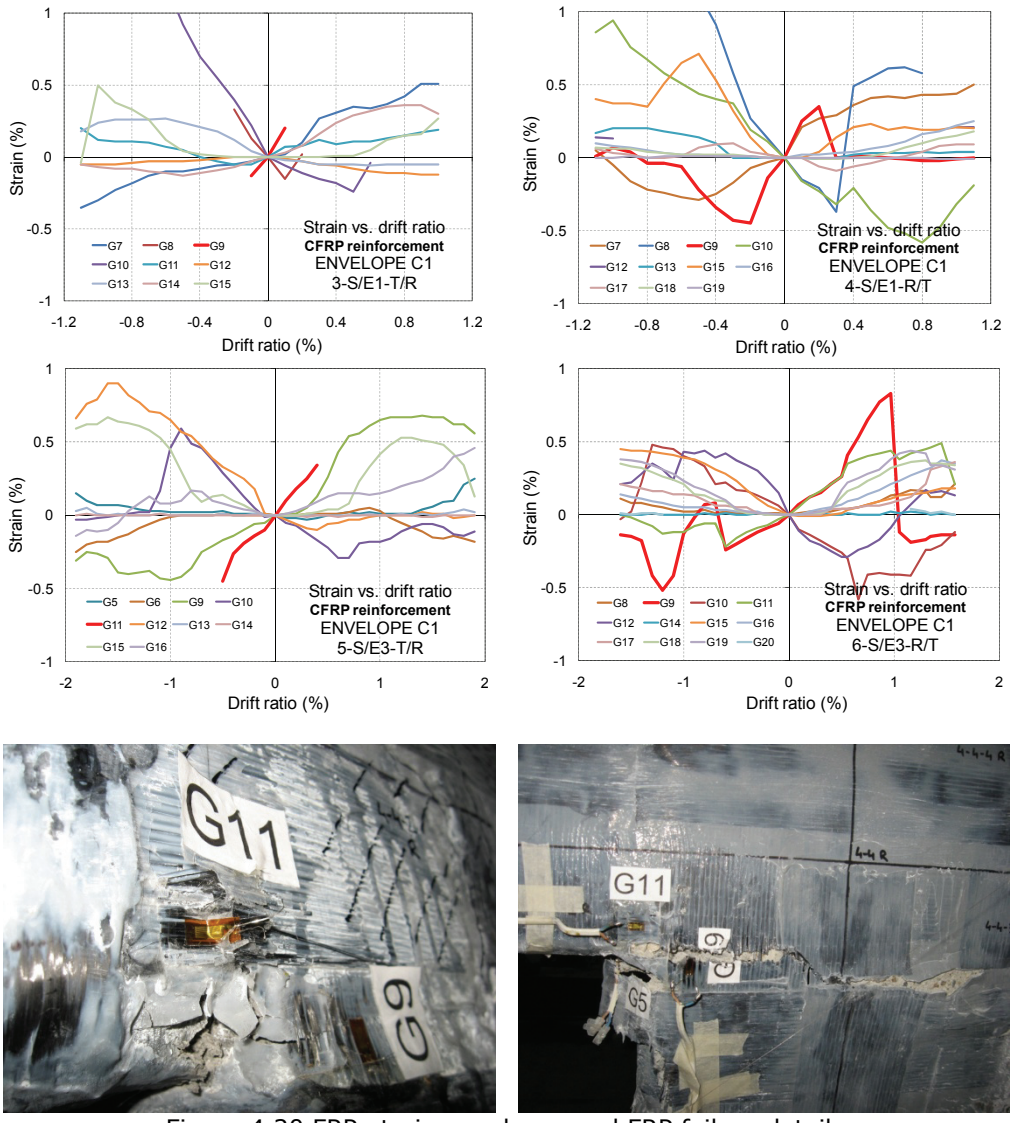

Figure 4.20 FRP-strain envelopes and FRP failure details

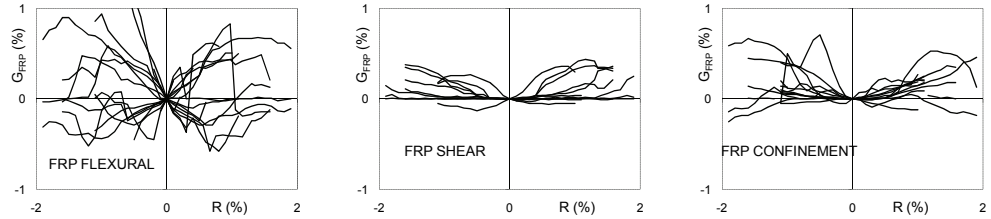

Figure 4.21 Flexural, shear and confinement FRP-strains

In order to assess the soundness of the previous reasoning in Figure 4.21 are shown the strain envelopes separately for the flexural, shear and confinement FRPs (refer also to strengthening strategy in section 3.1.3 and to the instrumentation in Appendix C). One can remark the significant tension-compression alternation of the flexural envelopes, whereas the shear and confinement strains indicate prevailing tension. It is noteworthy however that despite the harsh loading conditions, not all the flexural FRPs failed prematurely, some of them developing strains from -0.6% in compression to +1% in tension (G10, 4RT). The shear FRPs exhibited strains in the (-0.13÷+0.44)% range; meanwhile, some of the strips debonded at inclined crack crossing and peeled-off at the pier-to-wing anchorages but none failed by FRP fracture. The confinement FRPs reached (0.5÷0.7)% tensile strain at fracture.

4.5 Stiffness analysis

In civil engineering the stiffness (K) of a structural member is defined as the ratio of the applied load to the resulting deflection. The physical sense of the stiffness is a force which would induce, assuming linear load-displacement relationship, a unit deflection of the structural element at a specified point and in a given direction; in general this point and direction is the application point and direction of the load. On a load-displacement plot the definition of the stiffness can be translated geometrically into the slope of a line connecting either the origin to a point on the curve (secant stiffness, K_{sec}) or two subsequent points from the curve (tangent stiffness, K_{tan}). In Figure 4.22 are shown the stiffness definitions pertaining to the following load-drift responses: monotonic envelope, backbone and average loading curve. On the monotonic envelope $K_{sec,Ri}$ denotes the secant stiffness corresponding to the δ_i displacement amplitude (R_i drift ratio). The first in this series, namely when d=2.15 mm (R=0.1%), was referred to as initial stiffness and it was denoted by K_0. On the backbone envelope both secant and tangent stiffness definitions are indicated corresponding to the three load-displacement points and to the line segments joining (connecting) them, respectively. Finally, on the average loading curve is pointed out the tangent stiffness for each line segment between two subsequent drift levels up to the target drift amplitude. The first in the series, namely the one for the curve segment between d=R=0 and d=2.15 mm (R=0.1%), was referred to as reloading stiffness and it was denoted by $K_{0,Ri}$ where R_i stands for the target drift amplitude of the average loading curve.

The variation of the secant stiffness along the monotonic envelope curve is referred to as stiffness degradation and it can be displayed by plotting the subsequent stiffness values against the drift ratio; as mentioned above the first point of this stiffness-drift relationship is the initial stiffness.

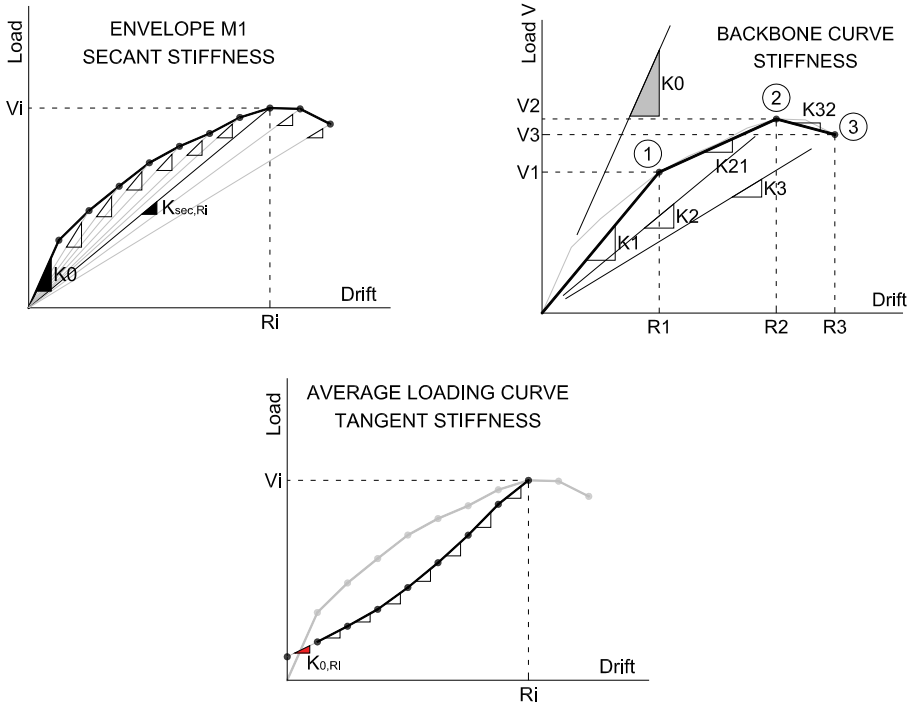

Figure 4.22 Stiffness definitions

The stiffness degradation graphs and the initial stiffness histograms are presented in Figure 4.23 both as absolute values and normalized to the initial stiffness of the solid reference wall. It can be observed that the degradation curves are grouped in three clusters according to the cut-out condition, while the influence of strengthening was quiet small. Note that the exceptionally high stiffness of the 4-S/E1-R/T specimen can be attributed to the 2.3 times higher concrete strength rather than to the FRP strengthening. The anomaly, that is, the sudden ascent of the degradation curve of specimen 3-S/E1-T at 0.4% drift ratio is the result of excessive axial loading (refer also to the test log in Appendix E.2). As exhibited on the stiffness histogram in Figure 4.23, the initial stiffness ranged from 40 to 150 kN/mm.

In the followings the discussion is continued along the comparison lines. Remind that the first comparison line displays the weakening effect of the door cut-outs and comprises the three bare walls, while the second and third lines show the effect of FRP-EBR strengthening on the seismic response of the specimen series with narrow and wide cut-outs, respectively. In Figure 4.24 are presented the stiffness degradation graphs and the performance ratio histograms pertaining to each comparison line. Note that the performance ratio histograms are dimensionless composite plots which indicate the variation of the initial stiffness and of the concrete strength along the comparison lines. Looking at the performance ratio histogram of the bare specimens (Line 1) one can assess the decrease of the initial stiffness caused by the cut-outs, meanwhile keeping an eye on the concrete strength variation too.

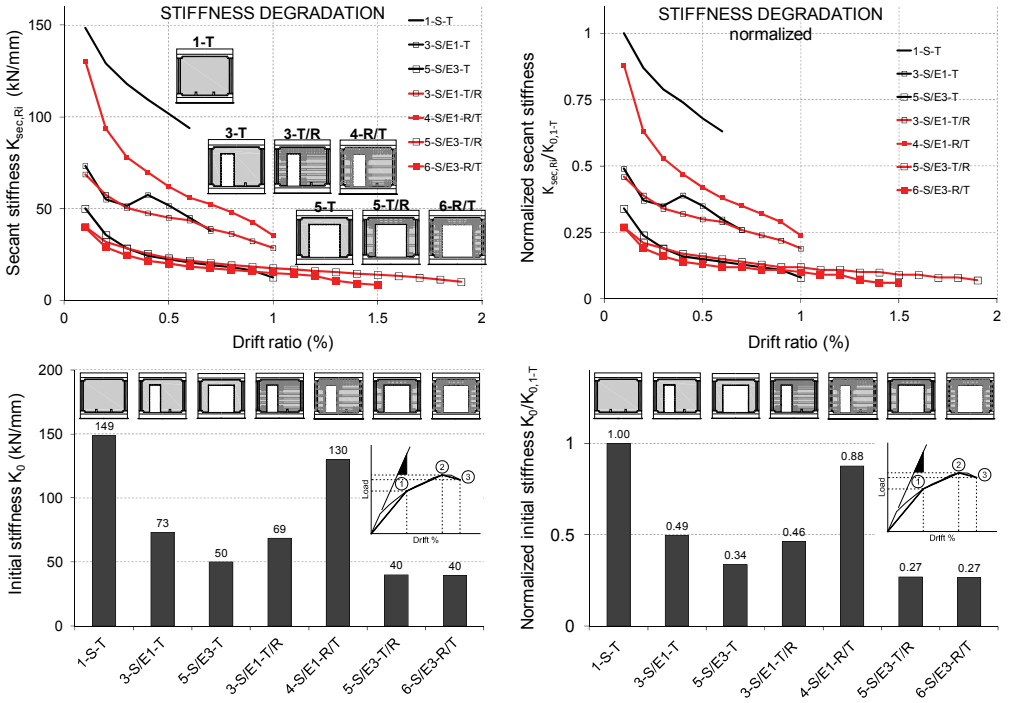

Figure 4.23 Stiffness degradation and initial stiffness

The relationship between the loss of initial stiffness and the size of the cut-out is displayed on the performance ratio vs. cut-out ratio plots in Figure 4.24 (for further details regarding this type of graph refer to the strength analysis section). Take notice of the difference between the two plots, namely the cut-out ratio was computed either as cross sectional ratio or as peripheral ratio. It is visible that in the latter case the initial stiffness ratio and the cut-out ratio are roughly complementary numbers (the sum of them equals unity) for both door sizes. As regards the other two comparison lines (Line 2 and 3) it can be observed that the post-damage repair and FRP-retrofitting restored 94% (3-S/E1-T/R) and 80% (5-S/E3-T/R) of the initial stiffness of the bare references; the tests on the prior-to-damage strengthened specimens (4-R/T and 6-R/T) yielded contradictory results which are plausibly the effect of the differences in concrete strength; however, one can assume that the initial stiffness slightly increase by prior-to-damage FRP-strengthening.

Similarly to way in which the load-displacement monotonic envelopes were improved by adding the average loading curves (refer to section 4.2.3), the stiffness degradation graphs were augmented by plotting also the tangent stiffness variation along each average loading curve. In Figure 4.25, besides the descending curves illustrating the secant stiffness degradation, the families of quasi parallel ascending curves represent the tangent stiffness variation. The decrease of the reloading stiffness is displayed by the falling starting points of the average stiffness curves. The degradation of the reloading stiffness is an important seismic response characteristic.

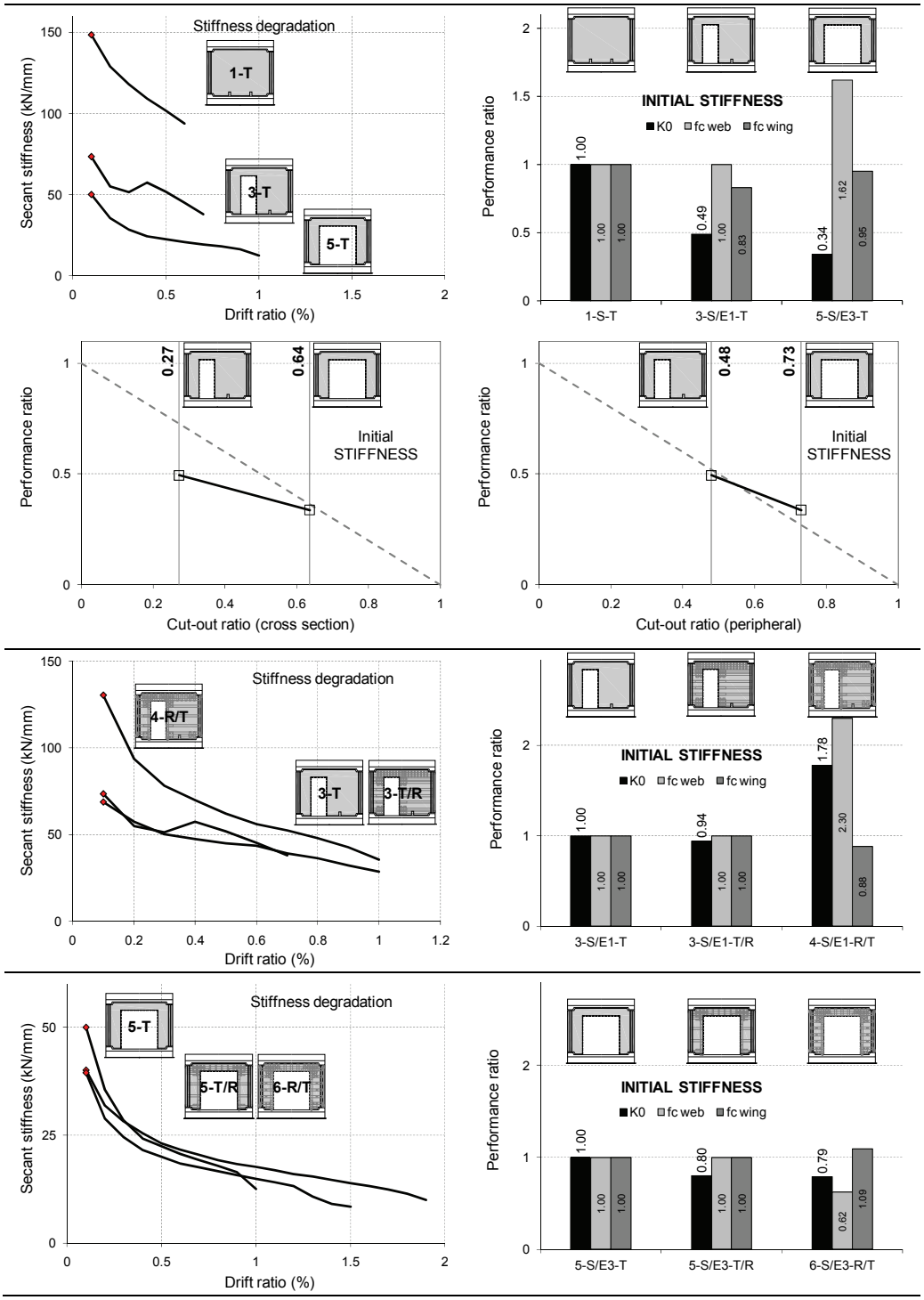

Figure 4.24 The effect of the experimental variables on the initial stiffness

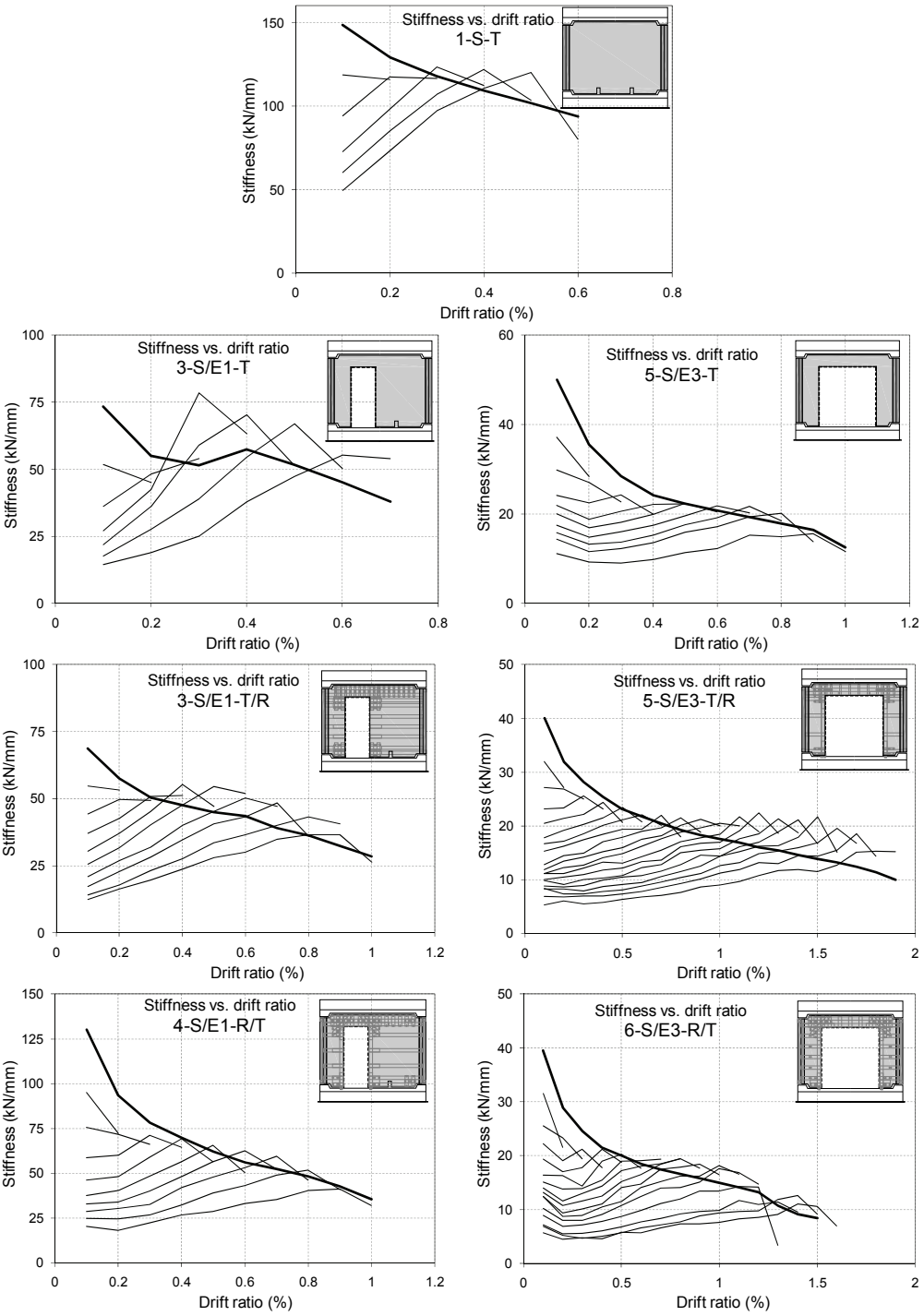

Figure 4.25 Stiffness degradation with tangent stiffness variation

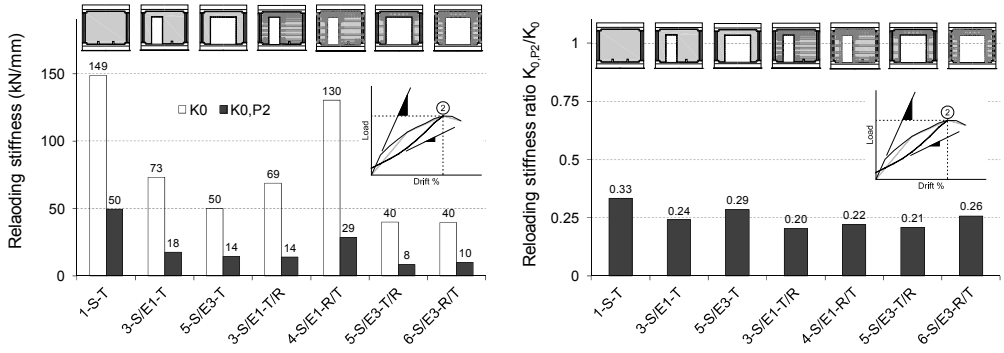

Figure 4.26 Reloading stiffness

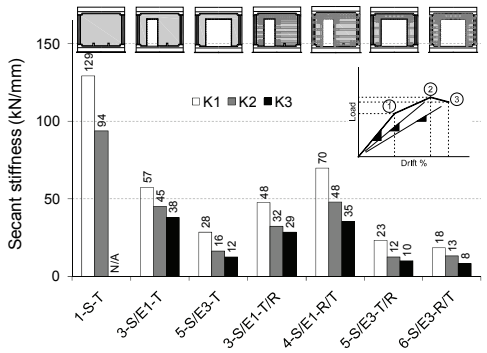

Figure 4.27 Backbone stiffness

In Figure 4.26 are shown the histograms comparing the initial stiffness to the reloading stiffness of the average loading curve corresponding to the peak load (point 2 on the backbone). It can be remarked that the reloading stiffness corresponding to the peak load is one fifth to one third part of the initial stiffness and that this ratio is quasi uniform amongst the specimens, irrespective of the cut-out or strengthening condition; hence, it may be looked at as a general response characteristic of the tested element types in the given loading conditions.

Finally, in Figure 4.27 is presented a histogram exhibiting the secant stiffness values for the three points on the backbone envelope. One should notice that the secant stiffness at peak load (K2) can be considerably higher than the reloading stiffness corresponding to the same (peak) load point ($K_{0,P2}$).

4.6 Energy dissipation analysis

4.6.1 Definitions

In seismic design philosophy the concept of energy dissipation (absorption) is a watershed between adequate and inadequate response and therefore its experimental assessment and analysis is of high importance. The energy dissipation is defined on the cyclic load-displacement plot as the area bounded by the

hysteresis loops, refer to Figure 4.28 and to [82÷88]. In general it is measured either in mechanical work units (Nm) or in joules (J), and it is noted by W or A. However, for the purpose of this analysis the energy dissipation and other related quantities were designated by acronyms; hence, the amount of Energy Dissipated during a complete load-displacement Cycle was denoted by ED C# (1 or 2), while the amounts corresponding to the negative and positive loading direction (half-cycle) were noted by ED C#- and ED C#+, respectively. It follows that the total amount of energy dissipated by a specimen during a test is the sum of the areas of the hysteresis loops. Considering the subsequent hysteresis loops arranged in the order of the load-displacement history (refer to the test logs in Appendix E), the partial sum of the areas from the beginning up to a certain displacement level is referred to as Cumulative Energy Dissipated (CED), as in [86, 89÷91]. As regards the calculation of the cumulative energy one can choose between two methods, namely by discrete summing of the cycle-by-cycle loop areas or by continuous integration of the load-displacement curve. In this thesis the latter method was employed. Accordingly, the cumulative energy dissipation was obtained by the continuous integration of the load-drift hysteretic response using the iterative (incremental) equation:

$$CED_j = CED_{j-1} + \left(\delta_j - \delta_{j-1}\right)(V_j/2 + V_{j-1}/2) \tag{4.1}$$

where

CED is the Cumulative Energy Dissipated;

j is a point on the load-displacement curve; in other words, j stands for a data line in the response data file;

δ_j, V_j are the corresponding drift and lateral load values, respectively.

Note that the displacements and the loads are taken with their signs. The reader is reminded that the average number of the recorded data lines during a test was about 20000; even after the so called "facelift" (refer to section 3.2.1) still remained in average about 11000 lines per test. In order to reduce the volume of calculations the load-displacement response data was filtered for specific drift values, namely for multiples of 1 mm and of 2.15 mm (0.1% drift ratio), that is, for 0, ±1, ±2, ±2.15, ±3, ±4, ±4.3, ±5, ±6, ±6.45, etc. mm; if not found in the recorded data, the corresponding load values were obtained by linear interpolation between the closest recorded neighbours. The resulting load-drift relationship, referred to as significant hysteretic response, comprised about 2000 lines per test; therefore, it was deemed reasonable to perform the integration on this response. As shown in Figure 4.28, two types of cumulative dissipation curves can be defined by plotting the cumulative energy either against the cyclic drift or against the Cumulative Drift (CD), similarly as in [86, 90, 92]. Likewise the cumulative energy, the cumulative drift is computed incrementally:

$$CD_j = CD_{j-1} + \left|(\delta_j - \delta_{j-1})\right| \tag{4.2}$$

where

CD is the Cumulative Drift;

Note 1: j and δ_j as defined in (4.1).

As illustrated in Figure 4.28, the cumulative drift during a complete load-displacement cycle equals approximately four times the drift amplitude:

$$CD_{Ci} \cong 4\delta_i \tag{4.3}$$

Where

Ci denotes a cycle at the i-th displacement level;

δ_i is the drift amplitude.

The cumulative drift ratio is defined by:

$$CR_j\% = (CD_j/2150) \cdot 100 \quad (4.4)$$

where

CR is the Cumulative Drift ratio;

CD is the cumulative Drift (in mm);

j is a point on the significant hysteretic response.

Note: 2150 mm stands for the distance between the top and bottom horizontal deflection measurement points the drift is calculated from, refer to Figure 3.19.

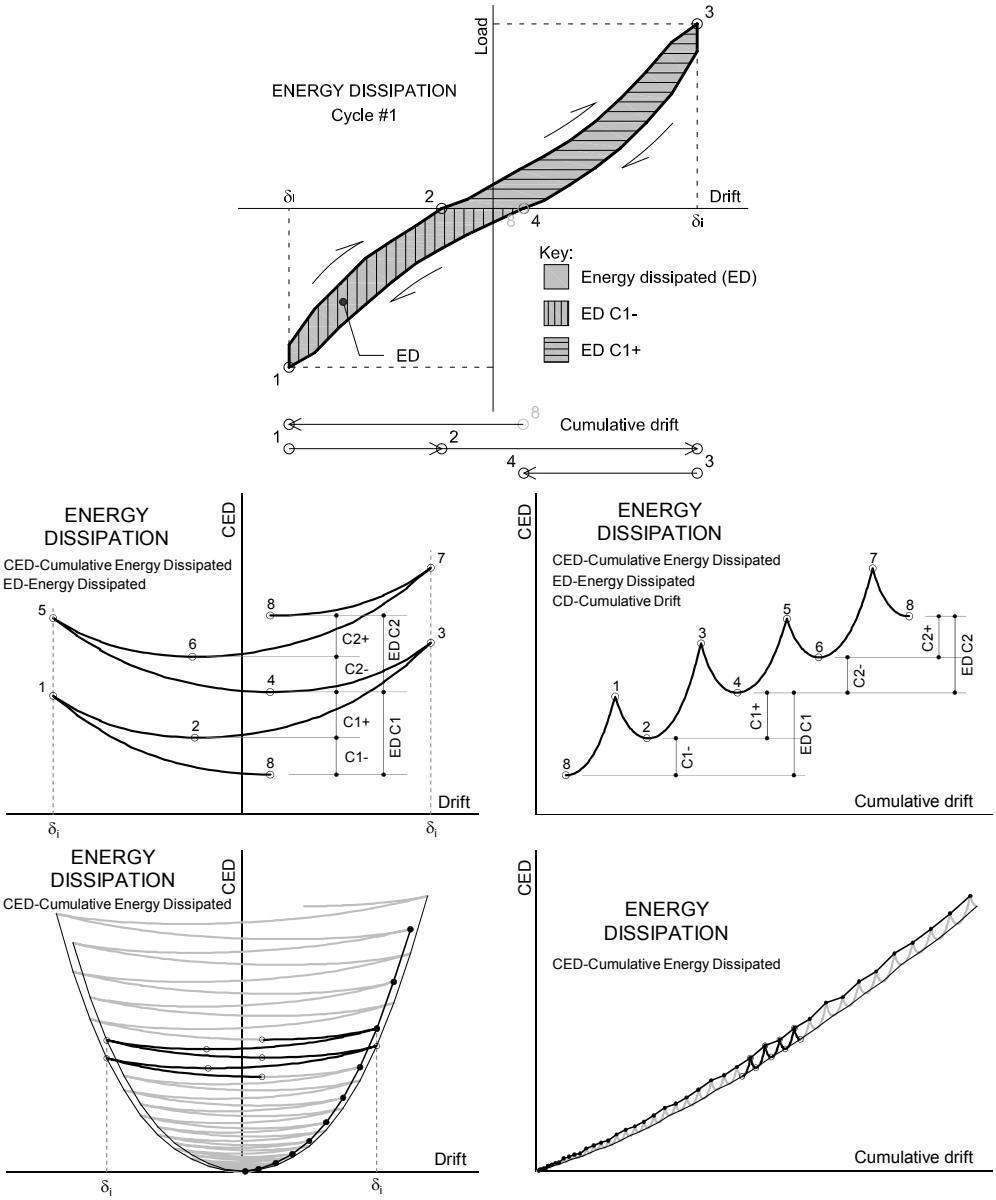

Figure 4.28 Definition and construction of the energy dissipation curves

Looking at the graphs in Figure 4.28, one can observe that the peak loading points (1, 3, 5, 7) and the reloading points (2, 4, 6, 8) are the local maximum and minimum points, respectively on the cumulative dissipation curves; moreover, it can be remarked that the difference in the level of cumulative energy between two subsequent local minimum points (reloading) is equal to the energy dissipated during the corresponding half-cycle; similarly, the energy dissipated during a complete load-displacement cycle can be computed as the difference in the level of cumulative energy at the end and start reloading points of the cycle (4-8 and 8-4). In this way the discrete calculation method is practically included in the continuous integration. Finally, the envelopes of the cumulative dissipation curves are presented in Figure 4.28. Note that on the CED vs. cyclic drift plot the envelopes are constructed by connecting one by one the local maximum points, that is the #1, #3, #5 and #7 series separately, whereas on the CED vs. cumulative drift graph the envelopes are drawn by connecting the local maximum points in one continuous series (#1-3-5-7) and the local minimums in another (#2-4-6-8).

4.6.2 Cumulative energy dissipation

In Figures 4.29 and 4.30 are presented the cumulative dissipation curves plotted to commensurate energy and drift limits along the three comparison lines. The first comparison line indicates the effect of the cut-out doors on the energy dissipation response of the solid reference while the second and third comparison lines exhibit the effect of FRP strengthening on the dissipation performance of the bare specimens with narrow and wide cut-out, respectively. Looking at the first comparison line on the CED vs. drift plots in Figure 4.29 one can construe that the energy dissipation of the solid reference is only slightly affected by the cut-outs; nevertheless this remark is not correct because the test on the solid specimen was incomplete (refer to the test log in Appendix E.1) and thus higher ultimate dissipation may be expected.

The second and third comparison lines indicate significant energy dissipation improvement of the FRP-strengthened specimens with respect to the bare references. As regards the CED vs. cumulative drift curves in Figure 4.30, the graphs in Line 1 show that the slope of the response diminish as the size of the cut-out increase, while the diagrams in Lines 2 and 3 exhibit significant extension for the responses of the strengthened specimens with respect to the bare ones.

The energy dissipation envelopes, specifically the point #7 CED vs. drift and the maximum point CED vs. cumulative drift envelopes, are depicted in Figure 4.31. There is an impressive augmentation of the energy dissipated by the FRP strengthened specimens with respect to the bare ones. As indicated on the dissipation histogram in Figure 4.32, the cumulative energy dissipated by the bare and strengthened specimens ranged within (24÷34) kNm and (56÷110) kNm, respectively. One should bear in mind, however, that the test on the solid specimen was incomplete, so its dissipation at ultimate might be significantly higher. Looking at the CED vs. cumulative drift envelopes it is visible that these are quasi-linear. In relation to this remark one can define a derived response characteristic, namely the ratio of the cumulative energy to the cumulative drift (CED/CD), referred to as dissipation rate. The units of measurement of this quantity and the corresponding physical senses are the following: kNm/m, the energy dissipated during a unit cumulative drift; kNm/%, the energy dissipated during a unit cumulative drift ratio; and kN, the force which would produce the same energy dissipation during a generic deformation equal to the cumulative drift assuming perfect-plastic response.

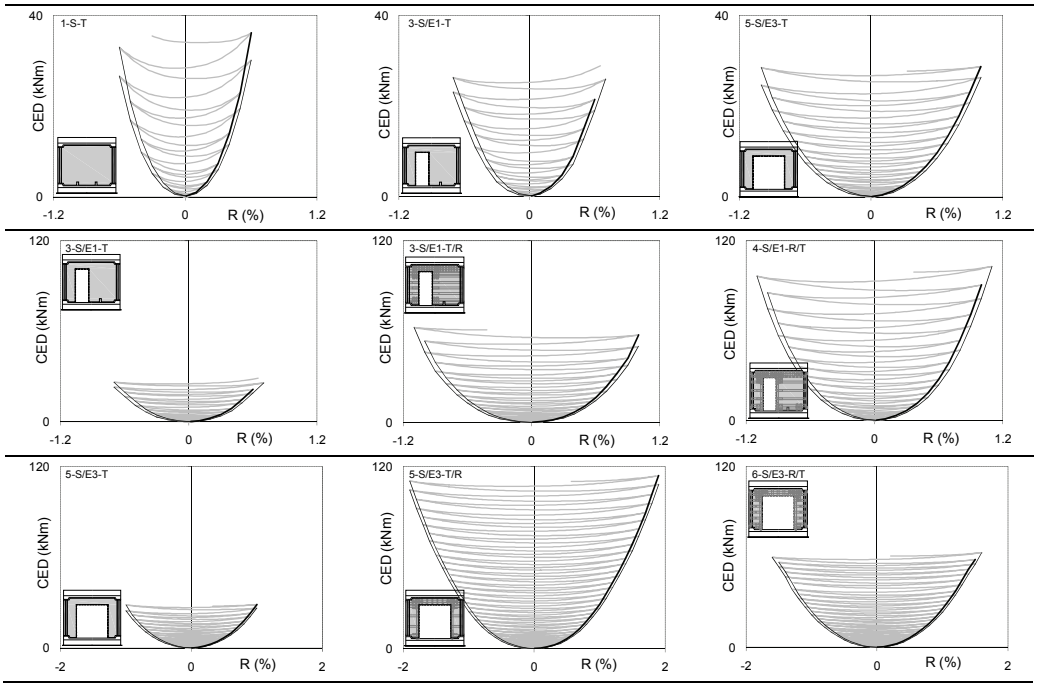

Figure 4.29 Cumulative energy vs. drift ratio comparison lines

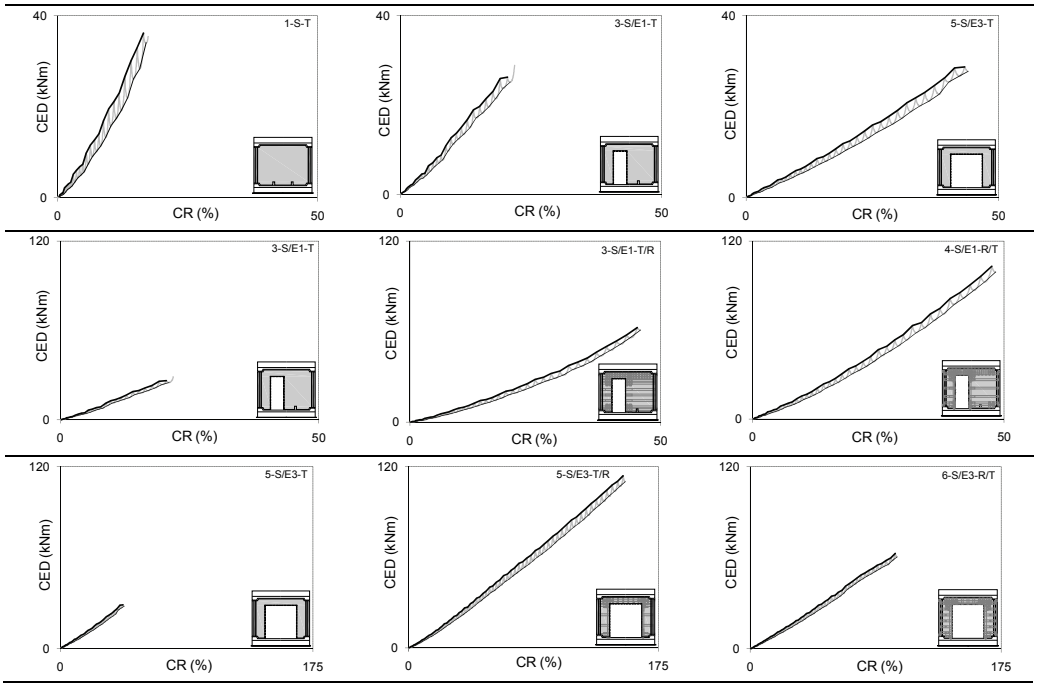

Figure 4.30 Cumulative energy vs. cumulative drift ratio comparison lines

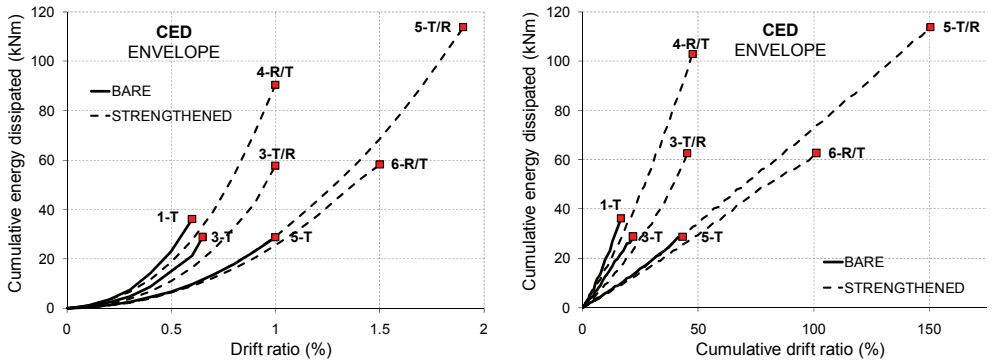

Figure 4.31 Energy dissipation envelopes

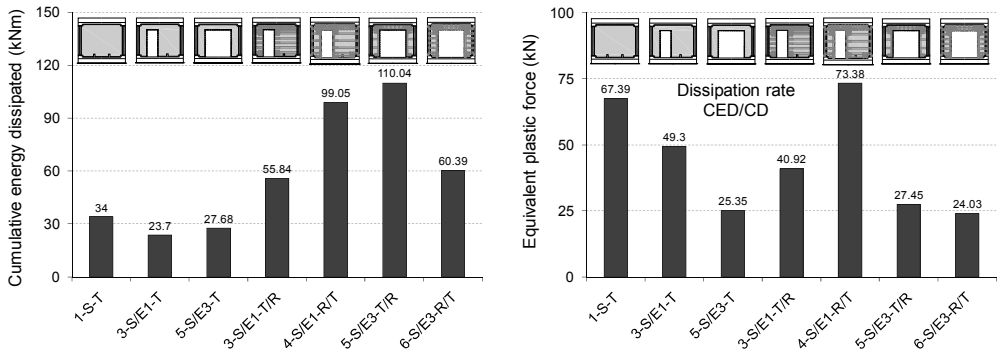

Figure 4.32 The energy dissipation of the wall specimens

In the context of the latter interpretation, the dissipation rate can be referred to as equivalent plastic force too. Returning to the previous observation regarding the CED vs. cumulative drift envelopes, the quasi-linearity translates into quasi-constant dissipation rate. As can be seen from the histogram in Figure 4.32, the dissipation rate (in other words the equivalent plastic force) varied in the (24÷73) kN range.

The effect of the experimental variables on the cumulative energy dissipation at ultimate and on the dissipation rate is presented on the performance ratio histograms in Figure 4.33. Apparently the effect of the cut-out condition on the energy dissipation is controversial; however, this should be viewed in the light of the differences in concrete strength and the incomplete test on the solid reference wall. Meanwhile, the dissipation rate clearly diminishes by the increase of the cut-out size. The effect of the FRP strengthening condition on the energy dissipation capacity is unequivocal: the retrofitted specimens dissipated from 2 to 4 times more energy at ultimate than their bare counterparts; meanwhile, the dissipation rate was only slightly affected by the FRP strengthening.

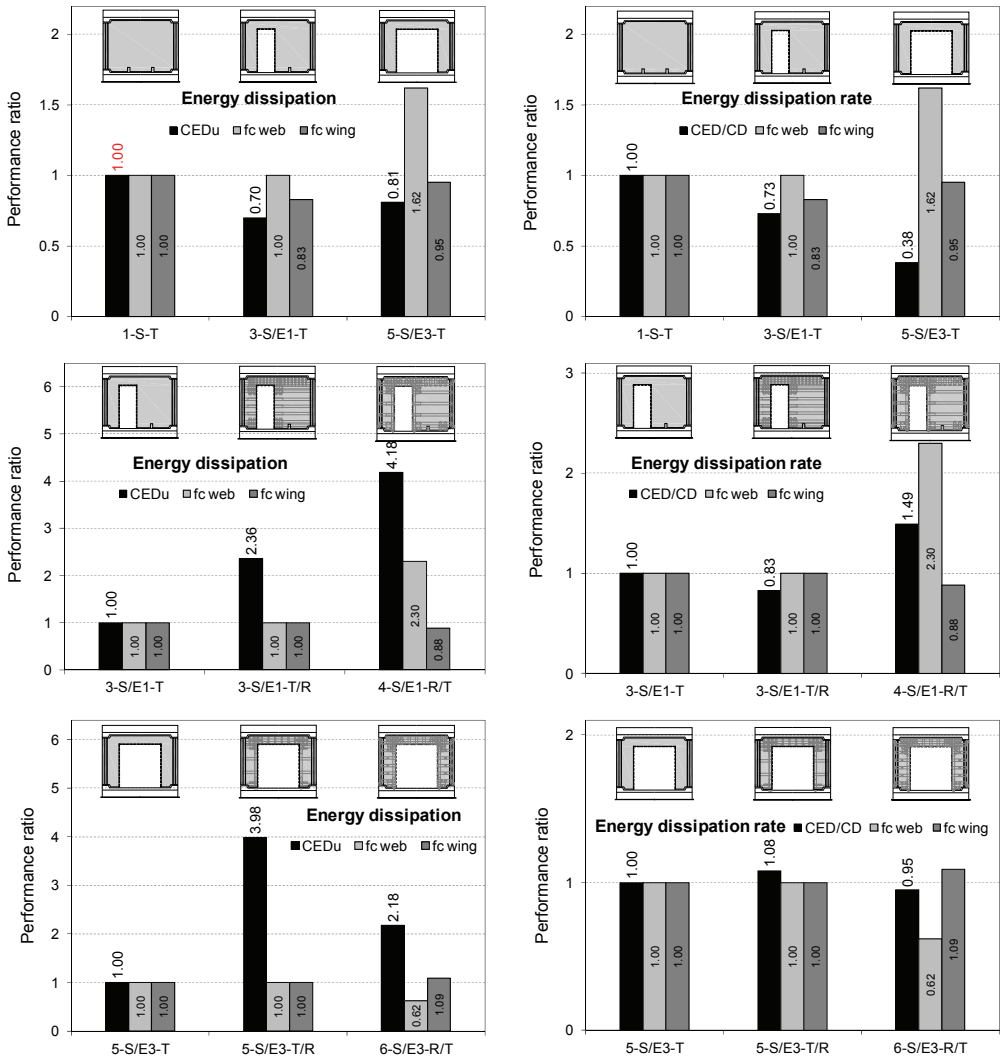

Figure 4.33 The effect of the experimental variables on the energy dissipation

4.6.3 Cyclic energy dissipation

In relation with the two calculation methods of the energy dissipation it was mentioned earlier in this chapter (section 4.6.1) that the discrete calculation method is practically included in the continuous integration. The cyclic and half-cyclic energy dissipation histograms of the 4-S/E1-R/T specimen are shown in Figure 4.34. One can observe that the energy dissipation in the second cycle is less than in the first cycle; moreover, it is noticeable a certain degree of directivity, that is, the wall dissipated slightly more energy in the positive half-cycles than in the negative ones. The complete set of the cyclic energy dissipation histograms for each specimen is provided in Appendix F.

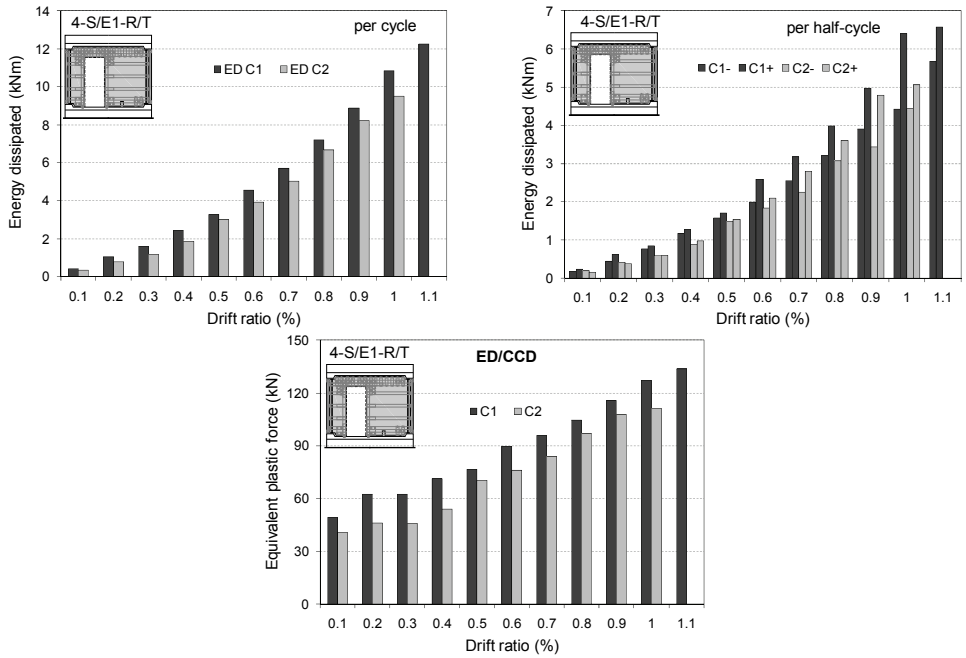

Figure 4.34 Cyclic energy dissipation

Similarly to the cumulative dissipation rate discussed in the previous section, one can define the cyclic dissipation rate as the ratio of the energy dissipated during a cycle (ED) to the Cyclic Cumulative Drift (CCD); similar, though not identical definition was reported by Kakaletsis and Karayannis in [65]. It is noteworthy that the cyclic dissipation rate geometrically translates to the local slope of the CED vs. cumulative drift minimum point envelope (see Figure 4.28). The 4-S/E1-R/T specimen's cyclic dissipation rate histogram is indicated in Figure 4.34, while the complete series for all specimens is provided in Appendix F.

4.6.4 Energy dissipation ratio

At the presentation of the experimental results (refer to section 3.2), it was stated several times that the most striking characteristic of the load-displacement responses in this experimental program is the extremely pinched shape of the hysteresis loops exhibiting quasi-parallel loading and unloading branches. In order to assess the degree of pinching one should compare the energy dissipated during a cycle (ED) to the maximum energy which could be theoretically dissipated (ED_{max}) within the same load and displacement limits, that is, assuming perfectly plastic response; these quantities are represented in Figure 4.35 by the area of the hysteresis loop (ED) and the area of the peak-to-peak rectangle (ED_{max}), respectively. The ratio between the actually dissipated energy and the maximum energy which could be hypothetically dissipated during a cycle (ED/ED_{max}) was referred to as dissipation ratio; similar definitions were reported by Hidalgo et al. in [82, 84] and by Olsen and Billington in [93]. The cyclic dissipation ratio histogram for the 4-S/E1-R/T specimen is shown in Figure 4.35, while the complete series are presented in Appendix F. As it was expected, the dissipation ratio yielded quite small values, namely it varied within 10÷15 % range.

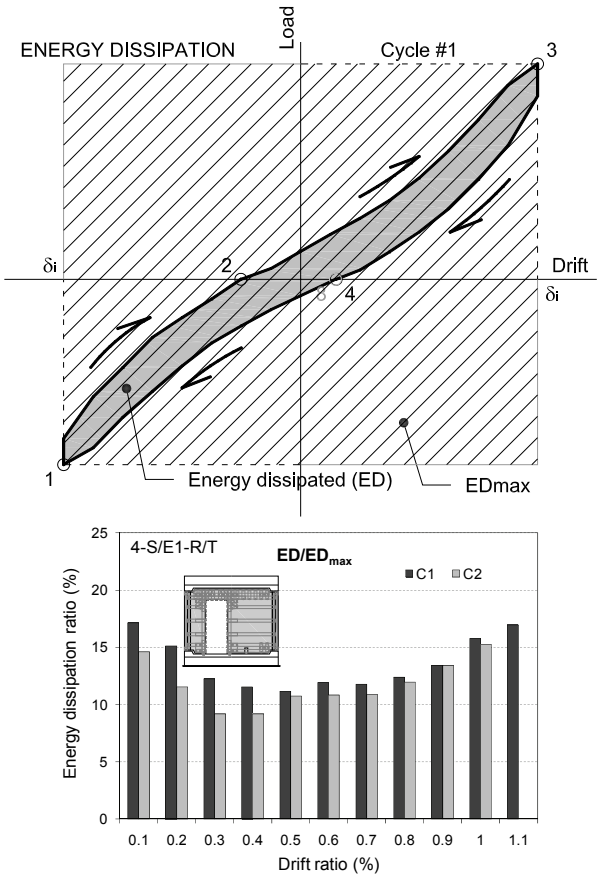

Figure 4.35 Definition of the dissipation ratio

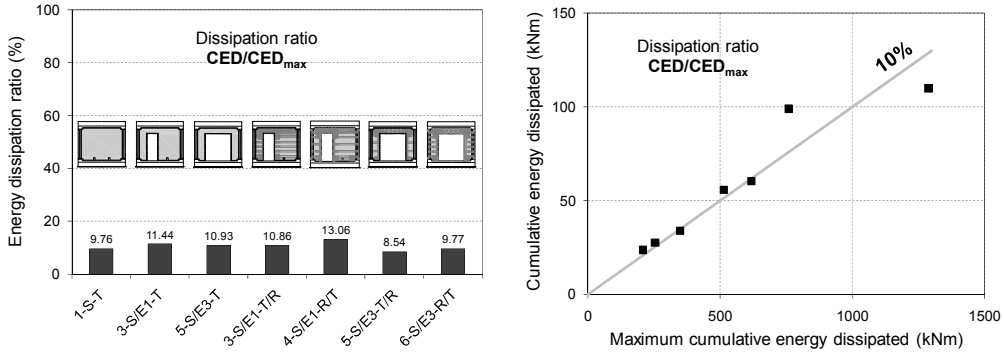

Figure 4.36 Cumulative energy dissipation ratio

The cumulative energy dissipation ratio was defined as the ratio of the cumulative energy dissipated (CED) to the cumulative sum of the maximum theoretical energies which might be dissipated (CED_{max}) assuming perfect plastic response. As can be seen from the CED/CED_{max} histogram in Figure 4.36, the cumulative dissipation ratio of the experimental specimens varied in the 8.5÷13 % range; it is noteworthy that neither the cut-out nor the strengthening condition affected significantly the dissipation ratio. Consequently, the value of 10% dissipation ratio can be considered as a general response characteristic of the RC wall panels in this experimental program. This observation is represented on the CED vs. CED_{max} plot in Figure 4.36.

4.7 Cracking, FRP distress and failure mode analysis

4.7.1 Cracking analysis

Besides the measured response, an important behavioural aspect peculiar to RC members is the cracking pattern. Due to the low tensile strength of concrete the cracking of a conventionally reinforced concrete element subjected to increasing load/deflections commence very early and, as a general rule, develop perpendicular to the local tension forces (except the cracks along the sliding deformations). Consequently, the observation of the cracking development and propagation is very useful to infer the load transfer mechanism and the behaviour mode from.

In general, the behaviour mode of a reinforced concrete wall subjected to in-plane lateral loading can be referred to as either flexural or shear; the flexural mode is characterised by horizontal cracks extending from the lateral edge in tension toward the opposite compressed side whereas the shear mode is marked by inclined cracks running across the web and/or straight sliding cracks at the linear joints. Nevertheless, it is quite frequent to observe cracks starting horizontally at the edge then sloping toward the compressed toe in the web; this situation can be regarded as flexural-shear behaviour.

A detailed account of the cracking development and propagation, or in other words of the cracking history, for each tested specimen is provided in the test logs in Appendix E. The condensed cracking histories of the experimental specimens, featuring the cracking patterns at the three load points of the backbone envelope, are presented in Figure 4.37. Looking at the cracking patterns, one can observe both flexural and shear cracks, but no flexural-shear cracks. The flexural cracks are located at the piers' base and at the pier-to-beam connection regions. In fact, the base cracks formed at the construction joint between the wall panel and the base beam, and not in the wall itself. Note that no or limited flexural cracking propagation occurred along the piers' vertical edges, whereas it was clearly noticeable on the coupling beams. This and a previous remark regarding the absence of flexural-shear cracks can be related to the axial loading conditions, the amount of vertical steel reinforcement anchored to the foundation and the premature failure of CFRP anchorages. The inclined shear cracks appeared primarily in the piers and to a lesser extent in the beam, whereas the horizontal and vertical sliding shear cracks developed at the base of the wide piers and along the narrow pier-to-wing connection zones, respectively. Note that the crack inclination angle was 50 deg in the solid wall (α_s=0.8), 50 to 60 deg in the wide pier (α_s=1.4) and 65 to 70 deg in the narrow piers (α_s=4.3), that is the larger the aspect ratio of the pier, the steeper were the cracks extending in it. This can be explained by diagonal compression dominated shear transfer, rather than by diagonal tension.

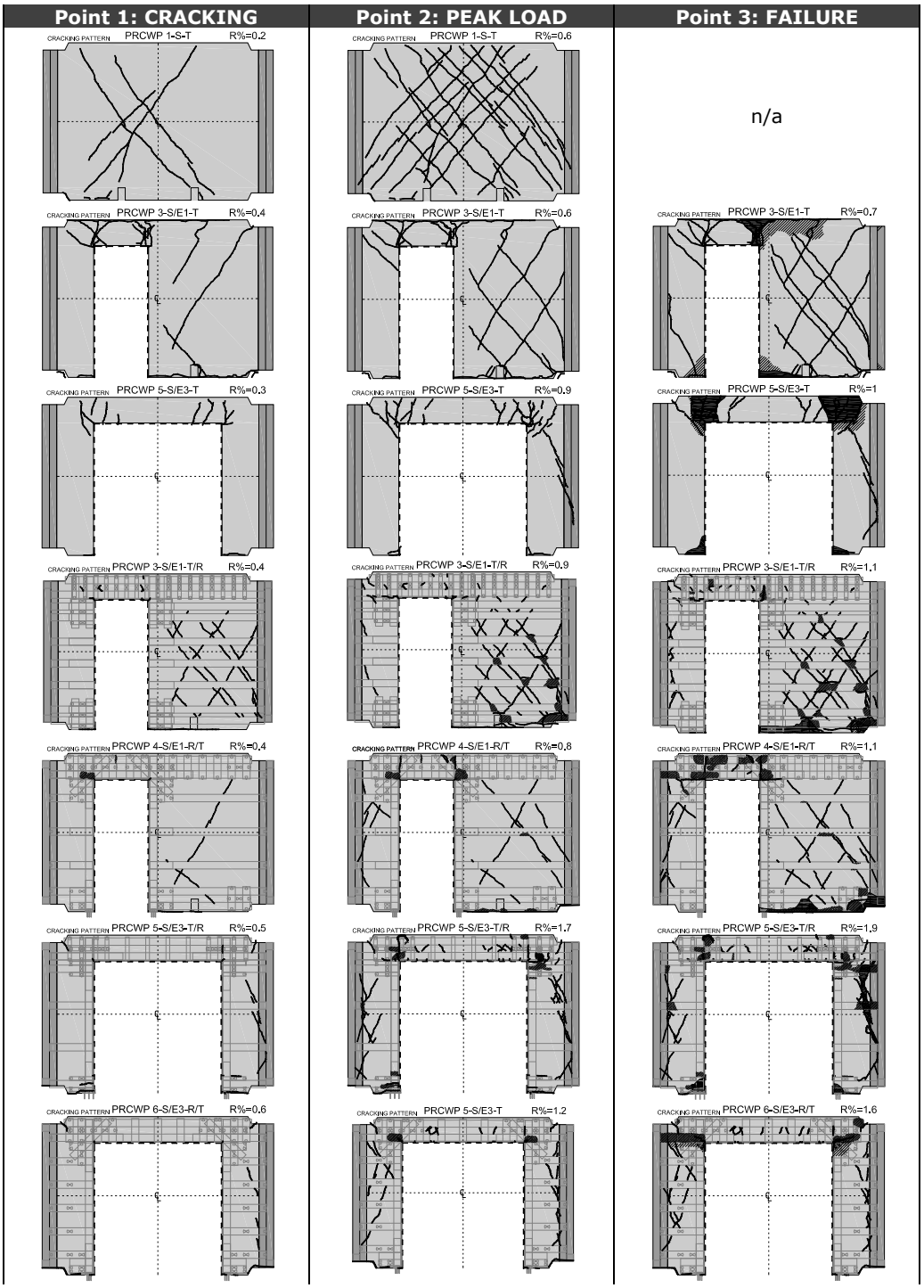

Figure 4.37 Condensed cracking history

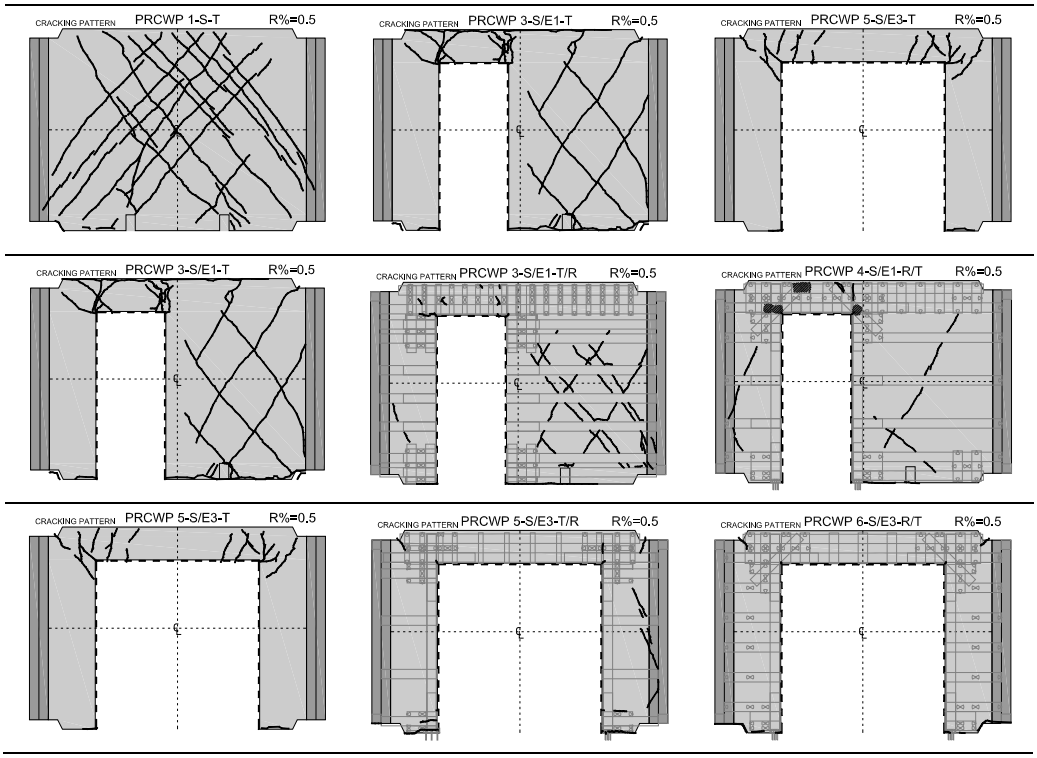

Figure 4.38 Comparison lines of the cracking pattern at 0.5% drift ratio

Horizontal sliding along the construction joints between the specimen and the base and cap beams was not investigated in this research and such, it was prevented by the slanted outline of the wall and beam ends. Vertical sliding at the pier-to-wing connection can be attributed to the drop in the steel reinforcement amount due to welded wire fabric cut-off and to peeling-off failure of the horizontal CFRP strips.

In order to assess the effect of the experimental variables on the cracking response, in Figure 4.38 the cracking patterns at 0.5% drift ratio were plotted along the three comparison lines. Looking at Line 1 it is quite obvious that the increase of the cut-out size results in the reduction of the number of inclined shear cracks across the piers whereas the flexural cracking intensifies at the opening corners. As regards the effect of the FRP retrofitting on the cracking response (refer to the second and third comparison lines) it is remarkable the difference between the post-damage and the prior-to-damage strengthening: in the former condition a large number of existing shear cracks opened whereas in the latter case the number of the shear cracks was much less. The flexural crack-tracking at the pier-to-spandrel connection was impeded by the FRP congestion.

4.7.2 FRP distress

In general, the externally bonded FRP reinforcements of a reinforced concrete element subjected to increasing load/deflections may exhibit two types of distress, namely bond failure and fibre fracture; there are several variants of bond failure depending on the FRP area affected and the interface involved; for example

the localised bond failure, that still allows for load transfer through it, is referred to as debonding whereas peeling-off refers to the complete loss of composite action between a large FRP area and the structural element [94].

The typical FRP distress and failure modes observed during this experimental program are presented in Figure 4.39. Note that the FRPs were regarded as flexural, shear or confinement strips, according to the adopted strengthening strategy (refer to section 3.1.3).

Figure 4.39 FRP-distress and failure modes

The flexural FRPs exhibited wide range of distress types: early fibre fracture at the pier-to-spandrel connection and at the pier-to-foundation anchorage (see Figure 4.39a); debonding and peeling-off at the pier-to-spandrel and pier-to-wing connection (see Figure 4.39c); and bulging of the vertical strips above the confined pier toes (see Figure 4.39d). The premature fracture of several flexural FRPs can be attributed to the alternate tension-compression forces acting parallel to the fibre direction (refer to the strain analysis section 4.4.2). However, it is not clear whether this type of failure is triggered by concrete substrate deterioration, i.e. local spalling and crushing, or directly by the adverse loading conditions; the author believes that both factors are involved.

The shear FRP strips debonded in the vicinity of the inclined cracks running across the wide piers (see Figure 4.39b) and peeled-off at the pier-to-wing connection when sliding shear occurred along this joint (see Figure 4.39e). It is noteworthy that the shear debonding was more extensive in the case of the post-damage strengthened specimen (3-S/E1-T/R) than for its prior-to-damage strengthened counterpart (4-S/E1-R/T); furthermore, the debonding was more intensive where the FRP overlaid an intersection of two inclined cracks. This type of shear debonding can be attributed to the concrete substrate deterioration during the cyclic friction between the wall portions separated by the inclined cracks.

The confinement FRP strips showed a stable performance and failed by fibre fracture (see Figure 4.39f and 4.39g). It is noteworthy that owing to the lack of the internal transverse reinforcement, the final failure of the strengthened wall panels was mostly triggered by the fracture of the FRP confinements.

4.7.3 Failure mode

In accordance with the behaviour modes presented previously, the failure mode of a laterally loaded RC wall can be of flexural or shear type; the flexural failure may occur at the tension and/or at the compressed toe by yielding and rupture of the vertical reinforcement (or by anchorage slip) and/or by concrete crushing, respectively; the shear mode may involve diagonal tension, diagonal compression and/or sliding failure.

In the present experimental program the RC walls failed predominantly by concrete crushing, refer to Figure 4.40. The tests on the bare specimens with cut-out openings (refer to Line 1 in Figure) showed that the critical regions are the pier-to-spandrel connections and the pier toes, that is, the extremities of the diagonal compression struts. At these locations the reduced concrete section with no transverse reinforcement couldn't withstand the increasing diagonal compression forces which resulted in spalling and crushing of concrete. It is noteworthy that one can construe this type of failure as flexural compression; however, one should bear in mind that the cracking pattern substantiates typical shear behaviour by diagonal compression (refer to the above discussion on the cracking pattern); therefore, the flexural failure interpretation is not acceptable.

Looking at Lines 2 and 3 in Figure 4.40, one can remark that the failure mode of the FRP-strengthened specimens was mainly similar to their bare counterparts'; it is noteworthy however, that the FRP confinement and the high-strength mortar repair significantly improved the load transfer response at the critical regions. In three cases (3-T/R, 4-R/T and 6-R/T) the failure of the walls was triggered by the fracture of the FRP confinements, whereas the 5-S/E3-T/R specimen failed by sliding shear along the pier-to-wing joint; this latter failure mode can be attributed to the reduction of the internal reinforcement due to the welded

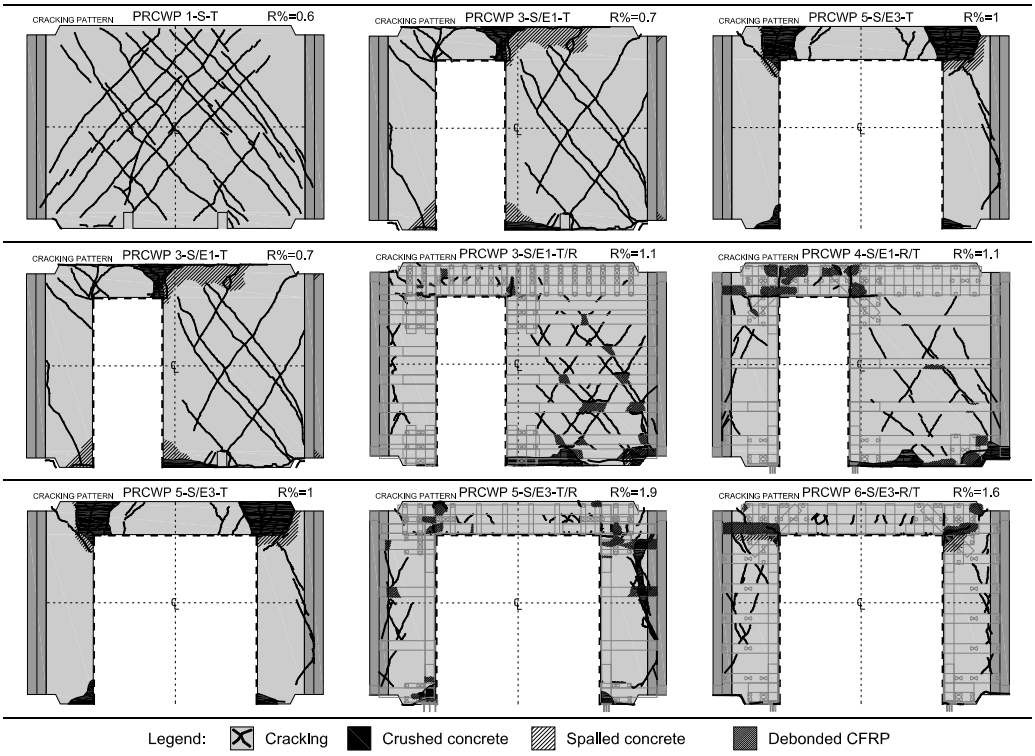

Figure 4.40 Comparison lines for the failure mode

wire mesh cut-off (refer to Figure 3.6) and to the peeling-off of the horizontal shear strips.

In relation with the test on the 5-S/E3-T/R specimen it is also important to note that the post-test investigation revealed crushed concrete inside the FRP-confined cores at the pier toes, even though the confinement itself was apparently undamaged.

5 ANALITYCAL MODELLING

5.1 Load transfer mechanism

Generally speaking, the shears between two parallel sections are transferred along a diagonal load path connecting the sections. Practically, there are two diagonal load paths, namely diagonal tension and diagonal compression, see Figure 5.1. The vertical (i.e. flexural) compressive and tensile forces along the wall edges can be looked at as ensued from the diagonal ones according to equilibrium conditions projected on the vertical axis, whereas the horizontal components defines the resistance against the lateral load. The proportion of the shears transferred by each path is a complex issue involving stiffness, loading and boundary conditions. An intuitive stiffness hierarchy of the above load transfer paths would place the flexural tension path at the beginning of the stiffness scale, followed by the diagonal tension, diagonal compression and flexural compression. Therefore, a laterally loaded reinforced concrete wall cantilever with no or low constant axial loads will transfer the shears primarily by diagonal compression and its resistance and stiffness will be limited generally by flexural tension (yielding of the vertical reinforcement at the boundary). However, other than cantilever boundary conditions (e.g. restrained rotation or additional moment, refer to section 2.3.5) may significantly alter the load transfer mechanism.

As shown in section 3.1.7, the present experimental program features restrained rotation boundary condition by additional eccentric axial loading (outrigger effect). In these circumstances the shear transfer mechanism is dominated by diagonal compression and the shear resistance is determined by the strength of the concrete compression strut. The above statement can be corroborated with experimental evidences and analytical modelling; to this end, the load and cracking response of the PRCWP 1-S-T specimen at R=0.4%, see Figure 5.1, and at ultimate is analysed in the subsequent paragraphs.

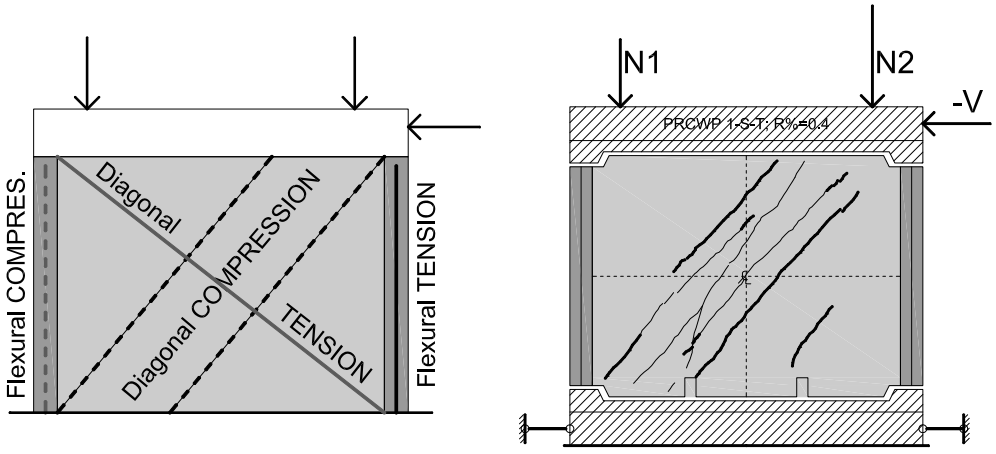

Figure 5.1 Shear transfer paths and experimental evidence

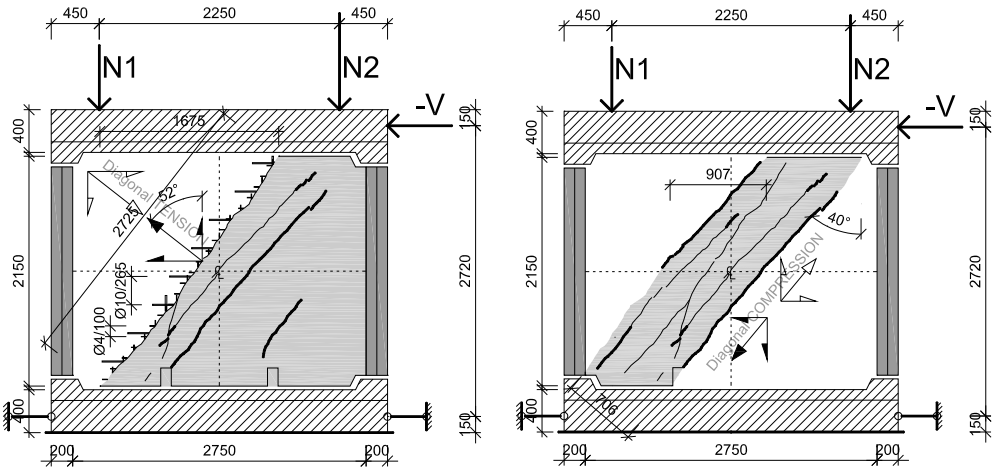

(a) (b)

Figure 5.2 Load transfer mechanism: (a) diagonal tension; (b) diagonal compression

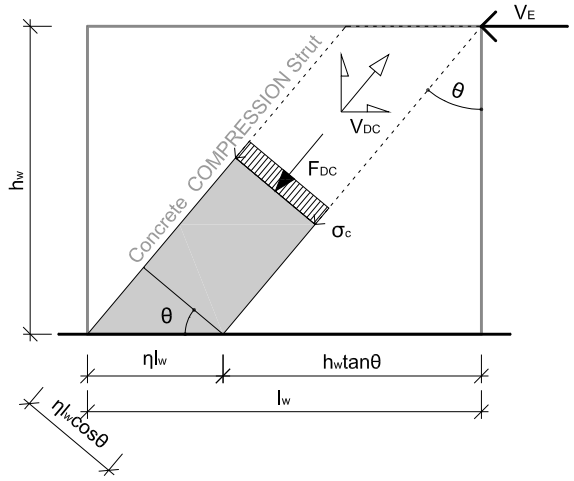

Figure 5.3 Geometric definition of the concrete strut

As shown in Figure 5.2, the shear resistance is provided by diagonal tension and/or diagonal compression load transfer. Assuming diagonal tension load transfer, see Figure 5.2a, the shears are conveyed by the horizontal and vertical reinforcements crossing the inclined crack; because the axial loads are acting contrary to the vertical component of the diagonal tension force, the shears are practically carried by the horizontal reinforcements, according to the following equation:

$$V_{DT} = n\, A_s \sigma_s \tag{5.1}$$

where

V_{DT} shear carried by the diagonal tension load transfer mechanism;
A_s area of the horizontal reinforcement;
n number of the horizontal re-bars;

σ_s tensile stress in the reinforcement: $\sigma_s = E_s\varepsilon_s$.

On the other hand, assuming diagonal compression load transfer, see Figure 5.2b, the shear force is conveyed by the concrete compression strut parallel to the inclined cracks. The shear carried by the concrete strut can be expressed by the relation:

$$V_{DC} = F_{DC}\sin\theta \tag{5.2}$$

where
V_{DC} is the shear carried by the concrete strut;
F_{DC} is the diagonal compression force in the concrete strut;
θ is the inclination angle of the concrete strut to the vertical direction.

The geometric definition of the concrete strut and the internal forces acting on it are shown in Figure 5.3. According to this approximation, the diagonal compression force can be written as:

$$F_{DC} = \eta l_w \cos(\theta)\, b_w \sigma_c \tag{5.3}$$

where
ηl_w is the length of the compression strut; with: $\eta = 1 - \alpha_s \tan\theta$; and $\alpha_s = \frac{h_w}{l_w}$;
h_w, l_w, b_w are the wall height, lenght and thickness, respectively;
σ_c is the compressive stress in the concrete strut;
θ is the inclination angle of the concrete strut to the vertical direction.

In the followings the calculations are provided for both the diagonal tension and diagonal compression load transfer mechanisms at R=-0.4% and at ultimate.

Diagonal TENSION (V_{DT}), at R=0.4%

Horizontal reinforcement (refer to Figure 5.2 and section 3.1.2):	
Ø10/265 grade PC52	$A_{s,\emptyset 10} = 78.5\ mm^2; n = 8$
Ø4/100 grade STPB	$A_{s,\emptyset 4} = 12.6\ mm^2; n = 21$
Tensile stress: Note: ε_s can be taken according to the strain measurements on the Ø10/265 grade PC bars (refer to Figure 4.5); the same ε_s can be assumed in the Ø4/100 grade STPB wire mesh.	$\varepsilon_{s,\emptyset 10} = \varepsilon_{s,\phi 4} = 0.0016$
$\sigma_s = E_s\varepsilon_s$	$\sigma_s = 210000 \cdot 0.0016 = 336\ MPa$
Shear carried by the diagonal tension load transfer mechanism Note: assume uniform strain distribution.	
$V_{DT} = n\, A_s \sigma_s$	$V_{DT} = (8 \cdot 78.5 + 21 \cdot 12.6) \cdot 336 = = 299914\ N = 300\ kN$

Diagonal TENSION (V_{DT}), at ultimate

Tensile stress: Note: σ_s is taken based on the measured steel strength (refer to Table 3.9)	$\sigma_{s,\emptyset 10} = f_y = 450\ MPa$ $\sigma_{s,\emptyset 4} = f_y = 618\ MPa$

Shear carried by the diagonal tension load transfer mechanism
Note: assume uniform strain distribution.

$$V_{DT} = n\,A_s\sigma_s$$

$$V_{DT} = 8 \cdot 78.5 \cdot 450 + 21 \cdot 12.6 \cdot 618 = 446123\ N = 446\ kN$$

Diagonal COMPRESSION (V_{DC}), at R=0.4%

Concrete section:

$$h_w = 2150\ mm; l_w = 2750\ mm; b_w = 100\ mm$$

Aspect ratio:

$$\alpha_s = \frac{h_w}{l_w}$$

$$\alpha_s = \frac{2150}{2750} = 0.782$$

Concrete strut angle: θ
Note: based on the crack inclination, see Figure 5.2

$$\theta = 40\ deg$$

Normalised length of the compression strut:

$$\eta = 1 - \alpha_s \tan\theta$$

$$\eta = 1 - 0.782 \cdot \tan 40 = 0.344$$

Compressive stress in the concrete strut:
Note: because the concrete is cracked in compression, one can assume that the compressive stress to be close to the concrete strength (refer to Tables 3.7 and 3.8)

$$\sigma_c = f_{cm} = 14\ MPa$$

Diagonal compression force in the concrete strut:

$$F_{DC} = \eta l_w \cos(\theta)\, b_w \sigma_c$$

$$F_{DC} = 0.344 \cdot 2750 \cdot \cos 40 \cdot 100 \cdot 14 = = 1014549\ N = 1014.5\ kN$$

Shear carried by the concrete strut:

$$V_{DC} = F_{DC} \sin\theta$$

$$V_{DC} = 1014.5 \cdot \sin 40 = 652.1\ kN$$

Diagonal COMPRESSION (V_{DC}), at ultimate

Width of the compression strut (see Figure 5.3):
Note: based on the measured distance between the extreme cracks (refer to section 3.2.2 and Figure E.10)

$$\eta l_w \cos\theta$$

$$\eta l_w \cos\theta = 1100\ mm$$

Compressive stress in the concrete strut:
Note: assuming that the compressive stress is close to the concrete strength (refer to Table 3.7)

$$\sigma_c = f_{cm} = 14\ MPa$$

Diagonal compression force in the concrete strut:

$$F_{DC} = \eta l_w \cos(\theta)\, b_w \sigma_c$$

$$F_{DC} = 1100 \cdot 100 \cdot 14 = 1540000\ N = 1540\ kN$$

Shear carried by the concrete strut:

$$V_{DC} = F_{DC} \sin\theta$$

$$V_{DC} = 1540 \cdot \sin 40 = 990\ kN$$

According to the measured response the average shear resistance at R=0.4% was $V_{0.4\%}$=940 kN and the average measured maximum load was $V_{0.6\%}$=1210 kN (refer to Figure 4.9). Note that the measured maximum load was

still on the ascending branch, i.e. it was not the peak load; therefore, the actual shear resistance can be expected to be slightly higher. It can be observed that the diagonal tension load transfer mechanism excessively underestimates the shear response: the P/M (Predicted/Measured) ratios results in $V_{P/M}$=300/940=0.32 at R=0.4% and $V_{P/M}$=446/1210=0.37 at ultimate. As regards the diagonal compression load transfer, the predictions are much closer to the experimental results: $V_{P/M}$=652/940=0.7 at R=0.4% and $V_{P/M}$=990/1210=0.82 at ultimate. Therefore, it can be concluded that the shear transfer mechanism was dominated by diagonal compression. Furthermore, it is important to remark that the diagonal tension mode calculation can be looked at as the maximum which can be attained (assuming uniform yielding of all horizontal reinforcement), whereas the diagonal compression mode (equations 5.2 and 5.3) allows for a series of strength reserves, namely the inclination angle of the strut (the less the θ angle the wider the concrete strut), the length of the wall (the greater the length the wider concrete strut), the wall thickness, and the compressive strength of the concrete (cylinder or cube strength). Taking into account some of these reserves, it is shown in the followings that the predicted shear resistance can approach the measured response.

Diagonal COMPRESSION (V_{DC}), at R=0.4% (modified)

Concrete section: Note: larger-than-nominal web thickness	$h_w = 2150\ mm; l_w = 2750\ mm;$ $b_w = 110\ mm$
Aspect ratio: $\alpha_s = \frac{h_w}{l_w}$	$\alpha_s = \frac{2150}{2750} = 0.782$
Concrete strut angle: θ Note: based on the crack inclination, see Figure 5.2	$\theta = 40\ deg$
Normalised length of the compression strut: $\eta = 1 - \alpha_s \tan\theta$	$\eta = 1 - 0.782 \cdot \tan 40 = 0.344$
Compressive stress in the concrete strut: Note: assuming that the compressive stress is close to the concrete cube strength (refer to Table 3.7)	$\sigma_c = f_{cm,cube} = 17.5\ MPa$
Diagonal compression force in the concrete strut: $F_{DC} = \eta l_w \cos(\theta)\, b_w \sigma_c$	$F_{DC} = 0.344 \cdot 2750 \cdot \cos 40 \cdot 110 \cdot 17.5 =$ $= 1395005\ N = 1395\ kN$
Shear carried by the concrete strut: $V_{DC} = F_{DC} \sin\theta$	$V_{DC} = 1395 \cdot \sin 40 = 897\ kN$

Diagonal COMPRESSION (V_{DC}), at ultimate (modified)

Concrete section: Note 1: wall length considering the boundary elements (refer to Figure 5.2b); Note 2: larger-than-nominal web thickness	$h_w = 2150\ mm; l_w = 3150\ mm;$ $b_w = 110\ mm$
Aspect ratio: $\alpha_s = \frac{h_w}{l_w}$	$\alpha_s = \frac{2150}{3150} = 0.683$

Concrete strut angle: θ Note: based on the crack inclination, see Figure 5.2	$\theta = 40\ deg$
Normalised length of the compression strut: $\eta = 1 - \alpha_s \tan\theta$	$\eta = 1 - 0.683 \cdot \tan 40 = 0.427$
Compressive stress in the concrete strut: Note: assuming that the compressive stress is close to the concrete cube strength (refer to Table 3.7)	$\sigma_c = f_{cm,cube} = 17.5\ MPa$
Diagonal compression force in the concrete strut: $F_{DC} = \eta l_w \cos(\theta)\, b_w \sigma_c$	$F_{DC} = 0.427 \cdot 3150 \cdot \cos 40 \cdot 110 \cdot 17.5 = = 1983459\ N = 1983.5\ kN$
Shear carried by the concrete strut: $V_{DC} = F_{DC} \sin\theta$	$V_{DC} = 1983.5 \cdot \sin 40 = 1275\ kN$

One can observe that in expressions 5.2 and 5.3 no reference is made to the contribution of the reinforcement to the diagonal compression load transfer mechanism. Nevertheless, it can be assumed that the horizontal reinforcements play an important role in the redistribution of the internal forces by tying the concrete portions separated after cross-inclined cracking.

5.2 Eurocode provisions

In Eurocode 2 [69] the shear resistance of a member is defined in terms of $V_{Rd,c}$, $V_{Rd,s}$ and $V_{Rd,max}$, with the corresponding expressions:

$$V_{Rd,c} = \left[C_{Rd,c} k (100 \rho_l f_{ck})^{1/3} + k_1 \sigma_{cp}\right] b_w d \geq \left(\upsilon_{min} + k_1 \sigma_{cp}\right) b_w d \qquad (5.4)$$

where

$V_{Rd,c}$ is the design shear resistance of the member without shear reinforcement;

Note: the other terms as in [69];

$$V_{Rd,s} = \frac{A_{sw}}{s} z f_{ywd} \cot\theta \qquad (5.5)$$

where

$V_{Rd,s}$ is the design value of the shear force which can be sustained by the yielding shear reinforcement;

Note: the other terms as in [69];

$$V_{Rd,max} = \alpha_{cw} b_w z \nu_1 f_{cd} / (\cot\theta + \tan\theta) \qquad (5.6)$$

where

$V_{Rd,max}$ is the design value of the maximum shear force, which can be sustained by the member, limited by crushing of the compression struts;

Note: the other terms as in [69].

In Eurocode 8, Part 1 [95], section 5, the walls with aspect ratio ($\alpha_s = h_w/l_w$) less than 1.5 are referred to as large lightly reinforced walls, which should be designed to DCM (medium ductility). The shear resistance of such members can be evaluated according to the Eurocode 2 provisions for $V_{Rd,c}$ and $V_{Rd,s}$. Although not stated explicitly, the Eurocode 8 assumes that for the large walls $V_{Rd,max} > V_{Rd,s}$ and

consequently the shear resistance is limited by the yielding of the shear reinforcement.

In the followings the shear resistance calculations are made according to the above equations replacing the design values with the measured material properties.

Shear resistance provided by horizontal reinforcement ($V_{R,s}$)

Concrete section: Note 1: wall length considering the boundary elements (refer to Figure 5.2a); Note 2: assume z=0.8l_w	$h_w = 2150\ mm;\ l_w = 3150\ mm$ $z = 2520\ mm$
Horizontal reinforcement (refer to Figure 5.2a and section 3.1.2):	
Ø10/265 grade PC52	$A_{sw,\phi10} = 78.5\ mm^2; s = 265\ mm$
Ø4/100 grade STPB	$A_{sw,\phi4} = 12.6\ mm^2; s = 100\ mm$
Tensile stress: Note: f_{yw} is taken based on the measured steel strength (refer to Table 3.9)	$f_{yw,\phi10} = 450\ MPa$ $f_{yw,\phi4} = 618\ MPa$
Concrete strut angle: θ Note: based on the crack inclination, see Figure 5.2	$\theta = 40\ deg$
Shear resistance: Note: replace z with h_w.	
$V_{R,s} = \frac{A_{sw}}{s} z f_{yw} \cot\theta$	$V_{R,s} = (78.5/265 \cdot 2150 \cdot 450 + 12.6/100 \cdot 2150 \cdot 618) \cdot \cot 40 = 540278\ N = 540\ kN$

Shear resistance provided by the concrete strut ($V_{R,max}$)

Concrete section: Note 1: wall length considering the boundary elements (refer to Figure 5.2b); Note 2: larger-than-nominal web thickness Note 3: assume z=0.8l_w	$h_w = 2150\ mm; l_w = 3150\ mm;$ $b_w = 110\ mm; z = 2520\ mm$
Concrete strut angle: θ Note: based on the crack inclination, see Figure 5.2	$\theta = 40\ deg$
Compressive strength of concrete: Note: replace design with measured value (refer to Table 3.8)	$f_{cm} = 14\ MPa$
$\nu_1 = \nu = 0.6\left[1 - \frac{f_{ck}}{250}\right]$	$\nu_1 = \nu = 0.6\left[1 - \frac{8.9}{250}\right] \cong 0.6$
Shear resistance:	
$V_{R,max} = \alpha_{cw} b_w z \nu_1 f_{cm} / (\cot\theta + \tan\theta)$	$V_{R,max} = 1 \cdot 110 \cdot 2520 \cdot 0.6 \cdot 14/2 = = 1164240\ N = 1165\ kN$

Again, it is remarkable that the P/M (Predicted/Measured) ratio at ultimate is excessively conservative when the evaluation is made accounting for the shear resistance provided by the horizontal reinforcement $V_{P/M}$=540/1210=0.45, whereas prediction based on the shear resistance of the concrete strut is much closer to the measured response $V_{P/M}$=1165/1210=0.96.

6 CONCLUSIONS

This chapter summarizes the main engineering conclusions which can be drawn based on the experimental tests and on the analysis of the results with regard to the cyclic response of the precast reinforced concrete wall panels weakened by doorway cut-outs and retrofitted by FRP-EBR. Recommendations are formulated for the engineering practice and an outlook is provided for future research directions. The chapter is concluded by an account of the author's publications and his personal contribution to this work.

6.1 Engineering practice

The experimental results regarding the weakening effect of the door cut-outs on the seismic response of the solid reference wall are presented in Figure 6.1; the cut-out ratio is a measure of the opening size relative to the solid reference wall calculated either as the horizontal cross section ratio or as the square root of the in-plane area ratio (peripheral ratio); the performance ratio indicates the response characteristic of the weakened specimen normalised to the corresponding characteristic of the sound (solid) reference; the situation of complementarity between the performance ratio and the cut-out ratio is represented by the dashed line joining the unities of the two axes. One can observe that there is experimental evidence on the complementarity relationship between specific performance and opening ratios: the strength and stiffness performance ratios are the complement of the peripheral ratio, whereas the energy dissipation rate performance ratio is the complement of the cross sectional ratio.

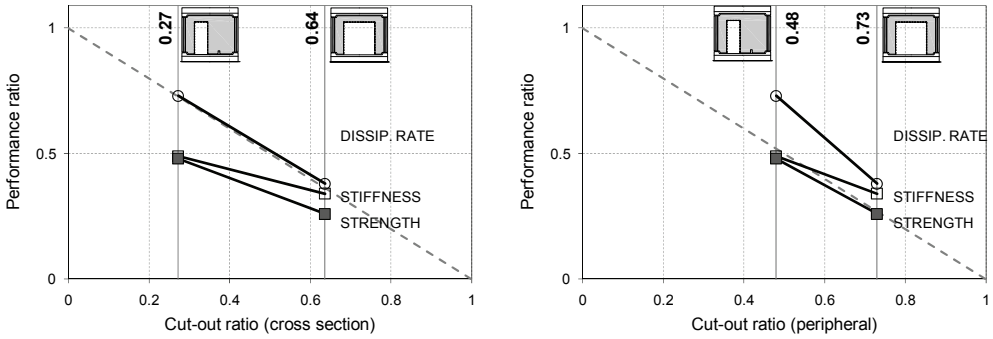

Figure 6.1 The weakening effect of the door cut-outs on the seismic response

Practicing engineers can use the experimental results to quickly approximate the response characteristics of the precast RC walls weakened by doorway cut-outs according to the following equations:

$$(R)_{weak} = (R)_{sound} \cdot \alpha_p \tag{6.1}$$

where

$(R)_{weak}$ is the response characteristic of the weakened member in terms of shear resistance, initial stiffness or energy dissipation rate;

$(R)_{sound}$ is the response characteristic of the sound (solid, as-built) member in terms of shear resistance, initial stiffness or energy dissipation rate;

α_p is the performance ratio, with:

$$\alpha_p = 1 - \eta \tag{6.2}$$

where

η is the opening ratio, given by:

$$\eta = \begin{cases} P = \sqrt{A_o / A_w} & \text{for (R): shear resistance and stiffness} \\ l_o / l_w & \text{for (R): energy dissipation rate} \end{cases} \tag{6.3}$$

where

P is the peripheral ratio;

A_o, A_w is the in-plane area of the opening and the wall, respectively;

l_o, l_w is the length of the opening and of the wall, respectively.

Note that expressions (6.1) and (6.2) were derived from the AIJ recommendation [96] as reported in [66]; however, the AIJ equation is reportedly [66, 97] applicable only for peripheral ratios less than 0.4 and it refers only to the shear strength and stiffness. In the present thesis the above equation was experimentally verified for two peripheral ratios (0.48 and 0.73); in-between these values one can assume linear performance ratio-to-peripheral ratio relationship. Moreover, it is important to bear in mind that the relationship given in equation (6.1) was validated for the specific loading and boundary conditions applied in the present experimental program (outrigger effect by additional axial loads); further investigations are required to widen the loading and boundary conditions range.

The effect of the FRP-EBR strengthening on the seismic response of the cut-out weakened specimens is presented in Figure 6.2; the performance ratio indicates the response characteristic of the FRP-strengthened specimen normalised to the corresponding characteristic of the cut-out weakened bare reference. It can be remarked that the response characteristics were differently influenced by the CFRP-

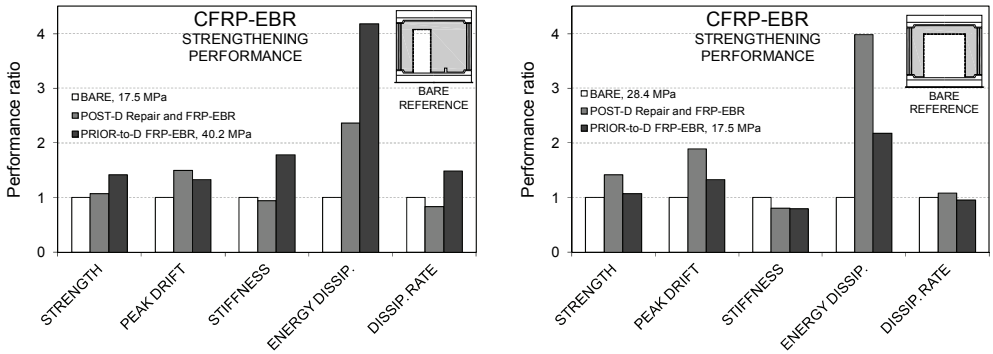

Figure 6.2 The effect of the FRP-EBR strengthening on the seismic response

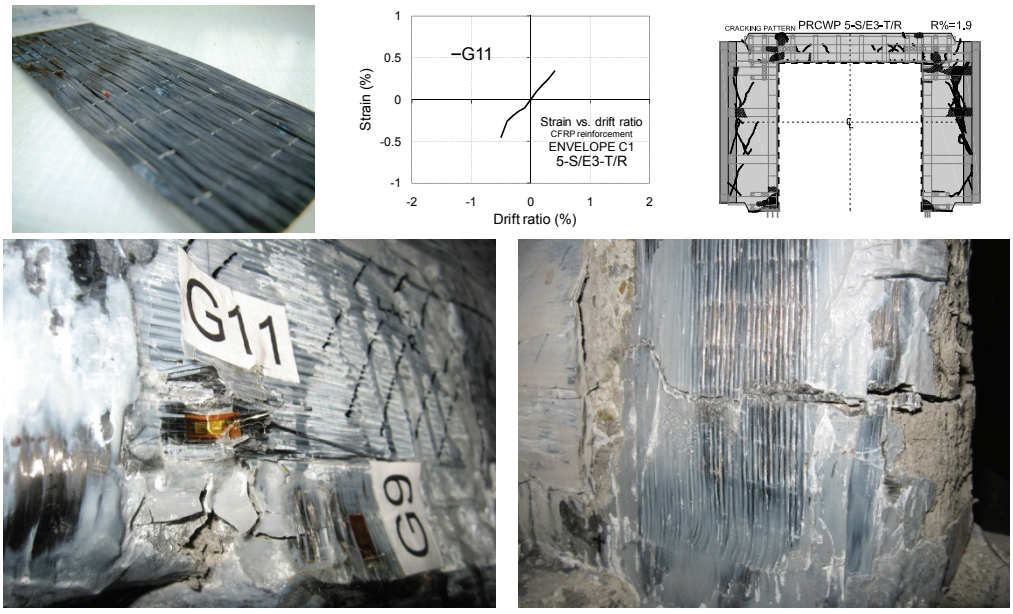

Figure 6.3 Flexural FRPs showing premature failure

EBR strengthening (generally in the range of 0.8÷1.9 performance ratio); outstanding improvement was achieved in terms of energy dissipation (2.2÷4.2 performance ratio). Furthermore, one can assess the differences the timing of the strengthening (post-damage or prior-to damage) had on the response. Note that the results should be viewed in the light of the concrete strength performance ratio (in the range of 0.62÷2.3) and of the loading and boundary conditions. As regards the contribution of the three components (flexural, shear and confinement) of the FRP strengthening to the above performance, it can be concluded that the confinement FRP strips show the most stable response; the shear FRP strips debond in the vicinity of the inclined cracks; and the flexural CFRP-strips subjected to alternating tension-compression reversals parallel to fibre direction are likely to fail prematurely, see Figure 6.3. In order to assess more clearly the components' contribution further subject-oriented investigations are necessary.

Practicing engineers can use the experimental results to evaluate the seismic response modifications which can be expected by CFRP-EBR retrofitting of the cut-out weakened precast concrete wall panels. CFRP layouts similar to the ones presented in this thesis would yield the following results: the shear strength increases in average by 25%; the peak drift increases by 50%; the initial stiffness and the energy dissipation rate remain roughly the same; and the cumulative energy dissipation at ultimate increases by 2÷4 times. One should bear in mind that in reversed cyclic applications the flexural CFRP-EBR is susceptible to premature failure; thus, the author recommends a safety factor of 3 for the flexural FRPs.

6.2 Seismic analysis

In the seismic design of RC wall systems the structural analysis methods rely on the capacity design principle which stipulates that shear failure modes should be avoided by ensuring that the shear resistance is safely higher than the shear corresponding to the flexural yielding, see Figure 6.4a. Assuming that flexural response is assured, the behaviour factor (q) quantifies the level of ductility and energy dissipation attainable by appropriate design and detailing.

The capacity design rule is based on laboratory experiments carried out on RC walls which indicated that the shear failure is brittle, occurs at low ductility level and implies limited amount of energy absorption, whereas the flexural failure is more ductile and much larger amount of energy is dissipated. However, laboratory investigations on cantilever walls tend to overestimate the shear span conditions relative to the as-built situation. A reduced shear span generated by restrained rotation boundary condition may change the failure mode from flexural to shear for the same specimen, refer to Figure 6.4b. Consequently, the appropriate modelling of the shear span conditions is very important in seismic design and analysis.

In the as-built actual seismic situation the shear span conditions of an RC wall can be extremely reduced due to the outrigger effect: the uplifting end of the laterally loaded wall attracts additional axial loads from the adjacent elements to the extent which these axial loads are available. This effect can be conveyed by a rigid diaphragm floor, orthogonal walls and/or the dynamic vertical uplifting combined with the vertical acceleration of the ground motion.

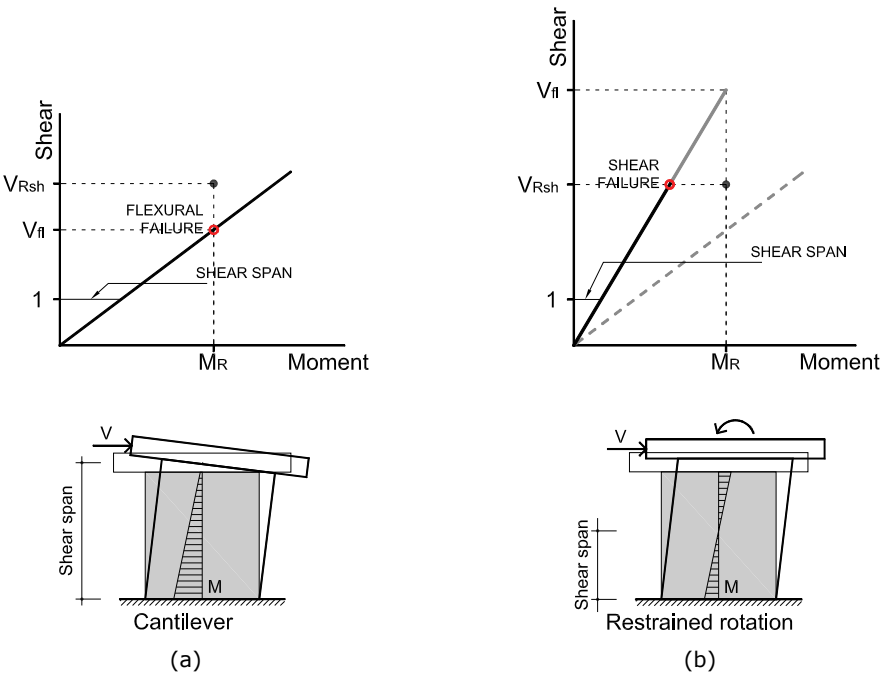

Figure 6.4 Failure mode and shear span conditions: (a) cantilever and (b) restrained rotation

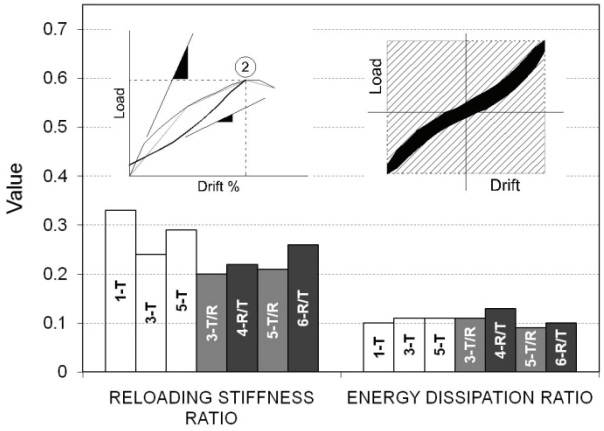

Figure 6.5 Diagonal compression response characteristics

Note that Eurocode 8 recognises the occurrence of the temporary additional axial loads: in clause 5.1.2 in relation to the definition of the large lightly reinforced walls; in paragraph 5.2.3.6(3) regarding the membrane reaction of the slabs mobilised by upward deflections of structural walls; in 5.4.2.4(2) in relation to the axial force fluctuation in coupled walls; and in paragraphs 5.4.2.5(3)P and (4) regarding the additional dynamic axial forces in large walls due to uplifting.

In the present experimental program the author addressed deliberately the outrigger effect by additional eccentric axial loading. It was shown that in these circumstances the response of the RC large panels is diagonal compression dominated, characterised by very high shear resistance, reloading stiffness ratio of (0.2÷0.33), and energy dissipation ratio of 10%, refer to Figure 6.5.

It can be concluded that the outrigger effect by additional eccentric axial loading may cause shear failure to be practically unavoidable, irrespective of the flexural detailing of the wall member; on the other hand, owing to the diagonal compression dominated response, the shear resistance of the RC walls is extremely high. These aspects may need further subject-oriented studies.

6.3 Personal contributions

The author considers the following contributions worthy of notice:

1. Assembling a **DATABASE** of RC wall seismic test programs, with emphasis on the boundary conditions. As of October 2011, the database contains 151 data lines and 222 reference lines.
2. Devising an **EXPERIMENTAL PROGRAM** to investigate the seismic performance of RC wall panels affected by cut-out openings and retrofitted by FRP composites:
   - preparatory studies on the precast large panel structures;
   - program with 5 near-full scale specimen (including 3 bare and 2 FRP-strengthened large panels), 7 tests, 3 comparison lines;
   - strategy of externally bonded FRP strengthening (including flexural, shear and confinement components);
   - test-setup with 4 loading degree of 1000 kN (2xQSC and 2xVertical);
   - restrained rotation control by additional eccentric axial loading;

- instrumentation scheme containing 29 data channels for each test.

3. **CONDUCTING** 7 quasi-static cyclic tests:
   - more than 56 active testing hours;
   - coordination of the loading procedure involving cyclic lateral and variable axial loads of 500 to 1000 kN.
4. **PROCESSING** of the observed and recorded data:
   - evaluation and quantification of possible errors;
   - more than 400 primary diagrams (11 000x7 data lines) including load versus displacement diagrams, load versus strain diagrams, expanded cyclic load and displacement histories, expanded cyclic lateral load versus drift hysteresis loops;
   - cracking history;
   - commentary on the behaviour mode, test events, and failure details.
5. **ANALYSIS** of the results in terms of:
   - **envelope comparison** (cyclic load-drift envelopes, cyclic displacement-drift envelopes, cyclic strain-drift envelopes, monotonic lateral load-drift envelopes with average loading branches, and backbone lateral load-drift);
   - **shear strength** (performance ratio histograms, performance ratio vs. opening ratio relationship, overstrength);
   - **displacement and strain** (cracking, peak and failure drift ratio comparison, ductility, normalised backbone envelopes, steel-strains, FRP-strains);
   - **stiffness** (initial stiffness, stiffness performance ratio vs. opening ratio, secant stiffness degradation, average loading curve tangent stiffness variation, reloading stiffness);
   - **energy dissipation** (continuous integration of the load-drift hysteretic response, cumulative energy dissipated, cumulative drift, energy dissipation rate, energy dissipation ratio).
6. Analytical **MODELLING** of the behaviour mode:
   - identification of the load transfer mechanism;
   - analytical calculations based on the load transfer mechanism;
   - verifications according to the Eurocode provisions.
7. **SYNTHESIS** of the results for engineering practice and further directions of research.

During his doctoral studies the author published 17 papers (9 abroad and 8 in Romania) on-topic and was the co-author of 14 additional papers related to other research programs on reinforced concrete, masonry and steel-concrete composite members. Meanwhile, the author was an active member of several research projects. A selection of representative papers, and the research contracts and grants is provided below.

Selected papers:

Demeter, I., Nagy-György, T., and Stoian, V. (2007). "Strengthening methods of RC walls with externally bonded fiber reinforced polymer composite materials. Literature review of experimental researches." Proc., Composite Materials, Elements and Structures for Construction, UPT Civil Engineering Department, 95-106.

Demeter, I., Nagy-György, T., Stoian, V., and Dan, D. (2008). "Quasi-static loading strategy for earthquake simulation on precast RC shear walls." Proc.,

12th WSEAS International Conference on Systems, WSEAS Press, Vol. 2, pp. 813-819.

Demeter, I. (2008). "RC wall panels strengthened with FRP composites." Proc., 7th International PhD Symposium in Civil Engineering, (CD-ROM), Paper No. 5.1.

Dăescu C., Stoian V., Nagy-György T., Dan D., **Demeter I.** (2008) Ductility increasing for concrete columns – experimental results, Proc., Fourth International Conference on FRP Composites in Civil Engineering (CICE2008), Zurich, Switzerland, 2008, ISBN 978-3-905594-50-8, pp. 56-62.

Demeter, I., Nagy-György, T., Stoian, V., Dăescu, A. C., and Dan, D. (2009). "Seismic retrofit of precast RC wall panels with cut-out openings using FRP composites." Proc., 9th International Symposium on Fiber Reinforced Polymer Reinforcement for Concrete Structures (FRPRCS-9), The University of Adelaide, Paper No. 213.

Demeter, I., Nagy-György, T., Stoian, V., Dăescu, A. C., and Dan, D. (2009). "Precast RC wall panels with cut-out openings retrofitted by CFRP composites." Proc., 11th National and 5th International Scientific Meeting, Planning, Design, Construction and Building Renewal (iNDiS 2009), University of Novi Sad, pp. 157-164.

Demeter, I., Nagy-György, T., Stoian, V., Dăescu, A. C., and Dan, D. (2009). "Seismic strengthening of precast RC wall panels by CFRP composites." Proc., 4th National Conference on Earthquake Engineering (4CNIS), Technical University of Civil Engineering of Bucharest, Vol. 2, pp. 251-256 (in Romanian).

T. Nagy-György, V. Stoian, D. Dan, C. Al. Dăescu, **I. Demeter**, Diaconu Dan (2009). Experimental Assessment On Shear Strengthening Of Clay Brick Masonry Walls Using Different Techniques, Protection of Historical Buildings, Proc., PROHITECH 09, Rome, Italy 21-24 June 2009, pp. 1275-1280, vol. II, ISBN 978-0-415-55805-1 (for 2nd volume) 978-0-415-55803-7.

D. Dan, V. Stoian, T. Nagy György, **I. Demeter** (2009). Experimental Studies on Steel and Steel Concrete Composite Joints Under Symmetrical and Asymmetrical Loads, Proc., STESSA'09, 16-20 august Philadelphia USA, ISBN 978-0-415-56326-0.

Demeter, I., Nagy-György, T., Stoian, V., Dăescu, A. C., and Dan, D. (2010). "Seismic performance of precast RC wall panels with cut-out openings retrofitted by externally bonded CFRP composites." Proc., 3rd fib International Congress and PCI Convention & Bridge Conference (fib 2010), PCI, Paper No. 593.

Demeter, I., Nagy-György, T., Stoian, V., Dăescu, A. C., and Dan, D. (2010). "Seismic performance of precast RC wall panels with cut-out openings" Proc., 14th European Conference on Earthquake Engineering (14ECEE), MAEE, Paper No. 1004.

Demeter, I., Nagy-György, T., Stoian, V., Dăescu, A. C., and Dan, D. (2010). "FRP composites for seismic retrofitting of RC wall panels with cut-out openings" Proc., First International Conference on Structures and Architecture (ICSA2010), CRC Press, Balkema, Taylor & Francis, Paper No. 240, pp. 1902-1908.

Research projects:

"Retrofit of RC walls and slabs with cut-out openings using FRP composites", financial support by the National University Research Council (CNCSIS), through grant No. 355/2006, CNCSIS, type A, coordinated by Prof. Stoian Valeriu, Politehnica University of Timisoara.

"Advanced strengthening systems of RC members, beams, columns, walls and slabs, using FRP composites", supported by the Ministry of Education and Research, Romania, through contract No. 1436/2006, CNCSIS, CEEX, type ET, coordinated by Dr. Nagy-György Tamás, Politehnica University of Timisoara.

"Reinforced concrete walls strengthened by composite materials", supported by the National University Research Council (CNCSIS-UEFISCSU), PNII-RU-TD8, through contract No. 2/2007, coordinated by Demeter István, Politehnica University of Timisoara.

"Innovative Structural Systems Using Steel-Concrete Composite Materials and Fiber Reinforced Polymer Composites", supported by the National University Research Council (CNCSIS-UEFISCSU), PNII-IDEI ID_1004/2008, through contract No. 621/2009, coordinated by Dr. Dan Daniel, Politehnica University of Timisoara.

BIBLIOGRAPHY

[1] ESC (1998), "European Macroseismic Scale 1998 EMS-98", Centre Europèen de Géodynamique et de Séismologie, Luxembourg.

[2] Iverson, J.K. and Hawkins, N.M. (1994), "Performance of precast/prestressed concrete building structures during Northridge earthquake", PCI J., 39(2), pp. 38-46.

[3] Elnashai, A.S., Bommer, J.J., Baron, C.I., Lee, D. and Salama, A.I. (1995), "Selected Engineering Seismology and Structural Engineering Studies of the Hyogo-ken Nanbu (Great Hanshin) Earthquake of 17 January 1995", Imperial College, ESEE Research Report, No. 95-2.

[4] EERI (2000), "Kocaeli, Turkey Earthquake of August 17, 1999 Reconnaissance Report", Earthquake Spectra, Supplement A to Volume 16, EERI Publication No. 2000-03.

[5] Berberian, M. (2005), "The 2003 Bam Urban Earthquake: A Predictable Seismotectonic Pattern Along the Western Margin of the Rigid Lut Block, Southeast Iran", Earthquake Spectra, 21(S1), pp. S35-S99.

[6] EERI (2008), "Learning from Earthquakes: The Wenchuan, Sichuan Province, China, Earthquake of May 12, 2008", EERI Newsletter, October 2008, EERI Special Earthquake Report.

[7] EERI (2009), "Learning from Earthquakes: The Mw=6.3 Abruzzo, Italy, Earthquake of April 6, 2009", EERI Newsletter, June 2009, EERI Special Earthquake Report.

[8] EERI (2010), "Learning from Earthquakes: The Mw 7.0 Haiti Earthquake of January 12, 2010: Report #1", EERI Newsletter, April 2010, EERI Special Earthquake Report.

[9] EERI (2010), "Learning from Earthquakes: The Mw 8.8 Chile Earthquake of February 27, 2010", EERI Newsletter, June 2010, EERI Special Earthquake Report.

[10] EERI (2010). "Learning from Earthquakes: The Mw 7.1 Darfield (Canterbury), New Zealand Earthquake of September 4, 2010", EERI Newsletter, November 2010, EERI Special Earthquake Report.

[11] EERI (2011). "Learning from Earthquakes: The M 6.3 Christchurch, New Zealand, Earthquake of February 22, 2011", EERI Newsletter, May 2011, EERI Special Earthquake Report.

[12] EERI (2011). "Learning from Earthquakes: The March 11, 2011, Great East Japan (Tohoku) Earthquake and Tsunami: Societal Dimensions", EERI Newsletter, August 2011, EERI Special Earthquake Report.

[13] Reitherman, R. (2008). "International aspects of the history of earthquake engineering", EERI, Oakland, California, USA.

[14] Incorporated Research Institutions for Seismology (IRIS), Global Seismographic Network, [Online], Available from: <http://www.iris.edu/hq/programs/gsn>, [accessed October 8, 2011].

[15] United States Geological Survey (USGS), ANSS - Advanced National Seismic System, [Online], Available from: <http://earthquake.usgs.gov/monitoring/anss/>, [accessed October 8, 2011].

[16] European-Mediterranean Seismological Centre (EMSC), [Online], Available from: <http://www.emsc-csem.org/#2>, [accessed October 8, 2011].
[17] Institutul National pentru Fizica Pământului (INFP), National Seismic Network, [Online], Available from: <http://www.infp.ro/en>, [accessed October 8, 2011].
[18] International Institute of Seismology and Earthquake Engineering (IISEE), Catalog of Damaging Earthquakes in the World (Through June, 2009), [Online], Available from: <http://iisee.kenken.go.jp/utsu/index_eng.html>, [accessed October 8, 2011].
[19] National Geophysical Data Center (NGDC), Global Significant Earthquake Database, [Online], Available from: <http://www.ngdc.noaa.gov/hazard/earthqk.shtml>, [accessed October 8, 2011].
[20] European-Mediterranean Seismological Centre (EMSC), Archive of Historical EArthquake Data (AHEAD), [Online], Available from: <http://www.seismicportal.eu/jetspeed/portal/explorers/historical.psml >, [accessed October 8, 2011].
[21] United States Geological Survey (USGS), Earthquake Lists and Maps, [Online], Available from: <http://earthquake.usgs.gov/earthquakes/eqarchives/>, [accessed October 8, 2011].
[22] Institutul National pentru Fizica Pământului (INFP), ROMPLUS Earthquake Catalogue, [Online], Available from: <http://www.infp.ro/catalog-seismic/evenimente>, [accessed October 8, 2011].
[23] Shebalin, N.V., Leydecker, G., Mokrushina, N.G., Tatevossian, R.E., Erteleva, O.O. and Vassiliev, V. (1998). "Earthquake catalogue for Central and South-Eastern Europe, 342 BC – 1990", European Commission, Final Report to Contract No ETNU-CT93-0087, Brussels.
[24] Bommer, J.J. and Boore, D.M. (2004), "Engineering Seismology", In: Encyclopaedia of Geology, Academic Press.
[25] Building Research Institute (BRI), BRI strong motion network, [Online], Available from: <http://smo.kenken.go.jp/smn>, [accessed October 8, 2011].
[26] National Research Institute for Earth Science and Disaster Prevention (NIED), Kyoshin Network, [Online], Available from: <http://www.k-net.bosai.go.jp/>, [accessed October 8, 2011].
[27] United States Geological Survey (USGS), National Strong Motion Network, [Online], Available from: <http://nsmp.wr.usgs.gov/stations.html>, [accessed October 8, 2011].
[28] National Institute for Research and Development in Construction, Urban Planning and Sustainable Spatial Development (URBAN-INCERC), ISC-INCERC Seismic Network, [Online], Available from: <http://www.incerc2004.ro/ISC-INCERC_Network.htm>, [accessed October 8, 2011].
[29] Building Research Institute (BRI), BRI strong motion database, [Online], Available from: <http://smo.kenken.go.jp/smdb>, [accessed October 8, 2011].
[30] Consortium of Organizations for Strong-Motion Observation Systems (COSMOS), COSMOS Virtual Data Center, [Online], Available from:

<http://db.cosmos-eq.org/scripts/default.plx>, [accessed October 8, 2011].

[31] USGS-CGS-ANSS: United States Geological Survey (USGS), California Geological Survey (CGS), Advanced National Seismic System (ANSS), Center for Engineering Strong Motion Data, [Online], Available from: <http://strongmotioncenter.org/>, [accessed October 8, 2011].

[32] Pacific Earthquake Engineering Research Center (PEER), PEER Strong Motion Database, [Online], Available from: <http://peer.berkeley.edu/smcat/>, [accessed October 8, 2011].

[33] Pacific Earthquake Engineering Research Center (PEER), NGA Database, [Online], Available from: <http://peer.berkeley.edu/nga/>, [accessed October 8, 2011].

[34] Istituto Nazionale di Geofisica e Vulcanologia (INGV), ITACA - ITalian ACcelerometric Archive, [Online], Available from: <http://itaca.mi.ingv.it/ItacaNet/>, [accessed October 8, 2011].

[35] National Institute for Research and Development in Construction, Urban Planning and Sustainable Spatial Development (URBAN-INCERC), Accelerograms recorded in RNSC during the Vrancea Earthquakes, [Online], Available from: <http://www.incerc2004.ro/accelerograms.htm>, [accessed October 8, 2011].

[36] Beattie, G.J., Megget, L.M. and Andrews, A.L. (2008), "The historic development of earthquake engineering in New Zealand", Proc., 14th World Conf. On Earthquake Engineering (14WCEE), Beijing, China.

[37] Abrams, D.P. (1991), "Laboratory definitions of behaviour for structural components and building systems", ACI, SP 124-4.

[38] National Institute of Statistics (2002), "Census of Population and Dwellings 2002", Vol. 3: B-D-H (Buildings-Dwellings-Households).

[39] Demeter, I. (2005), "Short history of large panel structures in Romania", Scientific Bulletin of the Politehnica University of Timisoara, Vol. 51(65), No. 1, 87-94.

[40] ISART (1973), "Clădiri de locuit P+4 din panouri mari. Proiect 1615/X", Bucharest, Romania.

[41] IPCT (1982), "Clădiri de locuit P+4 din panouri mari. Proiect 770-81", Vol. 12: Sectiunea Pb2 (P2a6), Bucharest, Romania.

[42] IPCT (1982), "Clădiri de locuit P+4 din panouri mari. Proiect 770-81", Vol. C: Elemente prefabricate, Bucharest, Romania.

[43] Ridell, R., Wood, S.L. and De La Liera, J.C. (1987), "The 1985 Chile Earthquake", University of Illinois at Urbana-Champaign, Urbana, Illinois, U.S.A.

[44] Farrar, C.R., Reed, J.W. and Salmon, M.W. (1993), "Failure modes of low-rise shear walls", Jrnl. of Energy Eng., ASCE, 119(2), 119-138.

[45] Greifenhagen, C. and Lestuzzi, P. (2005), "Static cyclic tests on lightly reinforced concrete shear walls", Engineering Structures, 25(2005), 1703-1712.

[46] Farvashany, F.M., Foster, S.J. and Rangan, B.V. (2008), "Strength and deformation of high-strength concrete shearwalls", ACI Struct. J., 105(1), 21-29.

[47] Orakcal, K., Massone, L.M. and Wallace, J.W. (2009), "Shear strength of lightly reinforced wall piers and spandrels", ACI Struct. J., 106(4), 455-465.

[48] Hirosawa, M. (1975), "Past experimental results on reinforced concrete shear walls and their analysis", (in Japanese, ref. in Orakcal et al., 2009).
[49] Wood, S.L. (1989), "Minimum tensile reinforcement requirements in walls", ACI Struct. J., 86(4), 582-591.
[50] Gulec, C.K. (2005), "Ultimate shear strength of squat rectangular reinforced concrete walls", MSc Thesis, Department of Civil, Structural and Environmental Engineering, State University of New York at Buffalo, Buffalo, NY.
[51] Wood, S.L. (1990), "Shear strength of low-rise reinforced concrete walls", ACI Struct. J., 87(1), 99-107.
[52] Stanic, A., Sigmund, V. and Guljas, I. (2003), "Behavior of the walls under in-plane horizontal loadings", Proc., fib-Symposium, Athens, Greece.
[53] Gulec, C.K. and Whittaker, A.S. (2009), "Performance-based assessment and design of squat reinforced concrete shear walls", Technical Report MCEER-09-0010.
[54] Panagiotakos, T.B. and Fardis, M.N. (2001), "Deformations of reinforced concrete members at yielding and ultimate" ,ACI Struct. J., 98(2), 135-148.
[55] Biskinis, D.E., Roupakias, G.K. and Fardis, M.N. (2004), "Degradation of shear strength of reinforced concrete members with inelastic cyclic displacements", ACI Struct. J., 101(6), 773-783.
[56] PEER, Structural performance database, [Online], Available from: <http://nisee.berkeley.edu/spd/>, [accessed December 3, 2010].
[57] Tokyo Institute of Technology, Kawashima Lab, Cyclic Loading Test Data of Reinforced Concrete Bridge Piers, [Online], Available from: <http://seismic.cv.titech.ac.jp/en/titdata/titdata.html>, [accessed September 14, 2011].
[58] University of Ottawa, Shear wall database, [Online], Available from: <http://by.genie.uottawa.ca/~palermo/Wall.htm>, [accessed May 5, 2011].
[59] University of Minho, DABASUM - Database for FRP-Based Shear Strengthening of Reinforced Concrete Beams, [Online], Available from: <http://dabasum.civil.uminho.pt/index.php>, [accessed May 5, 2011].
[60] RILEM, TC 223-MSC Data warehouse, MSC: masonry strengthening with composite materials, [Online], Available from: <https://rilem223dwh.isqweb.it/>, [accessed May 5, 2011].
[61] Demeter, I., Nagy-György, T. and Stoian, V. (2007), "Strengthening methods of RC walls with externally bonded fiber reinforced polymer composite materials. Literature review of experimental researches", Proc., Composite Materials, Elements and Structures for Construction, UPT Civil Engineering Department, 95-106.
[62] Demeter, I., Nagy-György, T. and Stoian, V. (2007), "Axial loading strategy for experimental tests on precast RC walls subjected to in-plane seismic actions", Scientific Bulletin of the "Politehnica" University of Timişoara, Vol. 52(66), No. 2, 11-16.
[63] Demeter, I., Nagy-György, T., Stoian, V. and Dan, D. (2008), "Quasi-static loading strategy for earthquake simulation on precast RC shear walls", Proc., 12th WSEAS International Conference on Systems, WSEAS Press, Vol. 2, pp. 813-819.
[64] Benjamin, J.R. and Williams, H.A. (1958), "Behavior of one-storey reinforced concrete shear walls", ACI J., 30(5), 605-618.

[65] Kakaletsis, D.J. and Karayannis, C.G. (2009), "Experimental Investigation of Infilled Reinforced Concrete Frames with Openings", ACI Struct. J., 106(2), 132-141.
[66] Warashina, M., Kono, S., Sakashita, M. and Tanaka, H. (2008), "Shear behavior of multi-story RC structural walls with eccentric openings", Proc., 14th World Conf. On Earthquake Engineering (14WCEE), Beijing, China.
[67] Yanez, F.V., Park, R. and Paulay, T. (1992), "Seismic behaviour of walls with irregular openings", Proc., 10th World Conf. On Earthquake Engineering (10WCEE).
[68] Umemura, H., Aoyama, H. and Hosokawa, Y. (1980), "Restoring force characteristics of RC walls with openings and reinforcing methods", Proc., 7th World Conf. on Earthquake Engineering (7WCEE).
[69] CEN/TC250 (2004), "EN 1992-1-1:2004:E Eurocode 2: Design of concrete structures - Part 1-1: General rules and rules for buildings", European Committee for Standardisation (CEN), Brussels, Belgium.
[70] Cadar, I., Clipii, T., and Tudor, A. (2004), "Beton armat, Editia a 2-a", Editura Orizonturi Universitare, Timisoara, (in Romanian).
[71] Demers, M., Neale, K.W., and Sheikh, S. (2008), "FRP rehabilitation of reinforced concrete structures. Design Manual No.4, Version 2", ISIS Canada Corporation, Winnipeg, Manitoba, Canada.
[72a] Sika Corporation (2003), "SikaWrap® Hex 230C Carbon fiber fabric for structural strengthening; Product Data Sheet; Edition 7.2003", Lyndhurst, NJ, USA.
[72b] Sika Corporation (2011), "Sikadur® 330 US High-modulus, high-strength, impregnating resin; Product Data Sheet; Edition 2.16.2011", Lyndhurst, NJ, USA.
[73a] Sika Corporation (2010), "SikaWrap® Hex 103C Carbon fiber fabric for structural strengthening; Product Data Sheet; Edition 6.23.2010", Lyndhurst, NJ, USA.
[73b] Sika Corporation (2008), "Sikadur® 300 High-modulus, high-strength, impregnating resin; Product Data Sheet; Edition 7.1.2008", Lyndhurst, NJ, USA.
[74a] Sika Deutschland GmbH (2009), "SikaWrap®-230 C/45 Kohlefasergewebe für die Bauteilverstärkung; Produktdatenblatt; Gültig ab 31.05.09", Stuttgart, Germany, (in German).
[74b] Sika Deutschland GmbH (2009), "Sikadur®-330 Armierungskleber; Produktdatenblatt; Gültig ab 07.12.09", Stuttgart, Germany, (in German).
[75] Sika Romania SRL (2004), " Sika Repair® 13 Mortar de reparatie; Fisa tehnica de produs; Editia 1, 2004", Brasov, Romania, (in Romanian).
[76] Taylor, C.P., Cote, P.A., and Wallace, J.W. (1998), "Design of slender reinforced concrete walls with openings", ACI Struct. J., 95(4).
[77] Kitano, A., Joh, O. and Goto, Y. (2004), "Experimental study on the strengthening and repair of R/C wall-frame structures with an opening by CF-sheets or CF-grids", Proc., 2nd International Conference on FRP Composites in Civil Engineering (CICE 2004), Adelaide, Australia.
[78] Sugiyama, T., Uemura, M., Fukuyama, H., Nakano, K. and Matsuzaki, Y. (2000), "Experimental study on the performance of the RC frame infilled cast-in-place non-structural RC walls retrofitted by using carbon

fiber sheets", Proc., 12th World Conf. on Earthquake Engineering, (CD-ROM), New Zealand, Paper No. 2153.

[79] Elnashai, A.S. and Pinho, R. (1998), "Repair and retrofitting of RC walls using selective techniques", Journal of Earthquake Engineering, 2(4), 525-568.

[80] Lombard, J., Lau, D. T., Humar, J. L., Foo, S. and Cheung, M. S. (2000), "Seismic strengthening and repair of reinforced concrete shear walls", Proc., 12th World Conf. on Earthquake Engineering, (CD-ROM), New Zealand, Paper No. 2032.

[81] Salonikios, T. N., Kappos, A. J., Tegos, I. A. and Penelis, G. G. (1999), "Cyclic load behavior of low-slenderness reinforced concrete walls: Design basis and test results", ACI Struct. J., 96(4), 649-660.

[82] Hidalgo, P. A. and Jordan, R. M. (1996), "Strength and energy dissipation characteristics of reinforced concrete walls under shear failure", Proc., 11th World Conf. on Earthquake Engineering (11WCEE).

[83] Barney, G. B., Shiu, K. N., Rabbat, B. G., Fiorato, A. E., Russell, H. G., and Corley W. G (1980), "Behavior of coupling beams under load reversals", PCA Research and Development Bulletin, RD068.01B.

[84] Hidalgo, P.A., Ledezma, C.A., and Jordan, R.M. (2002), "Seismic behavior of squat reinforced concrete shear walls", Earthquake Spectra, 18(2), pp. 287-308.

[85] Lestuzzi, P., and Bachmann, H. (2007), "Displacement ductility and energy assessment from shaking table tests on RC structural walls", Engineering Structures, 29(2007), pp. 1708-1721.

[86] Paulay, T., Priestley, M.J.N., and Synge A.J. (1982), "Ductility in earthquake resisting squat shearwalls", ACI J., July-August 1982, pp. 257-269.

[87] Salonikios, T.N., Kappos, A.J., Tegos, I.A., and Penelis, G.G. (2000), "Cyclic load behavior of low-slenderness reinforced concrete walls: failure modes, strength and deformation analysis, and design implications", ACI Struct J., 97(1), pp.132-142.

[88] Antoniades, K.K., Salonikios, T.N., and Kappos, A.J. (2007), "Evaluation of hysteretic response and strength of repaired RC walls strengthened with FRPs", Engineering Structures, 29(2007), pp. 2158-2171.

[89] Pilakoutas, K., and Elnashai, A.S. (1995), "Cyclic behavior of reinforced concrete cantilever walls, Part II: Discussions and theoretical comparisons", ACI Struct. ,J., 92(4), pp. 425-433.

[90] Sittipunt, C., Wood, S.L., Lukkunaprasit, P., and Pattararattanakul, P. (2001), "Cyclic behavior of reinforced concrete structural walls with diagonal web reinforcement", ACI Struct J., 98(4), pp. 554-562.

[91] Patterson, J., and Mitchell, D. (2003), "Seismic retrofit of shear walls with headed bars and carbon fiber wrap", Jrnl. of Struct. Eng., 129(5), pp. 606-614.

[92] Braz-César, M.T., Oliveira, D., Barros, R.C. (2008), "Comparison of cyclic response of reinforced concrete infilled frames with experimental results", Proc., 14th World Conf. on Earthquake Engineering (14WCEE).

[93] Olsen, E.C., and Billington, S.L. (2011), "Cyclic response of precast high-performance fiber-reinforced concrete infill panels", ACI Struct. J., 108(1), pp. 51-60.

[94] *fib* TG 9.3 (2001), "*fib* Bulletin 14: Externally bonded FRP reinforcement for RC structures", fédération internationale du béton (*fib*), Lausanne, Switzerland.

[95] CEN/TC250 (2004), "EN 1998-1:2004:E Eurocode 8: Design of structures for earthquake resistance -Part 1: General rules, seismic actions and rules for buildings", European Committee for Standardisation (CEN), Brussels, Belgium.
[96] AIJ (1999), "AIJ Standard for Structural Calculation of Reinforced Concrete Structures Based on Allowable Stress Concept", Architectural Institute of Japan.
[97] Taleb, R. and Kono, S. (2010), "Shear behavior of multi-story reinforced concrete walls with openings", Bulletin of IISEE, 45, 55-60.
[98] CEN (2001), "EN 12390-3:2001 Testing of hardened concrete – Part 3: Compressive strength of test specimens", European Committee for Standardisation (CEN), Brussels, Belgium.
[99] CEN (2002), "EN ISO 15630-1:2002 Steel for the reinforcement and prestressing of concrete – Test methods – Part 1: Reinforcing bars, wire rod and wire (ISO 15630-1:2002)", European Committee for Standardisation (CEN), Brussels, Belgium.
[100] CEN (2001), "EN 10002-1:2001 Metallic materials – Tensile testing – Part 1: Methods of test at ambient temperature", European Committee for Standardisation (CEN), Brussels, Belgium.

Appendix A Database of RC wall tests

Table A.1 – RC wall test database

PROGRAM ID	Country	Institute	References	SPECIMEN		
				Designation	Construction	Type (storey/bay/plane)
CURTIN-2008	Australia	Curtin Univ. of Technology	Farvashany et al., 2008	HSCW	civil	wall element
MMCAN-1969a-1	Canada	McMaster Univ.	Heidebrecht and Tso, 1969	A; B; C; D	civil	wall system (/2/1)
MMCAN-1969a-2	Canada	McMaster Univ.	Heidebrecht and Tso, 1969		civil	wall system
MMCAN-1974	Canada	McMaster Univ.	Alexander et al., 1974	Panel	civil	wall element
UTCAN-1981	Canada	Univ. of Toronto	Collins et al., 1981	PV; A; B; C; D	civil	wall component
UMA-1989a	Canada	Univ. of Manitoba	Rizkalla et al., 1989	NK; LK; SK	civil	wall component
UMA-1989b	Canada	Univ. of Manitoba	Foerster et al., 1989	SP	civil	wall component
CARLT-2000	Canada	Carleton Univ.	Hiotakis et al., 2004; Lombard et al., 2000	wall	civil	wall element
UTCAN-2001	Canada	Univ. of Toronto	Palermo and Vecchio, 2001, 2002; Vecchio et al., 2002;	DP	nuclear	wall element
MGILL-2003	Canada	McGill Univ.	Paterson and Mitchell, 2003	W	civil	wall system (3/1/1)
MMCAN-2004	Canada	McMaster Univ.	Ghobarah and Khalil, 2004	CW; RW	civil	wall element
UACAN-2005	Canada	Univ. of Alberta	Mobeen et al., 2005	A; B; C	civil	wall system (/1/1)
UMON-2009	Canada	Montreal Univ.	Ghorbani-Renani et al., 2009	A; B	civil	wall system (5/1/1)
PUCC-1998	Chile	Catholic Univ. of Chile	Hidalgo and Jordan, 1996; Hidalgo et al., 1998, 2002;	Specimen	civil	wall element
TSHUA-2000	China	Tsinghua Univ.	Zhang and Whang, 2000	SW; SRCW	civil	wall system (/1/1)
DUT-2004	China	Dalian Univ. of Technology	Li and Li, 2004	Wall	civil	wall element
HKUST-2008	China	Hong Kong Univ.	Kuang and Ho, 2008	U; C	civil	wall element
CUEG-2005	Egypt	Cairo Univ.	Labib et al., 2005	SW	civil	wall element
ELSA-2009a-1	EU	ELSA Ispra	Renda et al., 2009	Sample	nuclear	wall element
ELSA-2009a-2	EU	ELSA Ispra	Renda et al., 2009	Sample	nuclear	wall element
ELSA-2001	EU-France	ELSA Ispra	Ile et al., 2000; Naze and Sidaner, 2001; Gallitre et al., 2007; Pegon et al., 2009	T	nuclear	wall element

Table A.1 – RC wall test database (contd.)

							TEST SET-UP	LOADING	BOUNDARY cond.	PROGRAM ID
	Concrete techn.	Opening	Strengthening	No. of spec.	Scale mod/prot	Web thickness (mm)	type-N-V			
	monolithic	solid	non	7	0.33	75	A-1-1	QSM	CL	CURTIN-2008
	monolithic	solid; circular	non	8	small	15		QSM	cantilever	MMCAN-1969a-1
	monolithic	solid; circular	non		small			DYN	cantilever	MMCAN-1969a-2
	monolithic	solid	non	5	0.5	100	n/a-n/a-2	QSC	n/a	MMCAN-1974
	monolithic	solid	non	4		70	panel tester	QSM	shear panel	UTCAN-1981
	precast	n/a	non	7	full	200	universal testing machine	QSM	shear line	UMA-1989a
	precast	n/a	non	10	full	200	universal testing machine	QSM	shear line	UMA-1989b
	monolithic	solid	non; FRP EBR	7		100	A-0-2	QSC	CL	CARLT-2000
	monolithic	solid	non; repair	2	large	75	standard	QSC; QSM	cantilever	UTCAN-2001
	monolithic	solid	non; FRP-EBR; RC; headed bar	4		300	standard	QSC	cantilever	MGILL-2003
	monolithic	solid	non; FRP-EBR	3		120	C-4-2	QSC	AM	MMCAN-2004
	monolithic	solid	non	3	full	200	standard	QSC	cantilever	UACAN-2005
	monolithic	solid	non	4	full; 0.42	85; 200	standard	QSM; QSC	cantilever	UMON-2009
	monolithic	solid	non	32	full	80; 100; 120	B w/ P-1-2	QSC	RR	PUCC-1998
	monolithic	solid	non	4		100	standard	QSC	cantilever	TSHUA-2000
	monolithic	solid	non	9		100	A-1-2	QSC	CL	DUT-2004
	monolithic	solid	non	8	large	100	A-1-2	QSC	CL	HKUST-2008
	monolithic	solid	non	8	0.25	70	A-1-2	QSC	CL	CUEG-2005
	monolithic	solid	non			400	double L frames	PSD	modified	ELSA-2009a-1
	monolithic	solid	non			400	double L frames	QSC	modified	ELSA-2009a-2
	monolithic	solid	non; FRP EBR	13		200	restrained rotation	PSD	modified	ELSA-2001

Table A.1 – RC wall test database (contd.)

PROGRAM ID	Country	Institute	References	SPECIMEN Designation	Construction	Type (storey/bay/plane)
CEBTP-1989	France	CEBTP Saint Remy les Chevreuses	Coladant and Foure, 1989; Foure, 1992; Bisch and Coin, 2007	KV	nuclear	wall element
CEBTP-1992	France	CEBTP Saint Remy les Chevreuses	Lafolie and Bouchon, 1992	PH	nuclear	wall element
EMSI-1992	France	EMSI CEA Saday	Lafolie and Bouchon, 1992	PJ	nuclear	wall element
EMSI-1994	France	EMSI CEA Saday	Bisch and Coin, 1994, 2007	CASSBA	civil	wall system
EMSI-2002	France	EMSI CEA Saday	Bisch and Coin, 2002, 2007; Combescure et al., 2002; Ile and Reynouard, 2003, 2004; Colombo and Mazars, 2004; Sollogoub and Queval, 2007;	CAMUS 2000	civil	wall system
CEBTP-2004	France	CEBTP Saint Remy les Chevreuses	Bouchon et al., 2004	wall	nuclear	wall element
unknown	France		Ferrier, 2010			
unknown	France		Quazi et al., 2011			
EMSI-2000	France-EU	EMSI CEA Saday	Bisch and Coin, 1998, 2007; Sollogoub et al., 2000; Sollogoub and Queval, 2007; Fischinger and Isakovic, 2000; Ile and Reynouard, 2000; Fischinger et al., 2003; Combescure et al., 2001;	CAMUS 1 to 4	civil	wall system
TUDRM-1988a-1	Germany	Technical Univ. of Darmstadt	Rothe and Konig, 1988	T	civil	wall element
TUDRM-1988a-2	Germany	Technical Univ. of Darmstadt	Rothe and Konig, 1988	T	civil	wall element
AUTH-2003	Greece	Aristotle Univ. of Thessaloniki	Antoniades et al., 2003a, 2003b, 2005, 2007; Salonikios et al., 1996, 1999, 2000	MSW; LSW; FRPMSW; FRPLSW	civil	wall element
CBRI-1988	India	CBRI Roorkee	Chakrabarti et al., 1988	A; B; C; D; E; F	civil	wall component
BHRC-2000	Iran	BHRC Tehran	Tsanimi, 2000	SHW	civil	wall system (3/1/1)
UNIPV-1984	Italy	Univ. of Pavia	Cauvin and Zanon, 1984	A; B; C	civil	wall component

Table A.1 – RC wall test database (contd.)

							TEST SET-UP	LOADING	BOUNDARY cond.	PROGRAM ID
	Concrete techn.	Opening	Strengthening	No. of spec.	Scale mod/prot	Web thickness (mm)	type-N-V			
	monolithic	solid	non	7		100	standard	QSC	cantilever	CEBTP-1989
	monolithic	solid; door; window	non	10	1	100		DYN	cantilever	CEBTP-1992
	monolithic	solid; door; window	non	13		50	shaking table	DYN	cantilever	EMSI-1992
	monolithic	solid	non	1	0.33	60	shaking table	DYN	cantilever	EMSI-1994
	monolithic	solid	non	2	0.33	60	shaking table	DYN	cantilever	EMSI-2002
	monolithic	solid	non	3		100	standard	QSC	cantilever	CEBTP-2004
			FRP							unknown
			FRP							unknown
	monolithic	solid	non; FRP-EBR	4	0.33	60	shaking table	DYN	cantilever	EMSI-2000
	monolithic	solid	non	6		50; 80	A-1-2	QSC	CL	TUDRM-1988a-1
	monolithic	solid	non	5		50; 80	shaking table	DYN	cantilever	TUDRM-1988a-2
	monolithic	solid	non; FRP EBR	11	0.4	100	A-2-2	QSC	CL	AUTH-2003
	precast	n/a	non	29	1	125	sliding	QSM	shear line	CBRI-1988
	monolithic	solid	non	4	0.125	50	standard	QSC	cantilever	BHRC-2000
	precast	n/a	non	6	full	250	sliding	QSC	shear line	UNIPV-1984

Table A.1 – RC wall test database (contd.)

PROGRAM ID				SPECIMEN		
	Country	Institute	References	Designation	Construction	Type (storey/bay/plane)
UNIPV-1988	Italy	Univ. of Pavia	Calvi and Macchi, 1988	A; B; C	civil	wall element
PMIT-2001	Italy	Politecnico di Milano	Riva and Franchi, 2001	B; HR; CD	civil	wall element
UNIBS-2003	Italy	Univ. of Brescia	Riva et al., 2003a, 2003b, 2004	wall; repaired wall	civil	wall system (4/1/1)
UNIBS-2008	Italy	Univ. of Brescia	Marini and Meda, 2008, 2009	wall	civil	wall system (3/1/1)
OERL-1969	Japan	Ohbayashi-gumi	Watanabe and Shimaguchi, 1969	A; B; C	civil	wall system
KAJI-1974	Japan	Kajima Co.	Muto et al., 1974	Wall	civil	wall element
TOH-1974	Japan	Tohoku Univ.	Shiga et al., 1974	WB	civil	wall element
UTOK-1977	Japan	Univ. of Tokyo	Umemura et al., 1977	B; C	nuclear	wall system
BRI-1980	Japan	BRI Tokyo	Endo et al., 1980	W	civil	wall-frame system (1;2;3/1/1)
TAK-1980a-1	Japan	Takenaka RD Inst.	Yamaguchi et al., 1980	W	civil	wall-frame system (2/1/1)
TAK-1980a-2	Japan	Takenaka RD Inst.	Yamaguchi et al., 1980	R	civil	wall-frame system (2;3/3/1)
UTOK-1980a-1	Japan	Univ. of Tokyo	Umemura et al., 1980	B; BL; BO	nuclear	wall system
UTOK-1980a-2	Japan	Univ. of Tokyo	Umemura et al., 1980	I; IL	nuclear	wall element
UTOK-1980a-3	Japan	Univ. of Tokyo	Umemura et al., 1980	IO; IP; IX; ISO; I	nuclear	wall element
CHUG-1984	Japan	Chugoku-Electric Co.; Hiroshima Univ.	Shimazu and Araki, 1984	C; IS; B; E; O	civil	wall-frame system
TOH-1984	Japan	Tohoku Univ.	Takahashi et al., 1984	ST	civil	wall-frame system (4/2/1)
TOH-1988	Japan	Tohoku Univ.	Takahashi et al., 1988	SP; SM	civil	wall-frame system (2;3/1/1)
EPDC-1989a-1	Japan	Electric Power Development Co.	Murakami et al., 1989	A	nuclear	wall element
EPDC-1989a-2	Japan	Electric Power Development Co.	Murakami et al., 1989	A	nuclear	wall-frame system
EPDC-1989a-3	Japan	Electric Power Development Co.	Murakami et al., 1989	BJ; BT	nuclear	wall-slab system
TEPC-1989	Japan	Tokyo Electric Power Co.	Sato et al., 1989	Specimen	nuclear	wall element

Table A.1 – RC wall test database (contd.)

							TEST SET-UP	LOADING	BOUNDARY cond.	PROGRAM ID
	Concrete techn.	Opening	Strengthening	No. of spec.	Scale mod/prot	Web thickness (mm)	type-N-V			
	monolithic	solid	non	6		80	diagonal	QSC	diagonal compression	UNIPV-1988
	monolithic	solid	non	18	full	150	A-1-2	QSC	CL; AM	PMIT-2001
	monolithic	solid	non; repair	1	full	300	standard	QSC	cantilever	UNIBS-2003
	monolithic	solid	RC jacket	1	0.33	100	standard	QSC	cantilever	UNIBS-2008
	precast	window	non		full		shaking table	DYN		OERL-1969
	precast	solid; slitted	non	2			n/a-n/a-2	QSC	RR	KAJI-1974
	monolithic	solid	non	8		50	A-1-2	QSC	CL	TOH-1974
	monolithic	solid	non	7		80; 100	standard	QSC	cantilever	UTOK-1977
	monolithic	solid	non	20		50; 80; 100	standard	QSC; QSM	cantilever	BRI-1980
	monolithic	solid	non	16	0.2	50	beam type	QSC	modified	TAK-1980a-1
	monolithic	solid	non	3	0.2	50	standard	QSC	cantilever	TAK-1980a-2
	monolithic	solid; opening	non	8		80	standard	QSC	cantilever	UTOK-1980a-1
	monolithic	solid; opening	non	8		80	standard	QSC; QSC one-side	cantilever	UTOK-1980a-2
	monolithic	solid; opening	non	9		80	restrained rotation	QSC	modified	UTOK-1980a-3
	monolithic	solid; window	non	44	0.067	10	shaking table	DYN	cantilever	CHUG-1984
	monolithic	solid	non	2	0.1	30	standard	QSC	cantilever	TOH-1984
	monolithic	solid	non; repair	5	0.25; 0.2	50; 60	standard	QSC	cantilever	TOH-1988
	monolithic	solid	non	1		100	restrained rotation	QSC	modified	EPDC-1989a-1
	monolithic	solid	non	1		100	restrained rotation	QSC	modified	EPDC-1989a-2
	monolithic	solid	non	3		330	joint rotation	QSC out-of-plane	modified	EPDC-1989a-3
	monolithic	solid	non	22		150	standard	QSC	cantilever	TEPC-1989

Table A.1 – RC wall test database (contd.)

PROGRAM ID	Country	Institute	References	SPECIMEN		
				Designation	Construction	Type (storey/bay/plane)
HAZ-1992	Japan	Hazama Co.	Nakachi et al., 1992	Specimen	civil	wall system (3/1/1)
TAK-1992	Japan	Takenaka RD Inst.	Katori et al., 1992	1B; 2N; 2B; 3B	civil	wall-frame system (1;2;3/1/1)
TCU-1992	Japan	Tokyo City Univ. Musashi Inst of Tech	Mochizuki, 1992	WPC	civil	wall system (1/1/1)
TODA-1992	Japan	Toda Co.	Chiba et al., 1992	WL	civil	wall-frame system (2/1/1)
YNU-1992	Japan	Yokohama Natl. Univ.	Kabeyasawa and Matsumoto, 1992	NW	civil	wall element
NUPEC-1995	Japan	NUPEC	Nagashima et al., 1995; Kitada et al., 1997	U	nuclear	wall element
CRIEPI-1996	Japan	Central Res Inst of El Pow Industry	Yabana et al., 1996	A; B; C; D	nuclear	wall element
HAZ-1996	Japan	Hazama Co.	Nakachi et al., 1996	Specimen	civil	wall system (3/1/1)
KOGA-1996	Japan	Kogakuin Univ.	Mochizuki et al., 1996	PCW	civil	wall-frame system (1/1/1)
MATSU-1996	Japan	Matsumura-Gumi Co.	Tatsuya, 1996	M; P; MW	civil	wall element
TAK-1996	Japan	Takenaka RD Inst.	Kimura and Sugano, 1996	W	civil	wall element
TCU-1996	Japan	Tokyo City Univ. Musashi Inst of Tech	Mochizuki, 1996	Specimen	civil	wall-frame system (3/1/1)
NUPEC-1999a-1	Japan	NUPEC	Kitada et al., 1988; Umeki et al., 2003	D	nuclear	wall component
NUPEC-1999a-2	Japan	NUPEC	Kitada et al., 2003		nuclear	wall system
NUPEC-1999a-3	Japan	NUPEC	Torita et al., 2004	DT	nuclear	wall system
MAEDA-2000	Japan	Maeda Co.	Hosokawa et al., 2000	Specimen; SAW	civil	wall-frame system (2/1/1)
TMUJ-2000	Japan	Tokyo Metropolitan Univ.	Kitsutaka and Oh-Oka, 2000	W	civil	wall-frame system (1/1/1)
TOKYU-2000	Japan	Tokyu Constr Co.	Iso et al., 2000	T; U; RC; CF; CFR; AF	civil	column wing-wall
TUSJ-2000	Japan	Sci Univ. of Tokyo	Sugiyama et al., 2000	Specimen	civil	wall-frame system (1/1/1)
KAJI-2002	Japan	Kajima Co.	Nagai et al., 2002	WS	civil	wall element
HOKU-2004	Japan	Hokkaido Univ.	Kitano et al., 2004	WA	civil	wall-frame system (1/1/1)

Table A.1 – RC wall test database (contd.)

							TEST SET-UP	LOADING	BOUNDARY cond.	PROGRAM ID
	Concrete techn.	Opening	Strengthening	No. of spec.	Scale mod/prot	Web thickness (mm)	type-N-V			
	monolithic	solid	non	5	0.2	60	standard	QSC	cantilever	HAZ-1992
	precast	solid	non	11	0.25	100	standard	QSC	cantilever	TAK-1992
	precast	solid	non; FRP connection	2		125	standard	QSC	cantilever	TCU-1992
	monolithic	solid	non	2	0.25	100	standard	QSC	modified	TODA-1992
	monolithic	solid	non	6	0.25	80	A-4-2	QSC	CL; RR	YNU-1992
	monolithic	solid	non	2		75	shaking table	DYN	cantilever	NUPEC-1995
	monolithic	solid	non	4		40	shaking table	DYN	cantilever	CRIEPI-1996
	monolithic	solid	non	4	0.125	90	standard	QSC	cantilever	HAZ-1996
	precast	solid	non	12		40; 50; 60	standard	QSC	cantilever	KOGA-1996
	monolithic	solid	non	5	0.33	80	A-8-6	QSC in-plane and out-of-plane	AM	MATSU-1996
	monolithic	solid	non	5		80	C-1-2	QSC	AM	TAK-1996
	precast	solid	non	7	0.125	35	standard	QSC	cantilever	TCU-1996
	monolithic	solid	non	12	0.2	200	panel tester	QSC	shear panel	NUPEC-1999a-1
	monolithic	solid	non	17		75	standard	QSC	cantilever	NUPEC-1999a-2
	monolithic	solid	non	3		75	shaking table	DYN	cantilever	NUPEC-1999a-3
	precast	solid; slitted	non	4		70	standard	QSC	cantilever	MAEDA-2000
	M/P	solid	non; frame infill upgrade	5	0.33	60	standard	QSC	cantilever	TMUJ-2000
	monolithic	n/a	non; FRP-EBR	15		75	B-4-2	QSC	RR	TOKYU-2000
	monolithic	solid; door; window; frame	non; FRP-EBR	10	0.33	40	standard	QSC	cantilever	TUSJ-2000
	monolithic	solid	non	3		50; 75	A-1-2	QSC	CL	KAJI-2002
	monolithic	door; window	non; FRP-EBR	3	0.33	70	standard	QSC	cantilever	HOKU-2004

Table A.1 – RC wall test database (contd.)

PROGRAM ID	Country	Institute	References	SPECIMEN Designation	Construction	Type (storey/bay/plane)
KYO-2004	Japan	Kyoto Univ.	Sakashita et al., 2004	FLB	civil	wall-frame-foundation system (2/1/1)
NIED-2004	Japan	NIED Tsukuba	Matsui et al., 2004	Wall	civil	wall-frame system
KYO-2005	Japan	Kyoto Univ.	Kono et al., 2005	MNW; PCW	civil	wall-frame-foundation system (3/1/1)
NIED-2005	Japan	NIED Tsukuba	Kuramoto et al., 2005	Wall	civil	wall-frame system (2/1/1)
UFUK-2005	Japan	Univ. of Fukui	Kobayashi, 2005	W; specimen	civil	wall-frame system (1/1/1)
KYO-2008	Japan	Kyoto Univ.	Warashina et al., 2008; Wang et al., 2010; Taleb and Kono, 2010;	N; S; M; L	civil	wall-frame system (3/1/1)
URYU-2008	Japan	Univ. of Ryukyus	Takara et al., 2008	R	civil	wall-frame system (1/1/1)
HYU-2002	Korea S	Hanyang Univ.	Oh et al., 2002	WR; WB	civil	wall element
IZIIS-1984a	Macedonia	IZIIS Skopje	Simeonov, 1984	DFM	civil	wall system (3/1/1)
IZIIS-1992	Macedonia	IZIIS Skopje	Simeonov, 1992	C	civil	wall-frame-slab system (n/a)
IZIIS-1996	Macedonia	IZIIS Skopje	Bozinovski, 1996	FKPZ-M	civil	wall system (2/1/1)
IZIIS-1984b	Macedonia-USA	IZIIS Skopje	Velkov et al., 1984	PZ	civil	wall system (3/1/1)
UNAM-2008a-1	Mexico	UNAM	Carillo and Alcocer, 2008; Carillo, 2010;	MCN; MCC	civil	wall element
UNAM-2008a-2	Mexico	UNAM	Carillo and Alcocer, 2008; Carillo, 2010;	MCN; MCC	civil	wall element
UCNZ-1969	New Zealand	Univ. of Canterbury	Paulay, 1969	Beam	civil	wall component
UCNZ-1982	New Zealand	Univ. of Canterbury	Paulay et al., 1982	Wall	civil	wall element
UCNZ-1992	New Zealand	Univ. of Canterbury	Yanez et al., 1992	S	civil	wall system (3/1/1)
UCNZ-2007	New Zealand	Univ. of Canterbury	Ireland et al., 2006, 2007; Kam and Pampanin, 2008;	W	civil	wall element
CISMID-2009	Peru	CISMID Lima	Higa et al., 2009	MQE; MFIEN	civil	wall element
LNEC-2000	Portugal-EU	LNEC Lisbon	Elnashai et al., 2000	SW	civil	wall element

Table A.1 – RC wall test database (contd.)

							TEST SET-UP	LOADING	BOUNDARY cond.	PROGRAM ID
	Concrete techn.	Opening	Strengthening	No. of spec.	Scale mod/prot	Web thickness (mm)	type-N-V			
	monolithic	solid	non	2	0.2	60	pin supports	QSC	modified additional moment	KYO-2004
	monolithic	solid	non	2	0.33	80	shaking table	DYN	cantilever	NIED-2004
	M/P	solid; slitted filled	non	2	0.15	50	pin supports	QSC	modified additional moment	KYO-2005
	monolithic	solid	non	2	0.33	80	standard	QSC	modified	NIED-2005
	monolithic	solid	non; FRP-EBR	6		40	standard	QSC	cantilever	UFUK-2005
	monolithic	solid; door	non	5	0.4	80	standard	QSC	modified	KYO-2008
	monolithic	solid	non; SP-E	5		60; 175	standard	QSC	cantilever	URYU-2008
	monolithic	solid	non	4	full	200; 125	C-4-2	QSC	AM	HYU-2002
	precast	solid	non	5			standard	QSC	cantilever	IZIIS-1984a
	monolithic			1	0.1			QSC		IZIIS-1992
	precast	solid	non	4	0.5	80	standard	QSC	cantilever	IZIIS-1996
	precast	solid; door	non	6	0.33	50	standard	QSC	cantilever	IZIIS-1984b
	monolithic	solid; door; window	non	35	0.8	80	A-0-2	QSC	CL	UNAM-2008a-1
	monolithic	solid; door; window	non	4	0.8	80	shaking table	DYN	cantilever	UNAM-2008a-2
	monolithic	n/a	non		large	150		QSC	modified	UCNZ-1969
	monolithic	solid	non	4	near-full	100	A-0-2	QSC	CL	UCNZ-1982
	monolithic	solid; door; window	non	6	0.33	120	standard	QSC	cantilever	UCNZ-1992
	monolithic	solid; slitted	non; selective weakening; FRP-EBR	4	0.66	100; 125	A-n/a-2	QSC	CL	UCNZ-2007
	monolithic	solid	non	7	full	120	A-n/a-2	QSC	n/a	CISMID-2009
	monolithic	solid	non; repair; upgrade	8	0.66	120	shaking table	DYN	cantilever	LNEC-2000

Table A.1 – RC wall test database (contd.)

PROGRAM ID				SPECIMEN		
	Country	Institute	References	Designation	Construction	Type (storey/bay/plane)
LNEC-2005	Portugal-EU	LNEC Lisbon	Bisch and Coin, 2005, 2007	ECOLEADER	civil	wall system
INCC-1992	Romania	INCERC Cluj	Maniu et al., 1992	Unit	civil	wall-frame-slab system (5/1/2)
UPT-1992	Romania	Politehnica Univ. of Timisoara	Ianca, 1992		civil	wall system (4/1/1)
INCT-1998	Romania	INCERC Timisoara	Mirean, 1998	M; F	civil	wall system (3/1/1)
UPT-2005	Romania	Politehnica Univ. of Timisoara	Nagy-Gyorgy et al., 2005, 2007	SW; RW	civil	wall system (4/1/1)
UTCB-2007	Romania	Technical Univ. of Civil Eng Bucharest	Pavel et al., 2007	W	civil	wall system (2/1/1)
UPT-2010	Romania	Politehnica Univ. of Timisoara	Demeter et al., 2010	PRCWP	civil	wall element
UPT-2011	Romania	Politehnica Univ. of Timisoara	Dan et al., 2011	CSRCW	civil	wall system (3/1/1)
IMS-1996	Serbia	IMS Belgrade	Dimitrijevic, 1996	SW	civil	wall-frame system (3/1/1)
NTUSG-2010	Singapore	Nanyang Tech. Univ.	Li and Lim, 2010		civil	wall element
ZATL-1996	Slovenia	ZAT Ljubljana	Tomazevic et al., 1996	SW	civil	wall element
ETH-1999a	Switzerland	ETH Zurich	Dazio et al., 1999; Bachmann, 2000	WSH	civil	wall system (6/1/1)
ETH-1999b	Switzerland	ETH Zurich	Thiele et al., 1999; Bachmann, 2000;		civil	wall system
ETH-2000	Switzerland	ETH Zurich	Bachmann, 2000; Lestuzzi, 2002; Lestuzzi and Badoux; 2003a, 2003b; Lestuzzi and Bachmann, 2007;	WDH	civil	wall system
EPFL-2005	Switzerland	EPFL Lausanne	Greifenhagen and Lestuzzi, 2005; Greifenhagen et al., 2005	M	civil	wall element
NCKU-1988	Taiwan	Nat. Cheng Kung Univ. Tainan	Huang and Sheu, 1988	SWN	civil	wall element
NCKU-1996a-1	Taiwan	Nat. Cheng Kung Univ. Tainan	Sheu et al., 1996	SSW	civil	wall element
NCKU-1996a-2	Taiwan	Nat. Cheng Kung Univ. Tainan	Sheu et al., 1996	SSW	civil	wall-frame system (1;2/1/1)
NCKU-1998	Taiwan	Nat. Cheng Kung Univ. Tainan	Mo and Kuo, 1998	H	civil	wall element

Table A.1 – RC wall test database (contd.)

							TEST SET-UP	LOADING	BOUNDARY cond.	PROGRAM ID
	Concrete techn.	Opening	Strengthening	No. of spec.	Scale mod/prot	Web thickness (mm)	type-N-V			
	monolithic	door	non	2	0.33	60	shaking table	DYN	cantilever	LNEC-2005
	precast	solid	non	1	0.4	60	standard	QSC	cantilever	INCC-1992
	monolithic	door	non	9	0.36		standard	QSC	cantilever	UPT-1992
	precast	solid	non	6	0.5	160	standard	QSC	cantilever	INCT-1998
	monolithic	solid; door	non; FRP-EBR	5	0.25	80	standard	QSC; QSM	cantilever	UPT-2005
	monolithic	solid	non	5	0.25	100	restrained rotation	QSC	modified	UTCB-2007
	precast	solid; door cut-out	non; FRP-EBR	5	0.83	100	A-2-2	QSC	RR	UPT-2010
	monolithic	solid	non; FRP-EBR	6	0.33	100	standard	QSC	cantilever	UPT-2011
	precast	solid	non; repair	2	0.5	70	standard	QSC	cantilever	IMS-1996
	monolithic		FRP-EBR	4						NTUSG-2010
	monolithic	solid	non	10	0.33	50	A-2-2	QSC	modified	ZATL-1996
	monolithic	solid	non	6	0.5	150	standard	QSC	cantilever	ETH-1999a
	monolithic			3	0.33			PSD		ETH-1999b
	monolithic	solid	non	6	0.33	100	shaking table	DYN	cantilever	ETH-2000
	monolithic	solid	non	4	0.33	80; 100	A-1-2	QSC	CL	EPFL-2005
	monolithic	solid	non	30		100	A-n/a-2	QSC	CL	NCKU-1988
	monolithic	slitted	frame infill			100	A-n/a-4	QSC	CL	NCKU-1996a-1
	monolithic	slitted	frame infill			70	standard	QSC	cantilever	NCKU-1996a-2
	monolithic	solid	non	4	0.125	30	shaking table	DYN	cantilever	NCKU-1998

Table A.1 – RC wall test database (contd.)

PROGRAM ID				SPECIMEN		
	Country	Institute	References	Designation	Construction	Type (storey/bay/plane)
NCREE-2004a-1	Taiwan	NCREE Taipei	Liao et al., 2004	STB; STN	civil	wall element
NCREE-2004a-2	Taiwan	NCREE Taipei	Liao et al., 2004	LB; LN	civil	wall element
NCREE-2004b	Taiwan	NCREE Taipei	Hwang et al., 2004a, 2004b, 2004c	PF; WF	civil	wall-frame system (1/1/1)
NCREE-2006	Taiwan	NCREE Taipei	Chiou et al., 2006	PMLL; PMLH; PMHL	civil	wall element
YTIT-2010	Taiwan	Yung-Ta Institute of Technology	Liu et al., 2010	CW	civil	column wing-wall
CHULA-2001	Thailand	Chulalongkorn Univ.	Sittipunt et al., 2001	W	civil	wall element
ICL-1990	UK	Imperial College	Lefas et al., 1990; Lefas and Kotsovos, 1990;	SW	civil	wall element
ICL-1993a-1	UK	Imperial College	Elnashai et al., 1988, 1990;	SW	civil	wall element
ICL-1993a-2	UK	Imperial College	Pilakoutas and Elnashai, 1993, 1995a, 1995b; Elnashai et al., 1988, 1990;	SW	civil	wall element
ICL-1993a-3	UK	Imperial College	Pilakoutas and Elnashai, 1993, 1995a, 1995b; Elnashai et al., 1988, 1990;	SW	civil	wall element
ICL-1998	UK	Imperial College	Elnashai and Pinho, 1998		civil	wall element
ICL-2001	UK-Portugal	Imperial College and IST Lisbon	Lopes, 2001	SW	civil	wall element
STFU-1958	USA	Stanford Univ.	Benjamin and Williams, 1958	H; HII; HR; VRR	civil	wall element
PCA-1974	USA	PCA Skokie	Cardenas and Magura, 1973; Cardenas, 1974; Corley et al., 1983	SW	civil	wall system (7/1/1)
PCA-1976	USA	PCA Skokie	Barda et al., 1973, 1974, 1976; Corley et al., 1983;	B	civil	wall element
UILLI-1977b	USA	Univ. of Illinois	Sozen et al., 1977	D	civil	wall system
PCA-1980	USA	PCA Skokie	Barney et al., 1980	C	civil	wall component
PCA-1981	USA	PCA Skokie	Oesterle et al., 1977, 1980, 1984; Fiorato et al., 1977, 1983; Corley et al., 1981, 1983;	R; B; F	civil	wall system (5/1/1)

Table A.1 – RC wall test database (contd.)

							TEST SET-UP	LOADING	BOUNDARY cond.	PROGRAM ID
	Concrete techn.	Opening	Strengthening	No. of spec.	Scale mod/prot	Web thickness (mm)	type-N-V			
←	monolithic	solid	non	2		85	shaking table	DYN	modified	NCREE-2004a-1
	monolithic	solid	non	2		120	A-0-2	QSC	CL	NCREE-2004a-2
	monolithic	solid; frame	non; FRP-EBR	6	0.6	120; 150	standard	QSC	cantilever	NCREE-2004b
	precast	solid	frame infill	9	large	100	A-2-2	QSC	RR	NCREE-2006
	monolithic	n/a	non; wing-wall	10		100; 150	A-2-2	QSC	RR	YTIT-2010
	monolithic	solid	non	4	near-full	100	A-0-2	QSC	CL	CHULA-2001
	monolithic	solid	non; repair	17	0.42	70	A-1-2	QSC; QSM	CL	ICL-1990
	monolithic	solid	non	1	0.2	32	shake-table	DYN	cantilever	ICL-1993a-1
	monolithic	solid	non	2	0.2	32	A-0-2	QSC	CL	ICL-1993a-2
	monolithic	solid	non	6	0.4	60	A-0-2	QSC	CL	ICL-1993a-3
	monolithic	solid	non; SP-EBR		0.4	60	A-0-2	QSC	CL	ICL-1998
	monolithic	solid	non	8		45	B-0-2	QSC	RR	ICL-2001
	monolithic	solid; door; window	non	21	0.25	50	A-0-1	QSM	CL	STFU-1958
	monolithic	solid	non	13	0.25	75	standard	QSM	cantilever	PCA-1974
	monolithic	solid	non; repair	8	0.33	100	A-0-2	QSC; QSM	CL	PCA-1976
	monolithic	door	non	9	small	25	shaking table	DYN	cantilever	UILLI-1977b
	monolithic	n/a	non	8	0.33	90		QSC	modified	PCA-1980
	monolithic	solid	non; repair	16	0.33	100	standard	QSC; QSM	cantilever	PCA-1981

Table A.1 – RC wall test database (contd.)

PROGRAM ID	Country	Institute	References	SPECIMEN		
				Designation	Construction	Type (storey/bay/plane)
PCA-1982	USA	PCA Skokie	Shiu et al., 1982; Corley et al., 1983;		civil	wall system (6/1/1)
PCA-1984a	USA	PCA Skokie	Shiu et al., 1984; Corley et al., 1983;	CS; RCS	civil	wall system (6/1/1)
WSU-1984	USA	Wayne State Univ.	Tebbe and Aktan, 1984	Specimen	civil	wall component
LANL-1991a-1	USA	Los Alamos Nat. Lab.	Farrar and Bennett, 1989; Farrar and Baker, 1990; Farrar et al., 1991;	TRG	nuclear	wall element
LANL-1991a-2	USA	Los Alamos Nat. Lab.	Farrar and Bennett, 1989; Farrar and Baker, 1990; Farrar et al., 1991;	TRG	nuclear	wall element
BFRL-1996	USA	NIST BFRL	Magana and Schultz, 1996	GSS; PTT	civil	wall element
CLARK-1996	USA	Clarkson Univ.	Taylor et al., 1996, 1998; Thomsen and Wallace, 2004; Massone and Wallace, 2004; Orakcal and Wallace, 2006	RW; BW; TW	civil	wall system (4/1/1)
UCI-2000	USA	Univ. of California Irvine	Haroun et al., 2000	LU; LP; LN; HU; HP; HN	civil	wall element
UHTX-2002	USA	Univ. of Houston	Hsu and Mansour, 2002	CA; CE	civil	wall component
UCB-2003	USA	Univ. of California Berkeley	Mosalam et al., 2003	Panel	civil	wall component
UUTAH-2003	USA	Univ. of Utah	Volnyy and Pantelides, 1999; Pantelides et al., 2003; McMullin et al., 2003;	Specimen; wall assembly	civil	wall system (1/1/1)
UMICH-2004	USA	Univ. of Michigan	Parra-Montesinos and Kim, 2004	Specimen	civil	wall element
UCLA-2008	USA	Univ. of California Los Angeles	Orakcal et al., 2008, 2009	WP; WS	civil	wall element
UMICH-2011	USA	Univ. of Michigan	Olsen and Billington, 2011	P; V; Taper; Control	civil	wall component
UILLI-1977a	USA-Canada	Univ. of Illinois	Otani, 1977	F; W	civil	wall-frame system
PCA-1984b-1	USA-Japan	PCA Skokie	Morgan et al., 1984	wall frame	civil	wall-frame system
PCA-1984b-2	USA-Japan	PCA Skokie	Morgan et al., 1984	isolated wall	civil	wall system (5/1/1)
UCB-1984	USA-Yugoslavia	Univ. of California Berkeley	Oliva and Shahrooz, 1984	SOLID; FLANGED	civil	wall system
unknown			Asfa, 2010			

Table A.1 – RC wall test database (contd.)

							TEST SET-UP	LOADING	BOUNDARY cond.	PROGRAM ID
	Concrete techn.	Opening	Strengthening	No. of spec.	Scale mod/prot	Web thickness (mm)	type-N-V			
	monolithic	solid; window	non	2			standard	QSC	cantilever	PCA-1982
	monolithic	door	non; repair	1	0.33	100	standard	QSC	cantilever	PCA-1984a
	monolithic	n/a	non	32	0.33	100	double L frames	QSC	shear line	WSU-1984
	monolithic	solid	non	9	0.33	25; 100; 150	standard	QSC; QSM	cantilever	LANL-1991a-1
	monolithic	solid	non	7	0.33	50	shaking table	DYN	cantilever	LANL-1991a-2
	precast	solid	non	2	n/a	150	A-4-2	QSC	AM	BFRL-1996
	monolithic	solid; door	non	6	0.25	100	standard	QSC	cantilever	CLARK-1996
	monolithic	solid	non; repair	6	0.5	250	A-2-2	QSC out-of-plane	CL	UCI-2000
	monolithic	solid	non	15	full	180	panel tester	QSC	shear panel	UHTX-2002
	monolithic	solid	non; confining through-rods	14	n/a	460	universal testing machine	QSM	in-plane splitting	UCB-2003
	precast	solid	FRP-EBR connection upgrade	9	near-full	200	pin supports	QSC	shear line	UUTAH-2003
	monolithic	solid	non	2	near-full	100	A-0-2	QSC	CL	UMICH-2004
	monolithic	solid	non	14	0.75	150	B-4-2	QSC	RR	UCLA-2008
	precast	solid	frame infill	6	0.66	70	standard	QSC	cantilever	UMICH-2011
	monolithic	solid	non	4	n/a	25	shaking table	DYN	cantilever	UILLI-1977a
	monolithic	solid	non	1	0.29		standard	PSD	cantilever	PCA-1984b-1
	monolithic	solid	non	1	0.33		standard	QSC	cantilever	PCA-1984b-2
	precast	solid; door	non	3	0.33		shaking table	DYN	cantilever	UCB-1984
			FRP							unknown

Appendix B FRP strengthening layouts

The strengthening layout of the specimen PRCWP 3-S/E1-T/R is depicted in Figure B.1. Before strengthening the specimen was repaired. The S1-type flexural strips (f) were posed horizontally (f1 and f2) and vertically (f3) on the spandrel beam and on the piers along the opening, respectively. The shear strips (sh) were aligned parallel to the shear forces, i.e. horizontally on the piers (sh1 and sh2) and vertically on the spandrel beam (sh3 and sh4). At the opening side the sh1 and sh2 S1-type strips from one face of the piers overlapped their counterparts from the other face, so as to serve as anchorage and confinement. For the shear strengthening of the spandrel beam the S2-type strips were shaped similarly to the conventional stirrups. The sh3 and sh4 strips were closed by CFRP tows referred to as through-wall anchorages, being pulled through holes previously drilled in the wall, similar to the cross tie steel reinforcements (C/U ties and H ties). For confinement (c) purposes the same stirrup-like strips (c1 and c2) and two other configurations (c3 and c5) were employed at the opening-side pier corners, at the upper part of the piers and at the top and bottom of the wing walls. The material consumption of the strengthening was comprised of 6.35 m^2 CF-fabric and 10.5 kg epoxy resin for the S1 FRP, and 3.64 m^2 CF-fabric and 6.82 kg epoxy resin for the S2 FRP.

The strengthening layout of the specimen PRCWP 5-S/E3-T/R is depicted in Figure B.2. Before strengthening the specimen was repaired. The long flexural strips (f) were placed alongside the opening outline (f1 and f3) and along the upper edge of the spandrel beam (f2), while a second layer of shorter strips were added around the opening corners (f4, f5 and f6). By this time, as opposed to the previous wall, the flexural strips at the base of the piers were anchored to the foundation. For this purpose two anchoring solutions were employed on the two piers, namely with bolted steel angles on pier#1 and with CFRP tows on pier#2. These will be discussed later in a subsequent section of strengthening details. The shear strengthening of the piers consisted in S1-type U-shaped strips oriented horizontally (sh1) whilst on the spandrel beam vertical S2-strips (sh2 and sh3) were used in a similar fashion as the conventional steel hoops with open legs at the middle of the span and closed by through-wall CFRP-tows or overlapping legs at the extremities. The confinement was carried out using exclusively S2-type strips. At the piers' inside toes the legs of the hoop-like strips (c2) were connected, in addition to the end ties, at their mid-length by the through-wall H cross-tie CFRP tows while for the strips at the upper part of the piers (c1 and c2) this additional confinement was realised through orthogonal strips (c4). The pier to beam connection region was confined with these orthogonal strips (c3 and c4) having two independent legs and a series of cross-ties. The upper and bottom part of the wing walls was confined with the 100 mm wide c5-strips. The material consumption of the strengthening was comprised of 3.87 m^2 CF-fabric and 7.3 kg epoxy resin for the S1 FRP, and 1.52 m^2 CF-fabric and 4.1 kg epoxy resin for the S2 FRP.

The strengthening layout of the specimen PRCWP 4-S/E1-R/T is depicted in Figure B.3. This specimen was prior-to-damage strengthened. Except the cross-tie tows and the wing confinement (c5) the externally bonded reinforcements were S1 CF-sheets. The flexural strips (f) were arranged around the opening in the following

manner: continuous horizontal (f1 and f2) and vertical (f3) strips; additional second layer of shorter strips (f4, f5 and f6); and inclined strips (f7) at the upper corners of the openings. At the base of the piers the vertical f3 and f6 strips were anchored to the foundation with CFRP tows, which will be presented later in this section. The shear strips (sh) were disposed horizontally on the piers (sh1 to sh4) and vertically on the spandrel beam (sh3) so as to be parallel with the local shear forces. The horizontal sh1 and sh2 bands were anchored at their ends by overlapping with the U-shaped sh3 strips on the opening-side edges and by short tows with one inclined leg at the wing-side ends. On the spandrel the hoop-like sh3 strips were closed by cross-ties. CFRP confinement was provided at the inside toes of both piers and the outer toe of pier#2, at the pier-to-beam connection regions, along the upper edge of the wall panel and at the ends of the wing walls. The c1 confinement strips at the piers' bases were similar to the sh3 strips from the spandrel with additional cross-ties at the middle of their legs. The c2 stripes had 300 mm width of which the bottom 100 mm was overlapping the c1 strips. At the pier to beam connection an orthogonal configuration was realised of the c1, c3 and c4 strips. The c3 stripes were disposed along the upper edge of the piers while the outer corners of pier#2 were confined with an H-form c3 and c4 stripe arrangement. The wing ends were confined with the 100 mm wide S2-type c5 strips. The material consumption of the strengthening was comprised of 7.83 m^2 CF-fabric and 10 kg epoxy resin for the S1 FRP, and 1 m^2 CF-fabric and 2.55 kg epoxy resin for the S2 FRP.

The strengthening layout of the specimen PRCWP 6-S/E3-R/T is depicted in Figure B.4. This specimen was prior-to-damage strengthened. The CF-sheets were of the S1-type with the exception of the cross ties and the wing confinement. The flexural strips bounded continuously the opening (f1 and f3) while additional shorter strips were placed around the opening corners horizontally (f4), vertically (f5 and f6) and inclined (f7). The f2 continuous strips were placed along the upper edge of the wall. The vertical CFRPs at the base (f3 and f6) and the horizontal f1 strips were anchored to the base beam and to the wing walls, respectively. For shear strengthening U-shaped strips were used parallel to the local shear forces, that is, horizontally on the piers (sh1) and vertically on the spandrel (sh2). The ends of the sh1 strips were anchored to the wings and at the mid of the legs cross tie tows were provided, while on the spandrel open-leg CFRP-hoops were used in the mid-span and closed ones at the extremities. The confinement strengthening of the specimen consisted in horizontal CFRP-hoops (c1 and c2) at the piers' inside toes, a grid-like orthogonal layout with cross tie tows at the pier-to-beam connection and the S2-type c5 strips at the wing ends. Note that at the pier-toes the bottom 100 mm is confined by two layers of S1 CFRP while at the upper part, next to the opening corners only one layer of c1 confinement is provided. The material consumption of the strengthening was comprised of 6.15 m^2 CF-fabric and 9.4 kg epoxy resin for the S1 FRP, and 1.14 m^2 CF-fabric and 3.04 kg epoxy resin for the S2 FRP.

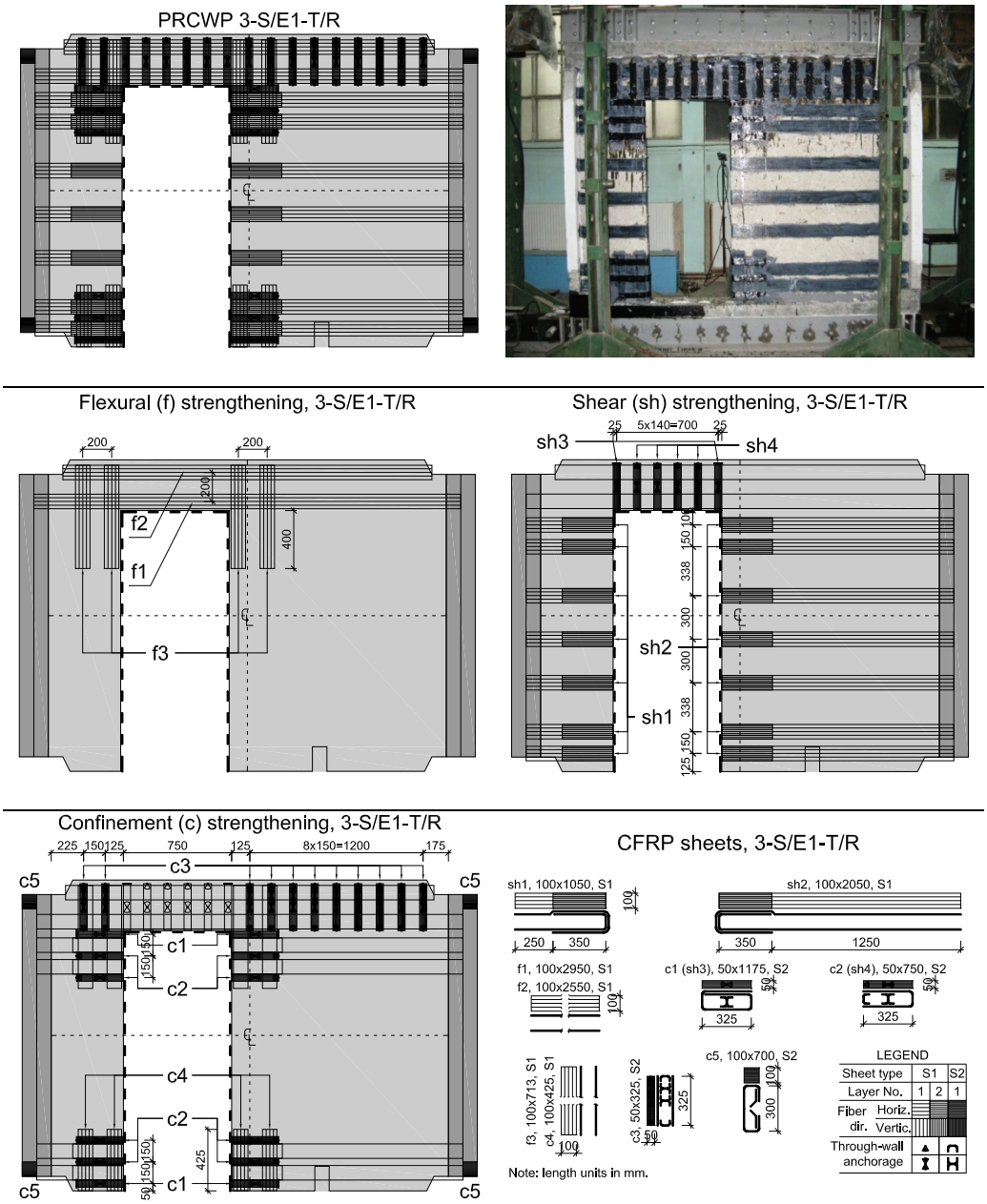

Figure B.1 FRP layout for the PRCWP 3-S/E1-T/R specimen

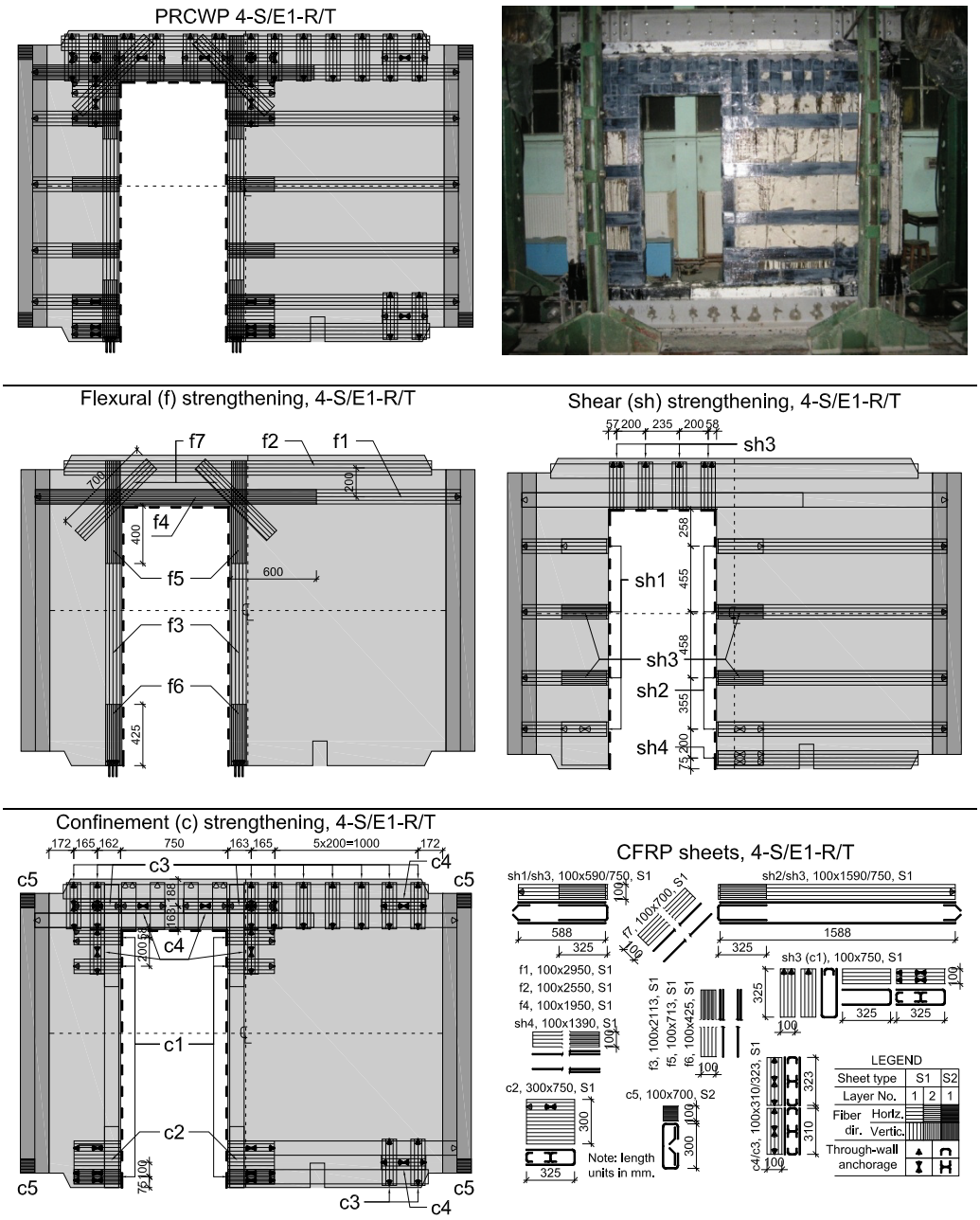

Figure B.2 FRP layout for the PRCWP 4-S/E1-R/T specimen

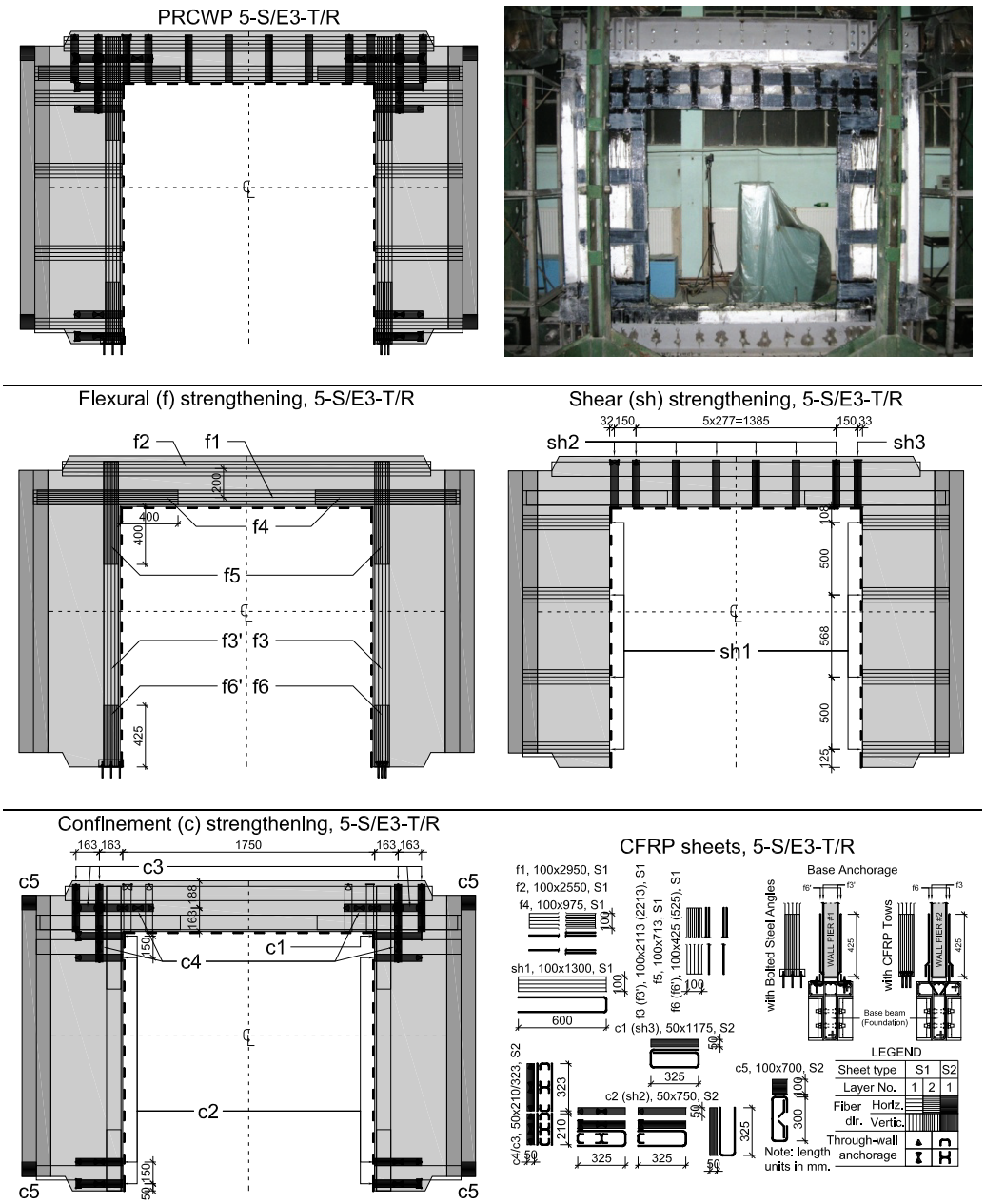

Figure B.3 FRP layout for the PRCWP 5-S/E3-T/R specimen

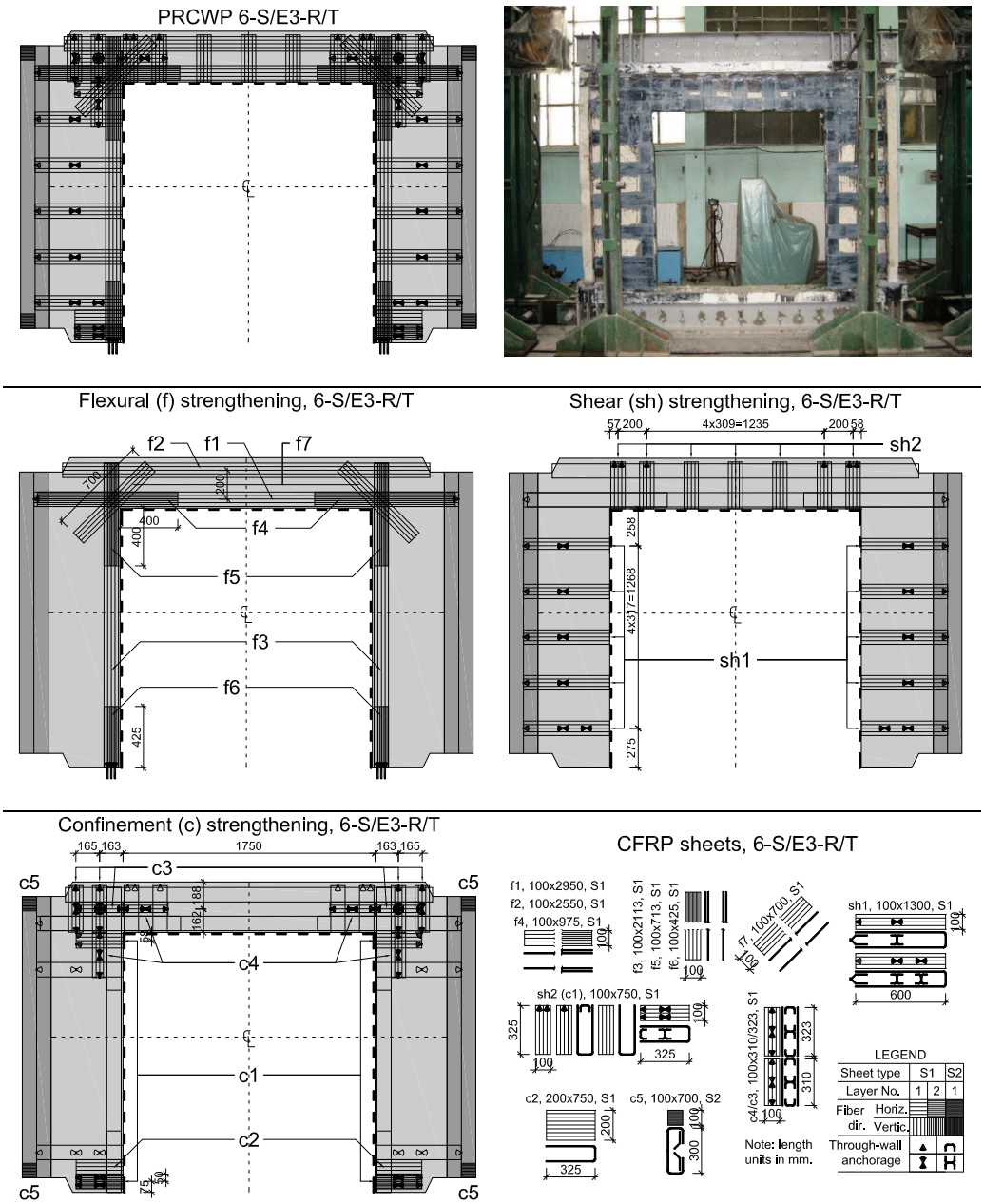

Figure B.4 FRP layout for the PRCWP 6-S/E3-R/T specimen

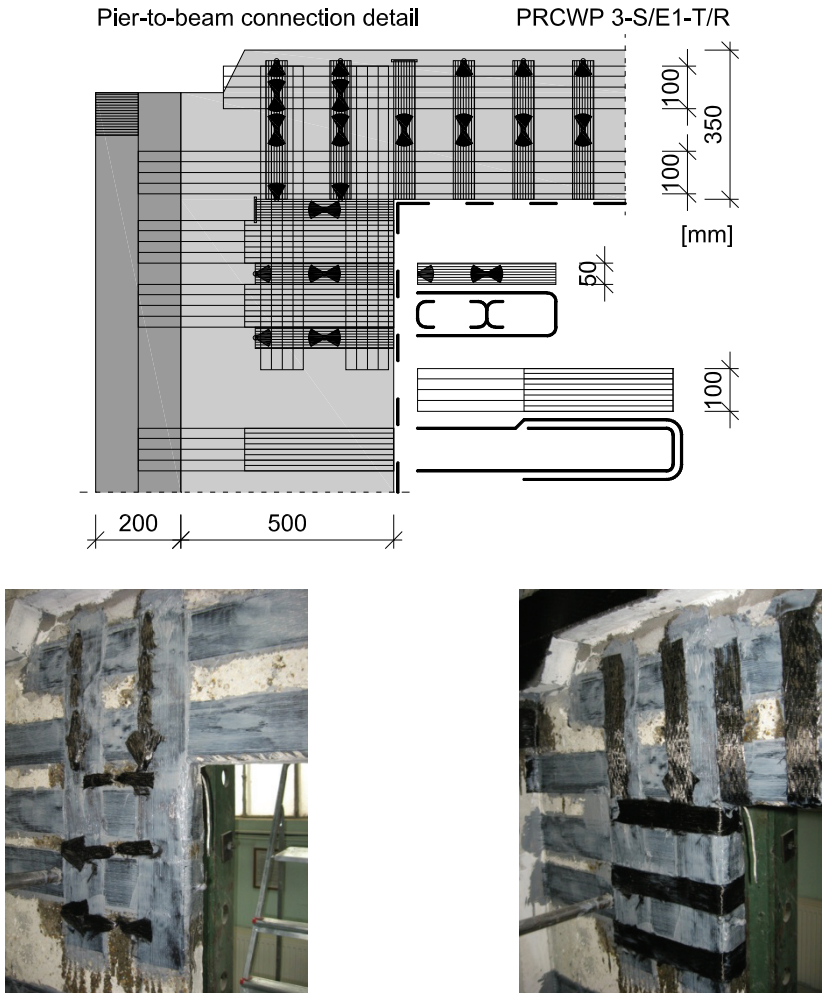

Figure B.5 FRP layout detail at the pier-to-beam connection of PRCWP 3-S/E1-T/R

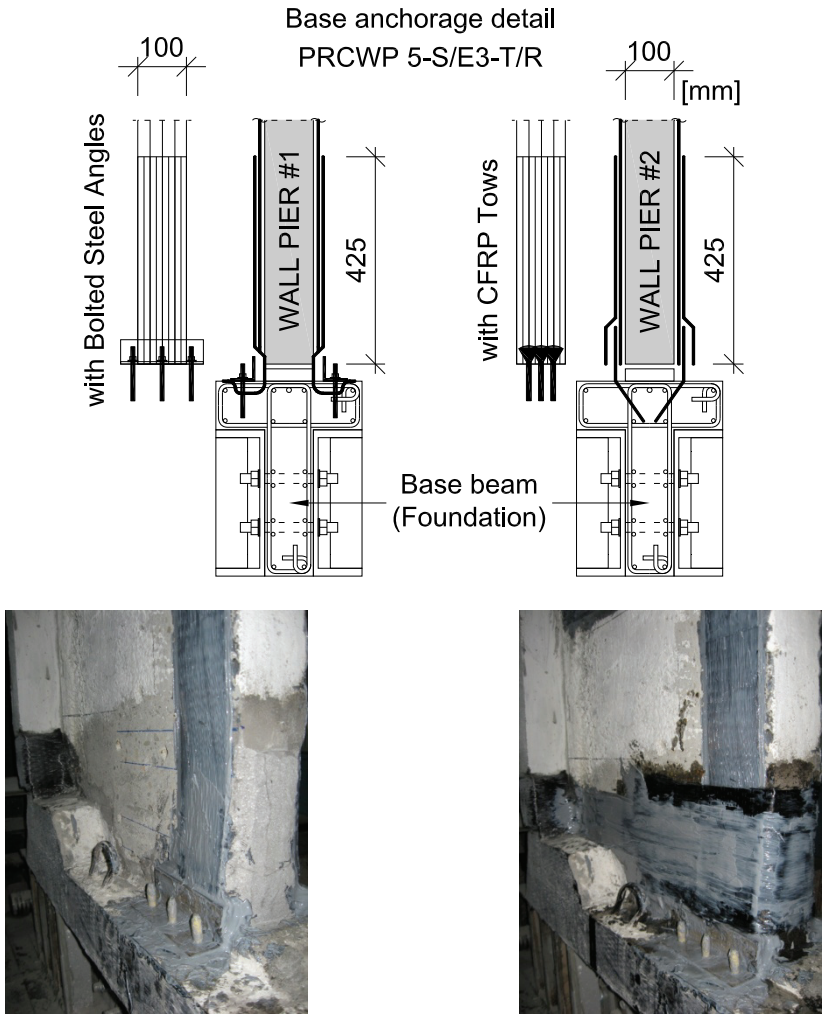

Figure B.6 FRP layout detail at the base anchorage of PRCWP 5-S/E3-T/R

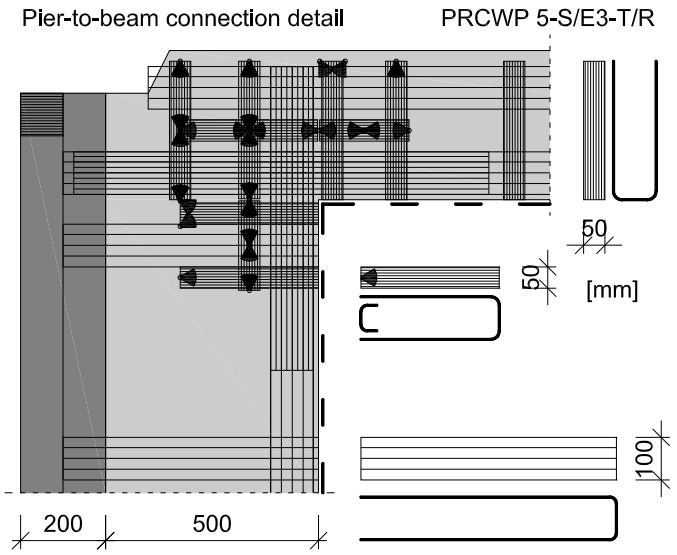

Figure B.7 FRP layout detail at the pier-to-beam connection of PRCWP 5-S/E3-T/R

Appendix C Instrumentation list

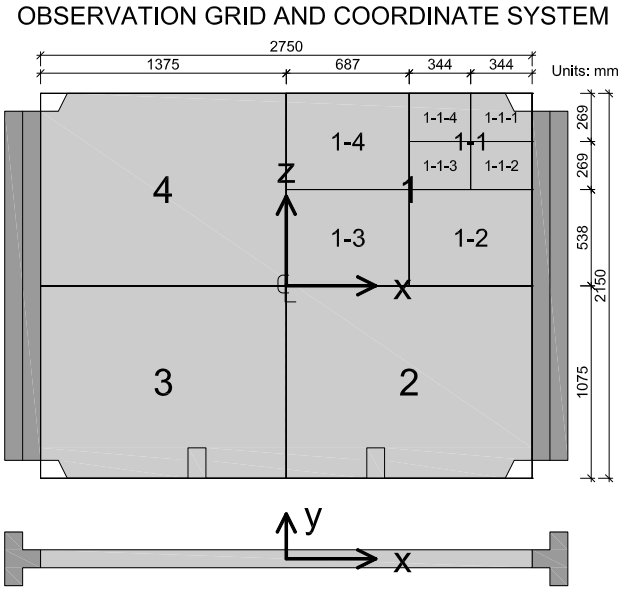

Figure C.1 Grid zonation of the experimental specimen

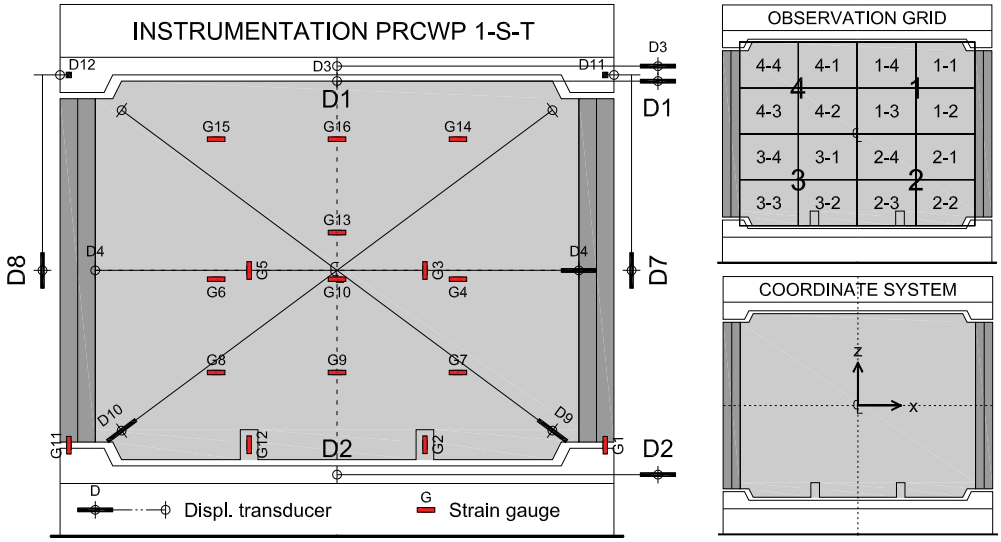

Figure C.2 Instrumentation layout of specimen PRCWP 1-S-T

Table C.1 Sensor list for specimen PRCWP 1-S-T

ID	Type	Location	x (mm)	y (mm)	z (mm)
D1	Displacement, top horizontal	1-4; 4-1	0	50	1075
D2	Displacement, bottom horizontal	Base beam	0	150	-1160
D3	Displacement, top horizontal	Cap beam	0	150	1160
D4 start	Displacement, mid horizontal	1-2	1375	50	0
D4 end		4-3	-1375	50	0
D7	Displacement, vertical	Cap beam	1575	0	1110
D8	Displacement, vertical	Cap beam	-1575	0	1110
D9 start	Displacement, diagonal	2-2	1225	50	-910
D9 end		4-4	-1225	50	910
D10 start	Displacement, diagonal	3-3	-1225	50	-910
D10 end		1-1	1225	50	910
D11	Displacement, out-of-plane	Cap beam	1525	-150	1110
D12	Displacement, out-of-plane	Cap beam	-1525	-150	1110
G1	Strain gauge, vertical steel rebar	Wing base	1525	0	-990
G2	Strain gauge, vertical steel rebar	2-3	500	0	-990
G3	Strain gauge, vertical steel rebar	1-3	500	0	0
G4	Strain gauge, horizontal steel rebar	2-4	688	0	-50
G5	Strain gauge, vertical steel rebar	4-2	-500	0	0
G6	Strain gauge, horizontal steel rebar	3-1	-688	0	-50
G7	Strain gauge, horizontal steel rebar	2-2	688	0	-580
G8	Strain gauge, horizontal steel rebar	3-2	-688	0	-580
G9	Strain gauge, horizontal steel rebar	2-3	0	0	-580
G10	Strain gauge, horizontal steel rebar	2-4	0	0	-50
G11	Strain gauge, vertical steel rebar	Wing base	-1525	0	-990
G12	Strain gauge, vertical steel rebar	3-2	-500	0	-990
G13	Strain gauge, horizontal steel rebar	1-3	0	0	215
G14	Strain gauge, horizontal steel rebar	1-1	688	0	745
G15	Strain gauge, horizontal steel rebar	4-1	-688	0	745
G16	Strain gauge, horizontal steel rebar	1-4	0	0	745
P1	Pressure, lateral load V	Hydraulic line	n/a		
P2	Pressure, axial load N1	Hydraulic line	n/a		
P3	Pressure, axial load N2	Hydraulic line	n/a		

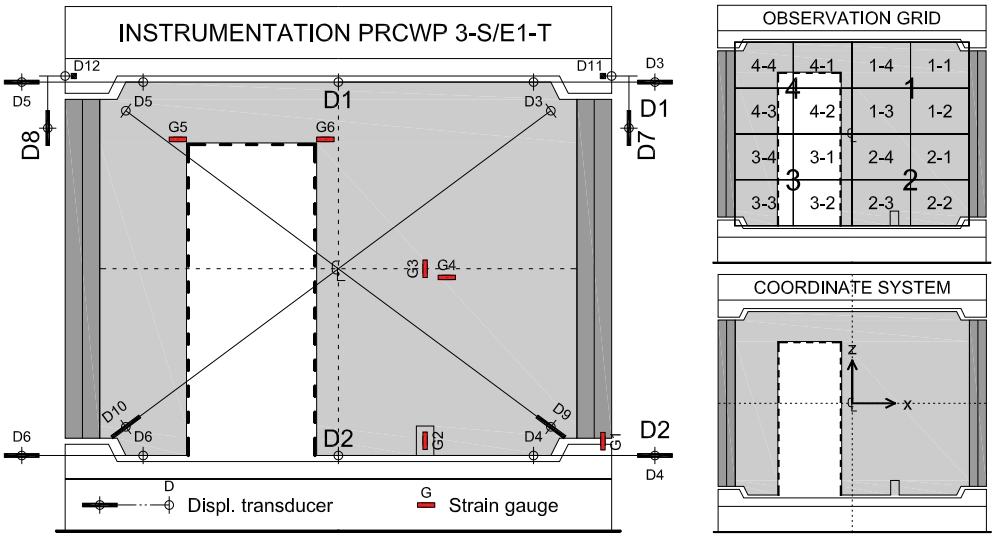

Figure C.3 Instrumentation layout of specimen PRCWP 3-S/E1-T

Table C.2 Sensor list for specimen PRCWP 3-S/E1-T

ID	Type	Location	x (mm)	y (mm)	z (mm)
D1	Displacement, top horizontal	1-4	0	50	1075
D2	Displacement, bottom horizontal	2-3	0	50	-1075
D3	Displacement, top horizontal	1-1	1125	50	1075
D4	Displacement, bottom horizontal	2-2	1125	50	-1075
D5	Displacement, top horizontal	4-4	-1125	50	1075
D6	Displacement, bottom horizontal	3-3	-1125	50	-1075
D7	Displacement, vertical	Cap beam	1575	0	1110
D8	Displacement, vertical	Cap beam	-1575	0	1110
D9 start	Displacement, diagonal	2-2	1225	50	-910
D9 end		4-4	-1225	50	910
D10 start	Displacement, diagonal	3-3	-1225	50	-910
D10 end		1-1	1225	50	910
D11	Displacement, out-of-plane, dial gauge	Cap beam	1525	-150	1110
D12	Displacement, out-of-plane, dial gauge	Cap beam	-1525	-150	1110
G1	Strain gauge, vertical steel rebar	Wing base	1525	0	-990
G2	Strain gauge, vertical steel rebar	2-3	500	0	-990
G3	Strain gauge, vertical steel rebar	1-3	500	0	0
G4	Strain gauge, horizontal steel rebar	2-4	625	0	-50
G5	Strain gauge, horizontal steel rebar	4-4	-925	0	745
G6	Strain gauge, horizontal steel rebar	4-1	-75	0	745
P1	Pressure, lateral load V	Hydraulic line	n/a		
P2	Pressure, axial load N1	Hydraulic line	n/a		
P3	Pressure, axial load N2, dial	Hydraulic line	n/a		

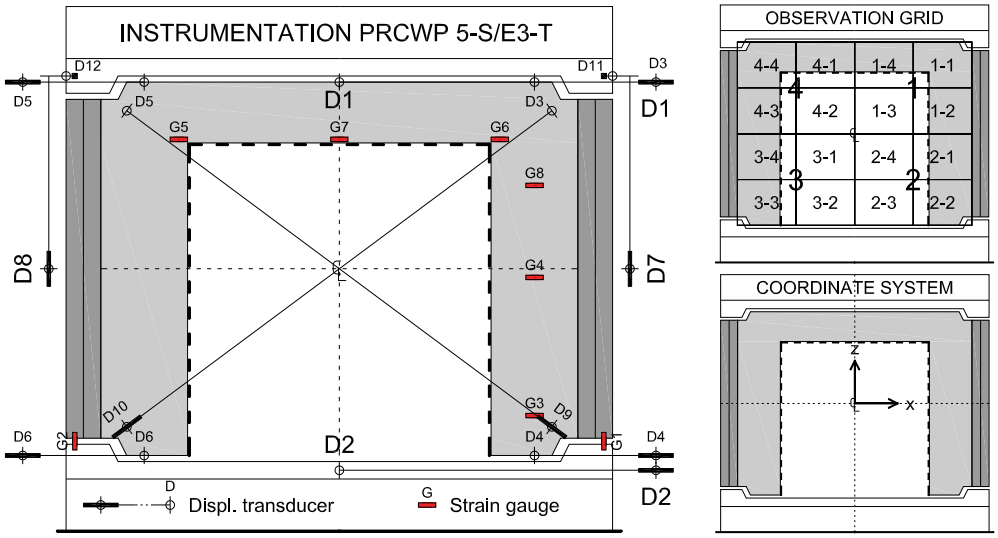

Figure C.4 Instrumentation layout of specimen PRCWP 5-S/E3-T

Table C.3 Sensor list for specimen PRCWP 5-S/E3-T

ID	Type	Location	x (mm)	y (mm)	z (mm)
D1	Displacement, top horizontal	1-4	0	50	1075
D2	Displacement, bottom horizontal	Base beam	0	150	-1160
D3	Displacement, top horizontal	1-1	1125	50	1075
D4	Displacement, bottom horizontal	2-2	1125	50	-1075
D5	Displacement, top horizontal	4-4	-1125	50	1075
D6	Displacement, bottom horizontal	3-3	-1125	50	-1075
D7	Displacement, vertical	Cap beam	1575	0	1110
D8	Displacement, vertical	Cap beam	-1575	0	1110
D9 start	Displacement, diagonal	2-2	1225	50	-910
D9 end		4-4	-1225	50	910
D10 start	Displacement, diagonal	3-3	-1225	50	-910
D10 end		1-1	1225	50	910
D11	Displacement, out-of-plane	Cap beam	1525	-150	1110
D12	Displacement, out-of-plane	Cap beam	-1525	-150	1110
G1	Strain gauge, vertical steel rebar	Wing base	1525	0	-990
G2	Strain gauge, vertical steel rebar	Wing base	-1525	0	-990
G3	Strain gauge, horizontal steel rebar	2-2	1125	0	-845
G4	Strain gauge, horizontal steel rebar	2-1	1125	0	-50
G5	Strain gauge, horizontal steel rebar	4-4	-925	0	745
G6	Strain gauge, horizontal steel rebar	1-1	925	0	745
G7	Strain gauge, horizontal steel rebar	1-4	0	0	745
G8	Strain gauge, horizontal steel rebar	1-2	1125	0	480
P1	Pressure, lateral load V	Hydraulic line	n/a		
P2	Pressure, axial load N1	Hydraulic line	n/a		
P3	Pressure, axial load N2	Hydraulic line	n/a		

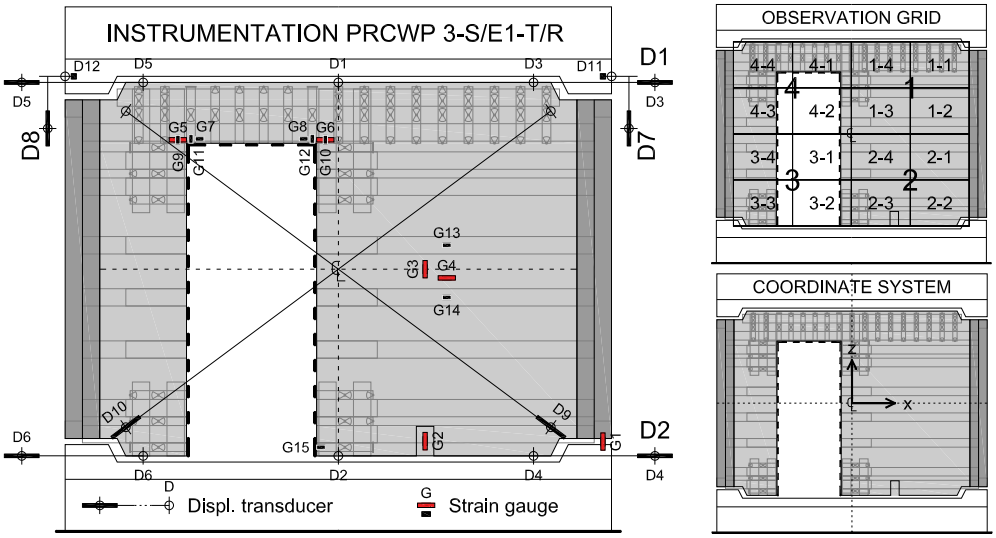

Figure C.5 Instrumentation layout of specimen PRCWP 3-S/E1-T/R

Table C.4 Sensor list for specimen PRCWP 3-S/E1-T/R

ID	Type	Location	x (mm)	y (mm)	z (mm)
D1	Displacement, top horizontal	1-4	0	50	1075
D2	Displacement, bottom horizontal	2-3	0	50	-1075
D3	Displacement, top horizontal	1-1	1125	50	1075
D4	Displacement, bottom horizontal	2-2	1125	50	-1075
D5	Displacement, top horizontal	4-4	-1125	50	1075
D6	Displacement, bottom horizontal	3-3	-1125	50	-1075
D7	Displacement, vertical	Cap beam	1575	0	1110
D8	Displacement, vertical	Cap beam	-1575	0	1110
D9 start	Displacement, diagonal	2-2	1225	50	-910
D9 end		4-4	-1225	50	910
D10 start	Displacement, diagonal	3-3	-1225	50	-910
D10 end		1-1	1225	50	910
D11	Displacement, out-of-plane	Cap beam	1525	-150	1110
D12	Displacement, out-of-plane	Cap beam	-1525	-150	1110
G1	Strain gauge, vertical steel rebar	Wing base	1525	0	-990
G2	Strain gauge, vertical steel rebar	2-3	500	0	-990
G3	Strain gauge, vertical steel rebar	1-3	500	0	0
G4	Strain gauge, horizontal steel rebar	2-4	625	0	-50
G5	Strain gauge, horizontal steel rebar	4-4	-925	0	745
G6	Strain gauge, horizontal steel rebar	4-1	-75	0	745
G7	Strain, horizontal CFRP	4-4	-800	50	750
G8	Strain, horizontal CFRP	4-1	-200	50	750
G9	Strain, vertical CFRP	4-4	-925	50	745
G10	Strain, vertical CFRP	4-1	-75	50	745
G11	Strain, vertical CFRP stirrup	4-4	-850	-50	750
G12	Strain, vertical CFRP stirrup	4-1	-150	-50	750
G13	Strain, horizontal CFRP	1-3	625	50	138
G14	Strain, horizontal CFRP	2-4	625	50	-163
G15	Strain, horizontal CFRP stirrup	3-2	-100	-50	-1025
P1	Pressure, lateral load V	Hydraulic line	n/a		
P2	Pressure, axial load N1	Hydraulic line	n/a		
P3	Pressure, axial load N2	Hydraulic line	n/a		

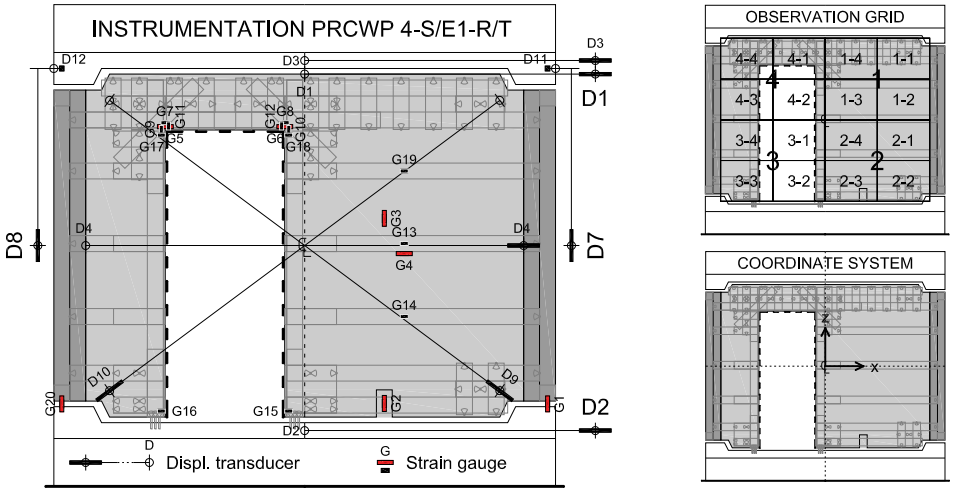

Figure C.6 Instrumentation layout of specimen PRCWP 4-S/E1-R/T

Table C.5 Sensor list for specimen PRCWP 4-S/E1-R/T

ID	Type	Location	x (mm)	y (mm)	z (mm)
D1	Displacement, top horizontal	1-4	0	50	1075
D2	Displacement, bottom horizontal	Base beam	0	150	-1160
D3	Displacement, top horizontal	Cap beam	0	150	1160
D4 start	Displacement, mid horizontal	1-2	1375	50	0
D4 end		4-3	-1375	50	0
D7	Displacement, vertical	Cap beam	1575	0	1110
D8	Displacement, vertical	Cap beam	-1575	0	1110
D9 start	Displacement, diagonal	2-2	1225	50	-910
D9 end		4-4	-1225	50	910
D10 start	Displacement, diagonal	3-3	-1225	50	-910
D10 end		1-1	1225	50	910
D11	Displacement, out-of-plane	Cap beam	1525	-150	1110
D12	Displacement, out-of-plane	Cap beam	-1525	-150	1110
G1	Strain, vertical steel rebar	Wing base	1525	0	-990
G2	Strain, vertical steel rebar	2-3	500	0	-990
G3	Strain, vertical steel rebar	1-3	500	0	170
G4	Strain, horizontal steel rebar	2-4	625	0	-50
G5	Strain, horizontal steel rebar	4-4	-875	0	745
G6	Strain, horizontal steel rebar	4-1	-125	0	745
G7	Strain, horizontal CFRP	4-4	-880	50	770
G8	Strain, horizontal CFRP	4-1	-120	50	770
G9	Strain, vertical CFRP	4-4	-900	50	730
G10	Strain, vertical CFRP	4-1	-100	50	730
G11	Strain, vertical CFRP stirrup	4-4	-855	50	750
G12	Strain, vertical CFRP stirrup	4-1	-145	50	750
G13	Strain, horizontal CFRP	1-3	625	50	10
G14	Strain, horizontal CFRP	2-4	625	50	-445
G15	Strain, horizontal CFRP stirrup	3-2	-100	50	-1035
G16	Strain, horizontal CFRP stirrup	3-3	-900	50	-1035
G17	Strain, horizontal CFRP stirrup	4-4	-900	50	690
G18	Strain, horizontal CFRP stirrup	4-1	-100	50	690
G19	Strain, horizontal CFRP	1-3	625	50	465
G20	Strain, vertical steel rebar	Wing base	-1525	0	-990
P1	Pressure, lateral load V	Hydraulic line	n/a		
P2	Pressure, axial load N1	Hydraulic line	n/a		
P3	Pressure, axial load N2	Hydraulic line	n/a		

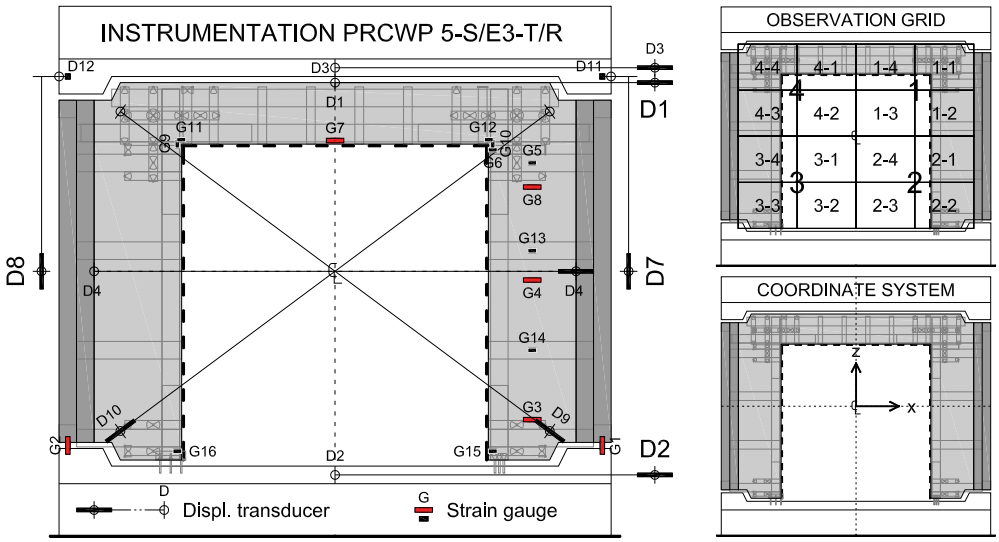

Figure C.7 Instrumentation layout of specimen PRCWP 5-S/E3-T/R

Table C.6 Sensor list for specimen PRCWP 5-S/E3-T/R

ID	Type	Location	x (mm)	y (mm)	z (mm)
D1	Displacement, top horizontal	1-4	0	50	1075
D2	Displacement, bottom horizontal	Base beam	0	150	-1160
D3	Displacement, top horizontal	Cap beam	0	150	1160
D4 start	Displacement, mid horizontal	1-2	1375	50	0
D4 end		4-3	-1375	50	0
D7	Displacement, vertical	Cap beam	1575	0	1110
D8	Displacement, vertical	Cap beam	-1575	0	1110
D9 start	Displacement, diagonal	2-2	1225	50	-910
D9 end		4-4	-1225	50	910
D10 start	Displacement, diagonal	3-3	-1225	50	-910
D10 end		1-1	1225	50	910
D11	Displacement, out-of-plane	Cap beam	1525	-150	1110
D12	Displacement, out-of-plane	Cap beam	-1525	-150	1110
G1	Strain, vertical steel rebar	Wing base	1525	0	-990
G2	Strain, vertical steel rebar	Wing base	-1525	0	-990
G3	Strain, horizontal steel rebar	2-2	1125	0	-845
G4	Strain, horizontal steel rebar	2-1	1125	0	-50
G5	Strain, horizontal CFRP	1-1	1125	50	618
G6	Strain, horizontal CFRP stirrup	1-1	900	50	693
G7	Strain, horizontal steel rebar	1-4	0	0	745
G8	Strain, horizontal steel rebar	1-2	1125	0	480
G9	Strain, vertical CFRP	4-4	-900	50	728
G10	Strain, vertical CFRP	1-1	900	50	728
G11	Strain, horizontal CFRP	4-4	-878	50	750
G12	Strain, horizontal CFRP	1-1	878	50	750
G13	Strain, horizontal CFRP	1-2	1125	50	118
G14	Strain, horizontal CFRP	2-1	1125	50	-450
G15	Strain, horizontal CFRP hoop	2-2	900	50	-1025
G16	Strain, horizontal CFRP hoop	3-3	-900	50	-1025
P1	Pressure, lateral load V	Hydraulic line	n/a		
P2	Pressure, axial load N1	Hydraulic line	n/a		
P3	Pressure, axial load N2	Hydraulic line	n/a		

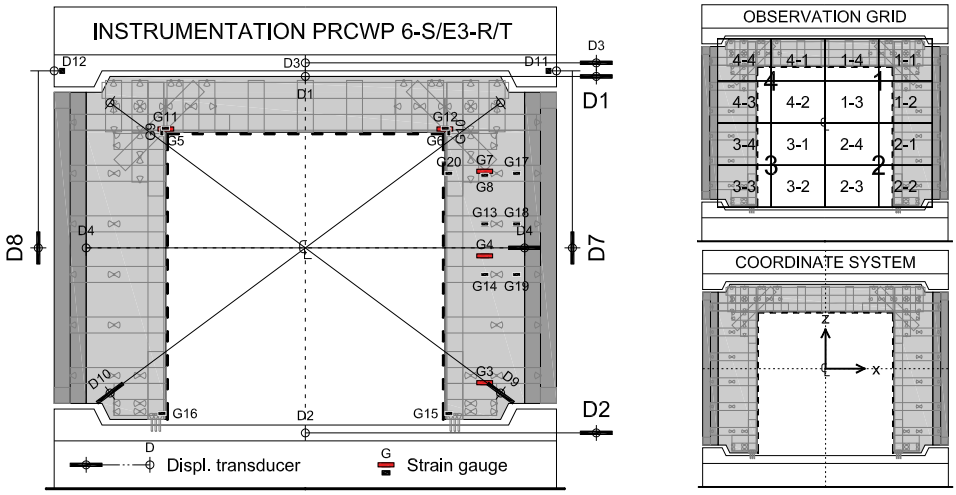

Figure C.8 Instrumentation layout of specimen PRCWP 6-S/E3-R/T

Table C.7 Sensor list for specimen PRCWP 6-S/E3-R/T

ID	Type	Location	x (mm)	y (mm)	z (mm)
D1	Displacement, top horizontal	1-4	0	50	1075
D2	Displacement, bottom horizontal	Base beam	0	150	-1160
D3	Displacement, top horizontal	Cap beam	0	150	1160
D4 start	Displacement, mid horizontal	1-2	1375	50	0
D4 end		4-3	-1375	50	0
D7	Displacement, vertical	Cap beam	1575	0	1110
D8	Displacement, vertical	Cap beam	-1575	0	1110
D9 start	Displacement, diagonal	2-2	1225	50	-910
D9 end		4-4	-1225	50	910
D10 start	Displacement, diagonal	3-3	-1225	50	-910
D10 end		1-1	1225	50	910
D11	Displacement, out-of-plane	Cap beam	1525	-150	1110
D12	Displacement, out-of-plane	Cap beam	-1525	-150	1110
G3	Strain, horizontal steel rebar	2-2	1125	0	-845
G4	Strain, horizontal steel rebar	2-1	1125	0	-50
G5	Strain, horizontal steel rebar	4-4	-875	0	745
G6	Strain, horizontal steel rebar	1-1	875	0	745
G7	Strain, horizontal steel rebar	1-2	1125	0	480
G8	Strain, horizontal CFRP	1-2	1125	50	455
G9	Strain, vertical CFRP	4-4	-900	50	728
G10	Strain, vertical CFRP	1-1	900	50	728
G11	Strain, horizontal CFRP	4-4	-878	50	750
G12	Strain, horizontal CFRP	1-1	878	50	750
G13	Strain, horizontal CFRP	1-2	1125	50	150
G14	Strain, horizontal CFRP	2-1	1125	50	-167
G15	Strain, horizontal CFRP hoop	2-2	900	50	-1038
G16	Strain, horizontal CFRP hoop	3-3	-900	50	-1038
G17	Strain, horizontal CFRP	1-2	1325	50	468
G18	Strain, horizontal CFRP	1-2	1325	50	150
G19	Strain, horizontal CFRP	2-1	1325	50	-167
G20	Strain, horizontal CFRP hoop	1-2	900	50	468
P1	Pressure, lateral load V	Hydraulic line	n/a		
P2	Pressure, axial load N1	Hydraulic line	n/a		
P3	Pressure, axial load N2	Hydraulic line	n/a		

Appendix D Measurement accuracy evaluation

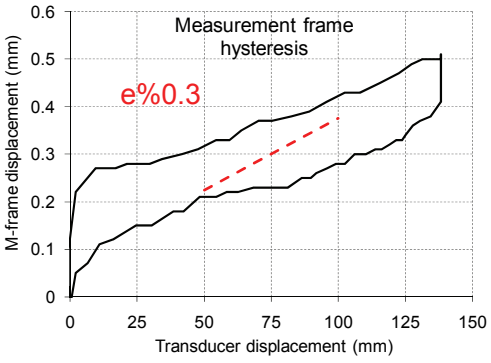

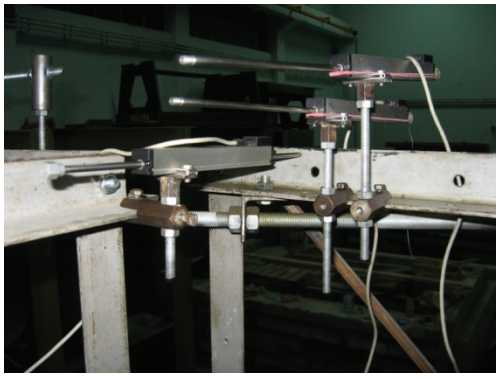

Figure D.1 Deflection of the independent steel frame

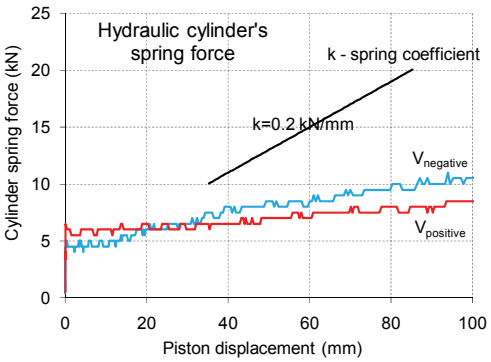

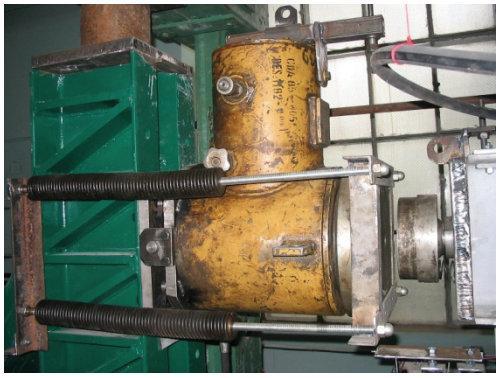

Figure D.2 Additional spring force

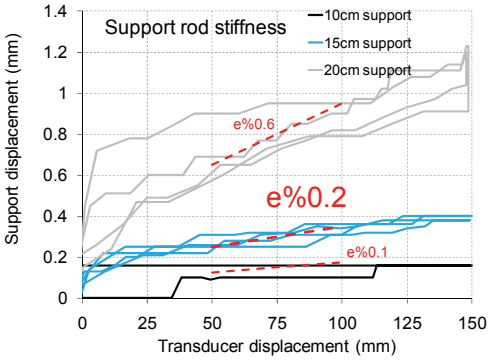

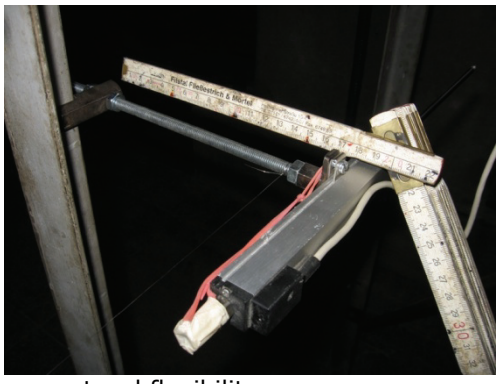

Figure D.3 Transducer support rod flexibility

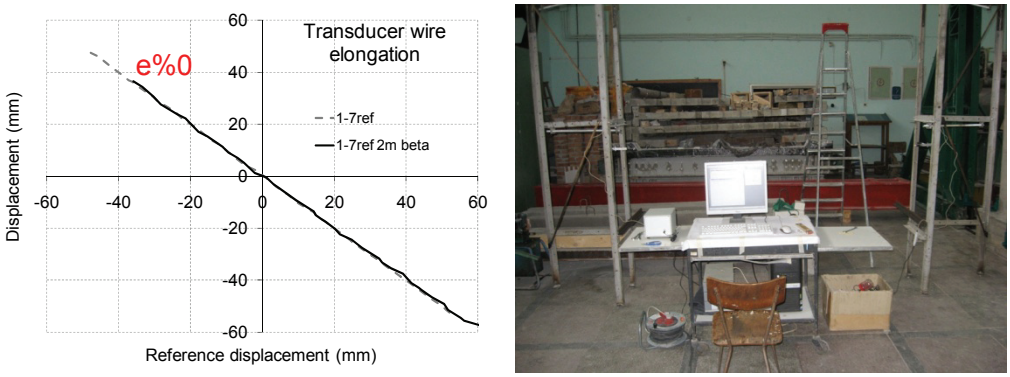

Figure D.4 Transducer wire elongation

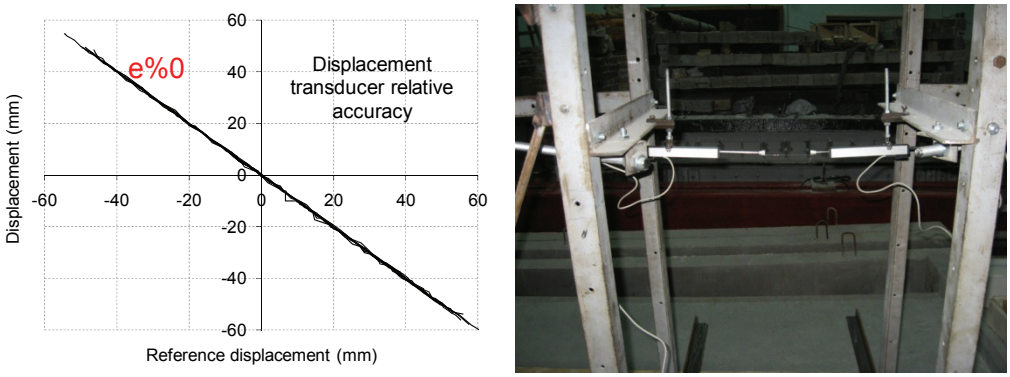

Figure D.5 Displacement transducer comparison

Appendix E Test logs

E.1 Test log of specimen PRCWP 1-S-T

The test was carried out during December 12-14, 2009 in the Reinforced Concrete Structures Laboratory of the Department of Civil and Industrial Buildings, Faculty of Civil Engineering, Politehnica University of Timisoara, Romania. The experiment was attended by the following individuals: István Demeter, PhD Stud., Tamás Nagy-György, PhD, Lect., Alexandru Fabian, PhD Stud., Simon Pescari, MSc Stud., Tamás Dencsák, PhD Stud., and Paul Paștiu, MSc Stud. The author expresses his grateful acknowledgement for the instrumental contribution of his fellows.

The actual testing time was 8 hours segmented in two parts by one day of interruption. The recorded data file comprises 27459 lines and 27 measuring input columns. The complete instrumentation of the specimen is presented in Appendix C. This test log contains all the recorded responses and the observed behaviour and failure mode in the following order: load versus displacement diagrams, load versus strain diagrams, expanded cyclic load and displacement histories, cracking history, expanded cyclic lateral load versus drift hysteresis loops, commentary on the behaviour mode and test events, and failure details.

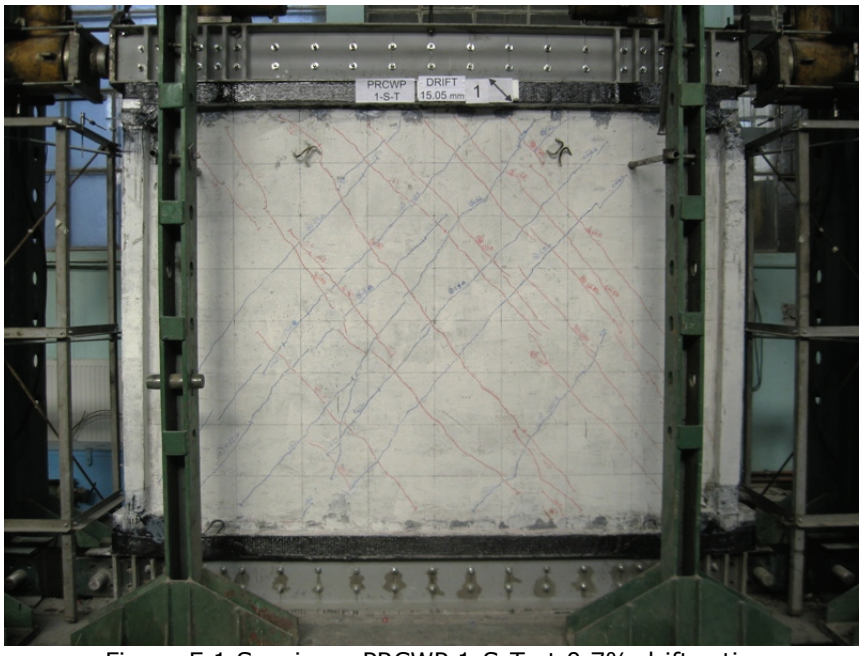

Figure E.1 Specimen PRCWP 1-S-T at 0.7% drift ratio

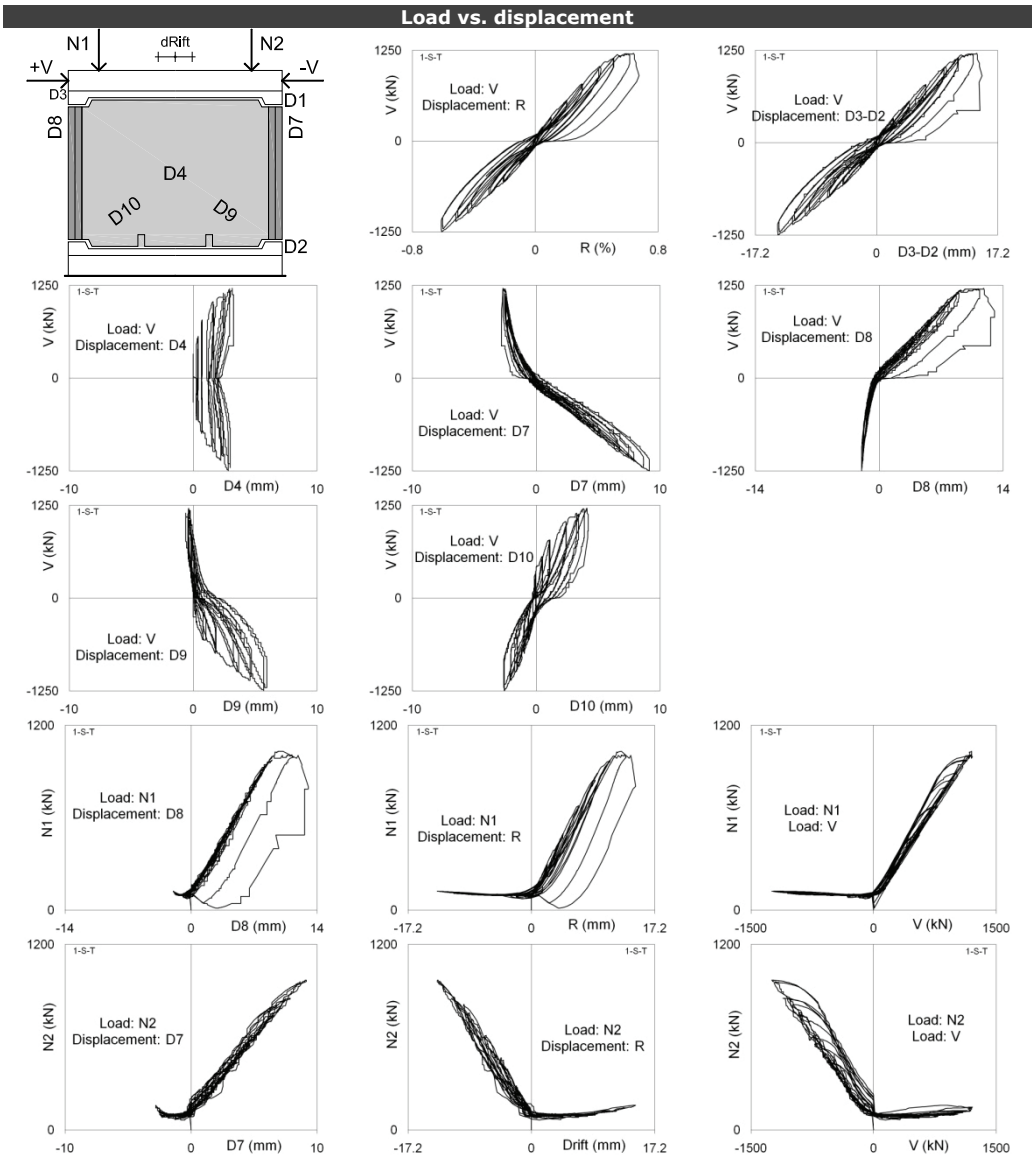

Figure E.2 Load-displacement responses for specimen PRCWP 1-S-T

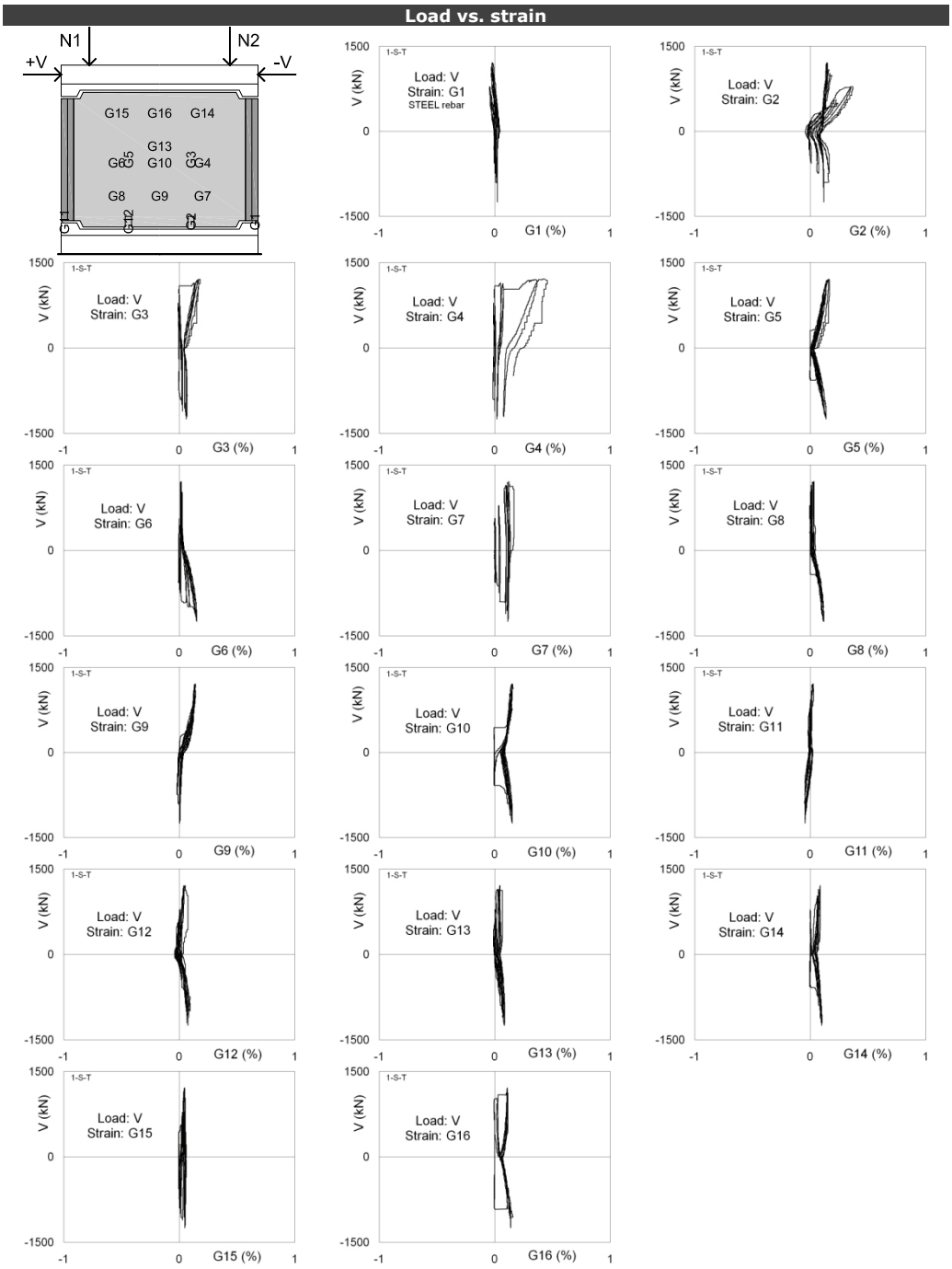

Figure E.3 Load-strain responses for specimen PRCWP 1-S-T

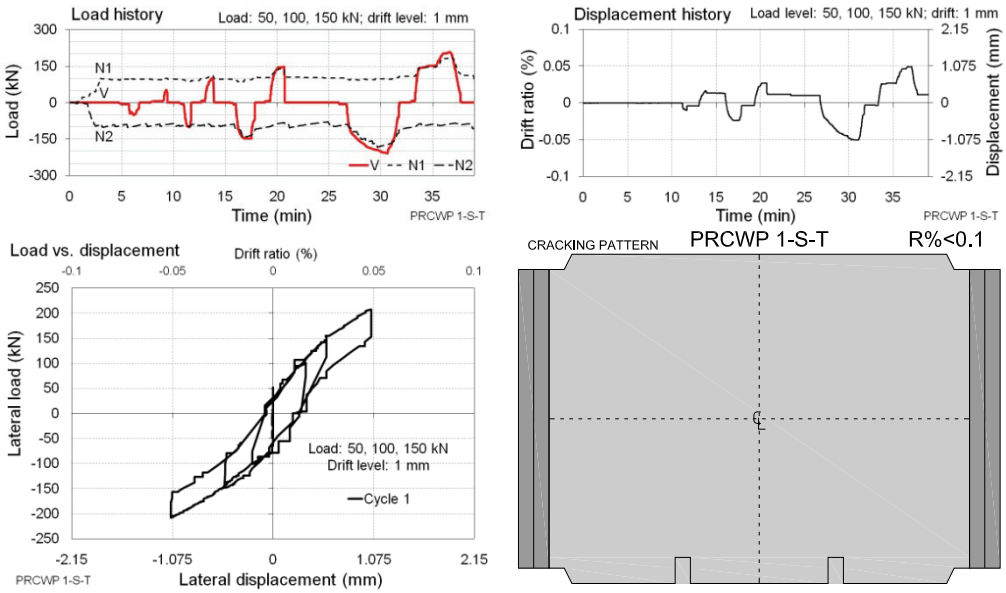

Observations: According to the loading procedure one cycle was performed at 50, 100 and 150 kN lateral load levels. The 10 kN cycle was not realised. Afterwards one cycle was imposed at 1 mm drift. No sign of degradation.

Figure E.4 Expanded cyclic response of PRCWP 1-S-T at the initial cycles

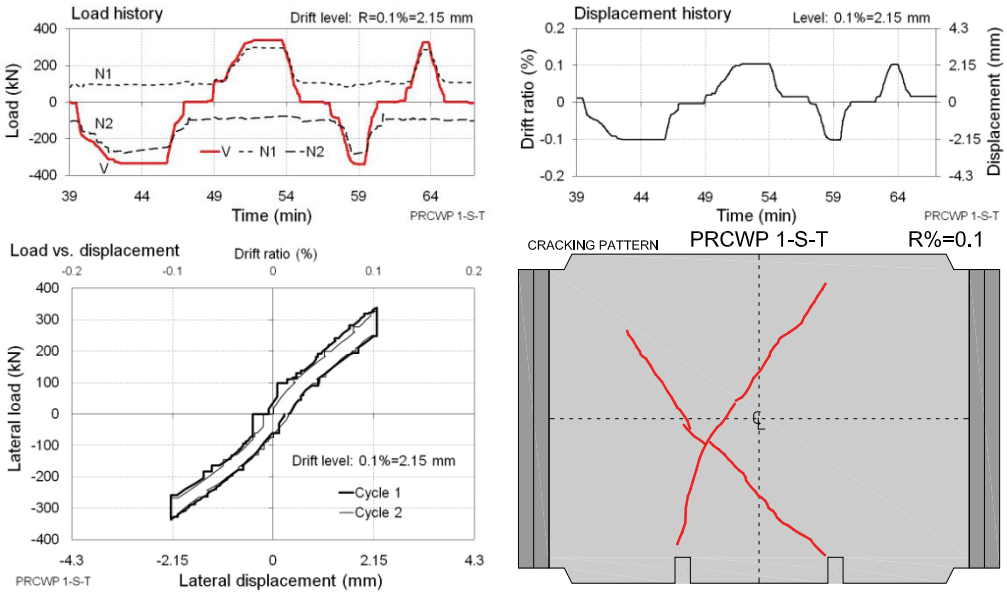

Comments: Pre-existing inclined cracks opened. These cracks appeared during the transportation and manipulation of the specimen.

Figure E.5 Expanded cyclic response of PRCWP 1-S-T at 0.1% drift ratio

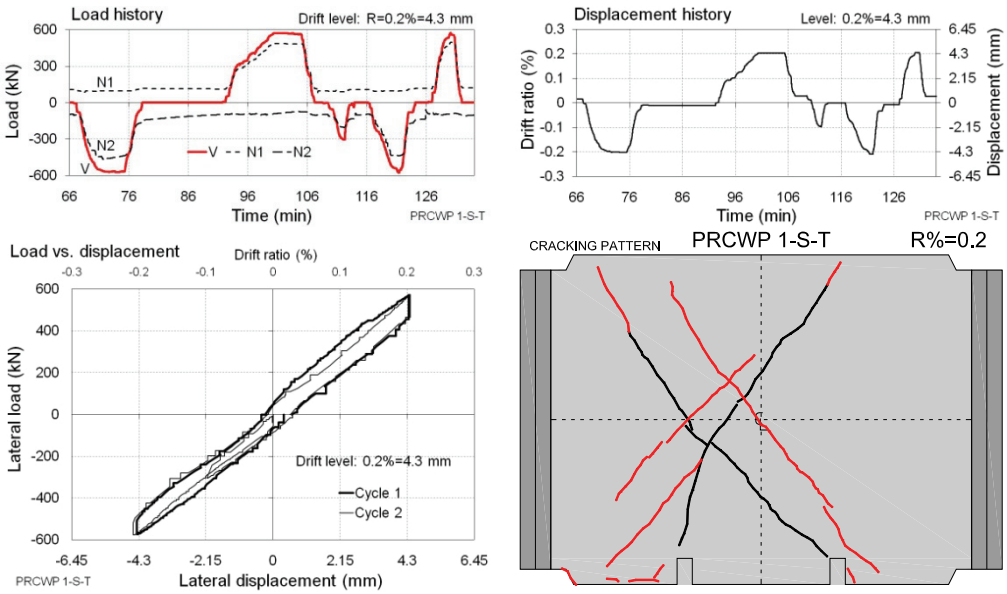

Notes: Straight cross-inclined cracks developed running at approximately 50 deg angles, extending from the top to the bottom edges. At the beginning of the second cycle the specimen was unloaded due to inadequate piston control.

Figure E.6 Expanded cyclic response of PRCWP 1-S-T at 0.2% drift ratio

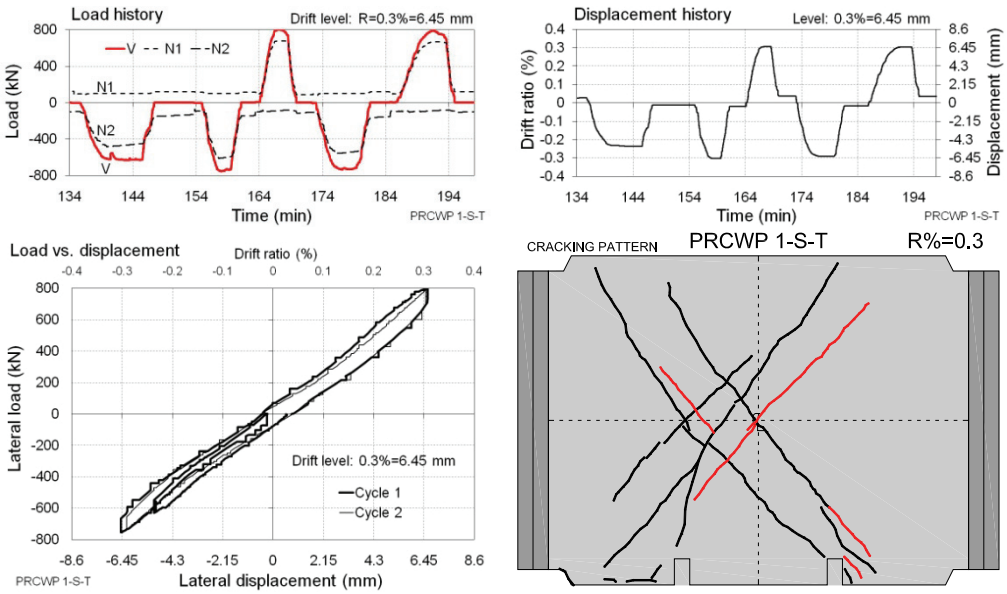

Behaviour mode: 50 deg inclined crack developed through the centre of the wall. Hydraulic power unit malfunction occurred in the negative loading direction of the first cycle. The wall was unloaded and the cycle was started over.

Figure E.7 Expanded cyclic response of PRCWP 1-S-T at 0.3% drift ratio

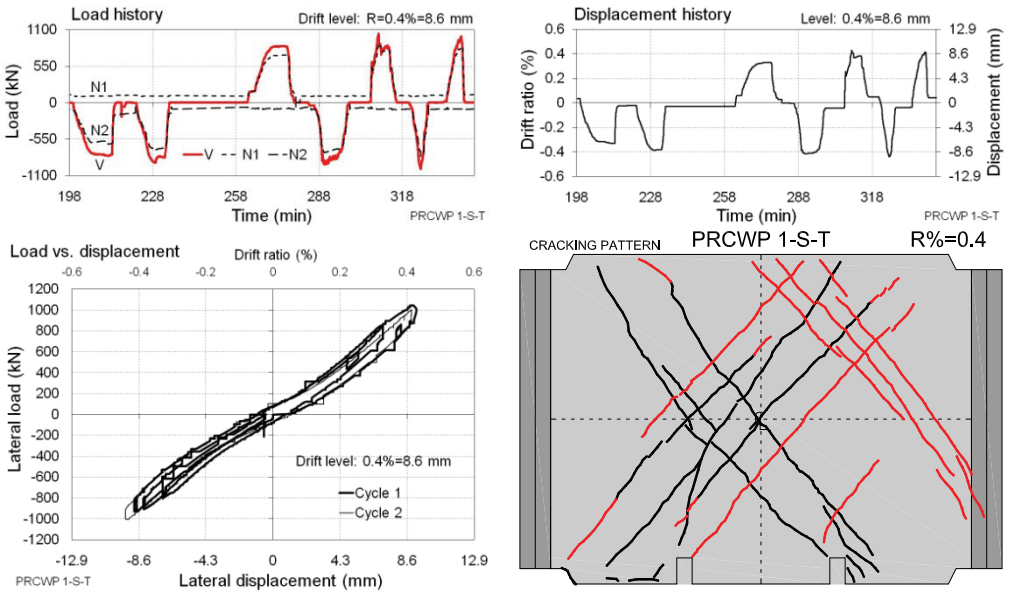

Notes: Severe cracking occurred in both directions. The propagation took place both by extension of the existing cracks and development of new ones parallel to the former. The malfunction of the hydraulic power unit persisted and more trials were made to attain the target drift level, eventually the test being halted due to the approach both of the oil pressure capacity (200 bar) and the nominal load resistance (1000 kN) of the pump and lateral reaction frames, respectively. After two days the hydraulic pump was replaced and the test continued by starting over the 0.4% (8.6 mm) drift level.

Figure E.8 Expanded cyclic response of PRCWP 1-S-T at 0.4% drift ratio

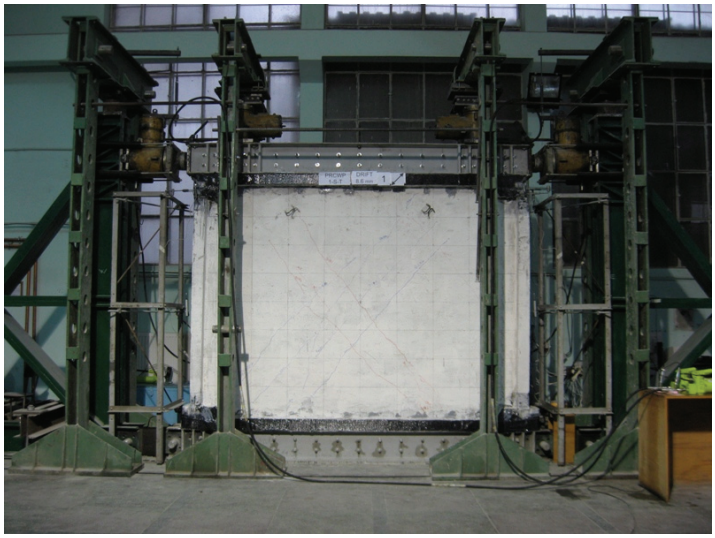

Figure E.9 Specimen PRCWP 1-S-T at 0.4% drift ratio

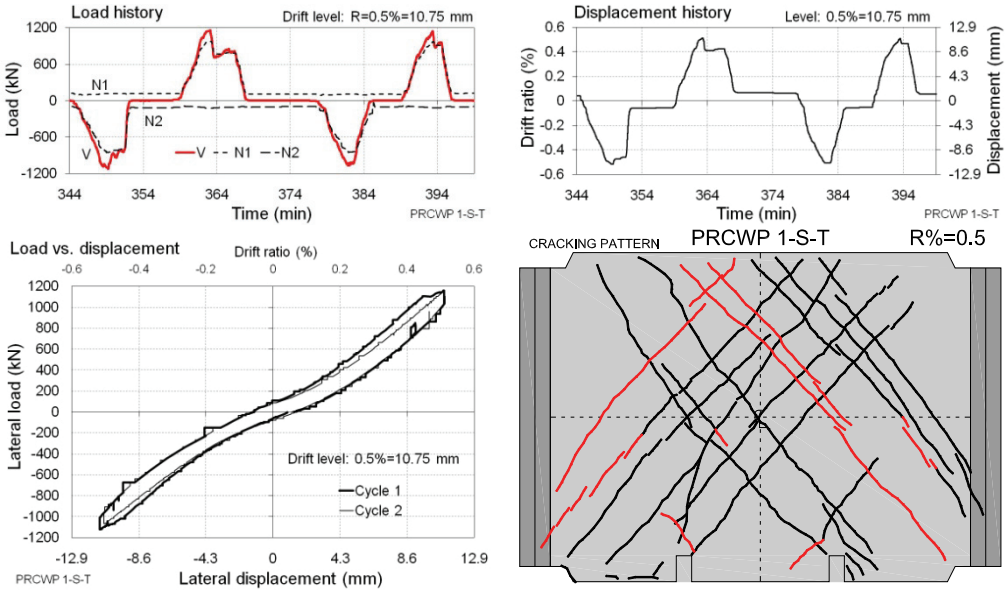

Comments: Further 50 deg inclined cracks occurred in both directions. The band-width of the cracked zone was approximately 110 cm measured perpendicular to the cracks. The post-peak load dropping noticeable in the load history diagram was a control issue, it was not related to the cracking or capacity loss.

Figure E.10 Expanded cyclic response of PRCWP 1-S-T at 0.5% drift ratio

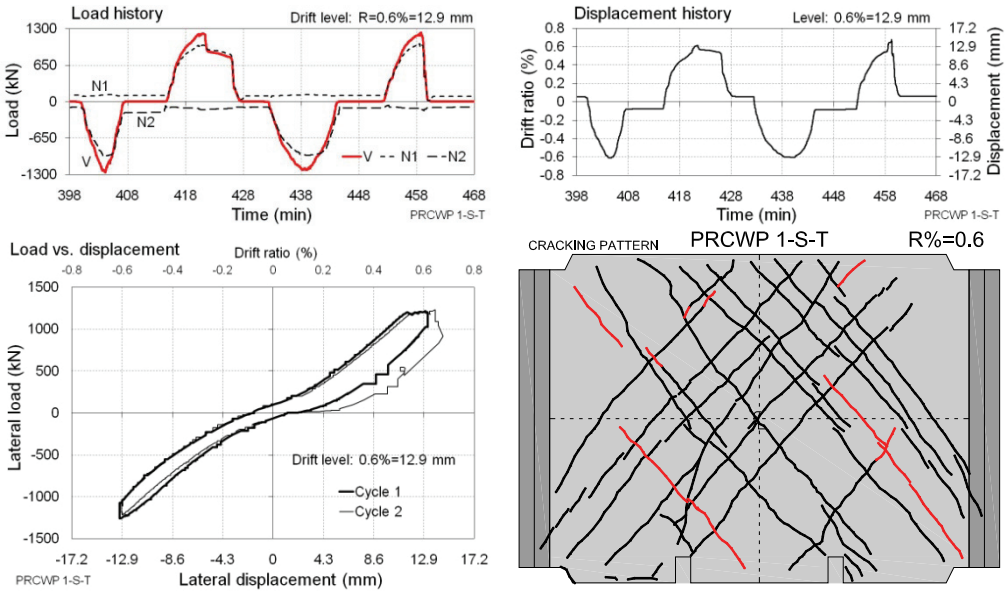

Comments: Existing cracks extended and new inclined cracks developed. In the load vs. displacement response the plateau in the positive direction is the result of the N1 axial load control which was not increased beyond 1000 kN, this being the nominal capacity of the hydraulic cylinder and of the vertical reaction frame, see also the N1-D8 and N1-R diagrams.

Figure E.11 Expanded cyclic response of PRCWP 1-S-T at 0.6% drift ratio

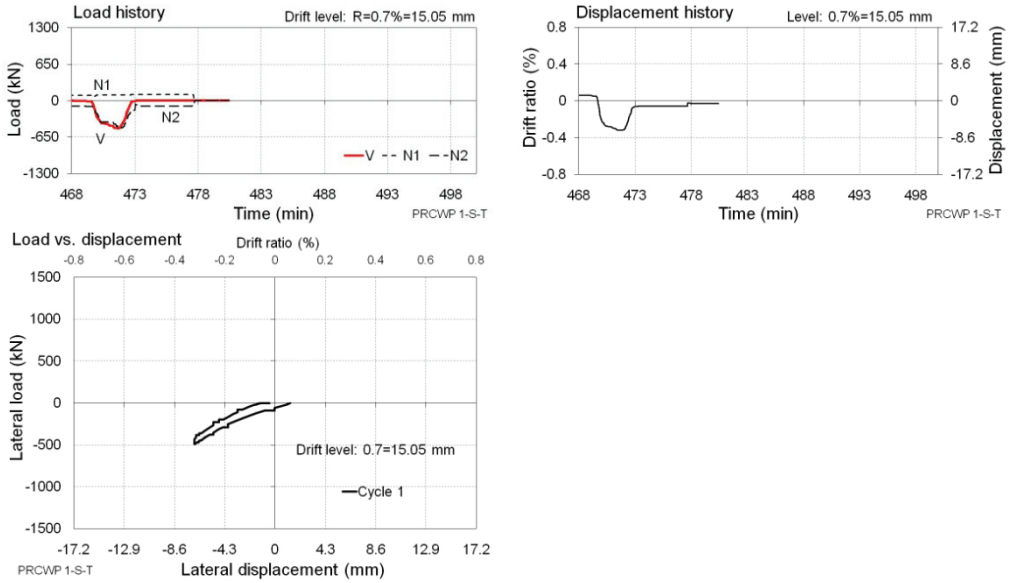

Note: The hydraulic power unit failed due to repeated overpressure sustained in the previous cycles (250 bar vs. 200 bar nominal capacity). The test was definitively interrupted.

Figure E.12 Expanded cyclic response of PRCWP 1-S-T at 0.7% drift ratio (incomplete cycle)

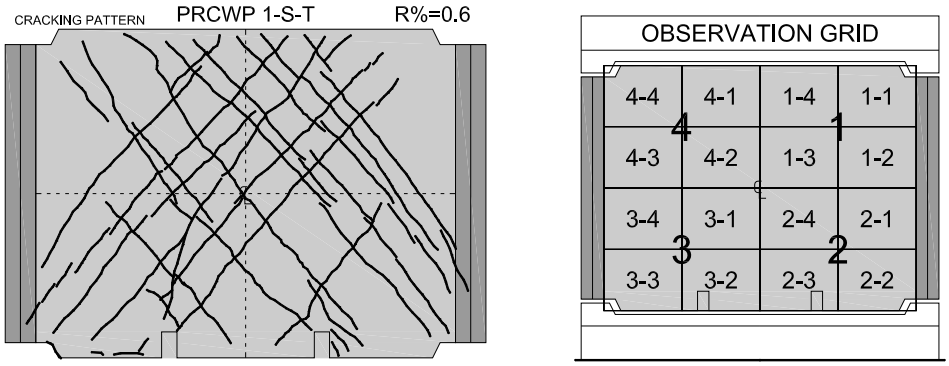

Figure E.13 Cracking pattern and observation grid PRCWP 1-S-T

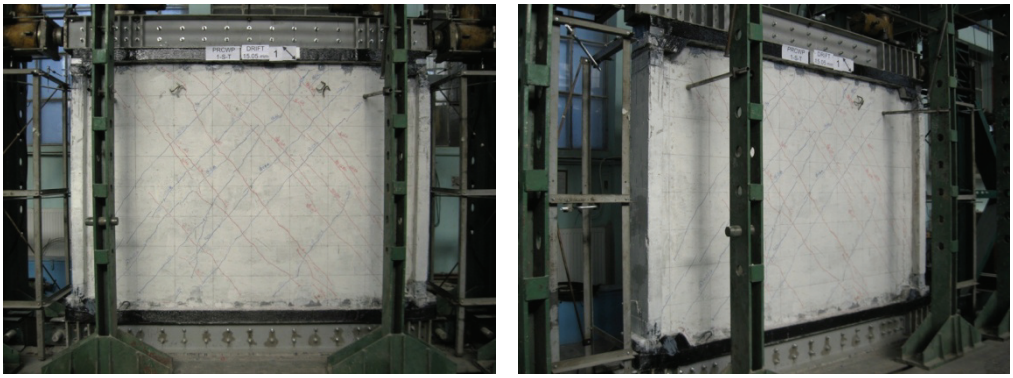

Figure E.14 Failure detail PRCWP 1-S-T: general views

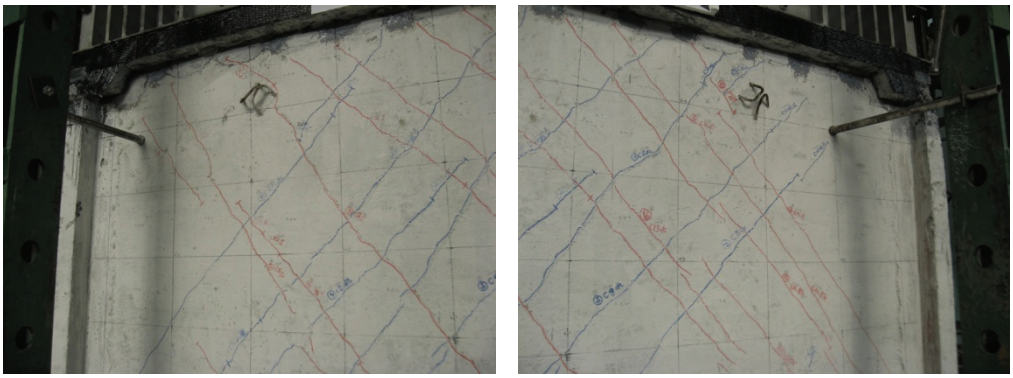

(a) (b)

Figure E.15 Failure detail PRCWP 1-S-T: (a) close-up on observation grid 4; (b) close-up on observation grid 1

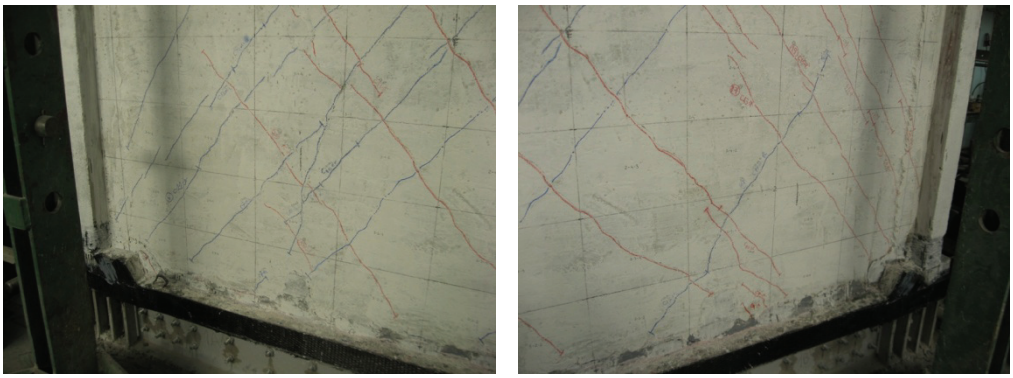

(a) (b)

Figure E.16 Failure detail PRCWP 1-S-T: (a) close-up on observation grid 3; (b) close-up on observation grid 2

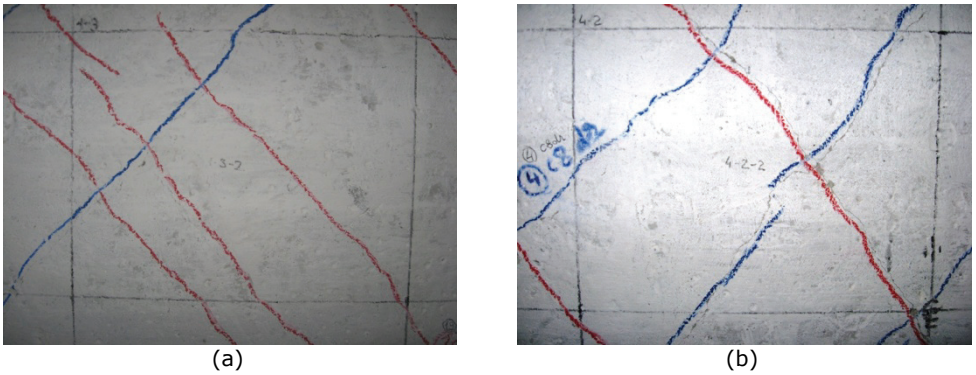

(a) (b)

Figure E.17 Failure detail PRCWP 1-S-T: (a) close-up on observation grid 1-3-2; (b) close-up on observation grid 4-2-2

E.2 Test log of specimen PRCWP 3-S/E1-T

The test was carried out during June 13-16, 2008 in the Reinforced Concrete Structures Laboratory of the Department of Civil and Industrial Buildings, Faculty of Civil Engineering, Politehnica University of Timisoara, Romania. The author was assisted by the following individuals: Tamás Nagy-György, PhD, Lect., Codruț Floruț, PhD Stud., Dan Diaconu, PhD Stud., and Cosmin Dăescu, PhD Stud., whose instrumental contribution is gratefully acknowledged.

The actual testing time was almost 9 hours segmented in two parts by two days of interruption. The recorded data file comprises 26218 lines and 18 measuring input columns. The complete instrumentation of the specimen is presented in Appendix C. This test log contains all the recorded responses and the observed behaviour and failure mode in the following order: load versus displacement diagrams, load versus strain diagrams, expanded cyclic load and displacement histories, cracking history, expanded cyclic lateral load versus drift hysteresis loops, commentary on the behaviour mode and test events, and failure details.

Figure E.18 Specimen PRCWP 3-S/E1-T at failure (0.7% drift ratio)

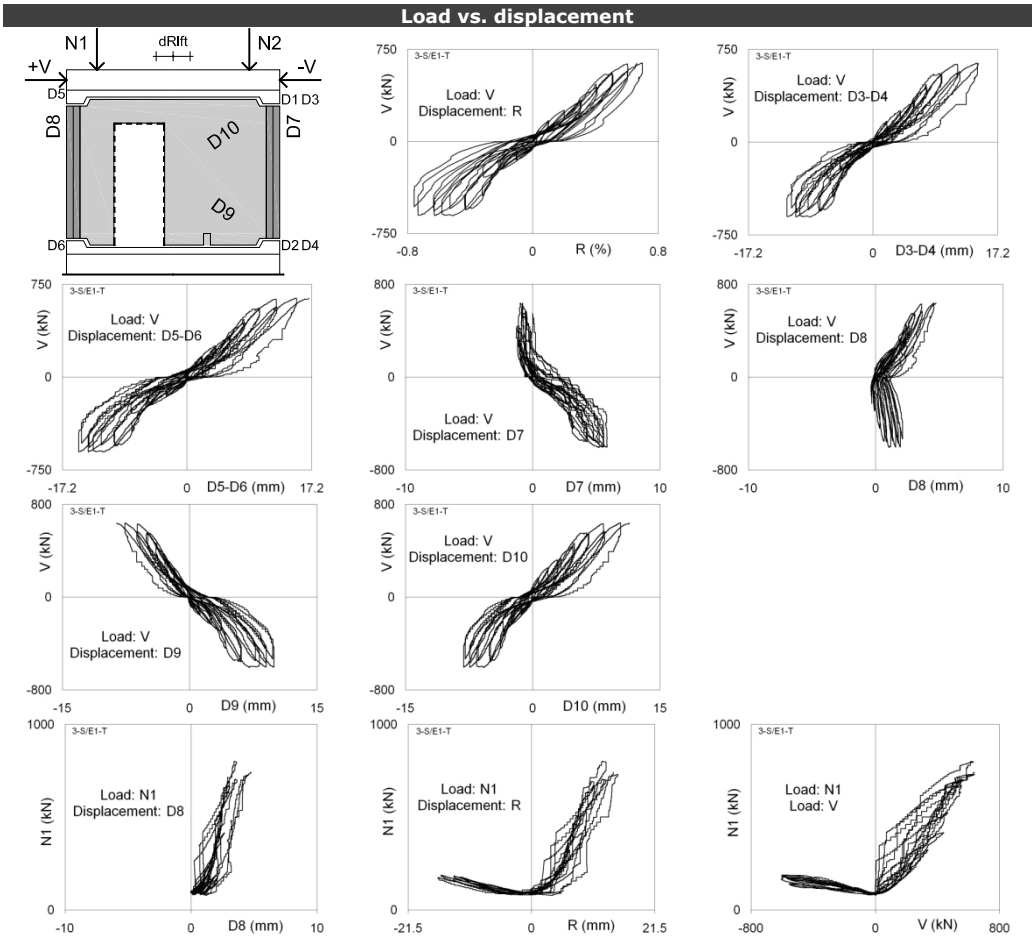

Figure E.19 Load-displacement responses for specimen PRCWP 3-S/E1-T

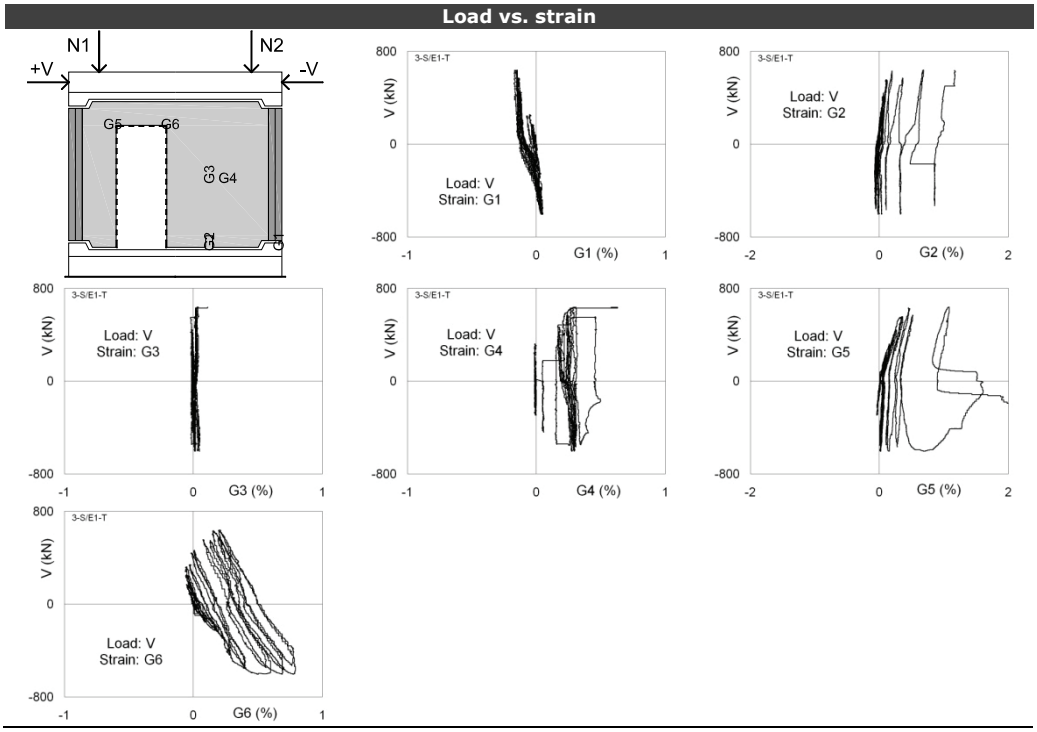

Figure E.20 Load-strain responses for specimen PRCWP 3-S/E1-T

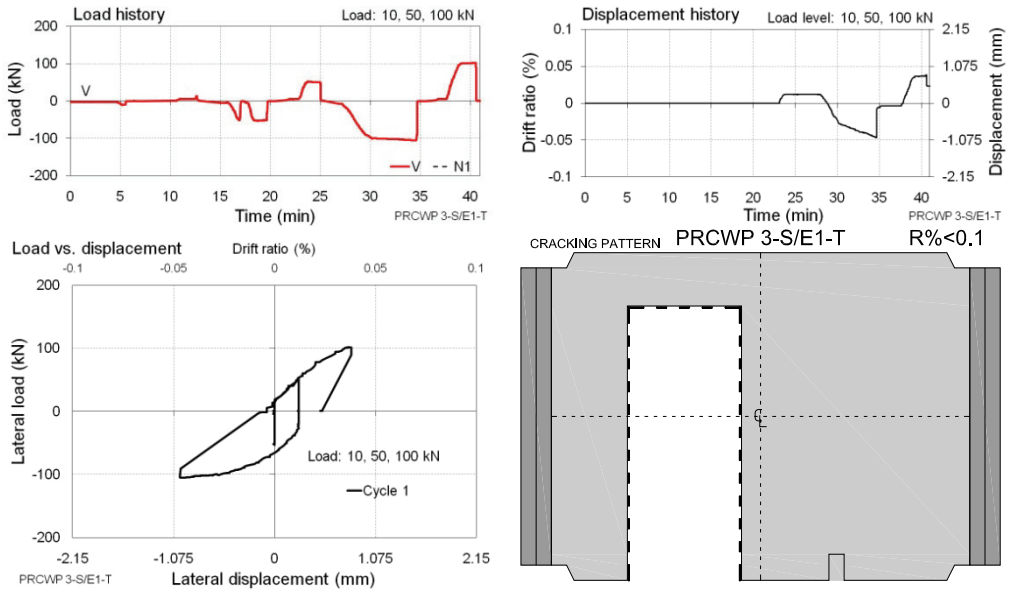

Commentary: The test started with load controlled cycles at 10, 50, 100 kN amplitudes. The 1 mm drift (shifting criterion from load to displacement control) was attained simultaneously with the 100 kN load. The axial loads, though were applied and kept constant at the designated level (N1=N2=95.5 kN), were not recorded yet.

Figure E.21 Expanded cyclic response of PRCWP 3-S/E1-T at the initial cycles

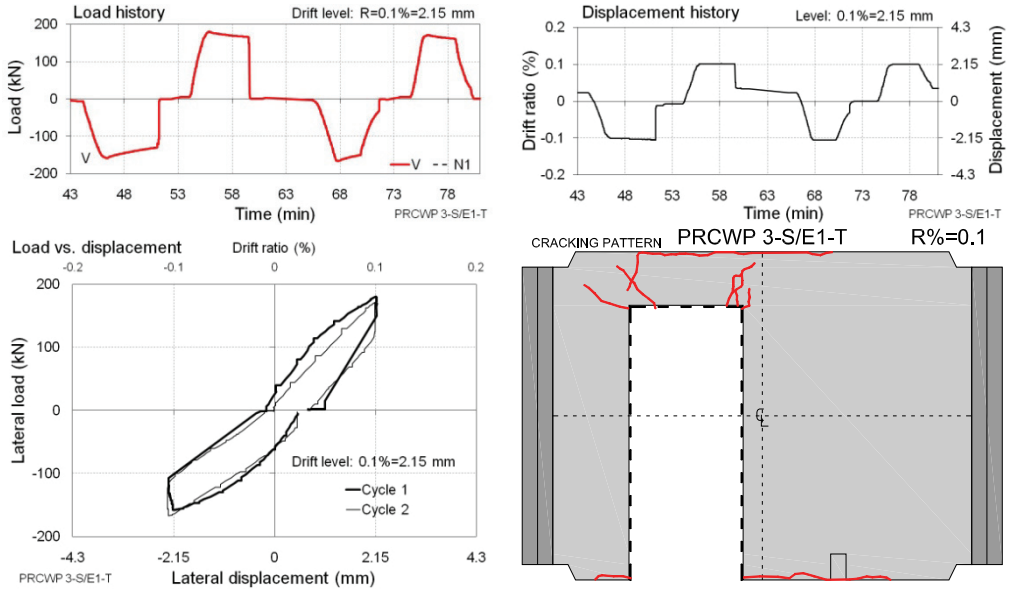

Commentary: Horizontal cracks developed at the base starting from the piers' inside toes concurrently with vertical cracking at the beam-to-pier connections. Along the wall-to cap beam joint also appeared a horizontal crack atop the spandrel. The 100 kN/mm rate of the additional axial loading was not yet adopted and a smaller rate was imposed.

Figure E.22 Expanded cyclic response of PRCWP 3-S/E1-T at 0.1% drift ratio

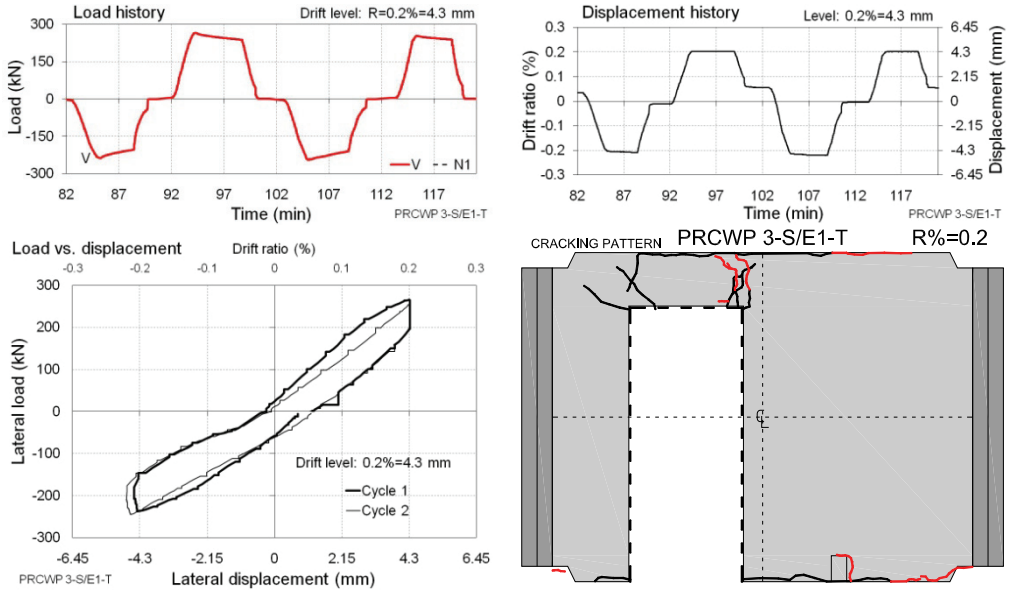

Commentary: Propagation of the horizontal cracks at the base and atop of the wall and of the vertical cracks at the spandrel-to-pier#2 connection. Variable axial load rate still smaller than 100 kN/mm.

Figure E.23 Expanded cyclic response of PRCWP 3-S/E1-T at 0.2% drift ratio

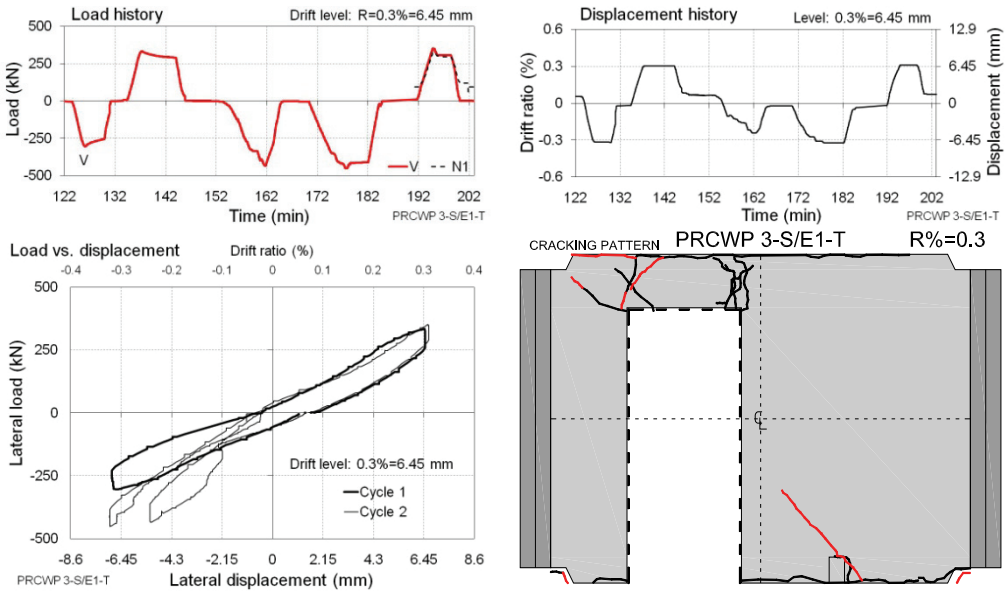

Commentary: The cycle #1 of this level was the last one carried out on June 13, thereafter the test was halted for two days. Inclined cracks appeared at the base of pier#2 and at the spandrel-to-pier#1 connection. The test was continued on June 16. Meanwhile the instrumentation was augmented by an additional pressure sensor installed on the hydraulic line of the N1 axial load, which was hence recorded digitally afterwards (see the load history diagram), while the N2 load was monitored as before with a dial manometer. The rate of the variable axial loading was increased excessively in the negative loading direction, which resulted in a very stiff response (see the load-displacement diagram). Moreover, the out-of-plane supports were not released, therefore the wall was unloaded and reloaded again.

Figure E.24 Expanded cyclic response of PRCWP 3-S/E1-T at 0.3% drift ratio

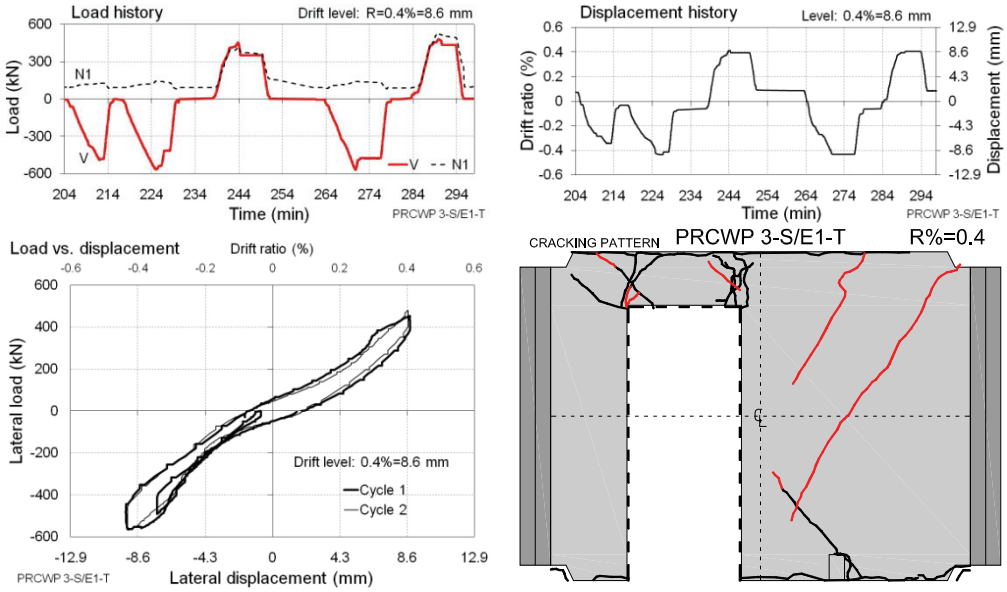

Commentary: the first loading attempt in the negative direction was unsuccessful due to a mistake in controlling the hydraulic pump, thus the wall was unloaded and reloaded in the same direction. Diagonal cracking occurred across pier#2 running at approx. 58 deg angle.

Figure E.25 Expanded cyclic response of PRCWP 3-S/E1-T at 0.4% drift ratio

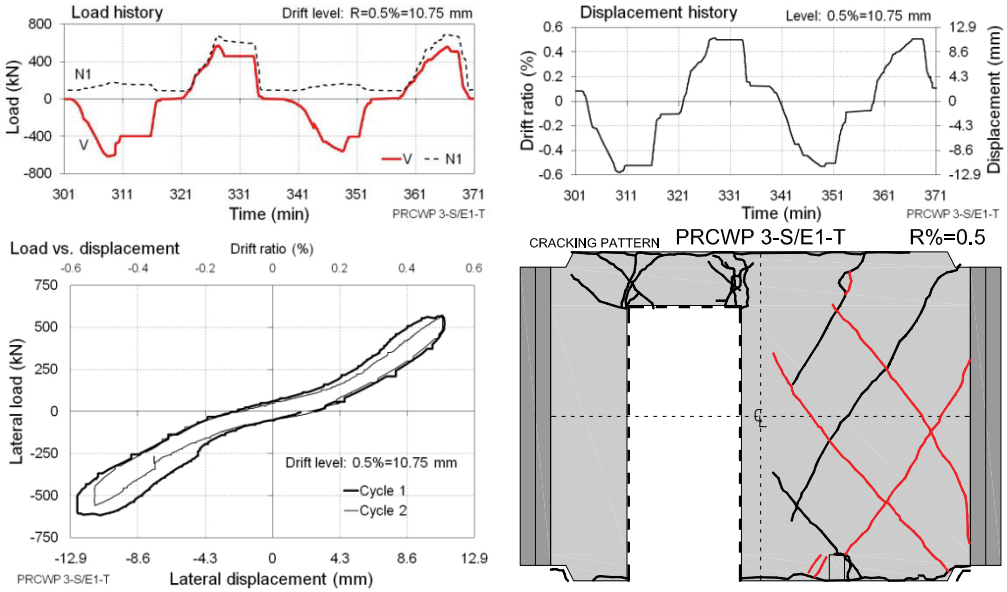

Commentary: Diagonal cracks, extending at 50÷60 deg angles, developed through pier#2 in both loading directions. Spalling initiation of the concrete was observed at the inside toe (near the opening) of pier#2.

Figure E.26 Expanded cyclic response of PRCWP 3-S/E1-T at 0.5% drift ratio

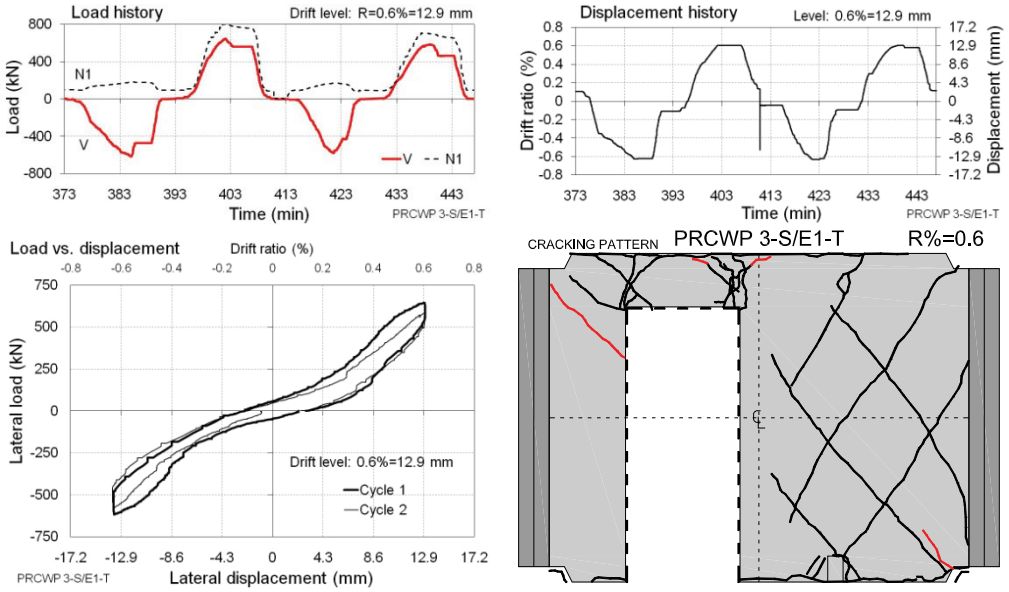

Commentary: In the positive loading direction of cycle #1 45 deg inclined cracking occurred at the upper portion of pier#1. The wall was completely unloaded for two hours. During cycle #2 concrete spalling occurred at the inside toe of pier#1, similarly as for the other pier in the previous drift level.

Figure E.27 Expanded cyclic response of PRCWP 3-S/E1-T at 0.6% drift ratio

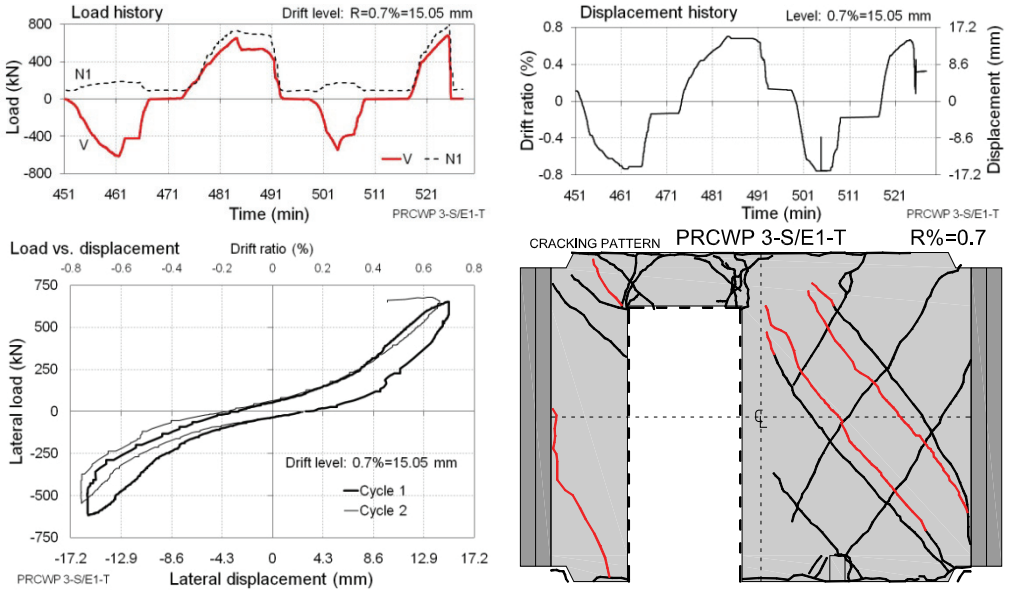

Commentary: Further cross-diagonal cracking developed in pier#2 and in the lower half of pier#1. The failure occurred in the positive loading direction of cycle #2 by severe crushing and spalling of the concrete at the spandrel-to-pier#2 connection and along the top of pier#2. It was noted that the wall slanted backward in the out-of-plane direction. At failure the measuring supports of D1 and D3 displacement transducers were eliminated by the falling debris, only the D5 support remained in function for drift measurement.

Figure E.28 Expanded cyclic response of PRCWP 3-S/E1-T at 0.7% drift ratio

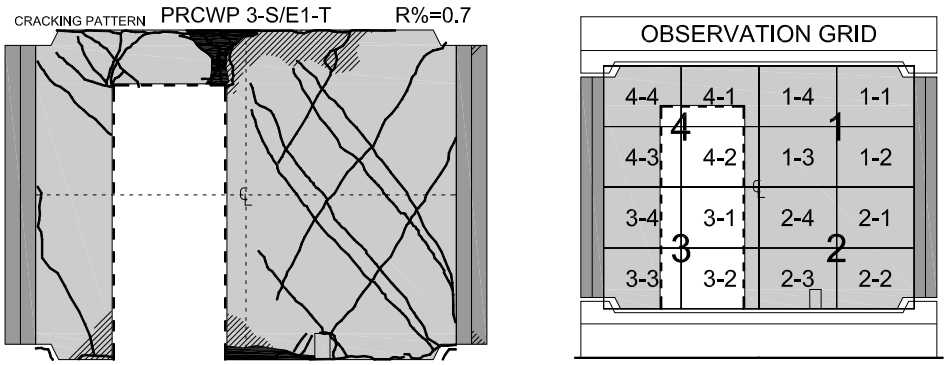

Figure E.29 Cracking pattern and observation grid PRCWP 3-S/E1-T

Figure E.30 Failure detail PRCWP 3-S/E1-T: concrete spalling and crushing at the inside toe of pier#2 (obs. grid 3-2)

Figure E.31 Failure detail PRCWP 3-S/E1-T: concrete spalling and crushing at the inside toe of pier#1 (obs. grid 3-3)

Figure E.32 Failure detail PRCWP 3-S/E1-T: concrete crushing at the spandrel-to pier#2 connection (close-up on grid 4-1)

Figure E.33 Failure detail PRCWP 3-S/E1-T: general view after the crushed concrete was removed

E.3 Test log of specimen PRCWP 5-S/E1-T

The test was carried out on September 19, 2008 in the Reinforced Concrete Structures Laboratory of the Department of Civil and Industrial Buildings, Faculty of Civil Engineering, Politehnica University of Timisoara, Romania. The experiment was attended by the following individuals: István Demeter, PhD Stud., Cosmin Dăescu, PhD Stud., and Tamás Nagy-György, PhD Lect. The author expresses his grateful acknowledgement for the instrumental contribution of his fellows.

The actual testing time was 7 hours, without interruption. The recorded data file comprises 5834 lines and 23 measuring input columns. The complete instrumentation of the specimen is presented in Appendix C. This test log contains all the recorded responses and the observed behaviour and failure mode in the following order: load versus displacement diagrams, load versus strain diagrams, expanded cyclic load and displacement histories, cracking history, expanded cyclic lateral load versus drift hysteresis loops, commentary on the behaviour mode and test events, and failure details.

Figure E.34 Specimen PRCWP 5-S/E3-T at failure (1% drift ratio)

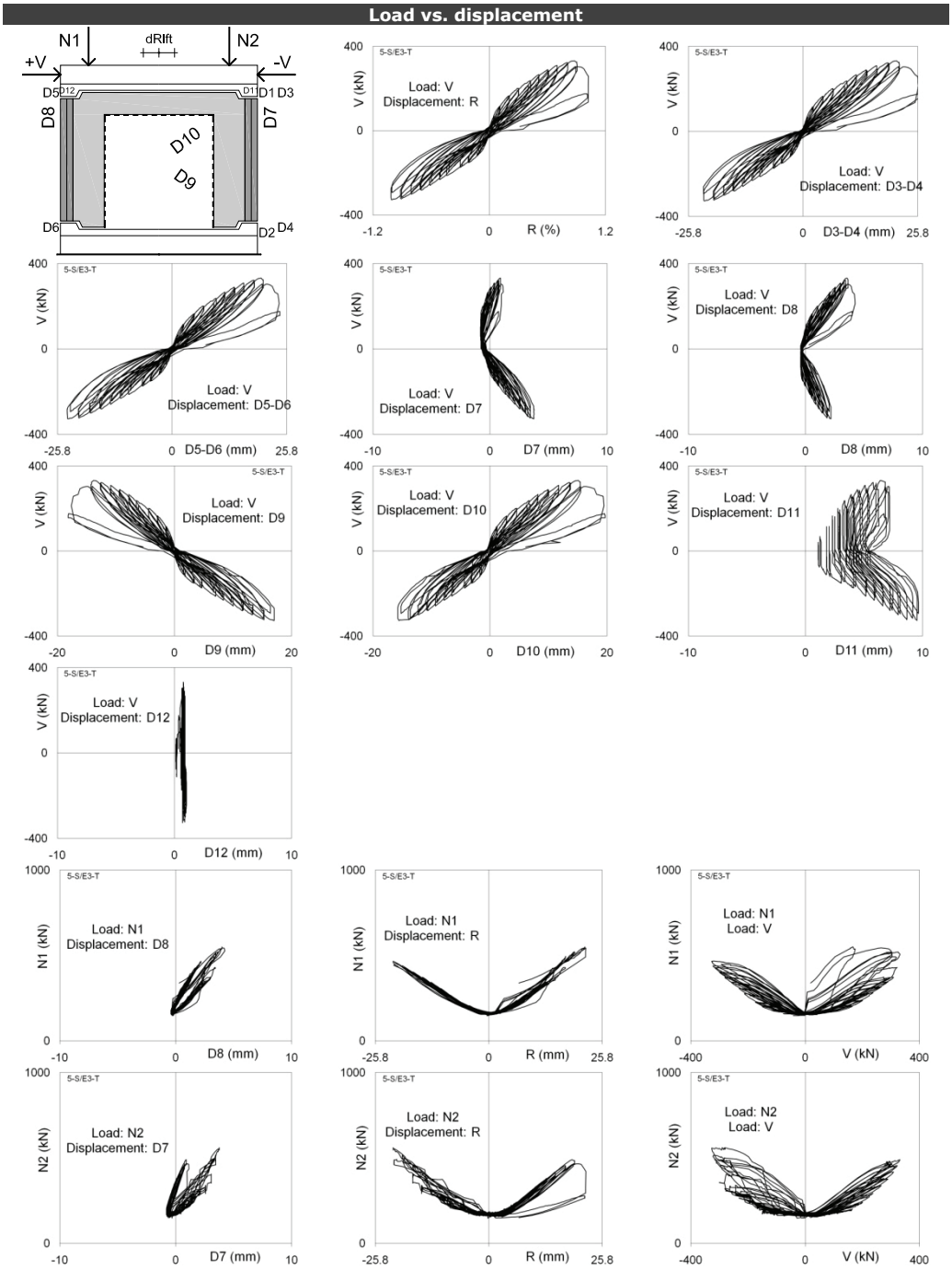

Figure E.35 Load-displacement responses for specimen PRCWP 5-S/E3-T

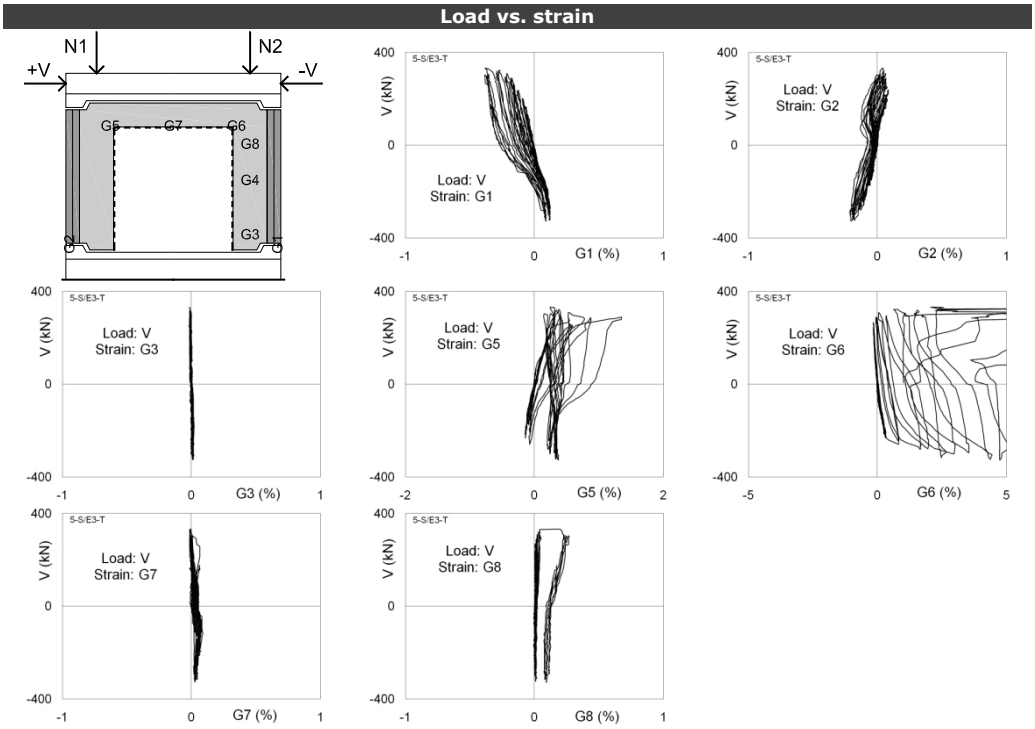

Figure E.36 Load-strain responses for specimen PRCWP 5-S/E3-T

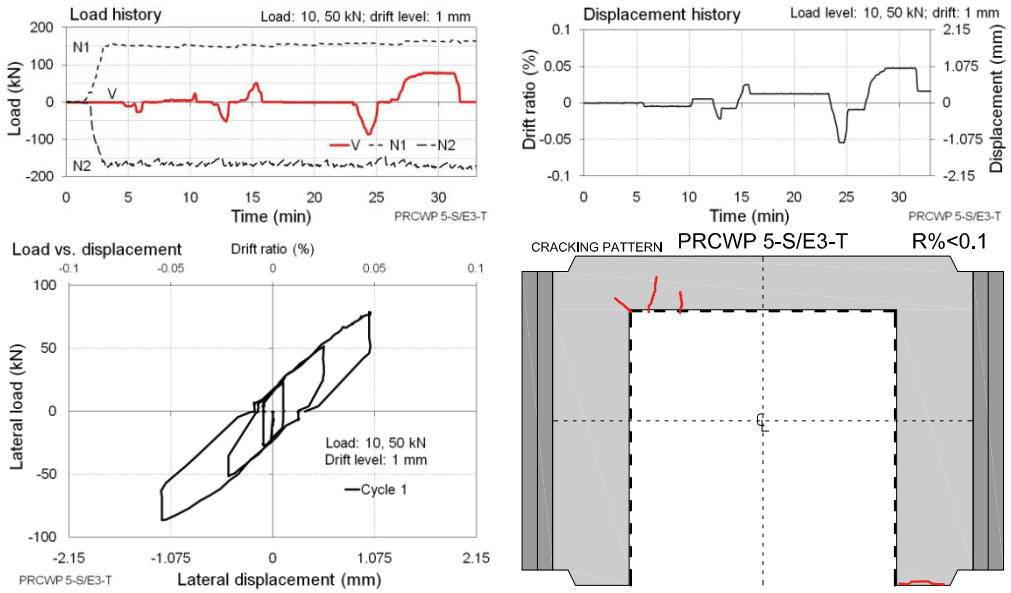

Commentary: Initial cycles were performed at 10 and 50 kN load amplitudes and 1 mm drift. Note the constant level of the axial loads. The N2 load was acting in the same direction as N1; its negative values serve only representation purposes. Cracking initiated at the corners of the opening.

Figure E.37 Expanded cyclic response of PRCWP 5-S/E3-T at the initial cycles

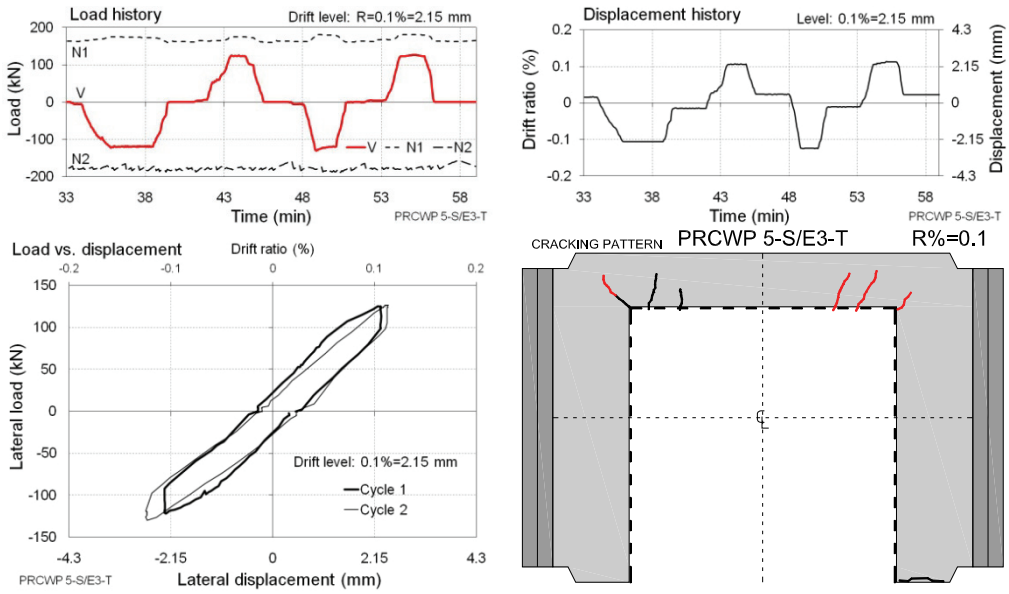

Commentary: Cracking appeared at the spandrel end and at the pier connection.

Figure E.38 Expanded cyclic response of PRCWP 5-S/E3-T at 0.1% drift ratio

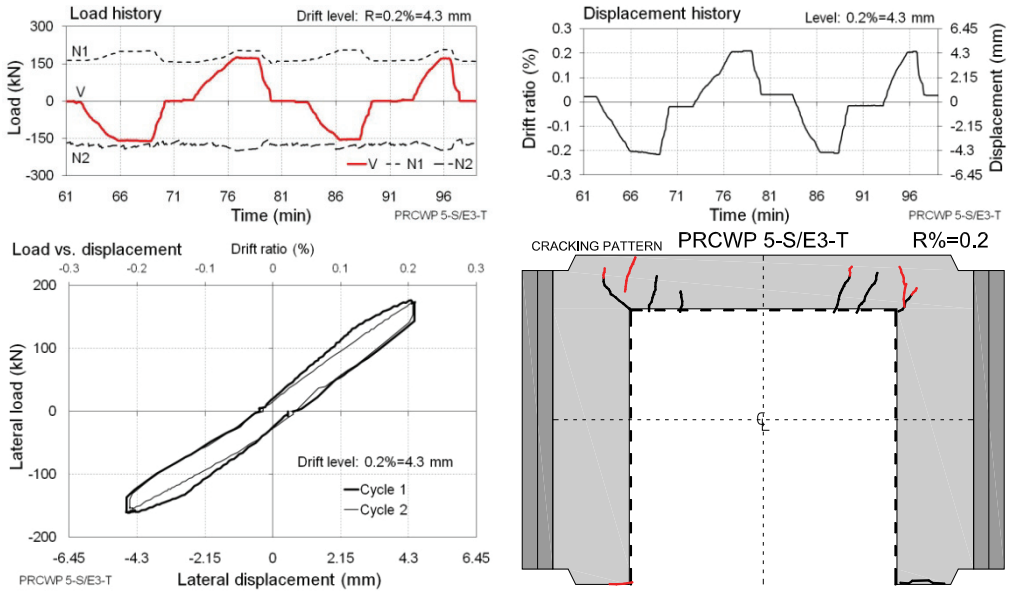

Commentary: Crack development occurred at the spandrel-to-beam connections and at the base of pier#1. Note the incipient waving of the axial loads.

Figure E.39 Expanded cyclic response of PRCWP 5-S/E3-T at 0.2% drift ratio

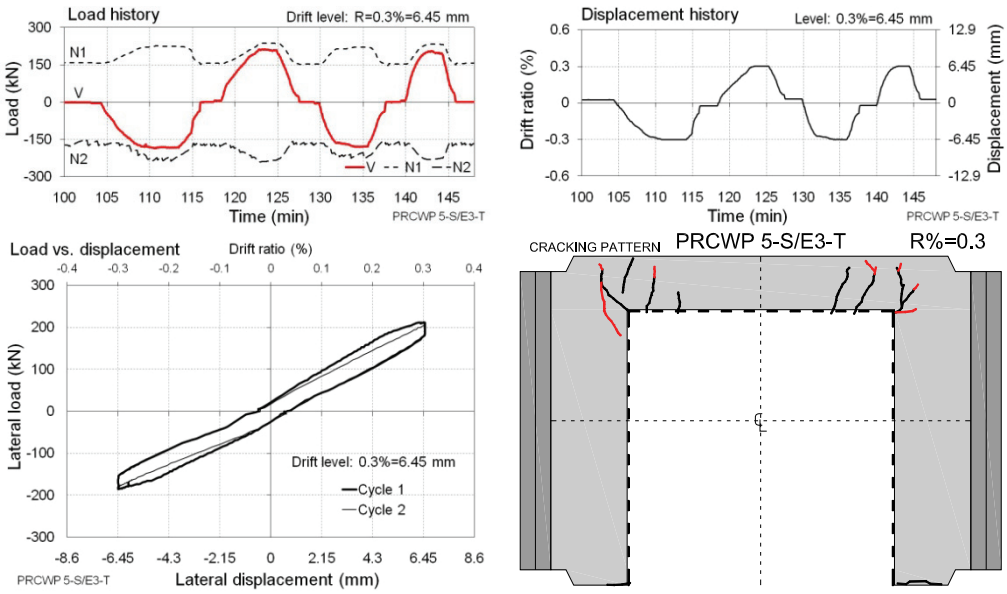

Commentary: The cracks extended at the spandrel-to-pier connections and an inclined crack appeared in pier#1 next to the spandrel end. Note the waving of the axial loads.

Figure E.40 Expanded cyclic response of PRCWP 5-S/E3-T at 0.3% drift ratio

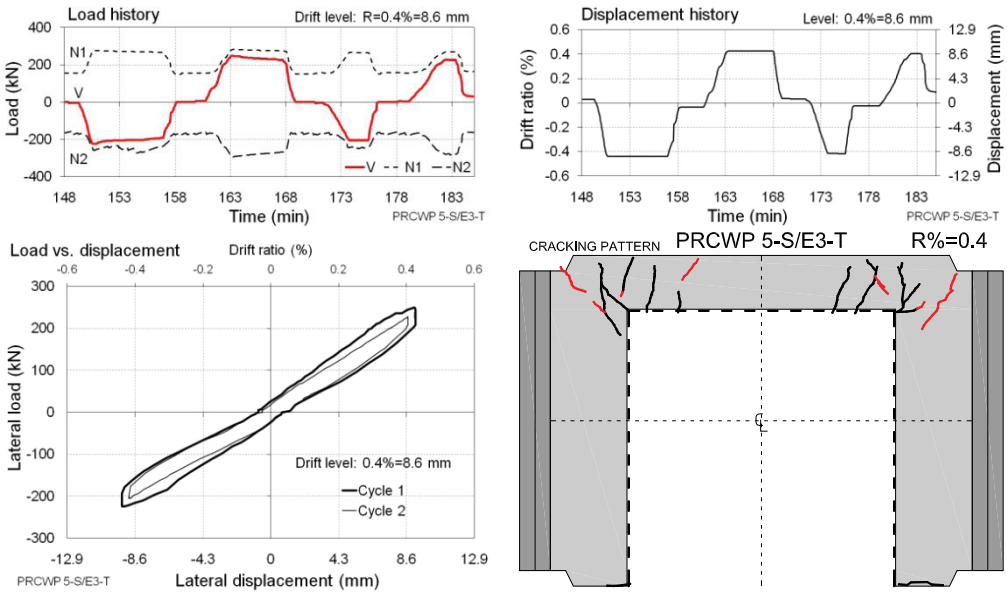

Commentary: Inclined cracks occurred at the top of both piers and at the spandrel beam's ends.

Figure E.41 Expanded cyclic response of PRCWP 5-S/E3-T at 0.4% drift ratio

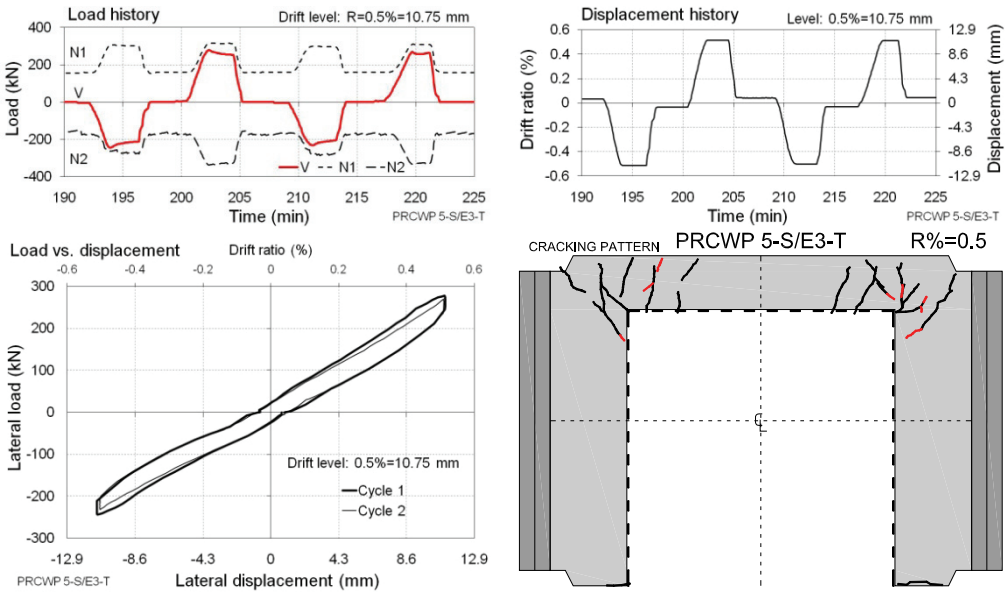

Commentary: Further crack development at the pier-to-beam connection regions.

Figure E.42 Expanded cyclic response of PRCWP 5-S/E3-T at 0.5% drift ratio

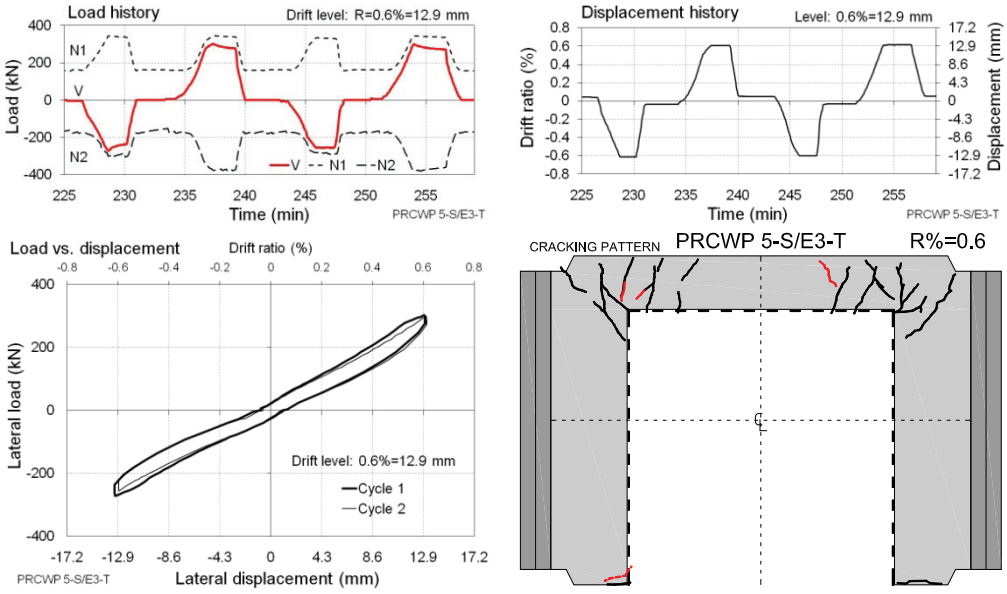

Commentary: In the positive loading direction spalling initiation was observed at the inside toe of pier#1. The inclined cracking at the spandrel end propagated.

Figure E.43 Expanded cyclic response of PRCWP 5-S/E3-T at 0.6% drift ratio

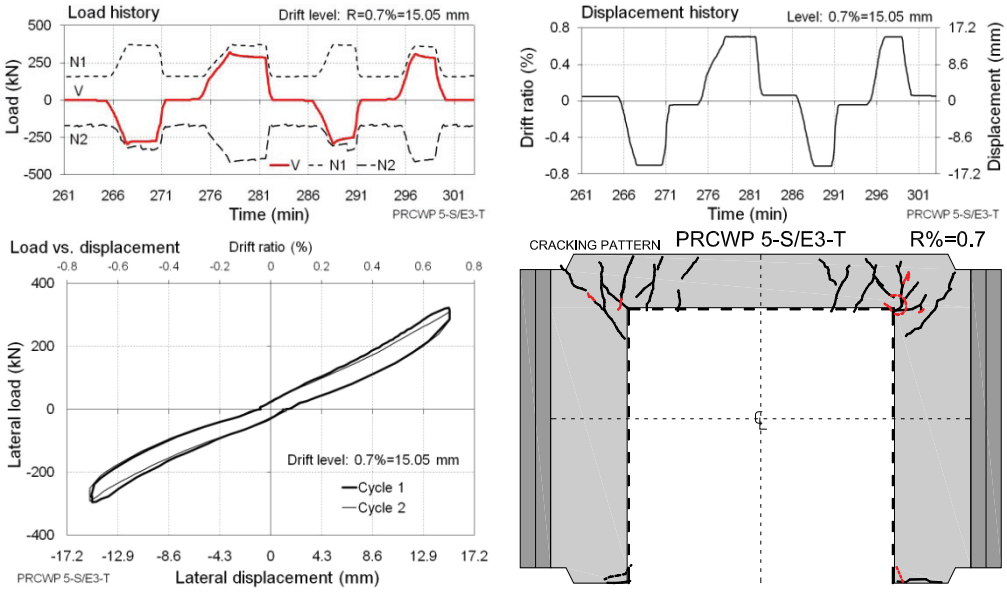

Commentary: Crushing initiation was observed at the upper-right corner of the opening and at the inside toe of pier#2.

Figure E.44 Expanded cyclic response of PRCWP 5-S/E3-T at 0.7% drift ratio

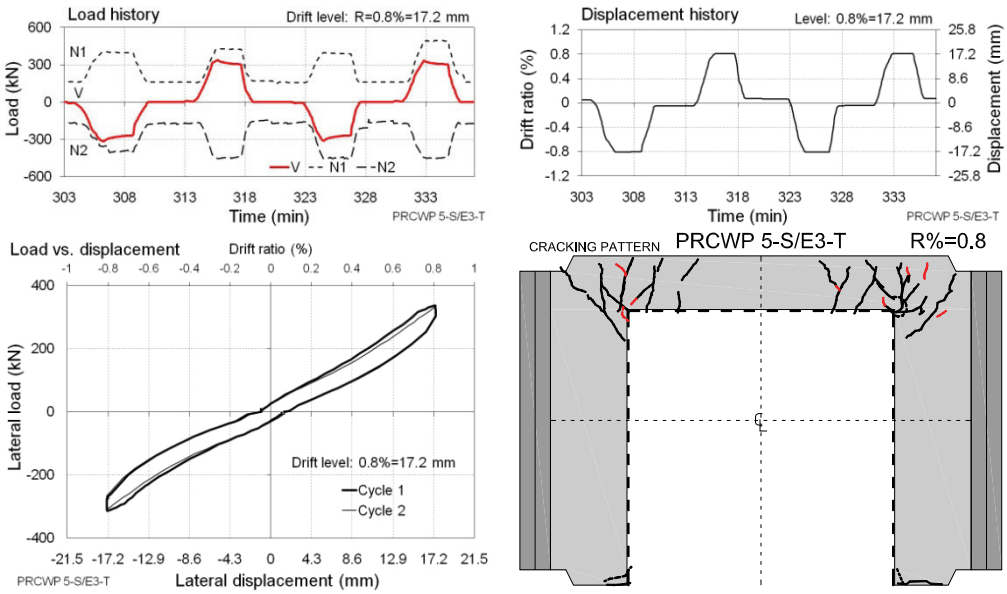

Commentary: Further crack development occurred at both pier-to-spandrel connection regions and crushing initiated at the upper-left corner of the opening.

Figure E.45 Expanded cyclic response of PRCWP 5-S/E3-T at 0.8% drift ratio

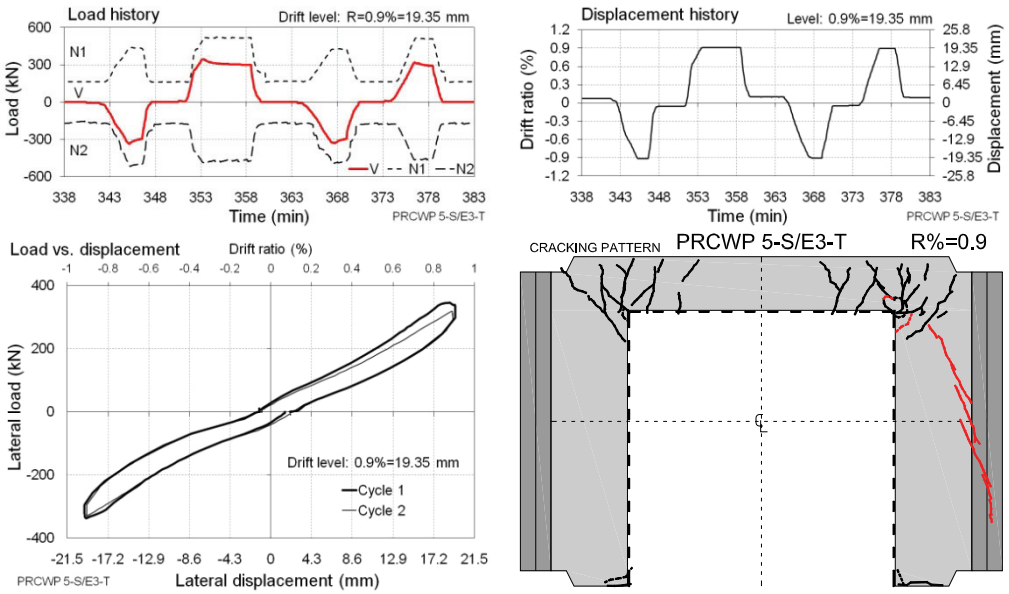

Commentary: In the positive loading direction inclined cracks appeared across pier#2 extending at 65 deg angle. Concrete crushing propagated next to the upper-right corner of the opening.

Figure E.46 Expanded cyclic response of PRCWP 5-S/E3-T at 0.9% drift ratio

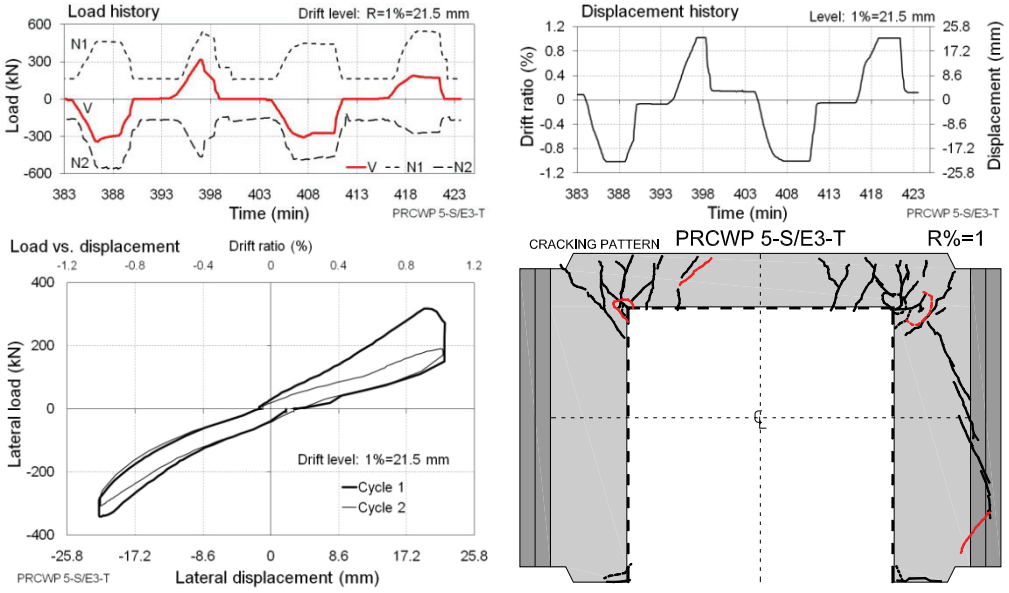

Commentary: In the negative loading direction crushing of concrete and inclined cracking propagated at the upper-left corner of the opening and on the spandrel beam, respectively. The failure occurred in the subsequent positive loading direction by severe concrete crushing at the spandrel-to-pier#2 connection. The examination of the wall specimen after the test revealed that the damage extension was much larger than it seemed at first glance: at both pier-to-beam connection regions the concrete was crushed in the full depth of the spandrel, refer to Figures.

Figure E.47 Expanded cyclic response of PRCWP 5-S/E3-T at 1% drift ratio

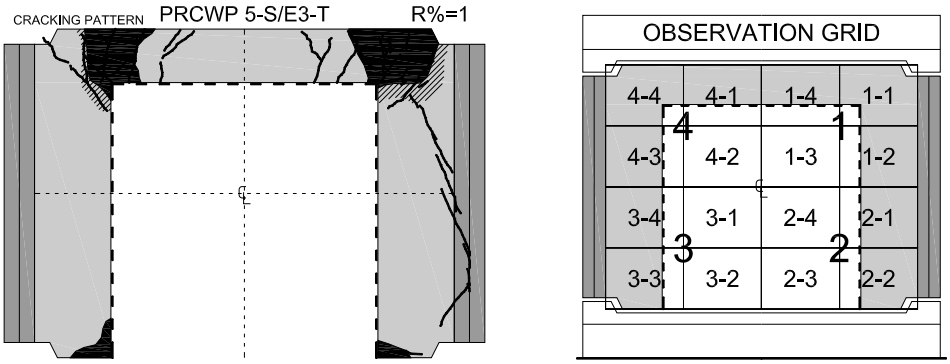

Figure E.48 Cracking pattern and observation grid PRCWP 5-S/E3-T

Figure E.49 Failure detail PRCWP 5-S/E3-T: concrete crushing at the spandrel-to-pier#2 connection (close-up on observation grid 1-1)

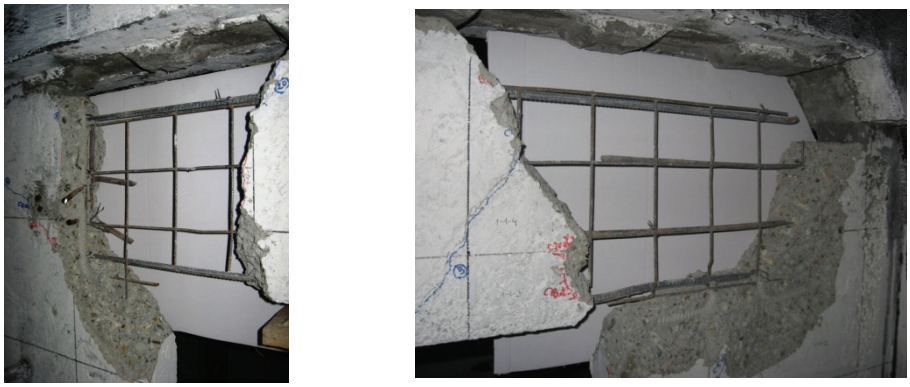

(a) (b)

Figure E.50 Failure detail PRCWP 5-S/E3-T: spandrel-to-pier connections after the crushed concrete was removed (close-up on observation grid 4-4 and 1-1)


Figure E.51 Failure detail PRCWP 5-S/E3-T: concrete crushing at the inside toe of pier#1 (close-up on grid 3-3)


Figure E.52 Failure detail PRCWP 5-S/E3-T: the pier toes after crushed concrete was removed (close-up on observation grid 3-3 and 2-2)

Figure E.53 Failure detail PRCWP 5-S/E3-T: general view after the crushed concrete was removed

E.4 Test log of specimen PRCWP 3-S/E1-T/R

The test was carried out during August 12-13, 2008 in the Reinforced Concrete Structures Laboratory of the Department of Civil and Industrial Buildings, Faculty of Civil Engineering, Politehnica University of Timisoara, Romania. The experiment was attended by the following individuals: István Demeter, PhD Stud., Tamás Nagy-György, PhD Lect., Cosmin Dăescu, PhD Stud., Gabriel Sas, PhD Stud., Codruț Floruț, PhD Stud., Valeriu Stoian, PhD Prof., and Mircea Marity, metal craftsman. The author expresses his grateful acknowledgement for the instrumental contribution of his fellows.

The actual testing time was 8½ hours, segmented in two parts by one day of interruption. The recorded data file comprises 5982 lines and 29 measuring input columns. The complete instrumentation of the specimen is presented in Appendix C. This test log contains all the recorded responses and the observed behaviour and failure mode in the following order: load versus displacement diagrams, load versus strain diagrams, expanded cyclic load and displacement histories, cracking history, expanded cyclic lateral load versus drift hysteresis loops, commentary on the behaviour mode and test events, and failure details.

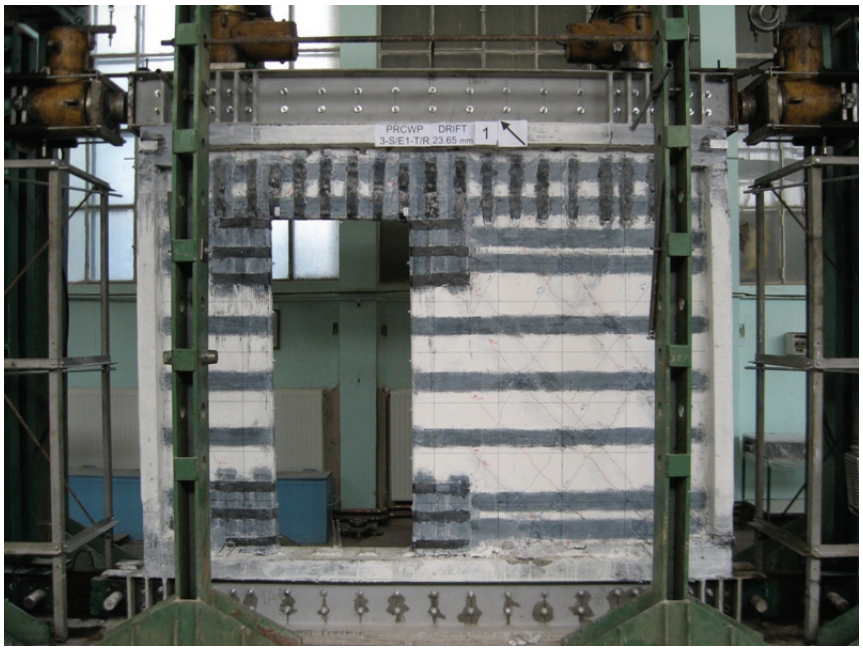

Figure E.54 Specimen PRCWP 3-S/E1-T/R at failure (1.1% drift ratio)

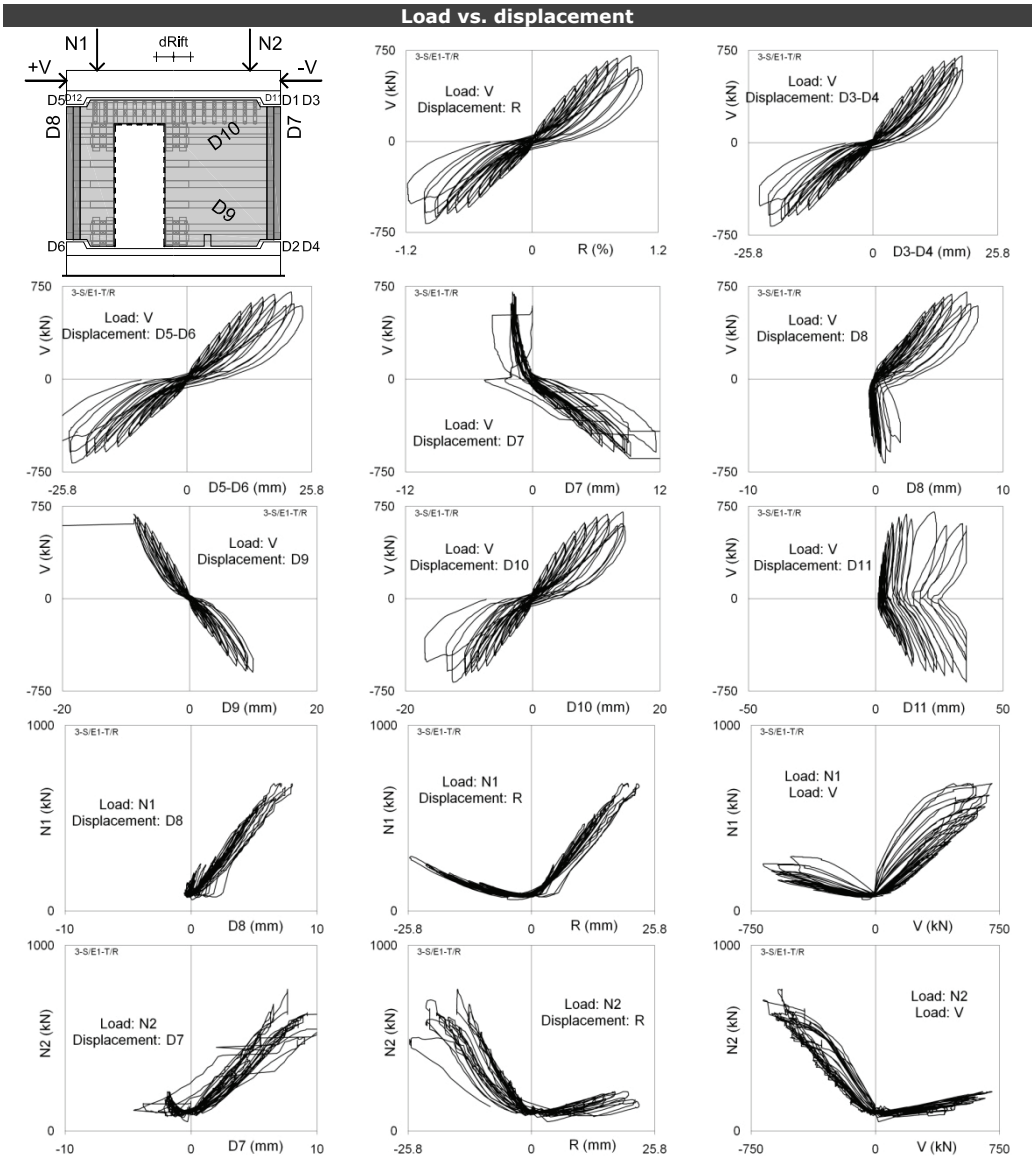

Figure E.55 Load-displacement responses for specimen PRCWP 3-S/E1-T/R

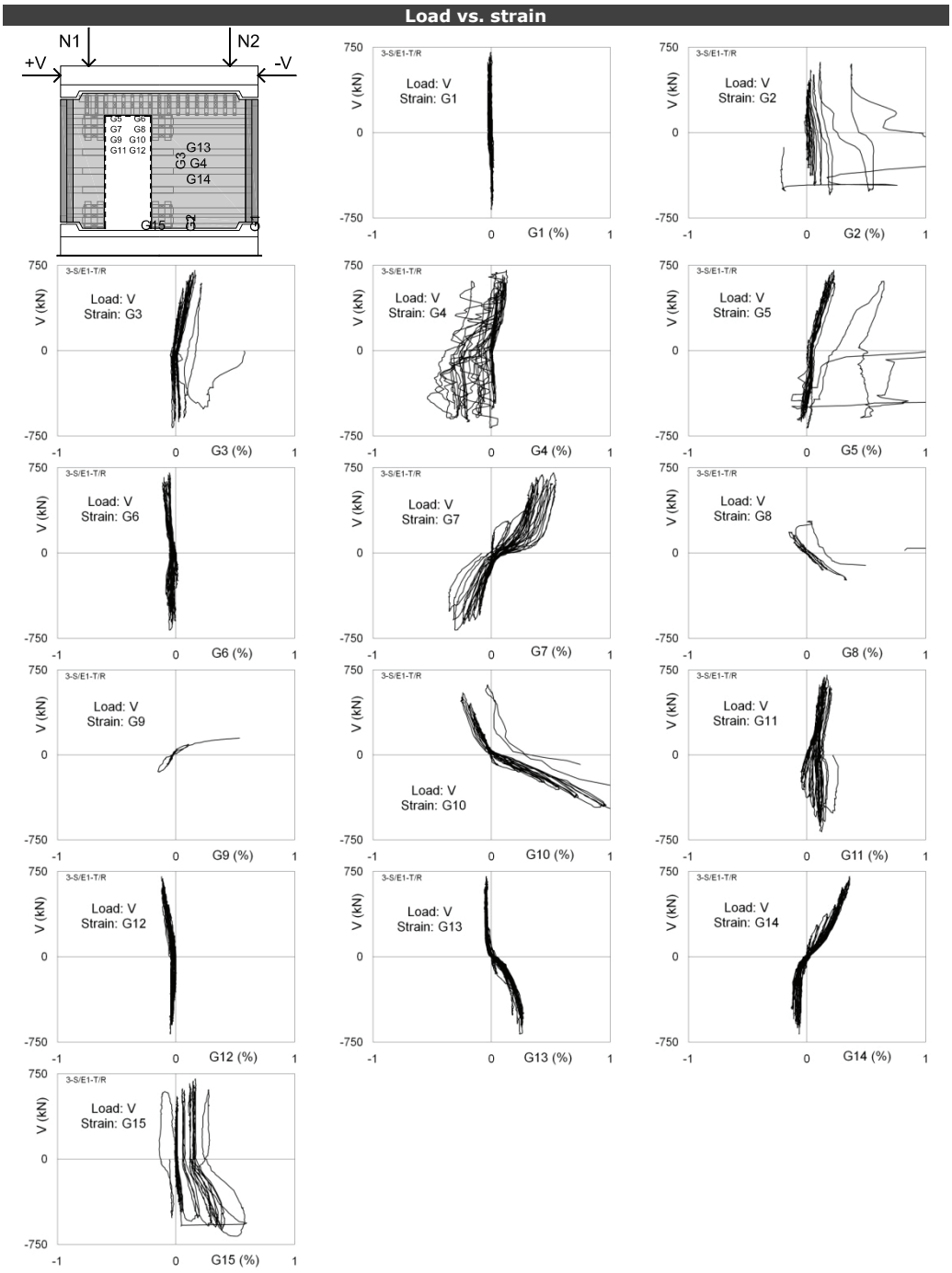

Figure E.56 Load-strain responses for specimen PRCWP 3-S/E1-T/R

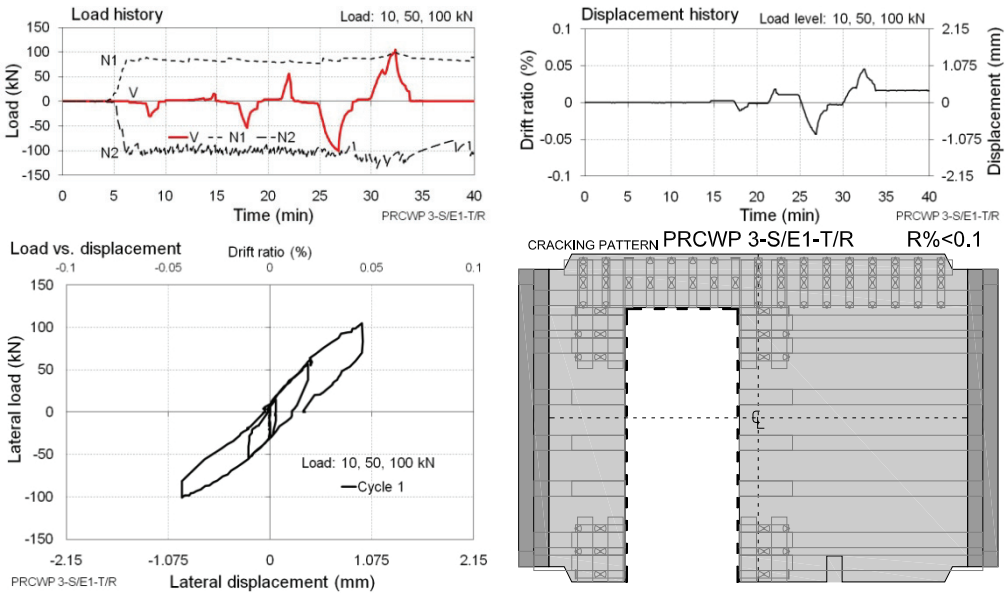

Commentary: Load-controlled cycles were performed at 10, 50, and 100 kN amplitudes. Soft snapping sounds were heard as the FRP composites deformed.

Figure E.57 Expanded cyclic response of PRCWP 3-S/E1-T/R at the initial cycles

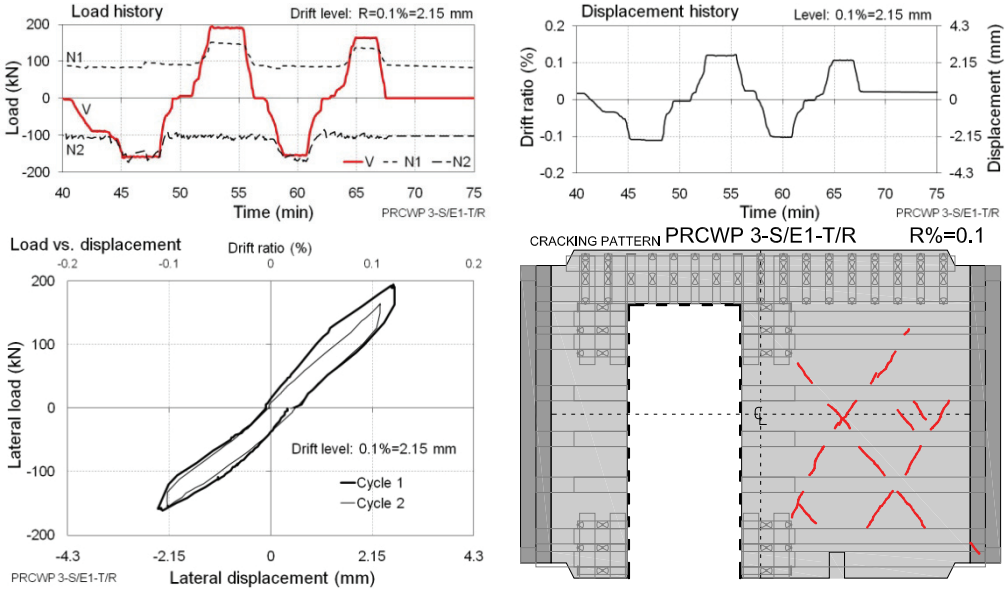

Commentary: Pre-existing inclined cracks opened across pier#2. The inspection for cracks at the spandrel-to-pier connection regions was impeded by the congestion of the FRP strips. The snapping sounds intensified as the FRPs deformed.

Figure E.58 Expanded cyclic response of PRCWP 3-S/E1-T/R at 0.1% drift ratio

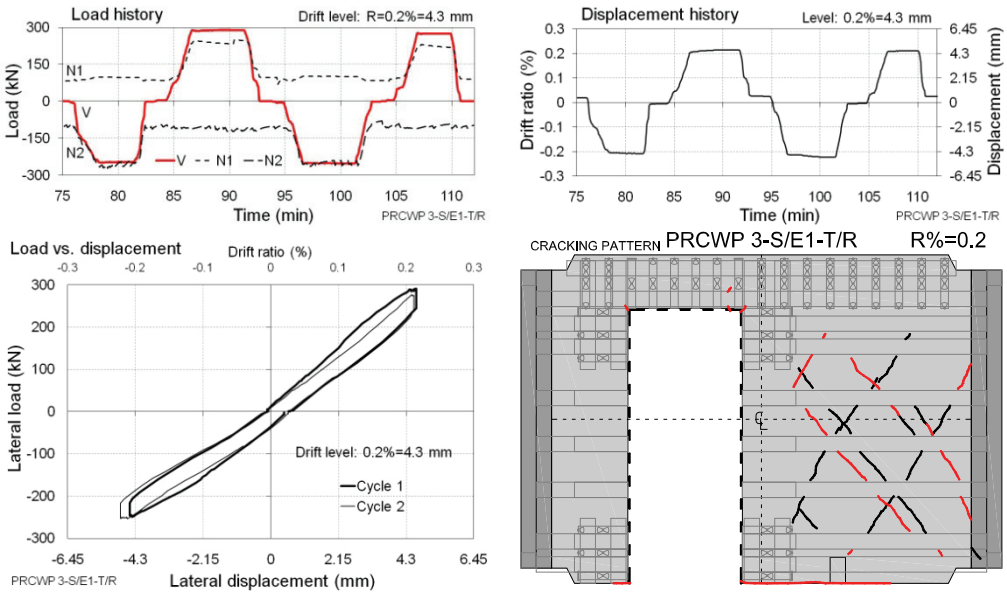

Commentary: Further existing cross-diagonal cracks opened in pier#2. Horizontal cracks developed along the wall-to-foundation joint. Short crack segments were noticed at the pier-to-beam connection extending from the opening corners.

Figure E.59 Expanded cyclic response of PRCWP 3-S/E1-T/R at 0.2% drift ratio

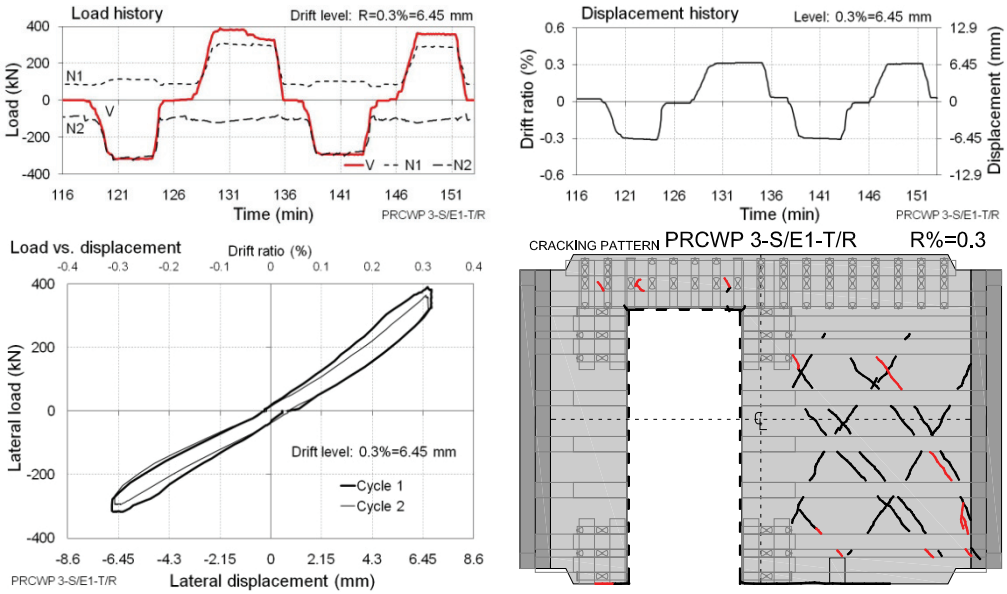

Commentary: Short inclined cracks appeared on the spandrel. Further existing cracks opened in pier#2.

Figure E.60 Expanded cyclic response of PRCWP 3-S/E1-T/R at 0.3% drift ratio

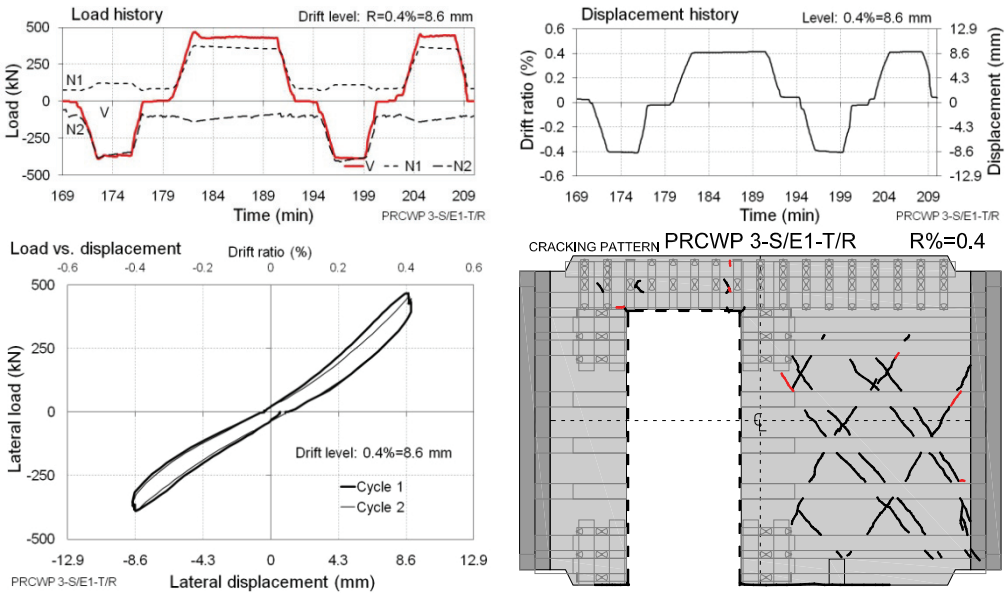

Commentary: Fracture of the vertical FRP strip occurred near the upper-left corner of the opening. Crack propagation was noticed through the FRP strips at the 1-2 observation grid (for the location of the observation grids refer to Annex and Figure)

Figure E.61 Expanded cyclic response of PRCWP 3-S/E1-T/R at 0.4% drift ratio

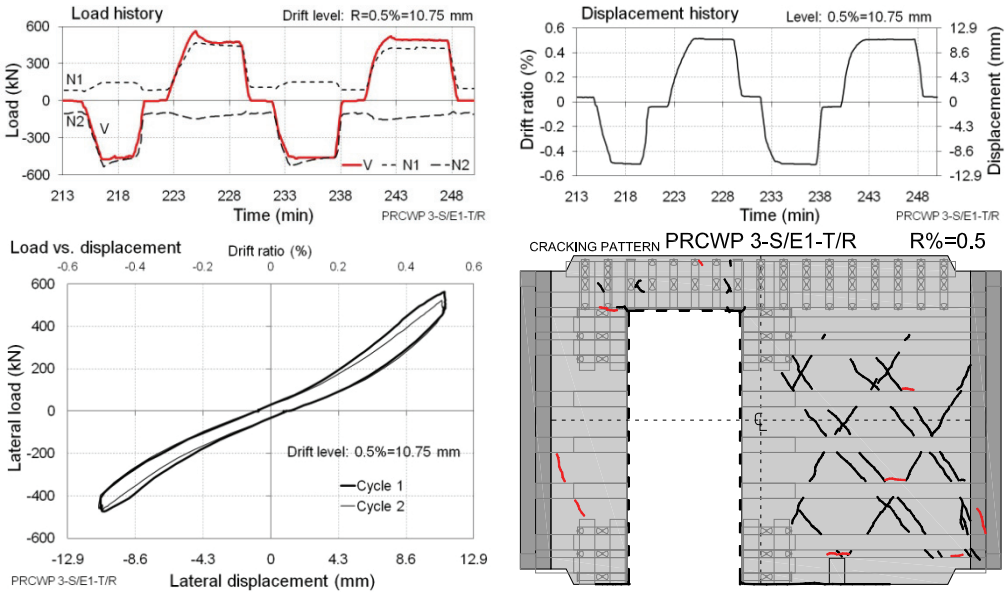

Commentary: Onset of FRP debonding was observed along the horizontal strips on pier#2 at the intersection with inclined cracks. Continuous FRP-snapping was heard during unloading.

Figure E.62 Expanded cyclic response of PRCWP 3-S/E1-T/R at 0.5% drift ratio

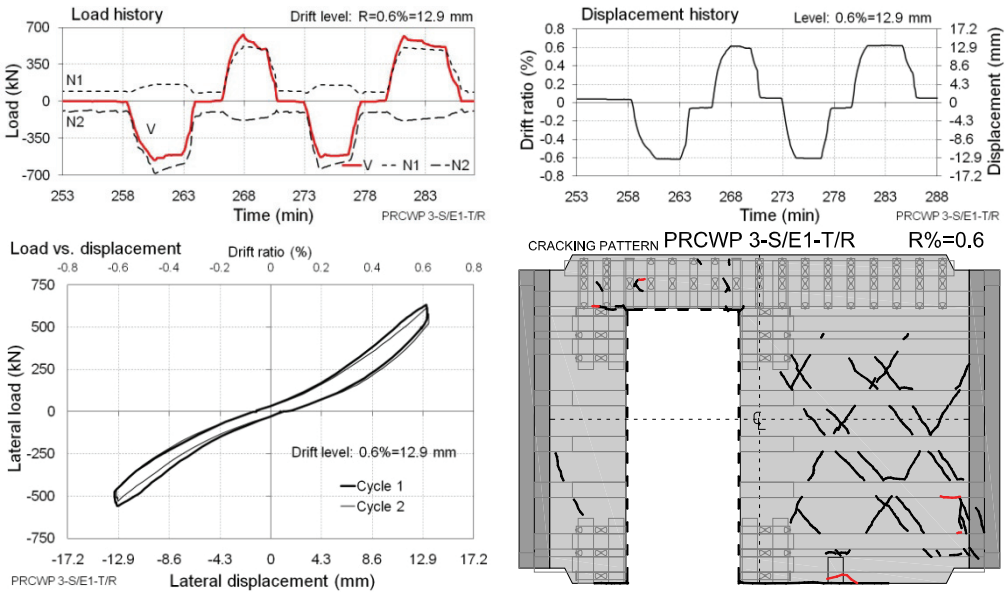

Commentary: Further FRP debonding initiation was noticed along the edge-line of horizontal strips at crack crossing on pier#2. The test was halted till the next day.

Figure E.63 Expanded cyclic response of PRCWP 3-S/E1-T/R at 0.6% drift ratio

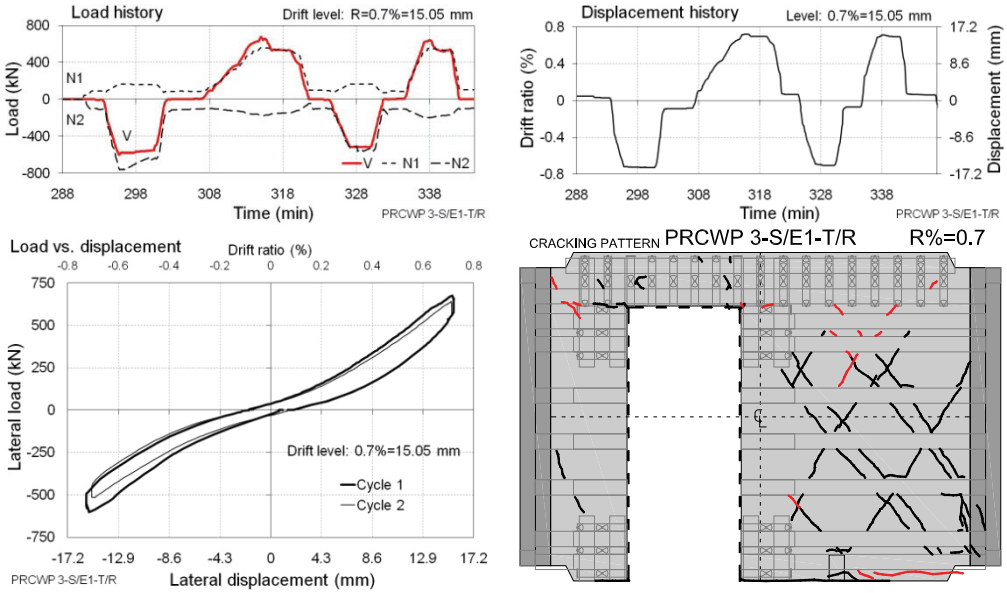

Commentary: New inclined crack occurred across pier#2 and the horizontal crack at the base extended significantly. Note the waving of the axial loads.

Figure E.64 Expanded cyclic response of PRCWP 3-S/E1-T/R at 0.7% drift ratio

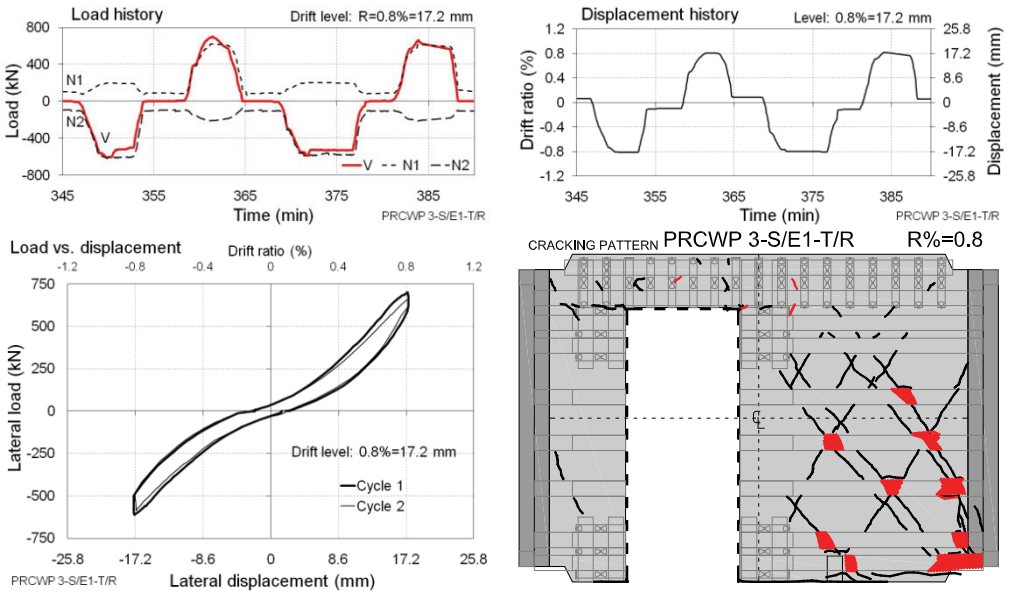

Commentary: A tapping inspection of the FRPs indicated that the horizontal strips on pier#2 debonded at the intersections with inclined cracks. Fracture of the vertical FRP strip occurred at the upper-right corner of the opening. The support of the D9 transducer fell off due to damage of the substrate at the outside toe of pier#2.

Figure E.65 Expanded cyclic response of PRCWP 3-S/E1-T/R at 0.8% drift ratio

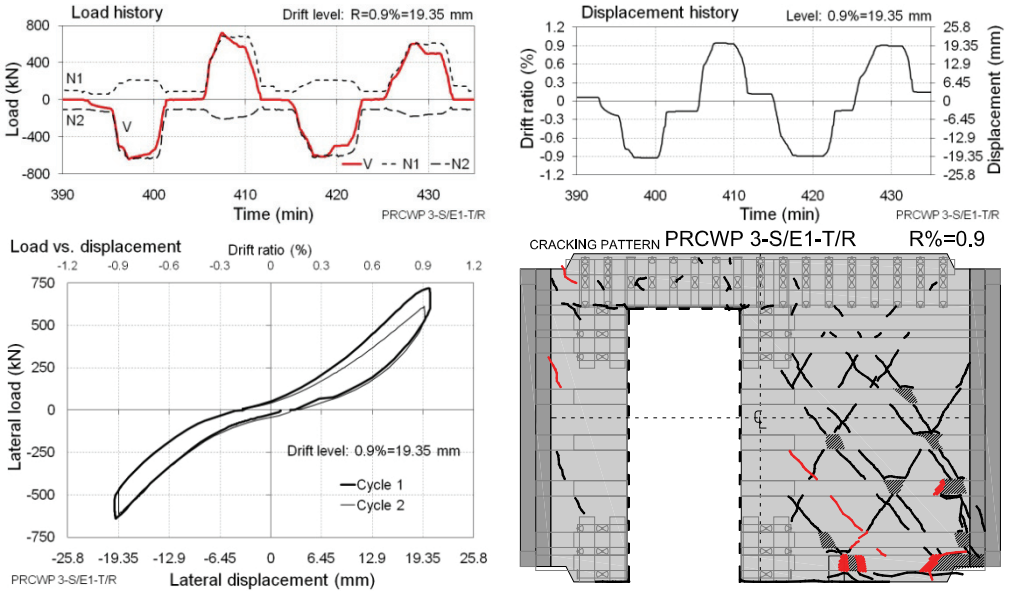

Commentary: Inclined crack appeared at the lower half of pier#2 in the positive loading direction of cycle #1. In the same direction of cycle #2 severe crushing of concrete occurred at the outside toe of pier#2 (observation grid 2-2).

Figure E.66 Expanded cyclic response of PRCWP 3-S/E1-T/R at 0.9% drift ratio

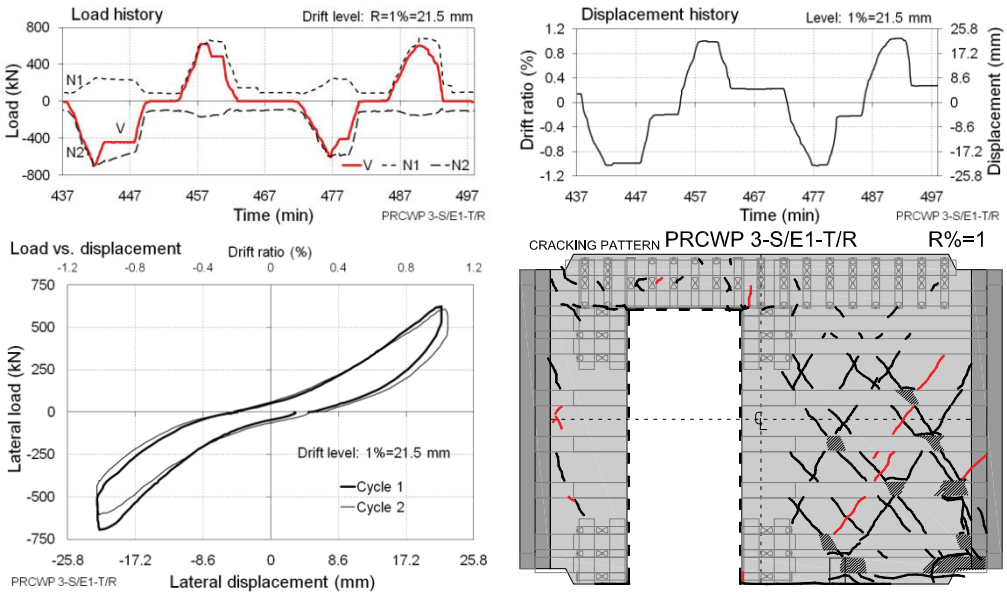

Commentary: Inclined cracking occurred across pier#2 in the negative loading direction of cycle #1. At the inside toe of pier#2 compression bulging of the vertical FRP strips was observed between the horizontal confinement strips. At the same location and in the same loading direction of cycle #2 the FRP-confinement fractured.

Figure E.67 Expanded cyclic response of PRCWP 3-S/E1-T/R at 1% drift ratio

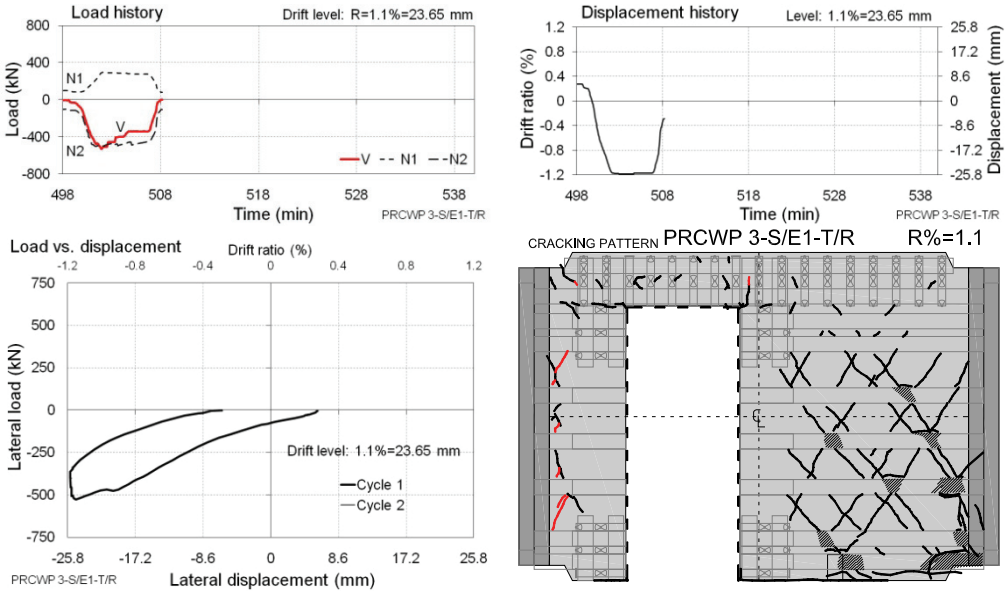

Commentary: The failure criterion of 20% loss of load capacity was accomplished. A series of vertical cracks developed along pier#1-to-wing joint.

Figure E.68 Expanded cyclic response of PRCWP 3-S/E1-T/R at 1.1% drift ratio

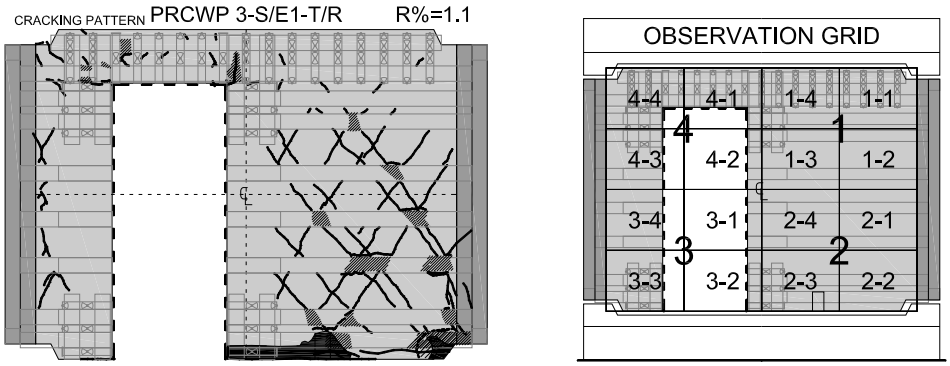

Figure E.69 Cracking pattern and observation grid PRCWP 3-S/E1-T/R

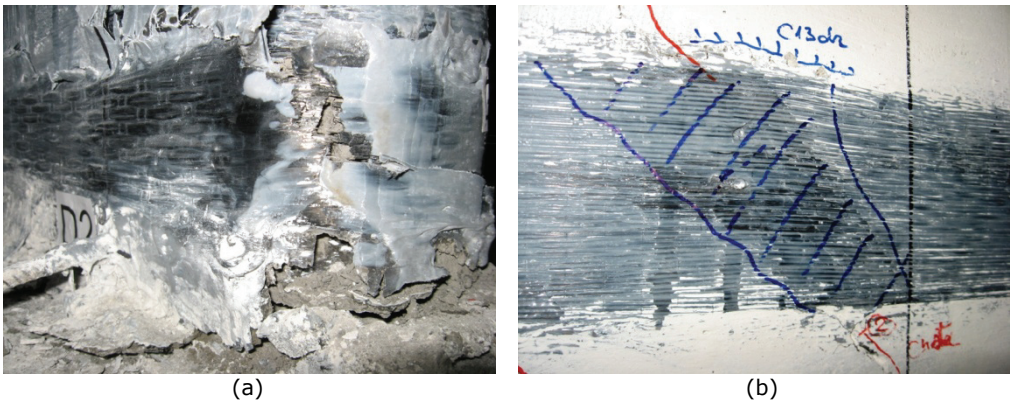

(a) (b)

Figure E.70 Failure detail PRCWP 3-S/E1-T/R: (a) FRP-confinement fracture at inside the toe of pier#2 (observation grid 3-2); (b) FRP debonding at inclined crack across pier#2 (observation grid 1-2)

Figure E.71 Failure detail PRCWP 3-S/E1-T/R: bulging of vertical FRP at the toe of pier#2 (observation grid 3-2)

Figure E.72 Failure detail PRCWP 3-S/E1-T/R: FRP debonding and concrete crushing at the outside toe of pier#2 (observation grid 2-2)

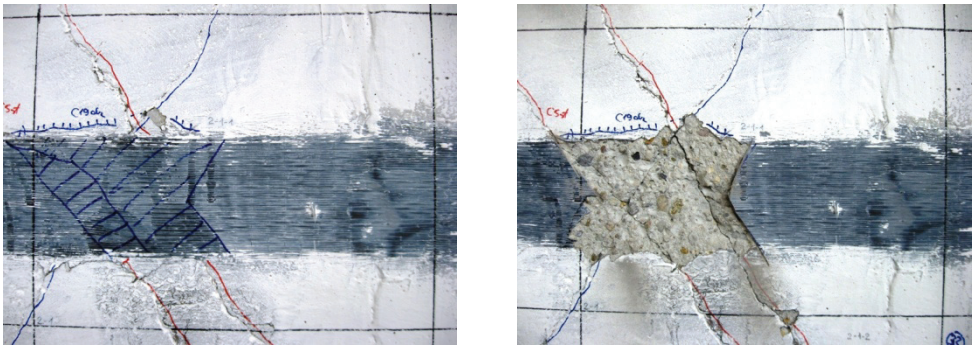

Figure E.73 Failure detail PRCWP 3-S/E1-T/R: FRP debonding at inclined crack crossing on pier#2 (observation grid 2-1)

E.5 Test log of specimen PRCWP 4-S/E1-R/T

The test was carried out during January 22-23, 2009 in the Reinforced Concrete Structures Laboratory of the Department of Civil and Industrial Buildings, Faculty of Civil Engineering, Politehnica University of Timisoara, Romania. The experiment was attended by the following individuals: István Demeter, PhD Stud., Tamás Nagy-György, PhD Lect., Cosmin Dăescu, PhD Stud., Codruț Floruț, PhD Stud., and Valeriu Stoian, PhD Prof. The author expresses his grateful acknowledgement for the instrumental contribution of his fellows.

The actual testing time was 7 hours, segmented in two parts by one day of interruption. The recorded data file comprises 30677 lines and 29 measuring input columns. The complete instrumentation of the specimen is presented in Appendix C. This test log contains all the recorded responses and the observed behaviour and failure mode in the following order: load versus displacement diagrams, load versus strain diagrams, expanded cyclic load and displacement histories, cracking history, expanded cyclic lateral load versus drift hysteresis loops, commentary on the behaviour mode and test events, and failure details.

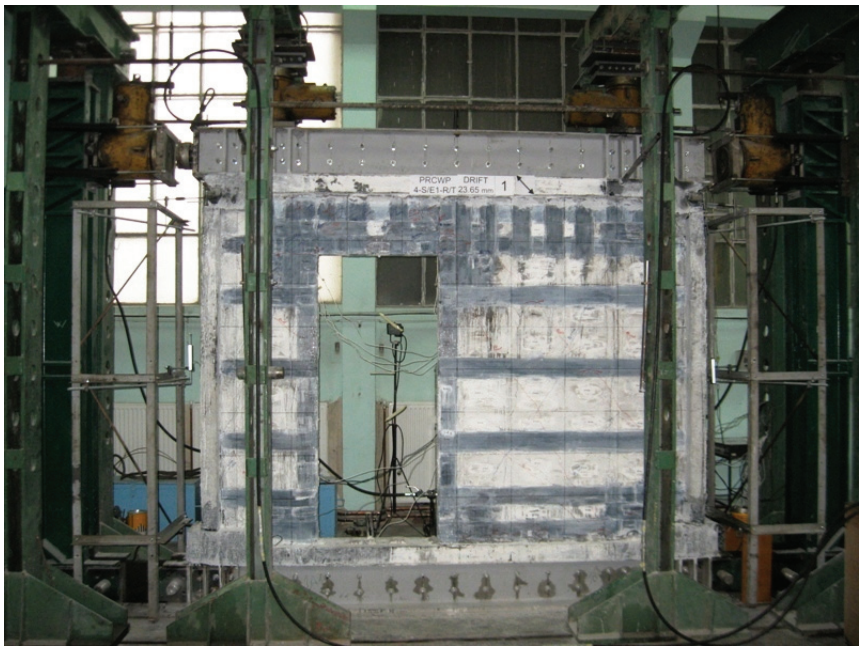

Figure E.74 Specimen PRCWP 4-S/E1-R/T at failure (1.1% drift ratio)

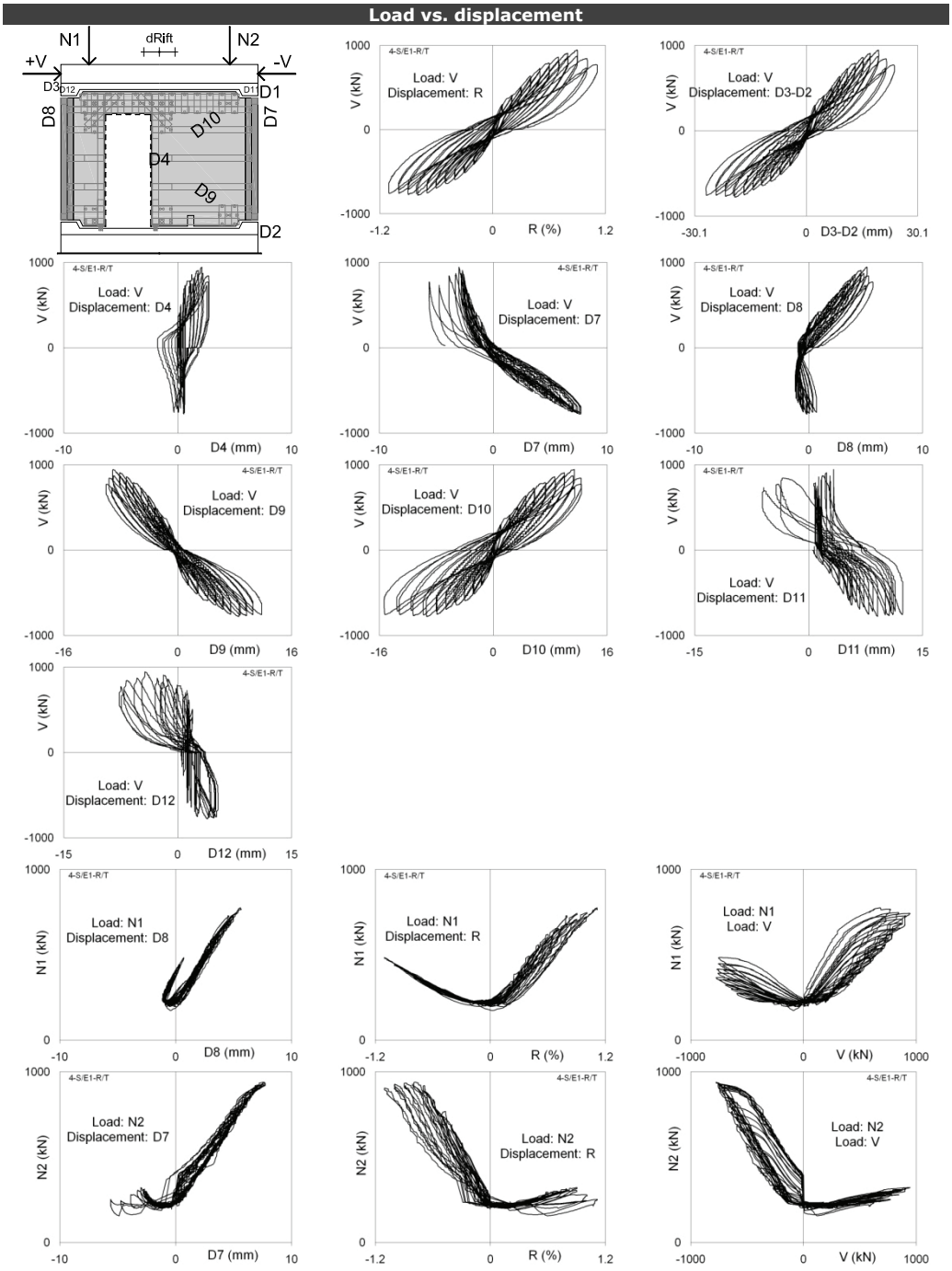

Figure E.75 Load-displacement responses for specimen PRCWP 4-S/E1-R/T

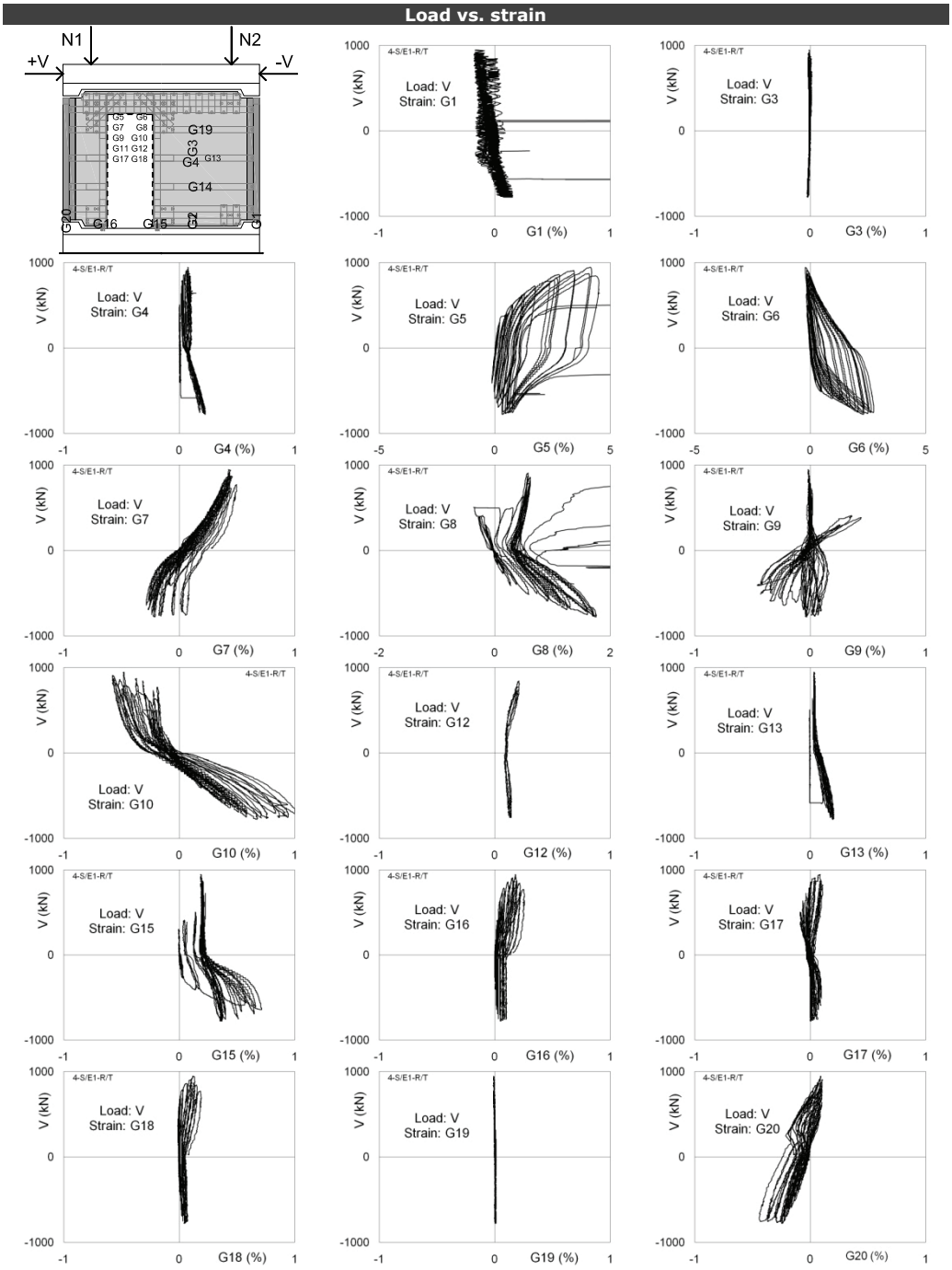

Figure E.76 Load-strain responses for specimen PRCWP 4-S/E1-R/T

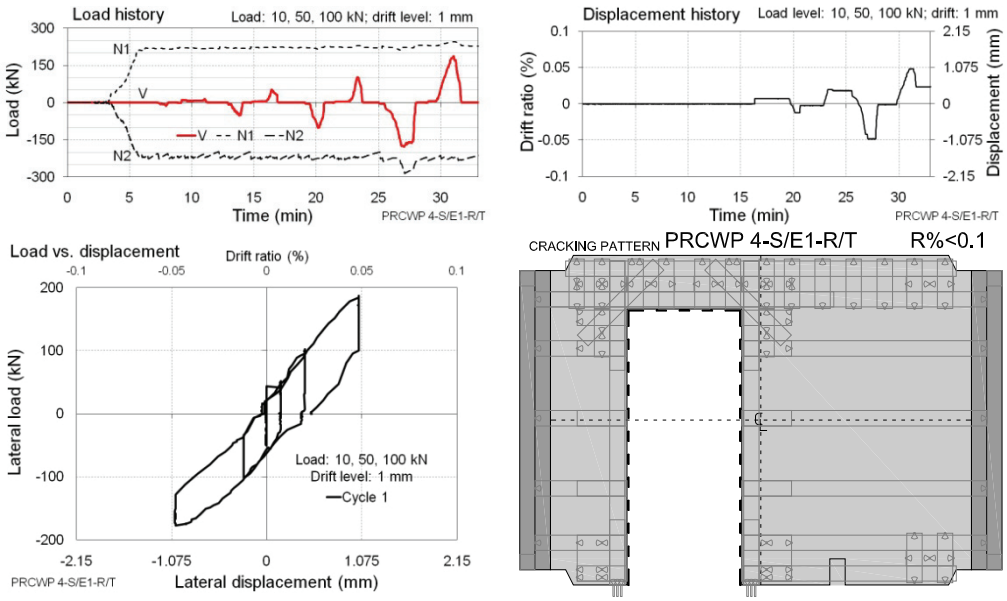

Commentary: Load reversals were carried out at 10, 50, 100 kN amplitudes and at 1 mm drift. Note the stillness of the axial loads at the initial level of N1=N2=219 kN.

Figure E.77 Expanded cyclic response of PRCWP 4-S/E1-R/T at the initial cycles

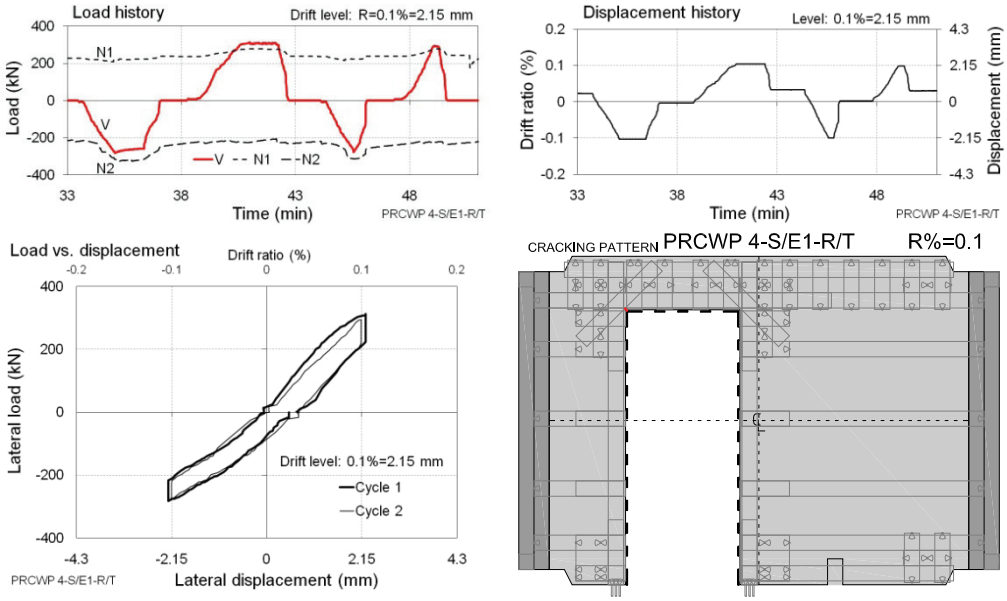

Commentary: Cracking initiation was observed at the pier#1-to-spandrel connection extending from the upper-left corner of the opening. Crack tracking at these regions was impeded by FRP congestion. Snapping sounds were heard as the FRPs deformed. Note the incipient waving of the axial loads.

Figure E.78 Expanded cyclic response of PRCWP 4-S/E1-R/T at 0.1% drift ratio

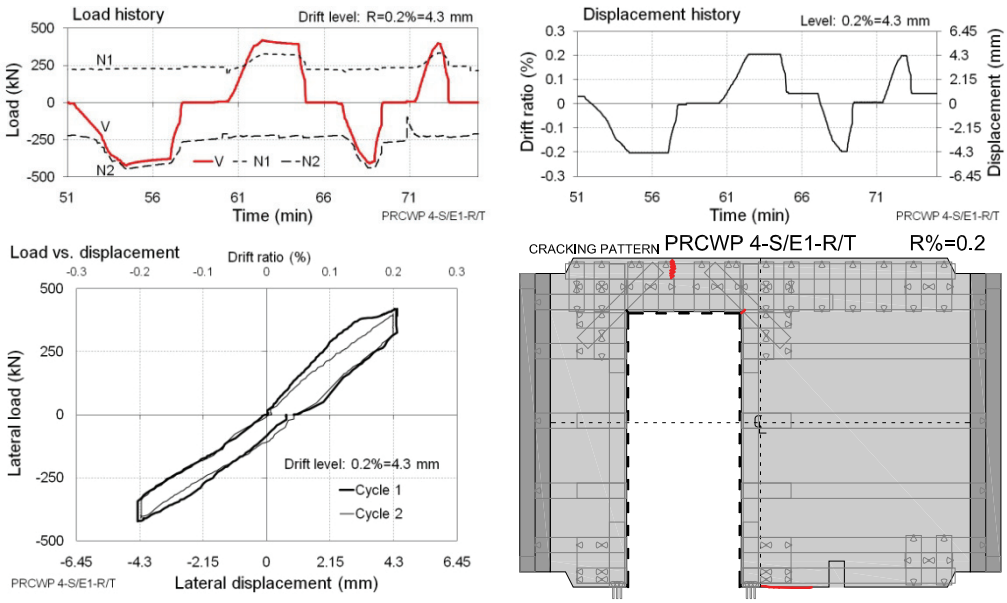

Commentary: Cracks appeared at the pier#2-to-spandrel connection extending from the upper-right corner of the opening and at the base of pier#2. FRP debonding was noticed on the spandrel accompanied by FRP-snapping sounds.

Figure E.79 Expanded cyclic response of PRCWP 4-S/E1-R/T at 0.2% drift ratio

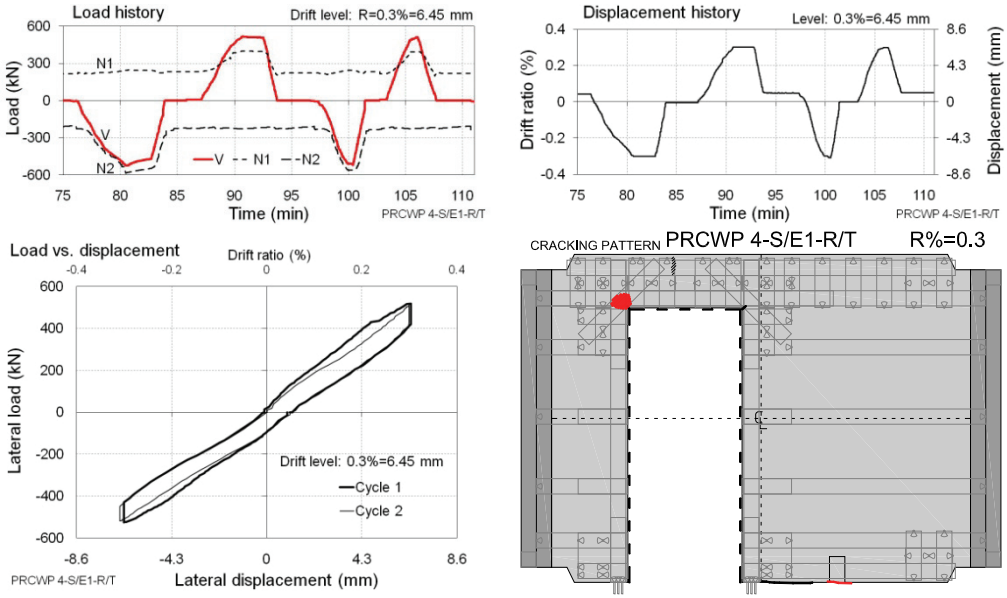

Commentary: FRP debonding occurred at the spandrel-to-pier#1 connection next to the opening corner. The base crack extended.

Figure E.80 Expanded cyclic response of PRCWP 4-S/E1-R/T at 0.3% drift ratio

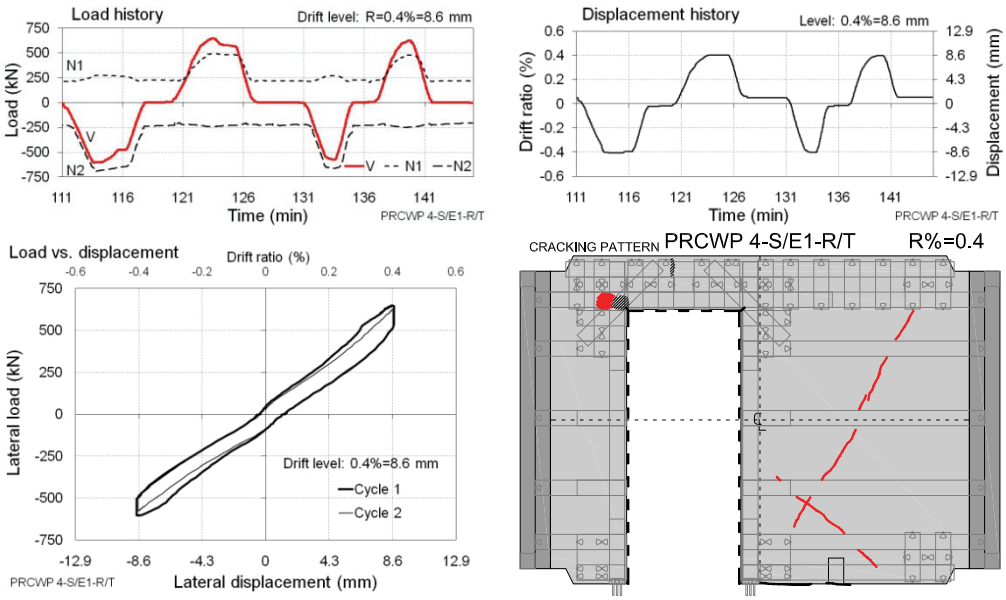

Commentary: Diagonal cracking developed in pier#2 running at 61 deg in the negative direction and at 42 deg in the positive direction. The FRP debonding extended. The cover concrete of the foundation beam spalled around the FRP-anchorage at the inside toe of pier#2.

Figure E.81 Expanded cyclic response of PRCWP 4-S/E1-R/T at 0.4% drift ratio

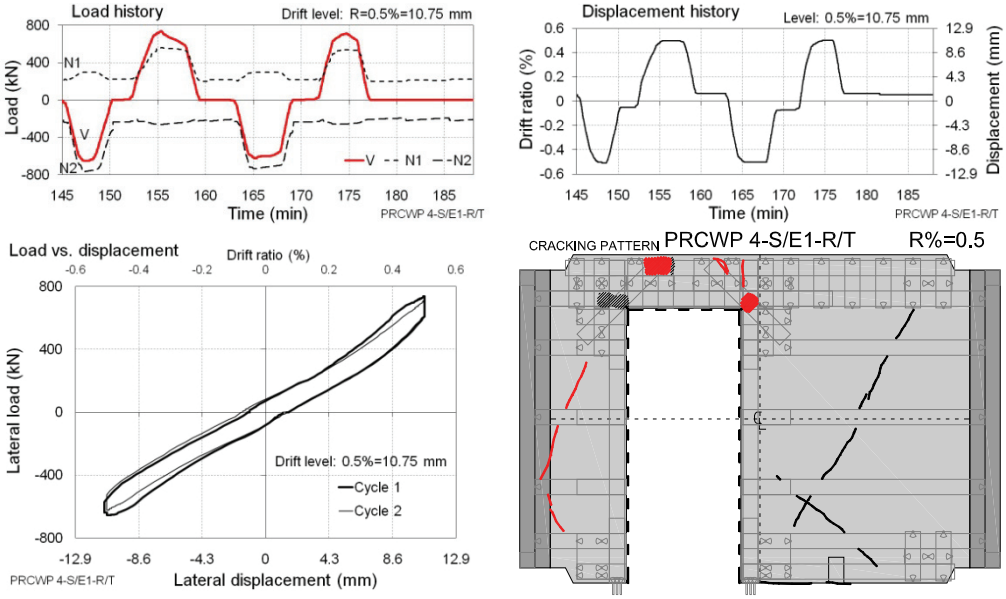

Commentary: In the positive loading direction of the first cycle FRP debonding was observed at the pier#2-to-spandrel connection next to the opening corner concurrently with the development of a vertical crack above this location. In the negative loading direction of cycle #2 diagonal cracking appeared across pier#1 extending at 68 deg angle and FRP debonding took place at the upper part of the spandrel.

Figure E.82 Expanded cyclic response of PRCWP 4-S/E1-R/T at 0.5% drift ratio

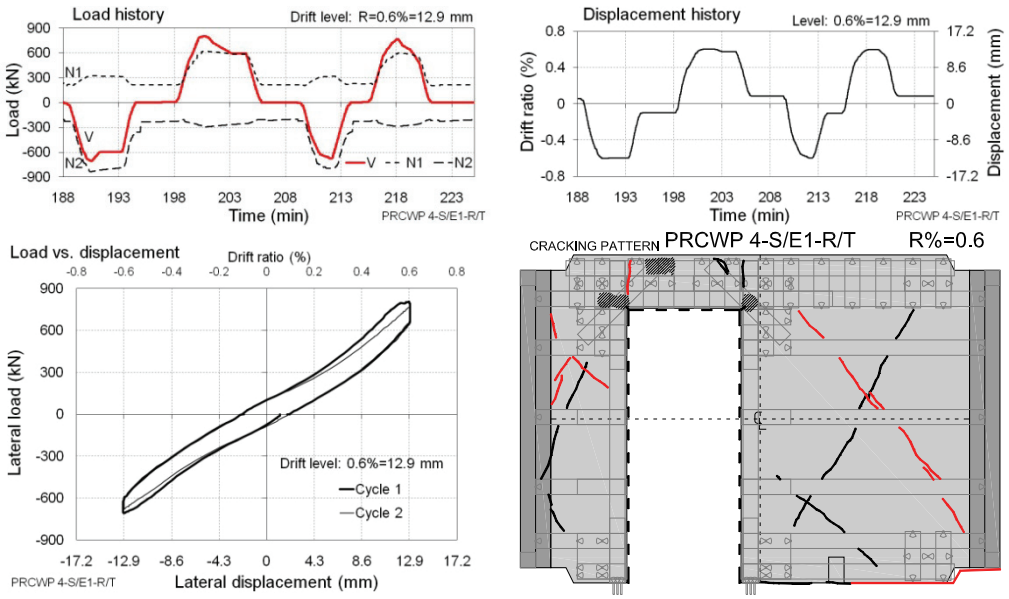

Commentary: Cross-diagonal cracking occurred through pier#2 running at 53 deg. The base crack extended along the length of pier#2-to-foundation joint. Further inclined cracking developed at the upper half of pier#1.

Figure E.83 Expanded cyclic response of PRCWP 4-S/E1-R/T at 0.6% drift ratio

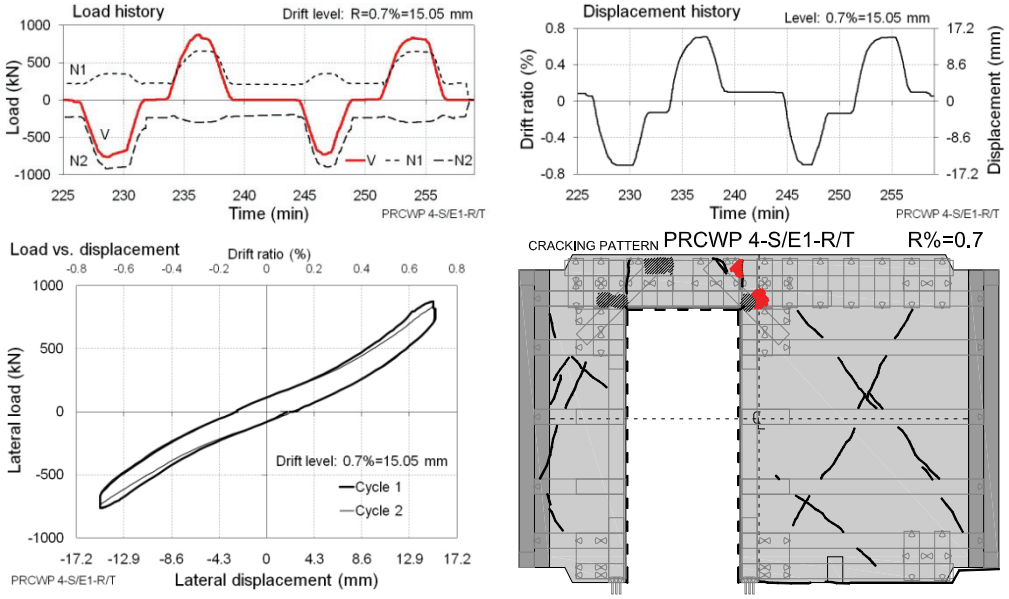

Commentary: FRP debonding extended at pier#2-to-spandrel connection. Note the waving of the axial loads. The test was halted till the next day.

Figure E.84 Expanded cyclic response of PRCWP 4-S/E1-R/T at 0.7% drift ratio

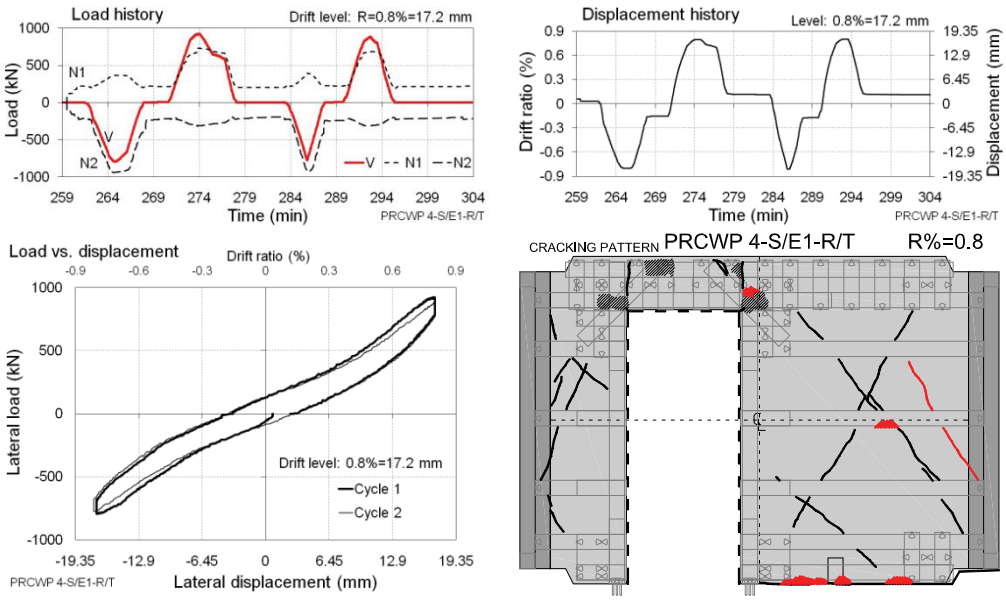

Commentary: Inclined cracking propagated in pier#2. Onset of debonding was noticed along the edge of the horizontal FRP strip at the crossing of diagonal crack on pier#2. Further FRP debonding occurred along the base joint due to concrete deterioration.

Figure E.85 Expanded cyclic response of PRCWP 4-S/E1-R/T at 0.8% drift ratio

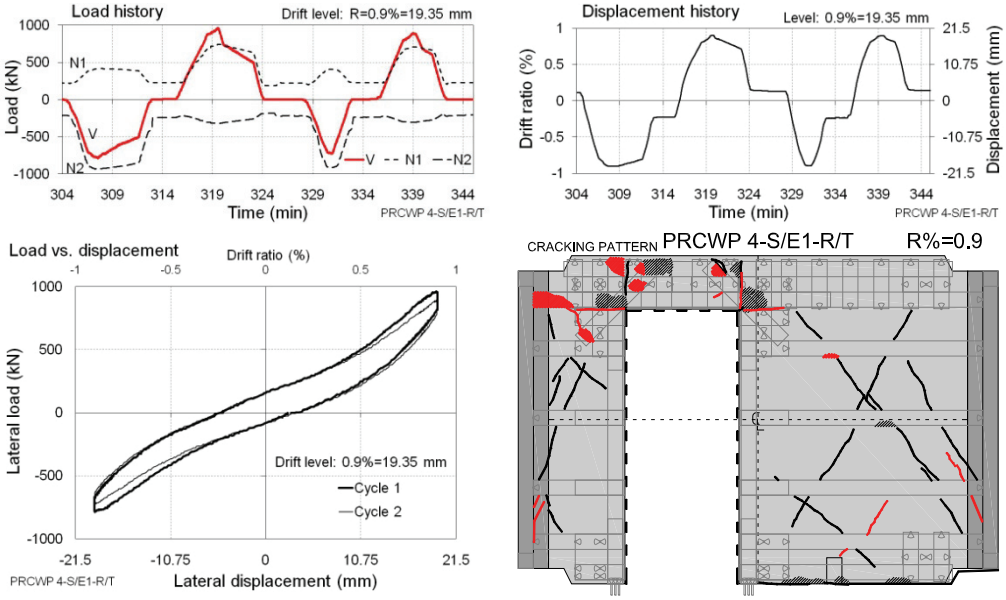

Commentary: The FRP-debonding propagated in the pier-to-spandrel connection area and orthogonal cracks developed extending from the opening corners. The horizontal FRP strip atop the opening debonded at its end-anchorage. The G8-gauge was disconnected and the released measuring channel was connected to the G12-gauge.

Figure E.86 Expanded cyclic response of PRCWP 4-S/E1-R/T at 0.9% drift ratio

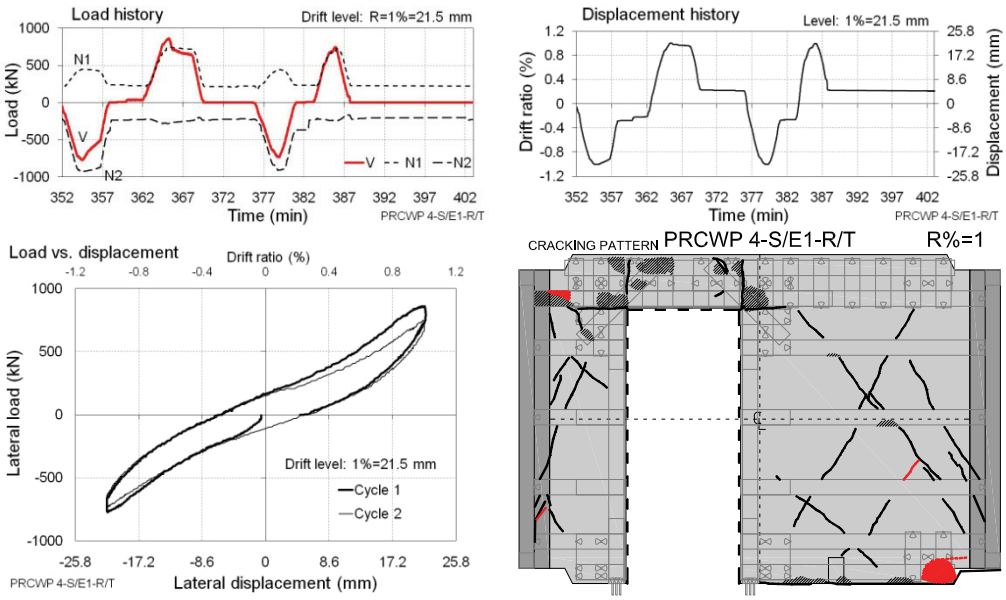

Commentary: Concrete crushing occurred in the positive loading direction at the compression toe of pier#2 and at the base of the adjacent wing element. The confinement FRPs in that region were severely damaged. In cycle #2 in the positive direction the load capacity dropped significantly and the failure criterion was fulfilled.

Figure E.87 Expanded cyclic response of PRCWP 4-S/E1-R/T at 1% drift ratio

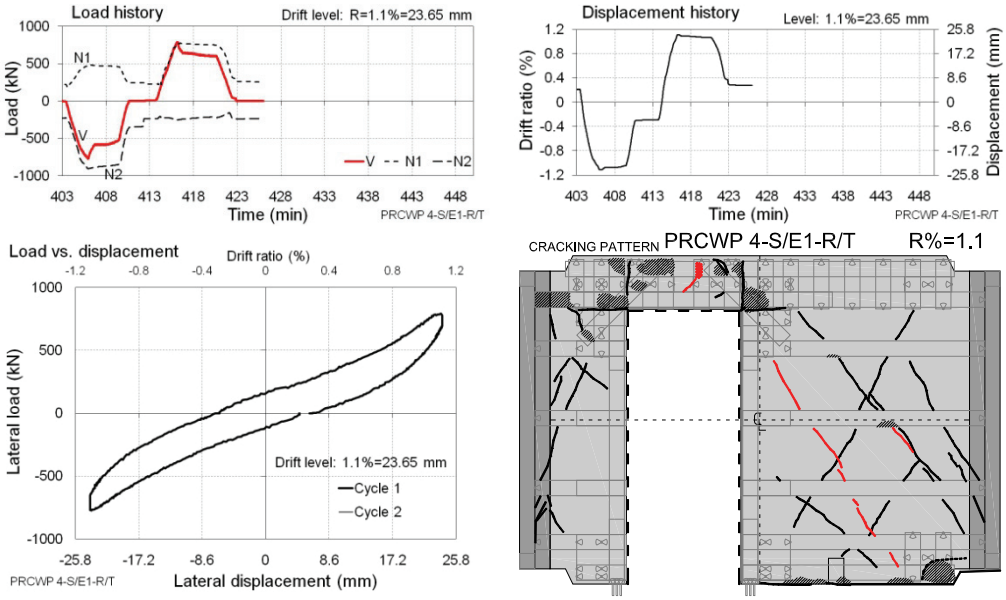

Commentary: A supplementary cycle was performed. In the positive loading direction diagonal cracking occurred across pier#2 extending at 59 deg.

Figure E.88 Expanded cyclic response of PRCWP 4-S/E1-R/T at 1.1% drift ratio

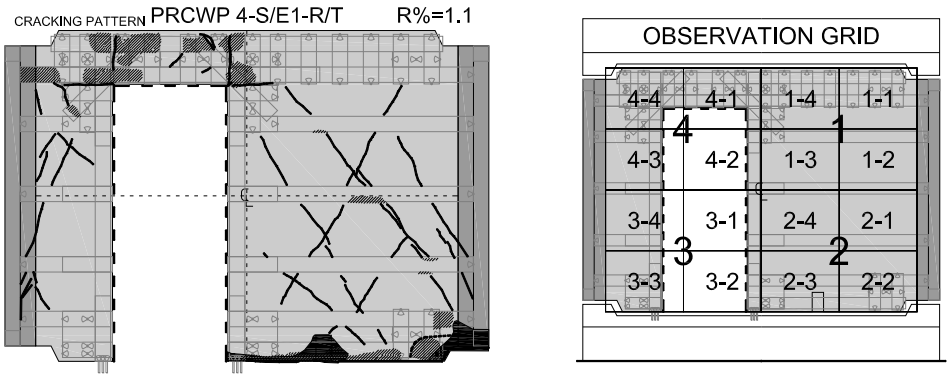

Figure E.89 Cracking pattern and observation grid PRCWP 4-S/E1-R/T

Figure E.90 Failure detail PRCWP 4-S/E1-R/T: the outside toe of pier#2 after removal of the crushed concrete (observation grid 2-2)

Figure E.91 Failure detail PRCWP 4-S/E1-R/T: the base of pier#2 at failure and after the crushed concrete was removed (obs. grids 3-2, 2-3, 2-2)

(a) (b)

Figure E.92 Failure detail PRCWP 4-S/E1-R/T: (a) FRP debonding at the spendrel-to-pier#2 connection (obs. grid 4-1); (b) onset of FRP debonding at inclined crack across pier#2 (obs. grid 2-1)

E.6 Test log of specimen PRCWP 5-S/E3-T/R

The test was carried out during November 4-11, 2008 in the Reinforced Concrete Structures Laboratory of the Department of Civil and Industrial Buildings, Faculty of Civil Engineering, Politehnica University of Timisoara, Romania. The experiment was attended by the following individuals: István Demeter, PhD Stud., Tamás Nagy-György, PhD, Lect., Valeriu Stoian, PhD, Prof., Cosmin Dăescu, PhD Stud., Ciprian Arvai, Stud., and Mihaela Ciurel, Stud. The author expresses his grateful acknowledgement for the instrumental contribution of his fellows.

The actual testing time was 16½ hours, segmented in three parts by one and 6 days of interruption. The recorded data file comprises 12315 lines and 29 measuring input columns. The complete instrumentation of the specimen is presented in Appendix C. This test log contains all the recorded responses and the observed behaviour and failure mode in the following order: load versus displacement diagrams, load versus strain diagrams, expanded cyclic load and displacement histories, cracking history, expanded cyclic lateral load versus drift hysteresis loops, commentary on the behaviour mode and test events, and failure details.

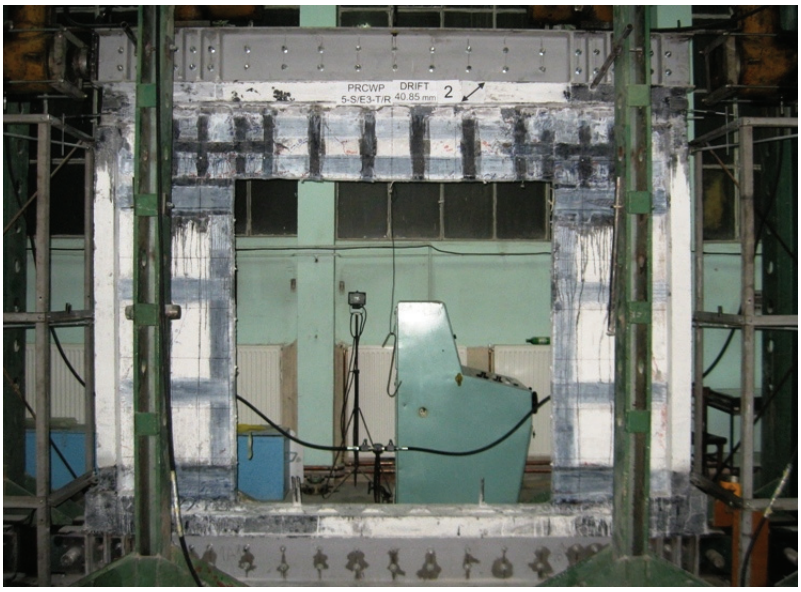

Figure E.93 Specimen PRCWP 5-S/E3-T/R at failure (1.9% drift ratio)

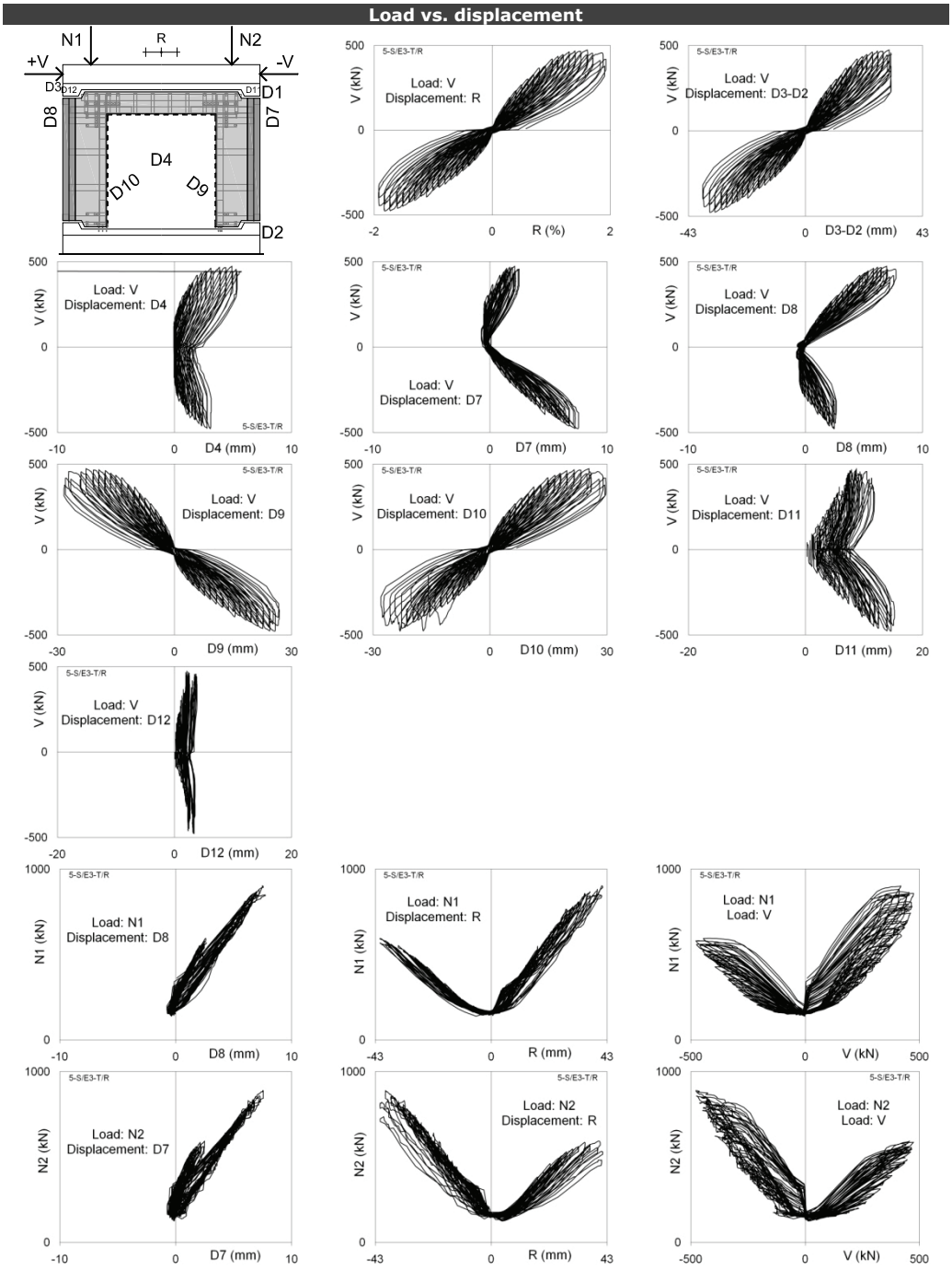

Figure E.94 Load-displacement responses for specimen PRCWP 5-S/E3-T/R

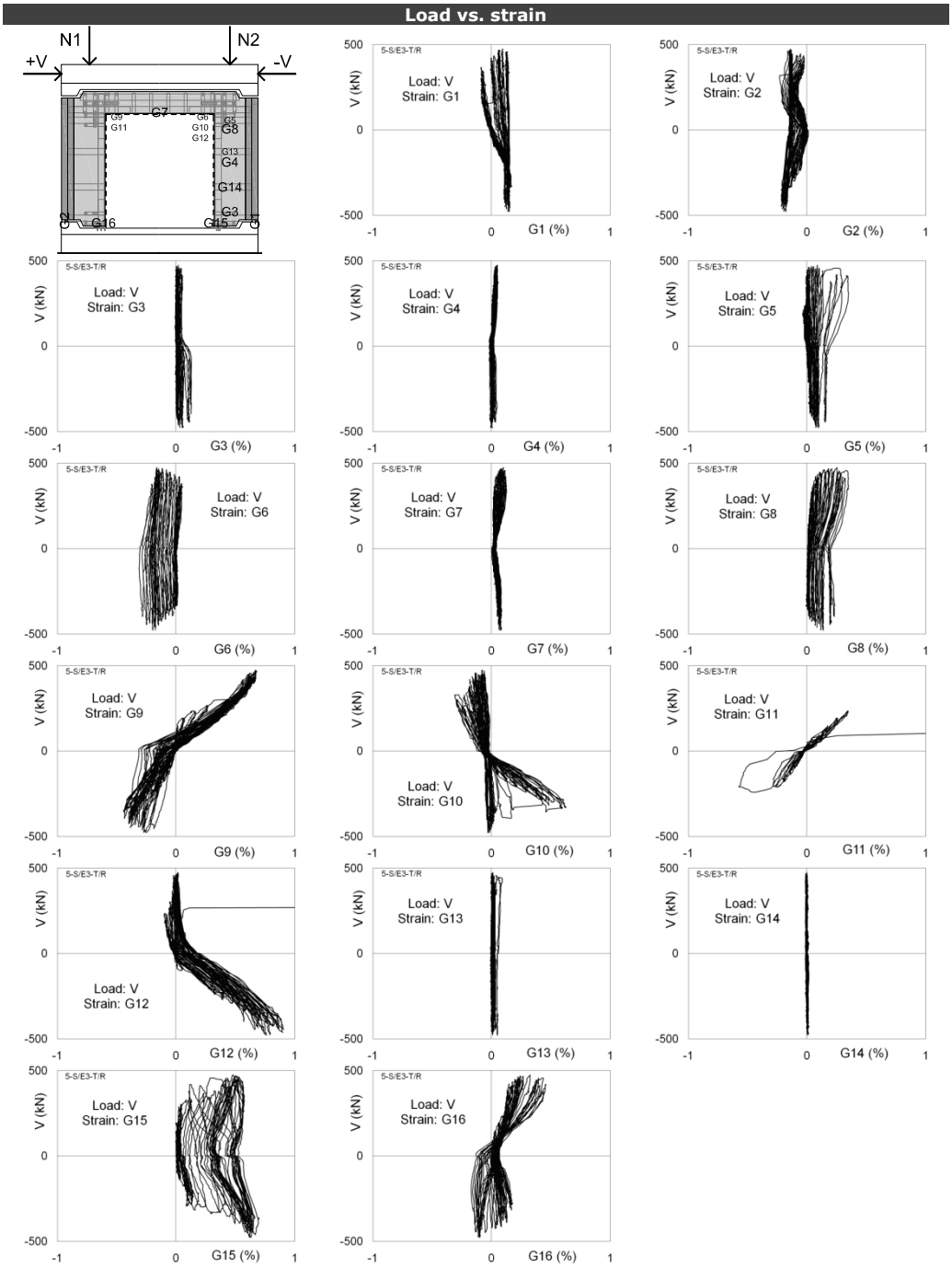

Figure E.95 Load-strain responses for specimen PRCWP 5-S/E3-T/R

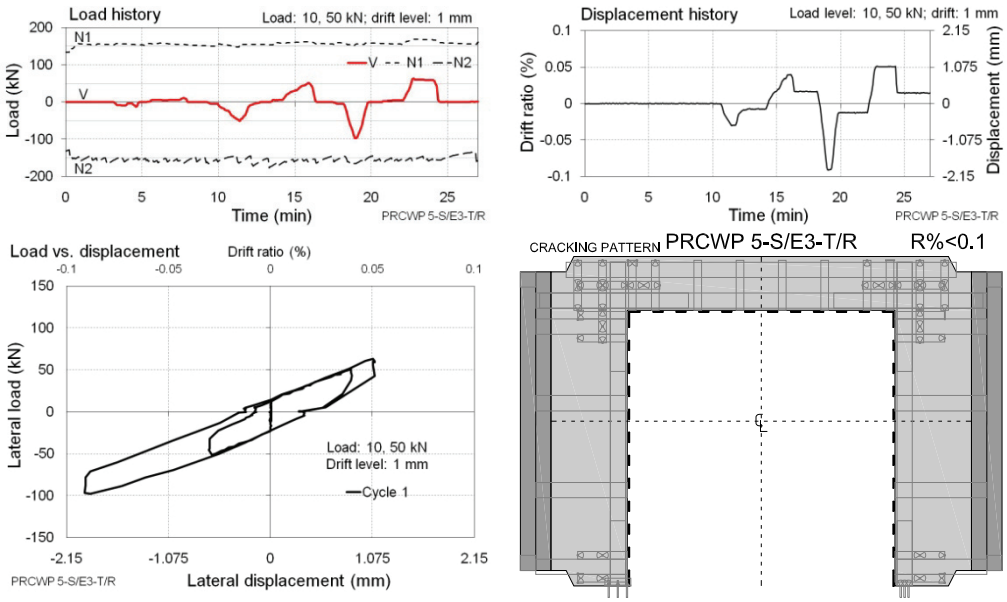

Commentary: The test commenced with load cycles at 10 and 50 kN amplitude followed by a 1 mm drift cycle. In the negative direction of the 1 mm drift level the wall was slightly overloaded. Note the constant level of the axial loads.

Figure E.96 Expanded cyclic response of PRCWP 5-S/E3-T/R at the initial cycles

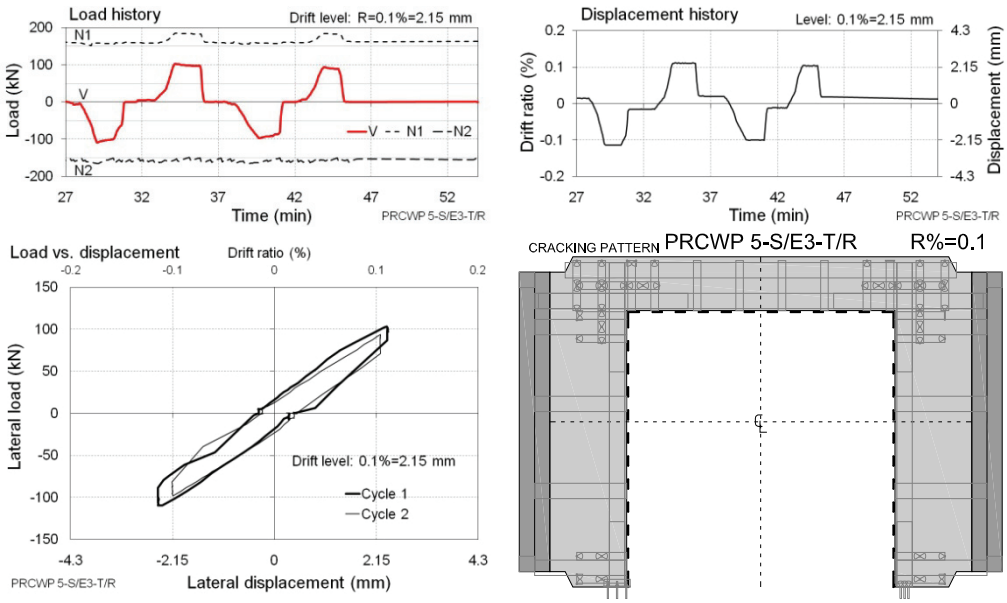

Commentary: Snapping sounds were audible as the FRPs deformed during the load reversals.

Figure E.97 Expanded cyclic response of PRCWP 5-S/E3-T/R at 0.1% drift ratio

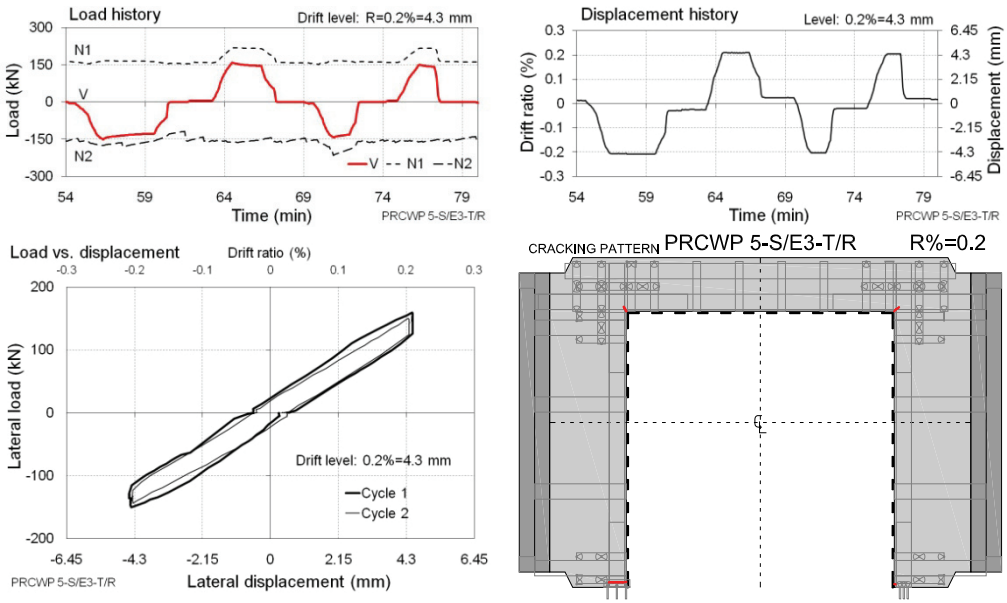

Commentary: Cracking onset was observed at the base of the piers and at the pier-to-spandrel connections extending from the corners of the opening. Crack-tracking at the connections was impeded by FRP congestion. Note the incipient waving of the axial loads.

Figure E.98 Expanded cyclic response of PRCWP 5-S/E3-T/R at 0.2% drift ratio

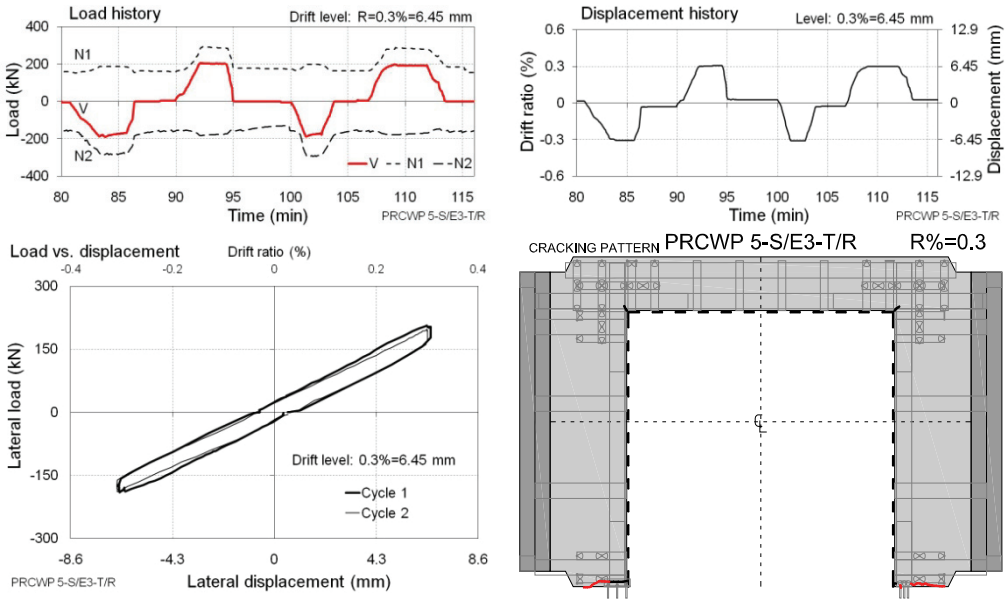

Comments: The horizontal cracks at the base extended.

Figure E.99 Expanded cyclic response of PRCWP 5-S/E3-T/R at 0.3% drift ratio

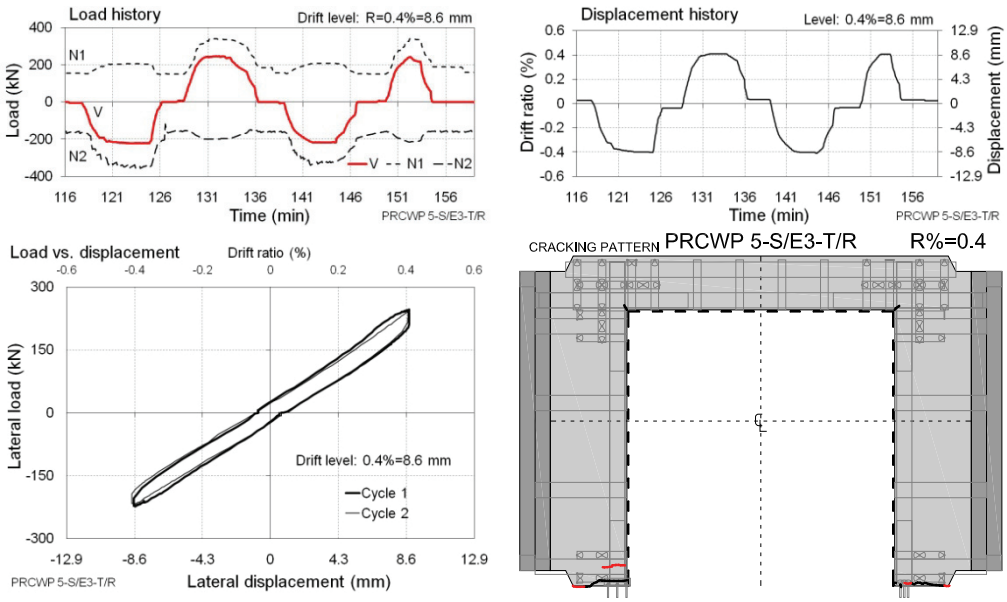

Commentary: The horizontal cracking at the piers' inside toes propagated upwardly. At the same location spalling of fine lime-powder was noticed on the vertical FRP strips just above the confined portion. Note the waving of the axial loads.

Figure E.100 Expanded cyclic response of PRCWP 5-S/E3-T/R at 0.4% drift ratio

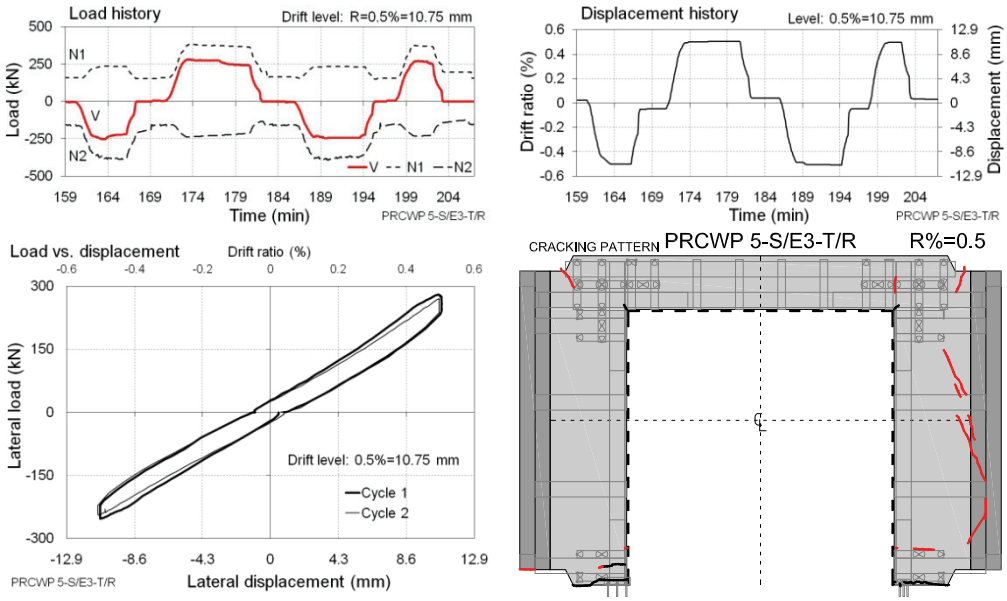

Commentary: The upward propagation of the horizontal cracks at the pier toes continued. The existing inclined cracks on pier#2 opened. At the pier-to-spandrel connections cracks appeared extending from the outside edge of the wall. The G11 FRP strain gauge (glued on the horizontal strip atop the upper-left corner of the opening) indicated local FRP failure.

Figure E.101 Expanded cyclic response of PRCWP 5-S/E3-T/R at 0.5% drift ratio

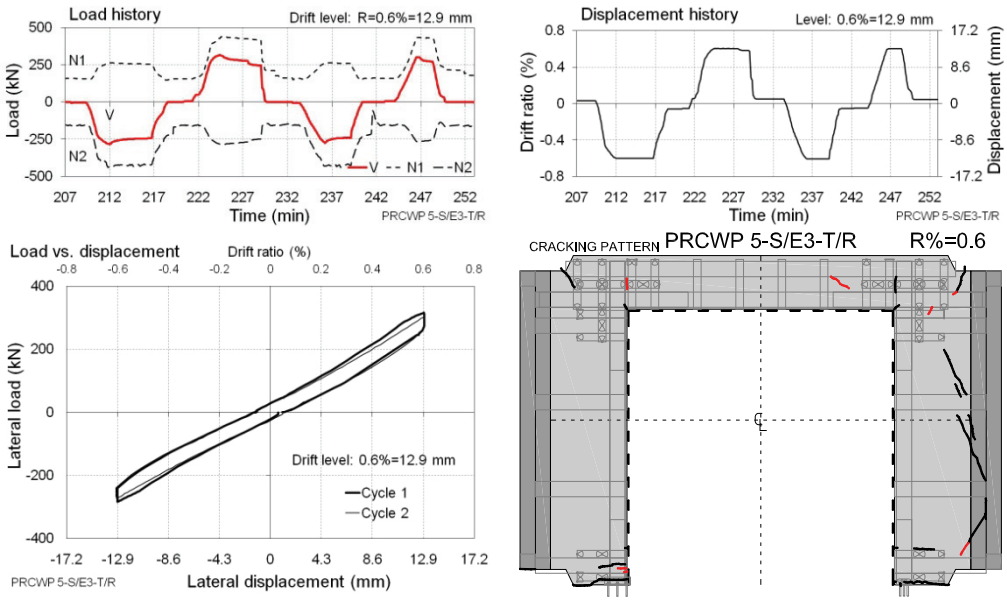

Commentary: Cracking propagation occurred at the base and at the pier-to-spandrel connections. 45 deg inclined crack appeared in the spandrel's right end.

Figure E.102 Expanded cyclic response of PRCWP 5-S/E3-T/R at 0.6% drift ratio

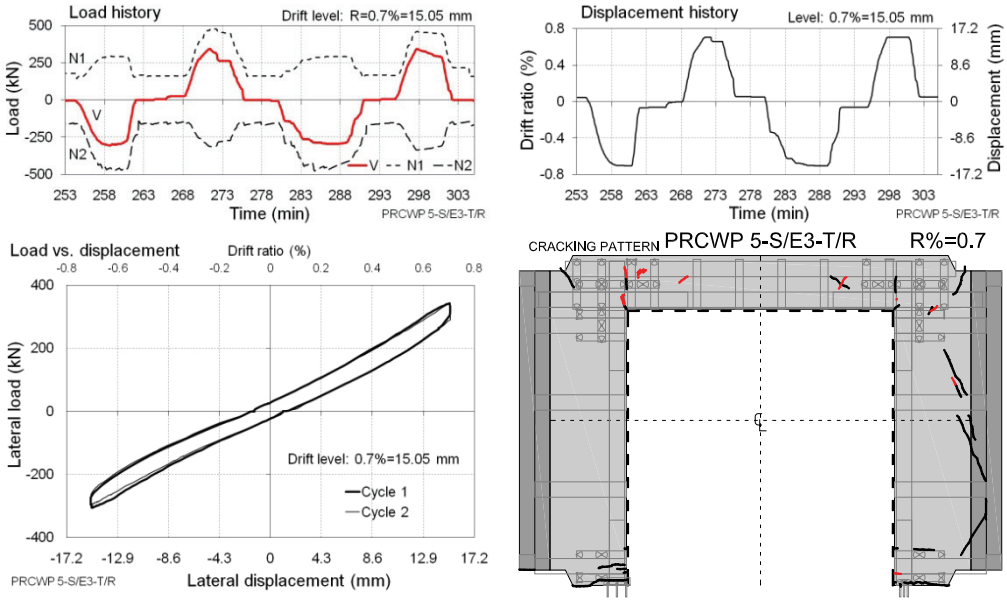

Commentary: The cracks propagated at the pier-to-spandrel connections, along the spandrel and at the base. FRP-snapping sounds were heard. Onset of FRP debonding was observed at the pier-to-spandrel connections.

Figure E.103 Expanded cyclic response of PRCWP 5-S/E3-T/R at 0.7% drift ratio

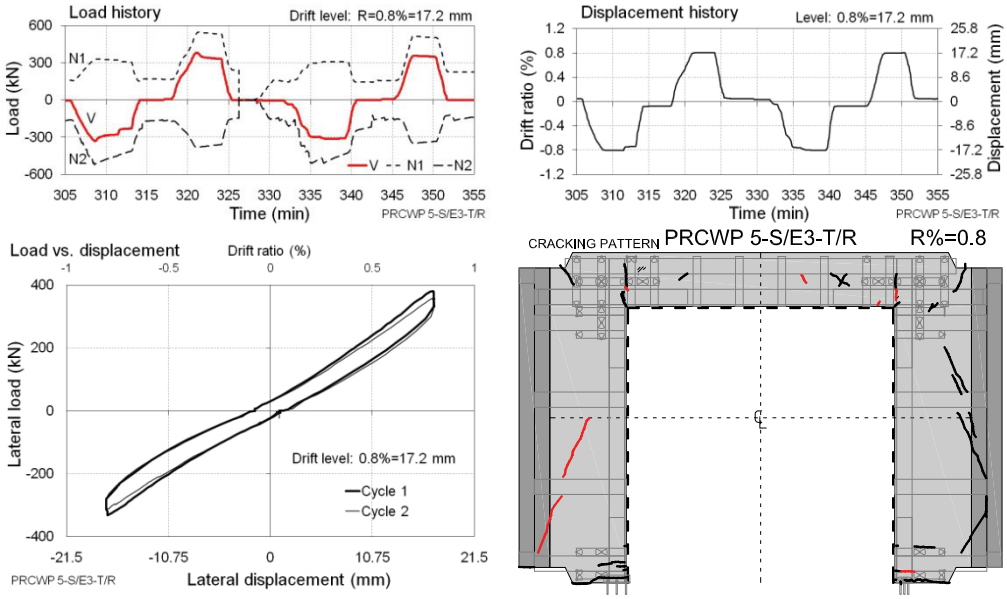

Commentary: In the negative loading direction of the first cycle diagonal cracking occurred across pier#1 running at 69 deg. After cycle#1 the test was halted till the next day. During the second cycle the 45 deg inclined cracks propagated along the spandrel.

Figure E.104 Expanded cyclic response of PRCWP 5-S/E3-T/R at 0.8% drift ratio

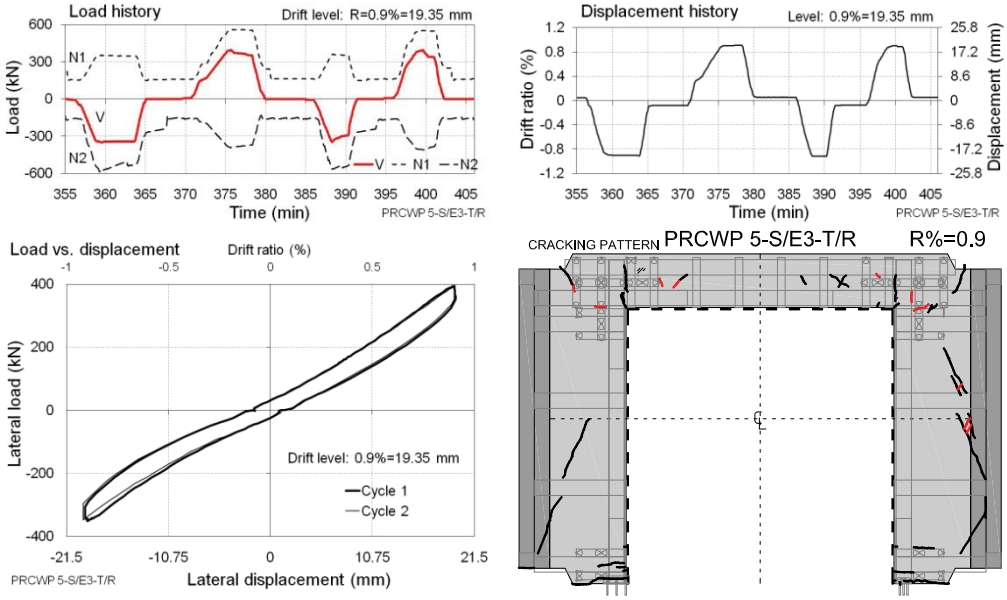

Commentary: Cracking propagation occurred at the spandrel-to-pier connection regions. Short inclined cracks developed between the diagonal cracks on pier#2. Extensive opening of the horizontal cracks at the piers' inside toes was noticed.

Figure E.105 Expanded cyclic response of PRCWP 5-S/E3-T/R at 0.9% drift ratio

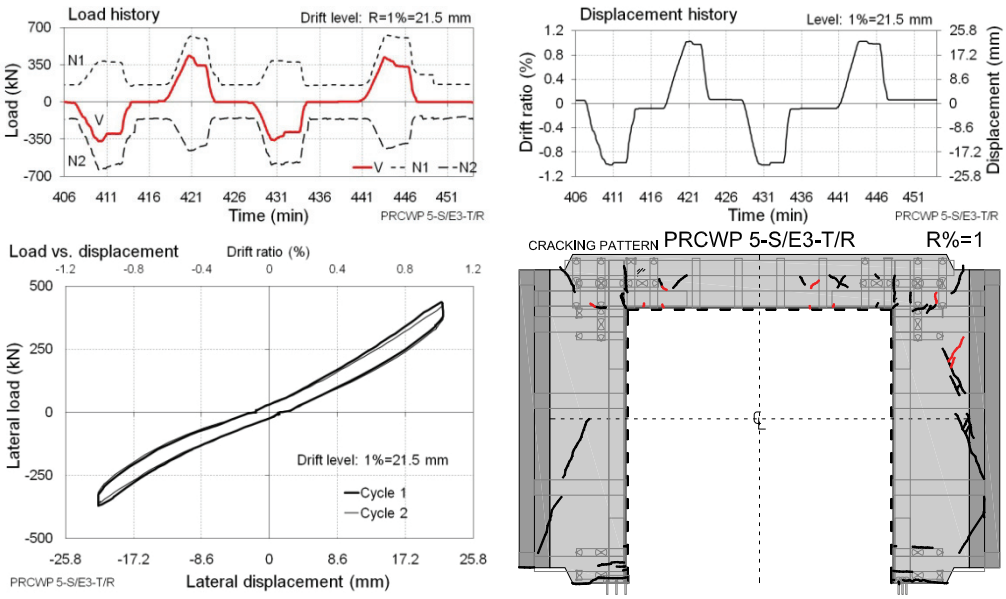

Commentary: Cracking propagation occurred along the spandrel and in pier#2; the horizontal cracks at the piers' base extensively opened.

Figure E.106 Expanded cyclic response of PRCWP 5-S/E3-T/R at 1% drift ratio

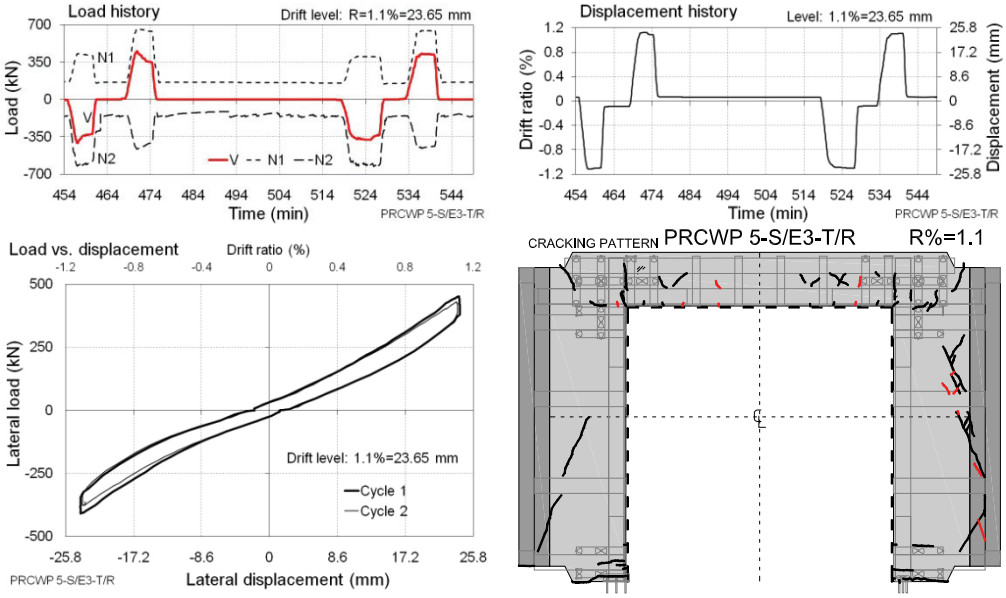

Commentary: Crack propagation occurred along the spandrel and in pier#2.

Figure E.107 Expanded cyclic response of PRCWP 5-S/E3-T/R at 1.1% drift ratio

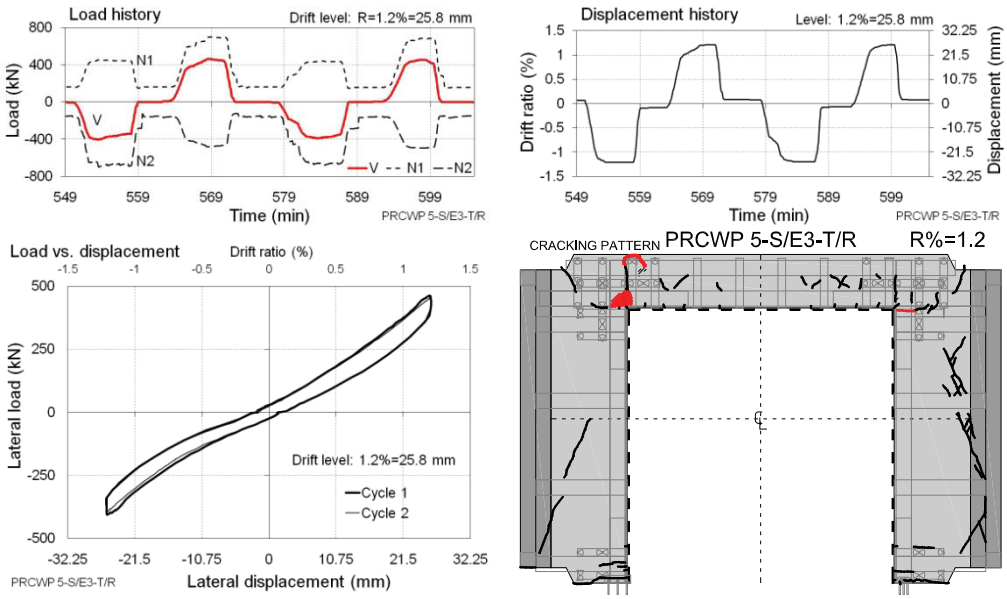

Commentary: FRP-debonding was detected by tapping inspection at pier#1-to-spandrel connection. Likewise in the previous cycles the base cracks opened considerably.

Figure E.108 Expanded cyclic response of PRCWP 5-S/E3-T/R at 1.2% drift ratio

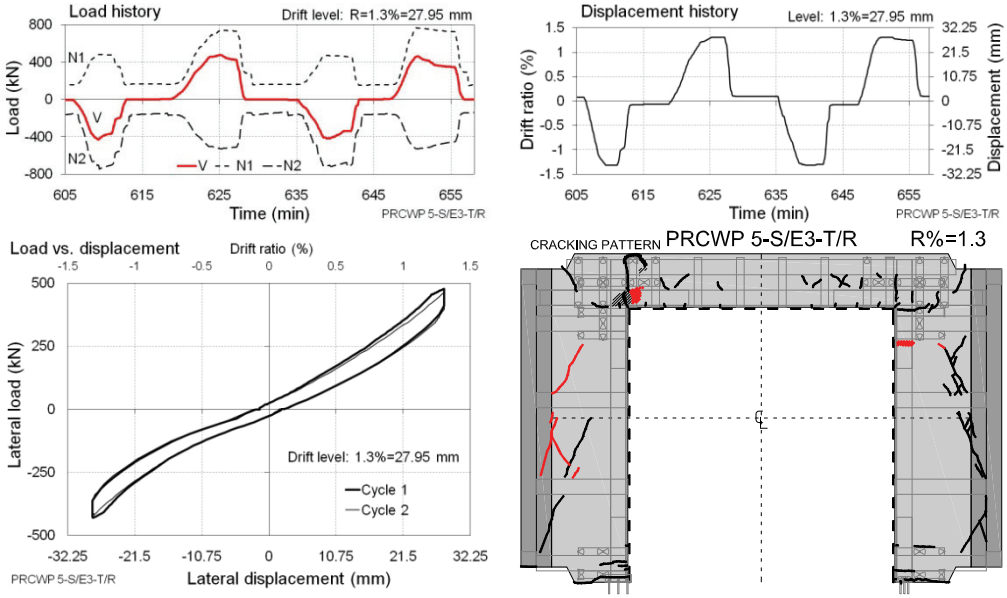

Commentary: Diagonal cracks developed across pier#1 extending at 61÷72 deg. The FRP-debonding propagated at the pier#1-to-spandrel connection. Onset of FRP bulging (buckling) in compression was noticed at the vertical strip beneath the confinement of pier#2-to-spandrel connection.

Figure E.109 Expanded cyclic response of PRCWP 5-S/E3-T/R at 1.3% drift ratio

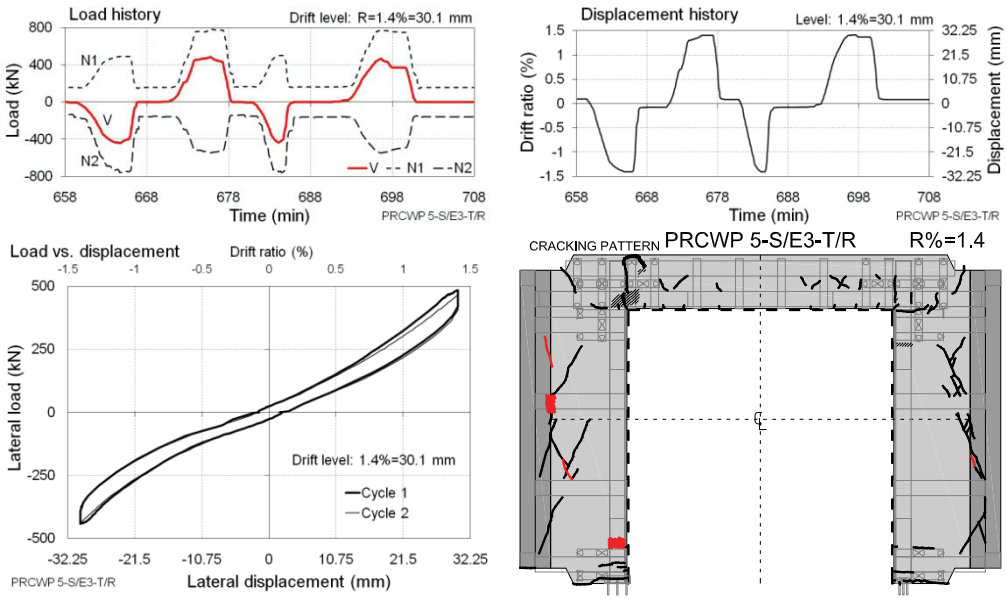

Commentary: FRP bulging (buckling) was detected on the vertical strip in compression over the base confinement of pier#1. FRP debonding was observed at the inclined crack-horizontal strip intersection on pier#1.

Figure E.110 Expanded cyclic response of PRCWP 5-S/E3-T/R at 1.4% drift ratio

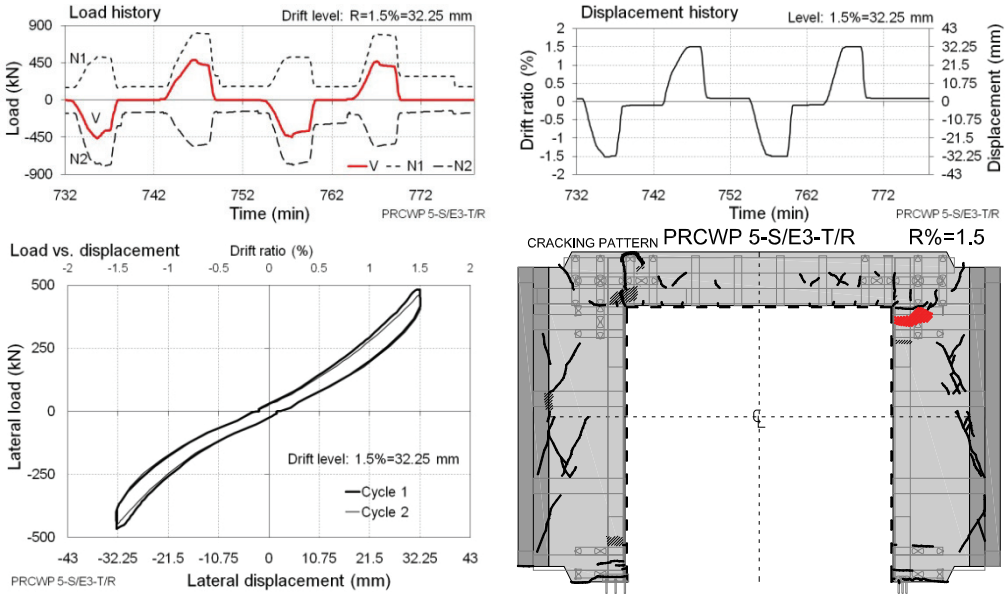

Commentary: Extensive FRP debonding was detected at the pier#2-to-spandrel connection. The width of the horizontal cracks at the base was about 10 mm.

Figure E.111 Expanded cyclic response of PRCWP 5-S/E3-T/R at 1.5% drift ratio

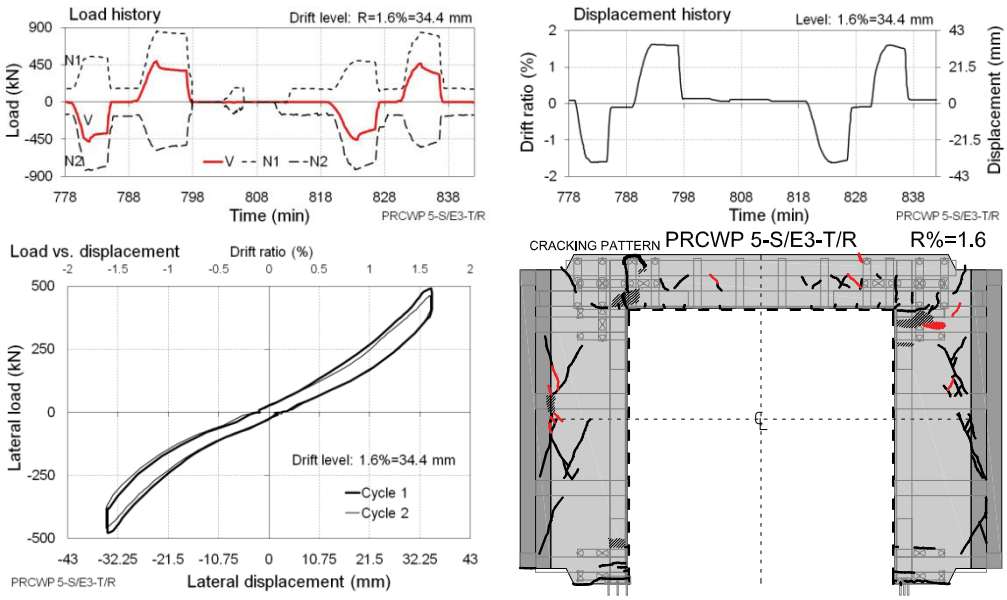

Commentary: Crack propagation occurred along the pier-to-wing joints and in the spandrel. The test was halted after the first cycle for 6 days.

Figure E.112 Expanded cyclic response of PRCWP 5-S/E3-T/R at 1.6% drift ratio

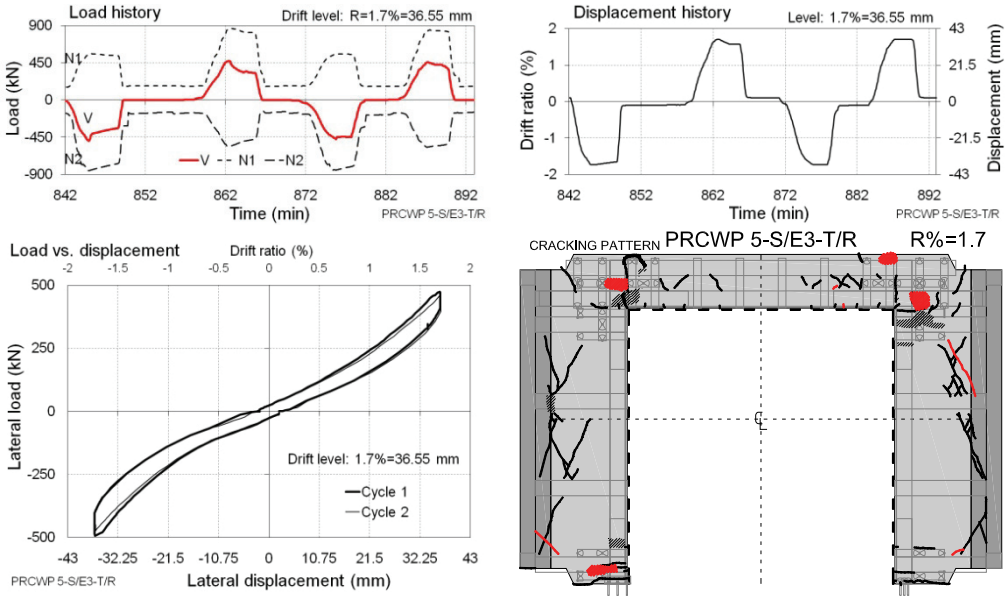

Commentary: The FRP debonding propagated at the pier-to-spandrel connections and at the pier#1 base. Inclined cracks occurred in both piers.

Figure E.113 Expanded cyclic response of PRCWP 5-S/E3-T/R at 1.7% drift ratio

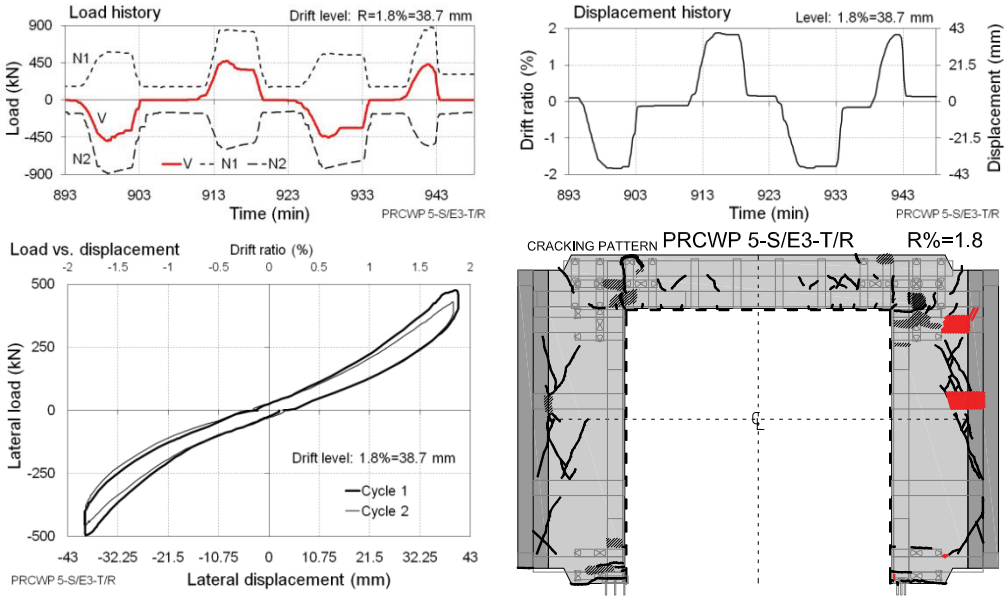

Commentary: FRP peeling-off failure occurred at the end-anchorages of the horizontal strips on pier#2. The FRP confinement fractured at the inside toe of pier#2. The D4 displacement transducer fell off due to deterioration of the support.

Figure E.114 Expanded cyclic response of PRCWP 5-S/E3-T/R at 1.8% drift ratio

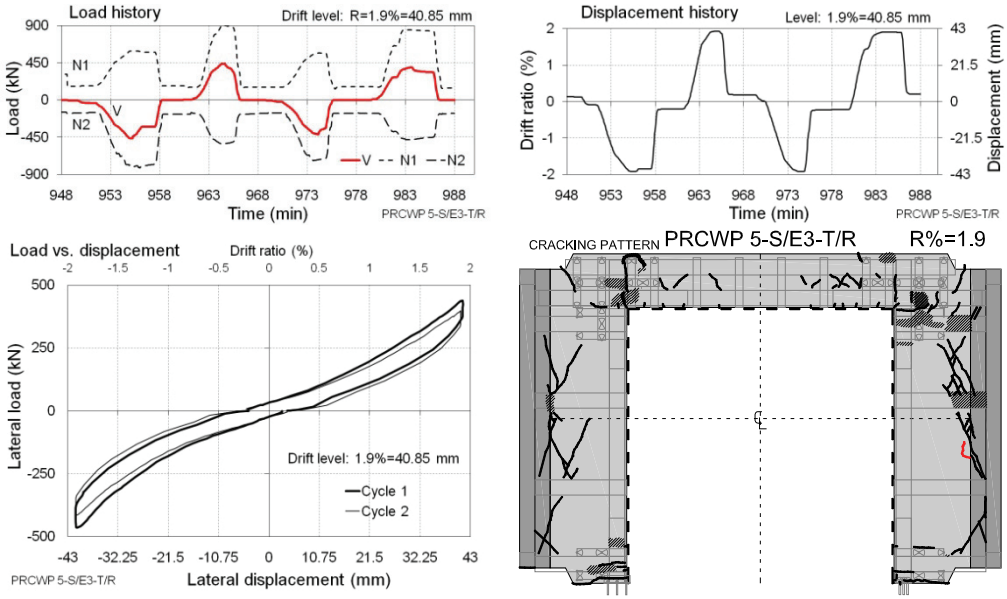

Commentary: The wall failed by sliding shear along the vertical joint between pier#2 and the adjacent wing element. The inspection of the wall after the test revealed extensive concrete crushing along the pier-to-wing joint; fracture of the flexural FRP strips at the base anchorages and at the pier-to-spandrel connections next to the corners of the opening; and crushed concrete inside the FRP confinement at the pier toes, refer to Figure.

Figure E.115 Expanded cyclic response of PRCWP 5-S/E3-T/R at 1.9% drift ratio

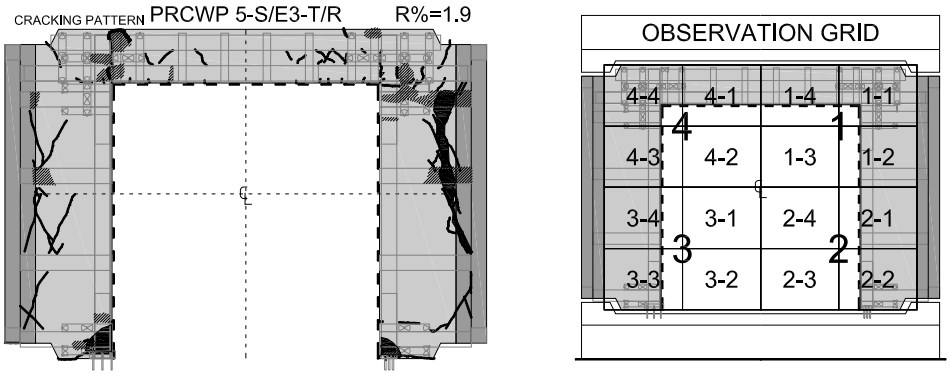

Figure E.116 Cracking pattern and observation grid PRCWP 5-S/E3-T/R

Figure E.117 Failure detail PRCWP 5-S/E3-T/R: FRP strip-end peeling-off at the pier#2-to-wing connection (obs. grid 1-1, 1-2)

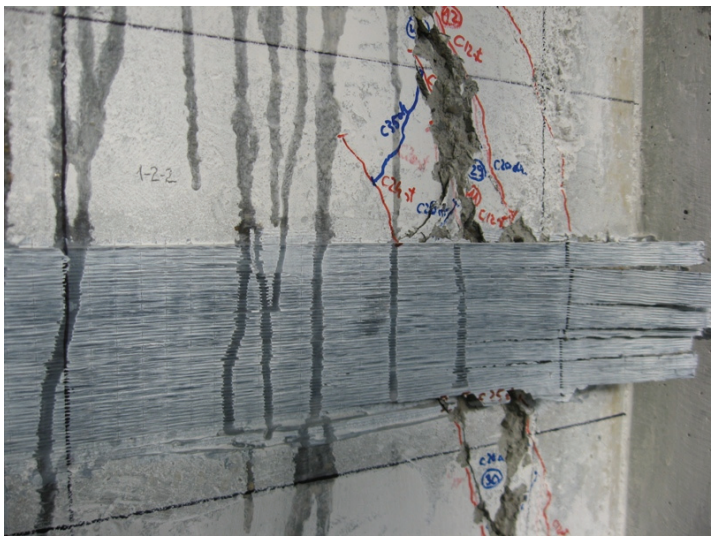

Figure E.118 Failure detail PRCWP 5-S/E3-T/R: FRP peeling-off (obs. grid 1-2)

(a)

Figure E.119 Failure detail PRCWP 5-S/E3-T/R: (a) excessive crack opening at the inside toe of pier#2; (b) vertical FRP fracture is revealed after the removal of the FRP confinement (observation grid 2-2)

Figure E.120 Failure detail PRCWP 5-S/E3-T/R: the same failure is observed at the opposite face of pier#2 (obs grid 2-2 rear)

(a) (b)

Figure E.121 Failure detail PRCWP 5-S/E3-T/R: (a) the FRP confinement at the inside toe of pier#1; (b) FRP bulging above the confinement (obs. grid 3-3)

(a) (b)

Figure E.122 Failure detail PRCWP 5-S/E3-T/R: (a) concrete crushing is revealed inside the confined toe of pier#1 (obs. grid 3-3); (b) vertical sliding along the pier#2-to-wing connection (obs. grid 1-2, 2-1)

E.7 Test log of specimen PRCWP 6-S/E3-R/T

The test was carried out on August 7, 2009 in the Reinforced Concrete Structures Laboratory of the Department of Civil and Industrial Buildings, Faculty of Civil Engineering, Politehnica University of Timisoara, Romania. The experiment was attended by the following individuals: István Demeter, PhD Stud., Tamás Nagy-György, PhD Lect., Sebastian Pop, Cătălin Suciu, and Florin Mitrana graduate students. The author expresses his grateful acknowledgement for the instrumental contribution of his fellows.

The testing time was 9 hours, with one hour interruption. The recorded data file comprises 33345 lines and 29 measuring input columns. The complete instrumentation of the specimen is presented in Appendix C. This test log contains all the recorded responses and the observed behaviour and failure mode in the following order: load versus displacement diagrams, load versus strain diagrams, expanded cyclic load and displacement histories, cracking history, expanded cyclic lateral load versus drift hysteresis loops, commentary on the behaviour mode and test events, and failure details.

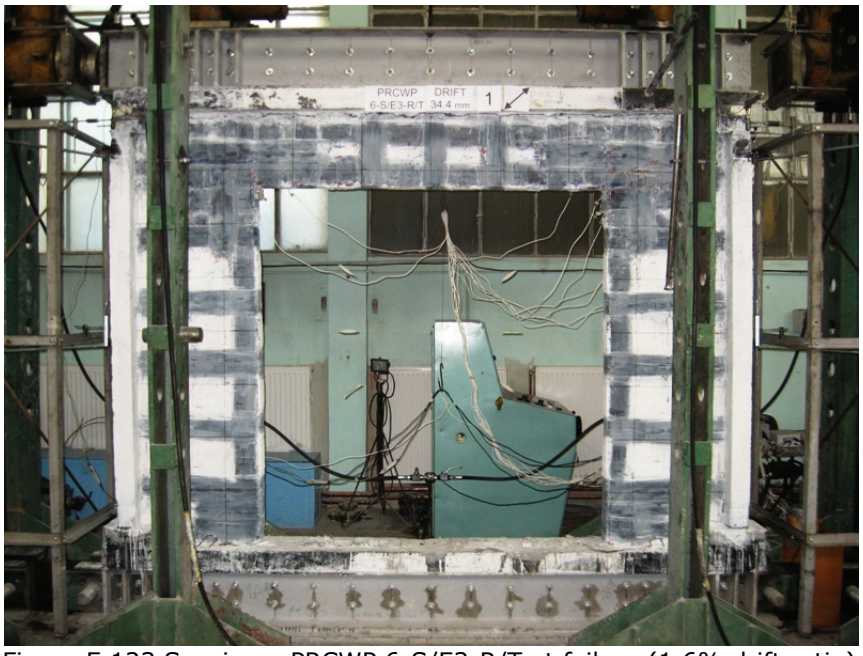

Figure E.123 Specimen PRCWP 6-S/E3-R/T at failure (1.6% drift ratio)

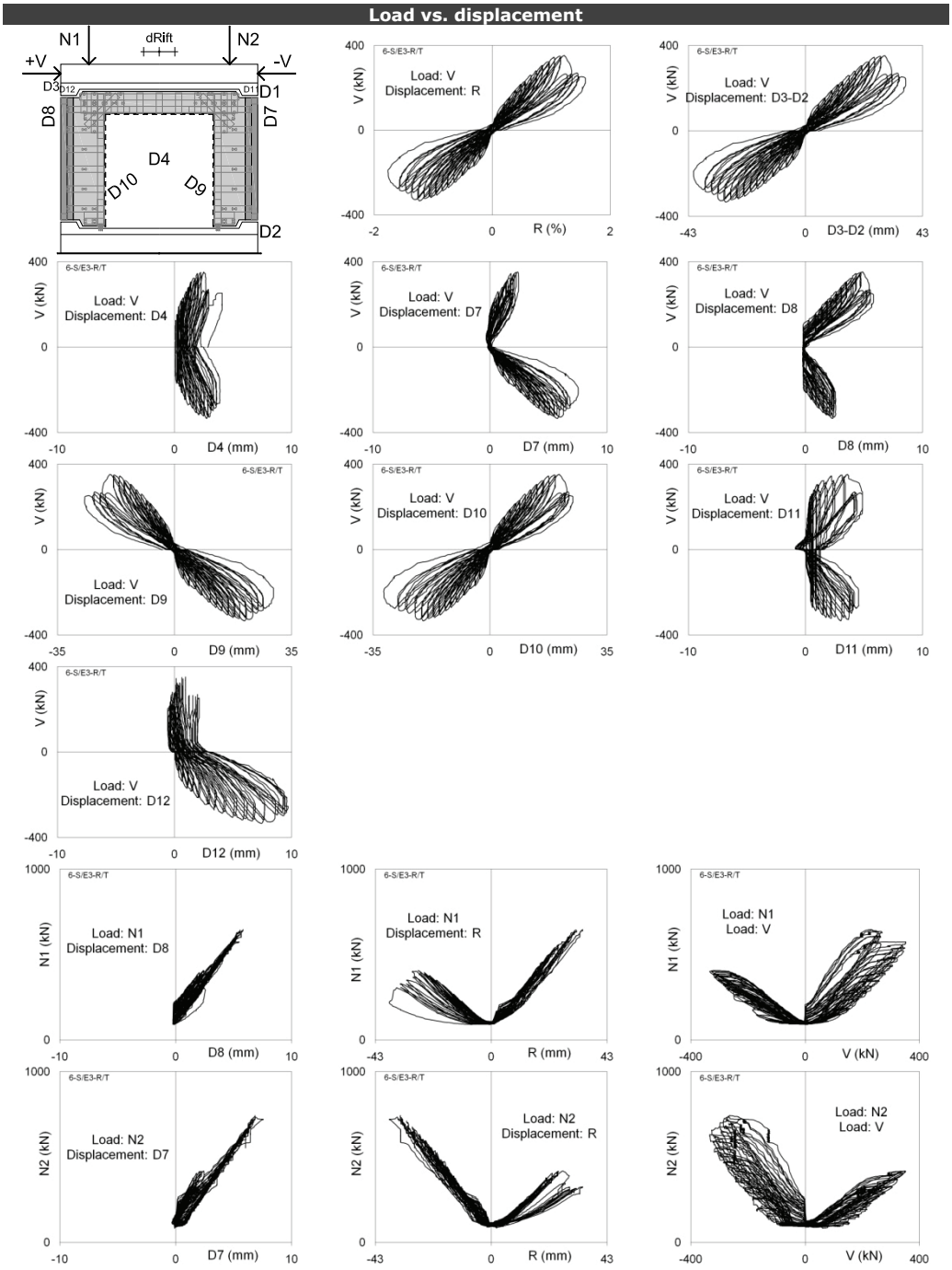

Figure E.124 Load-displacement responses for specimen PRCWP 6-S/E3-R/T

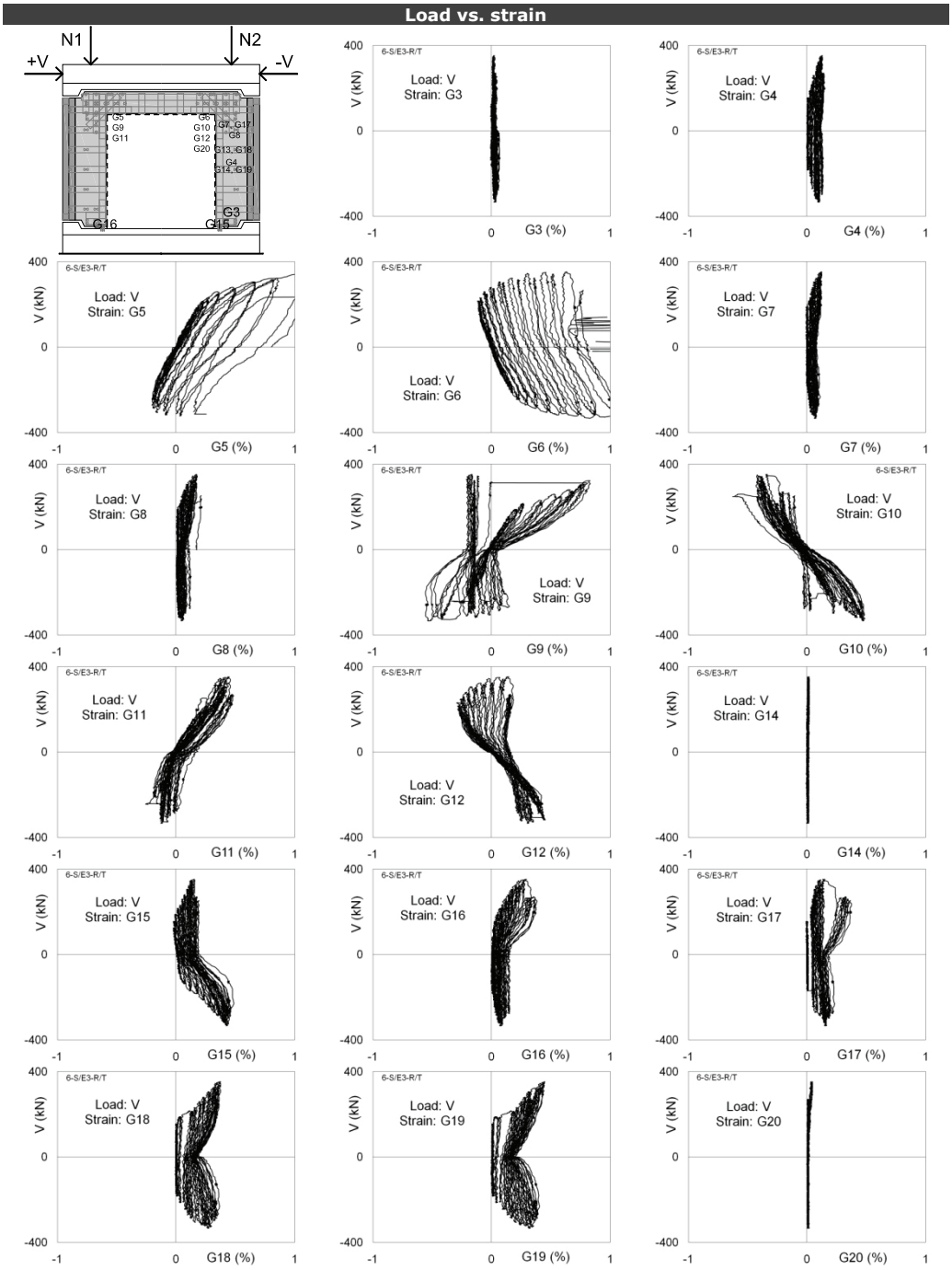

Figure E.125 Load-strain responses for specimen PRCWP 6-S/E3-R/T

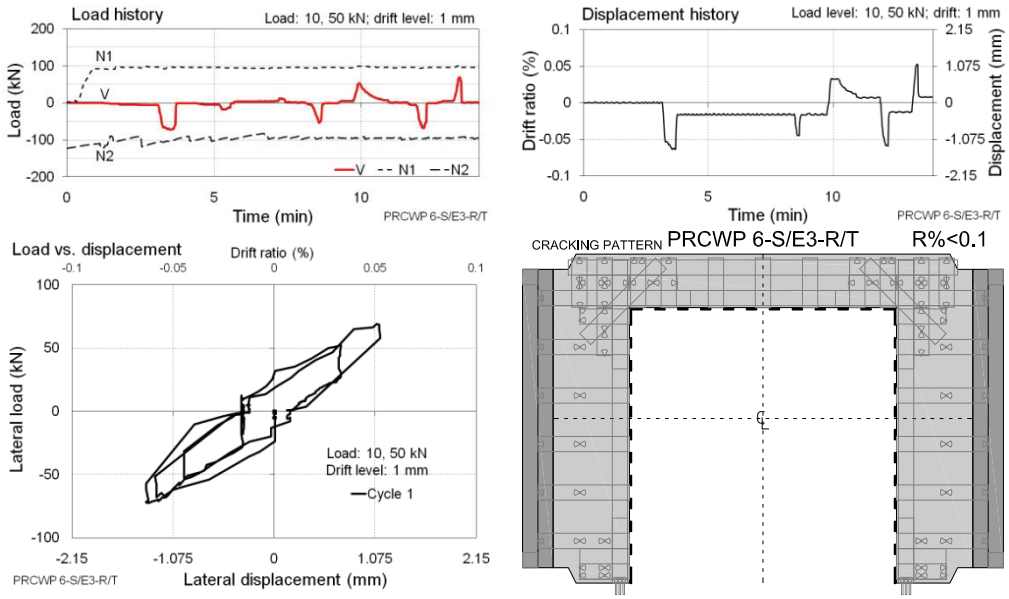

Commentary: The test commenced with load cycles at 10 and 50 kN amplitudes. Thereafter the loading shifted into displacement control starting with the 1 mm drift level. Note the constant level of the axial loads at N1=N2=95.5 kN.

Figure E.126 Expanded cyclic response of PRCWP 6-S/E3-R/T at the initial cycles

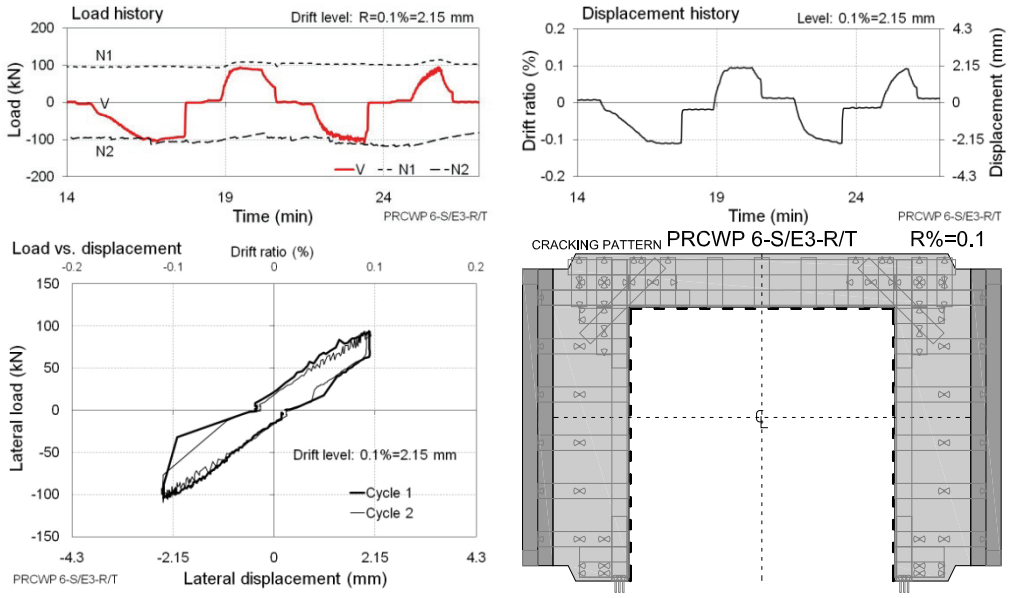

Commentary: No sign of damage was observed. Note the incipient waving of the axial loads. The trembling of the lateral load curve was caused by pressure transducer malfunction.

Figure E.127 Expanded cyclic response of PRCWP 6-S/E3-R/T at 0.1% drift ratio

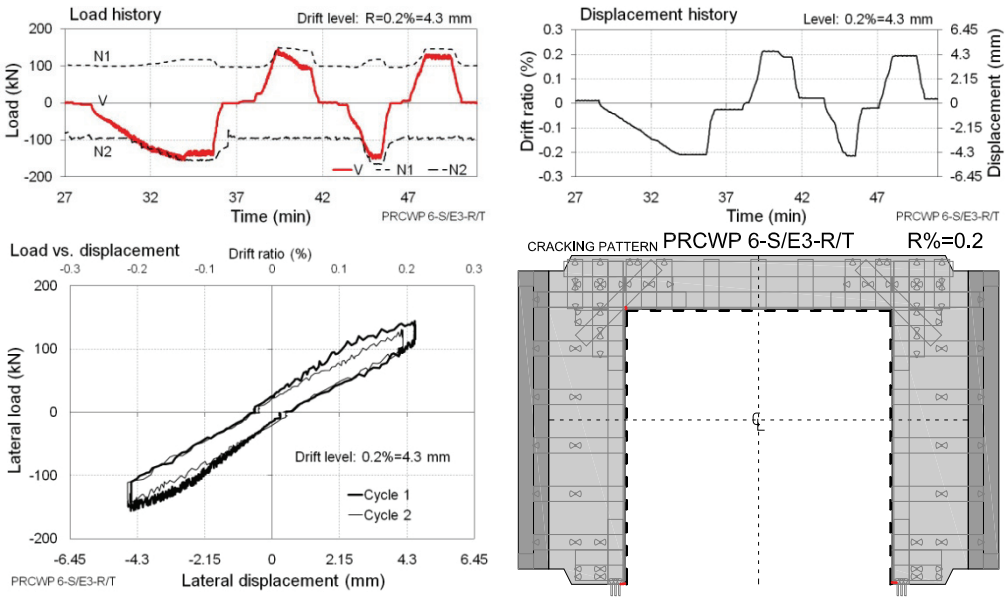

Commentary: Cracking onset was observed extending from the opening corners at the pier toes and at the spandrel-to-pier connections.

Figure E.128 Expanded cyclic response of PRCWP 6-S/E3-R/T at 0.2% drift ratio

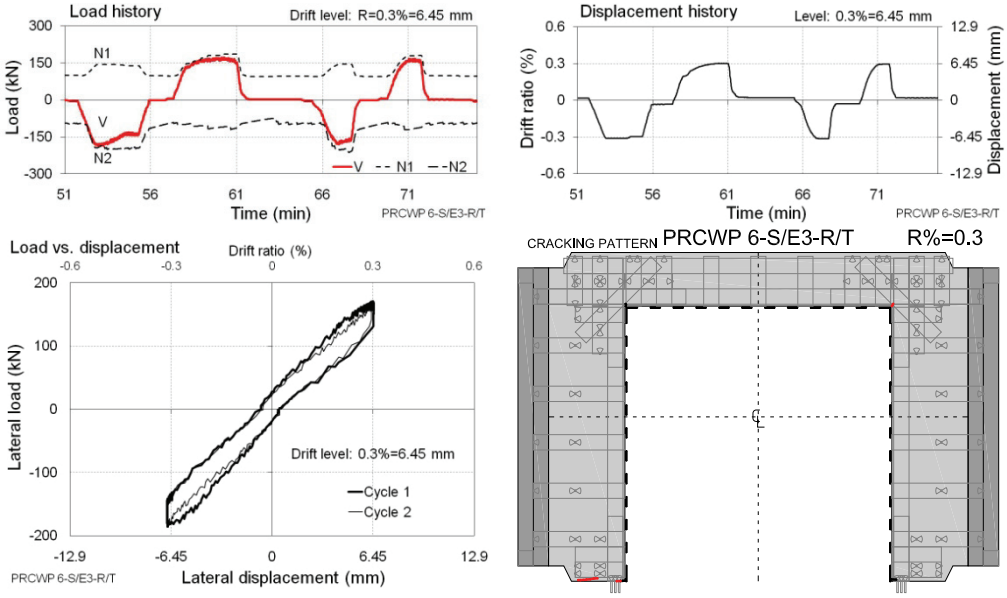

Commentary: The horizontal crack extended at the base of pier#1. The tracking of the cracks at the spandrel-to-beam connections was impeded by FRP congestion. Note the waving axial loads.

Figure E.129 Expanded cyclic response of PRCWP 6-S/E3-R/T at 0.3% drift ratio

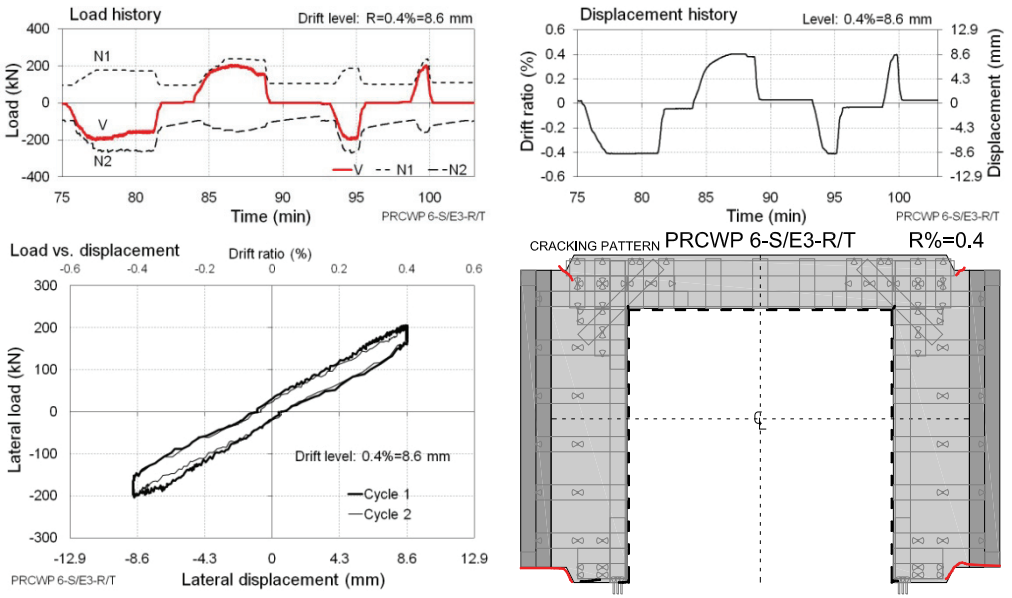

Commentary: Crack development occurred at the pier bases and at the spandrel-to-pier connections extending from the outer edge of the wall. A snapping sound denoted rupture of an internal reinforcement at the base of pier#2 (possibly of the vertical continuity bar).

Figure E.130 Expanded cyclic response of PRCWP 6-S/E3-R/T at 0.4% drift ratio

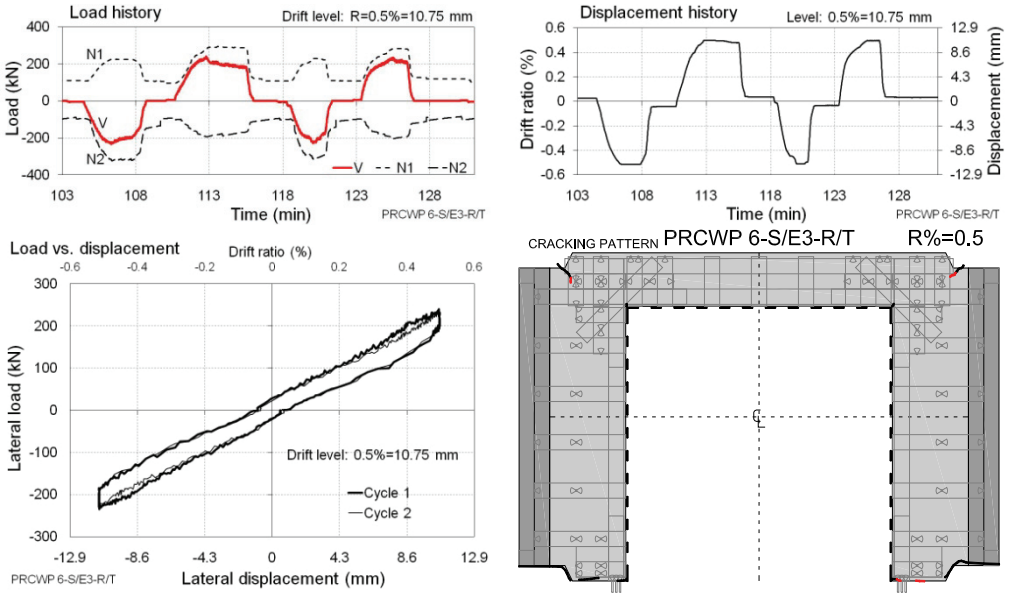

Commentary: Crack development was observed at the base and at the spandrel-to-pier connections.

Figure E.131 Expanded cyclic response of PRCWP 6-S/E3-R/T at 0.5% drift ratio

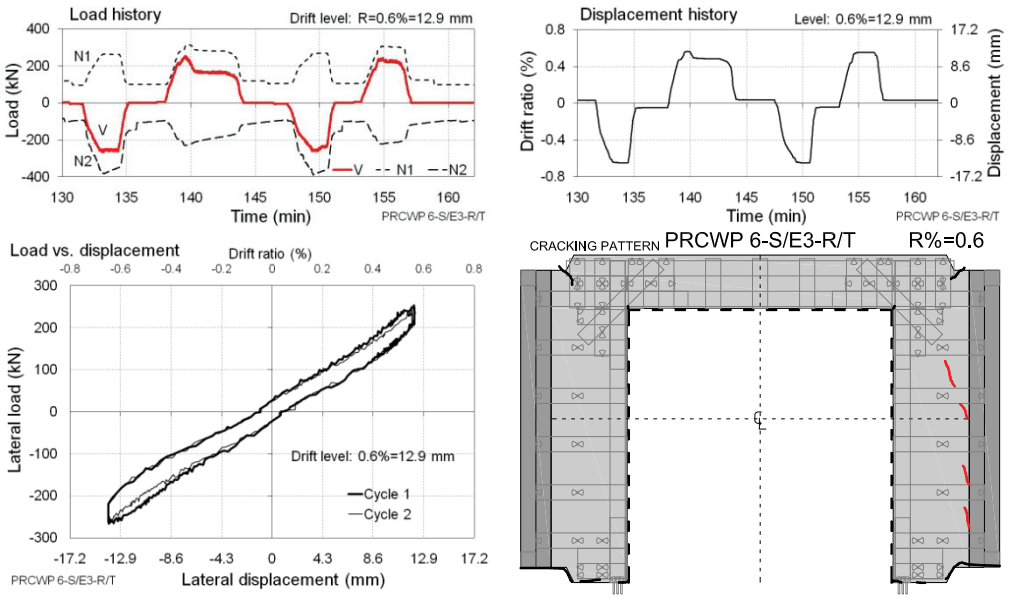

Commentary: Diagonal cracking appeared across pier#2 running at approx. 68 deg.

Figure E.132 Expanded cyclic response of PRCWP 6-S/E3-R/T at 0.6% drift ratio

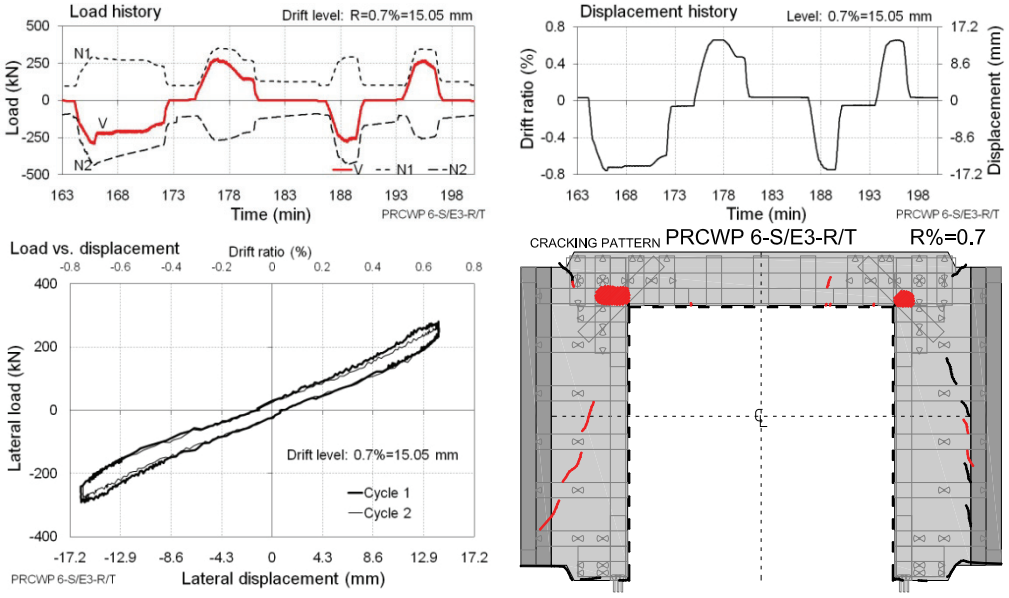

Commentary: Inclined cracking occurred across pier#1 extending at 57÷68 deg angles. The tapping inspection of the FRPs at the spandrel-to-pier connection indicated large debonded areas next to the corners of the opening. The FRP anchorage at the base of pier#1 exhibited pull-out distress.

Figure E.133 Expanded cyclic response of PRCWP 6-S/E3-R/T at 0.7% drift ratio

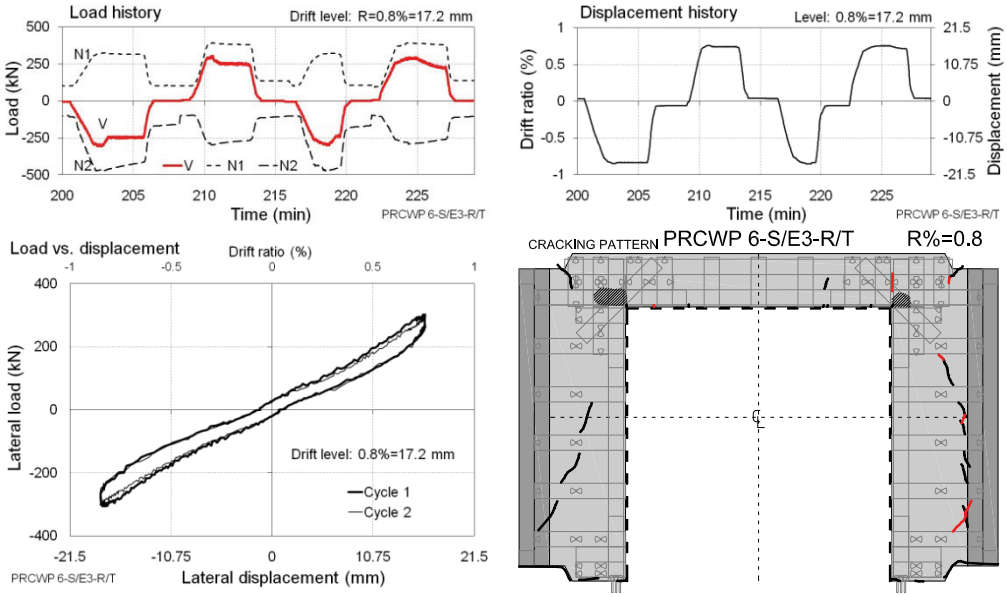

Commentary: Short link cracks developed between the inclined cracks along the pier#2-to-wing joint. FRP snapping sounds were heard during unloading.

Figure E.134 Expanded cyclic response of PRCWP 6-S/E3-R/T at 0.8% drift ratio

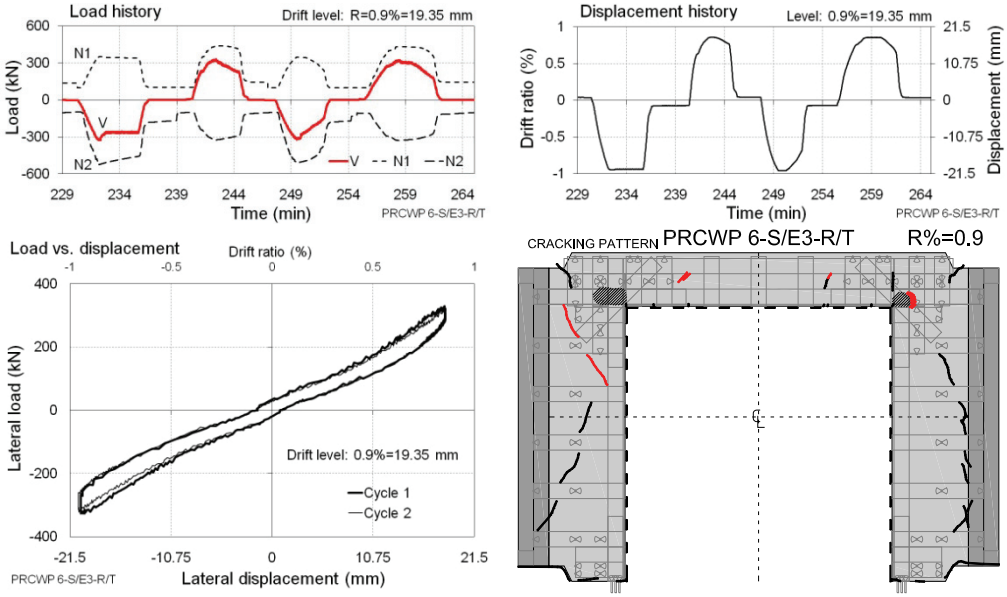

Commentary: In the positive loading direction of cycle #2 inclined cracking occurred at the upper half of pier#1 running at 61 deg. FRP bulging (buckling) was observed at the debonded areas on the spandrel-to-beam connections.

Figure E.135 Expanded cyclic response of PRCWP 6-S/E3-R/T at 0.9% drift ratio

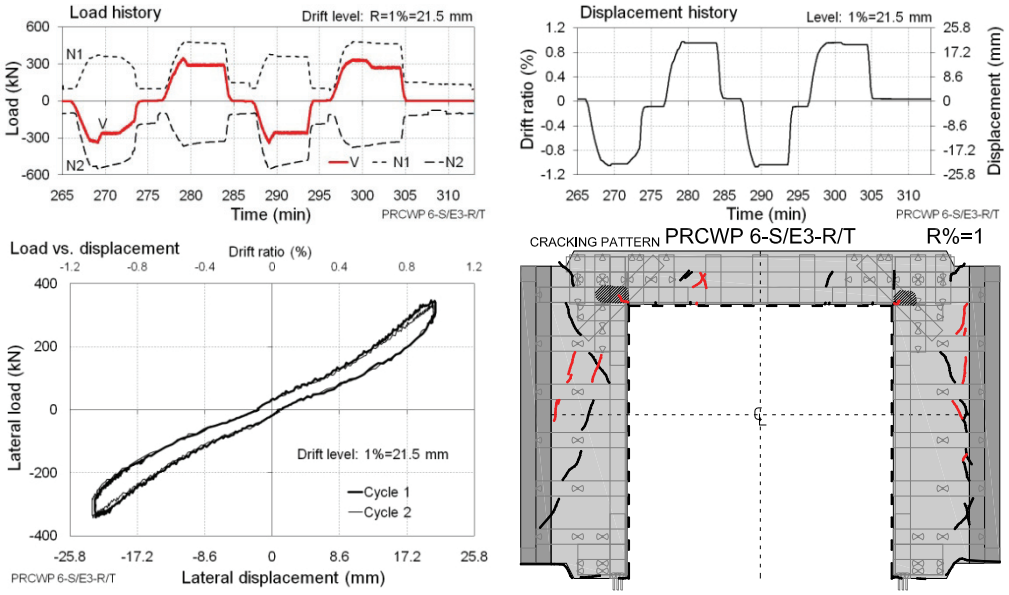

Commentary: Cracking propagation occurred across pier#1, at the pier#2-to-wing joint, at the pier-to-spandrel connections and along the spandrel. Incipient fracture of the flexural FRP strips was observed at the pier-to-spandrel connections next to the opening corners.

Figure E.136 Expanded cyclic response of PRCWP 6-S/E3-R/T at 1% drift ratio

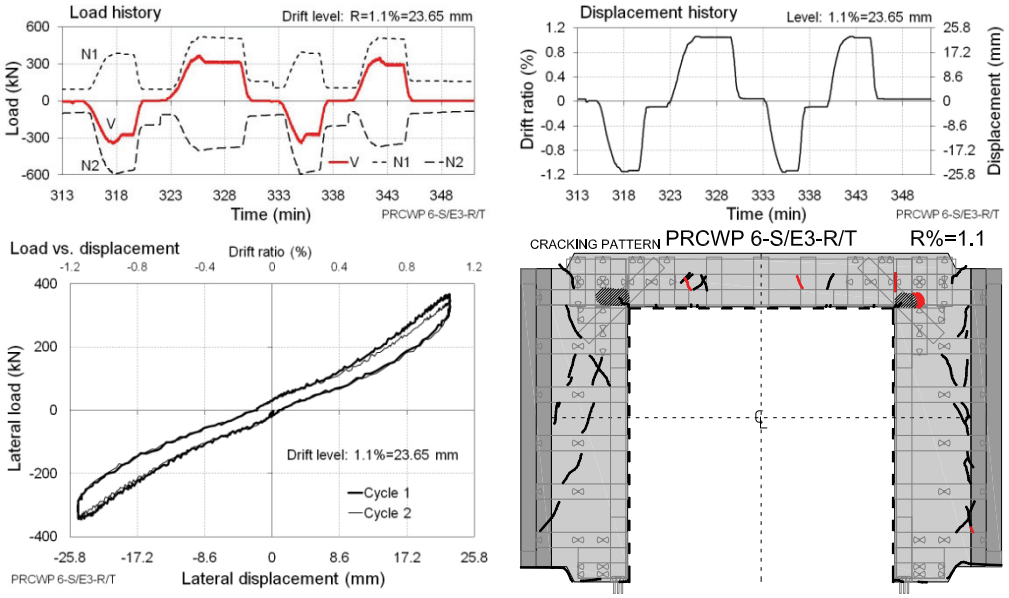

Commentary: Severe FRP bulging and onset of fracture of the flexural strips occurred at the pier-to-spandrel connections, next to the opening corners. The G5 strain gauge was disconnected and the G20 gauge was connected to the data acquisition system.

Figure E.137 Expanded cyclic response of PRCWP 6-S/E3-R/T at 1.1% drift ratio

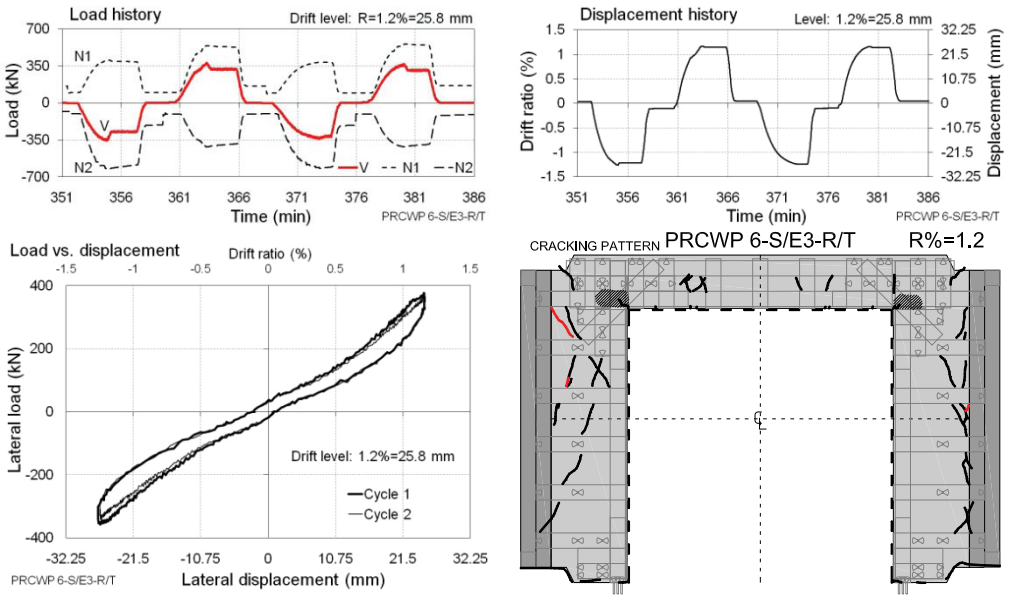

Commentary: Crack linking developed along the pier#2-to-wing joint. The FRP anchorage at the base of pier#2 displayed pull-out distress.

Figure E.138 Expanded cyclic response of PRCWP 6-S/E3-R/T at 1.2% drift ratio

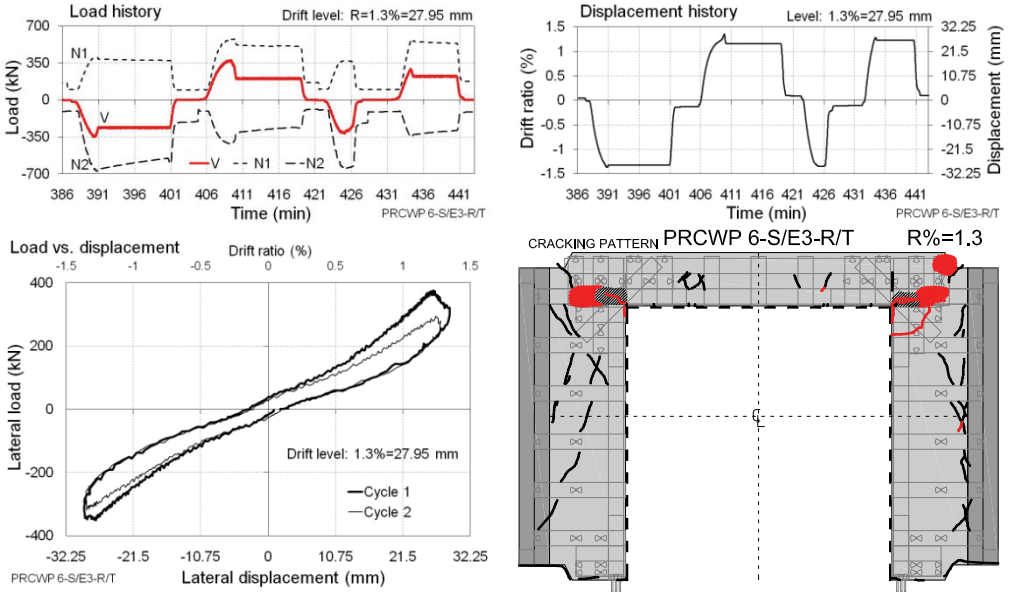

Commentary: Severe concrete crushing, FRP debonding, bulging and fracture occurred at the spandrel-to-pier connections around the opening corners. The FRP confinement strips on the piers under the opening corners fractured at the edges and the flexural FRPs bulged and fractured in compression. The load resistance dropped considerably in cycle #2 and by this the failure criterion was attained.

Figure E.139 Expanded cyclic response of PRCWP 6-S/E3-R/T at 1.3% drift ratio

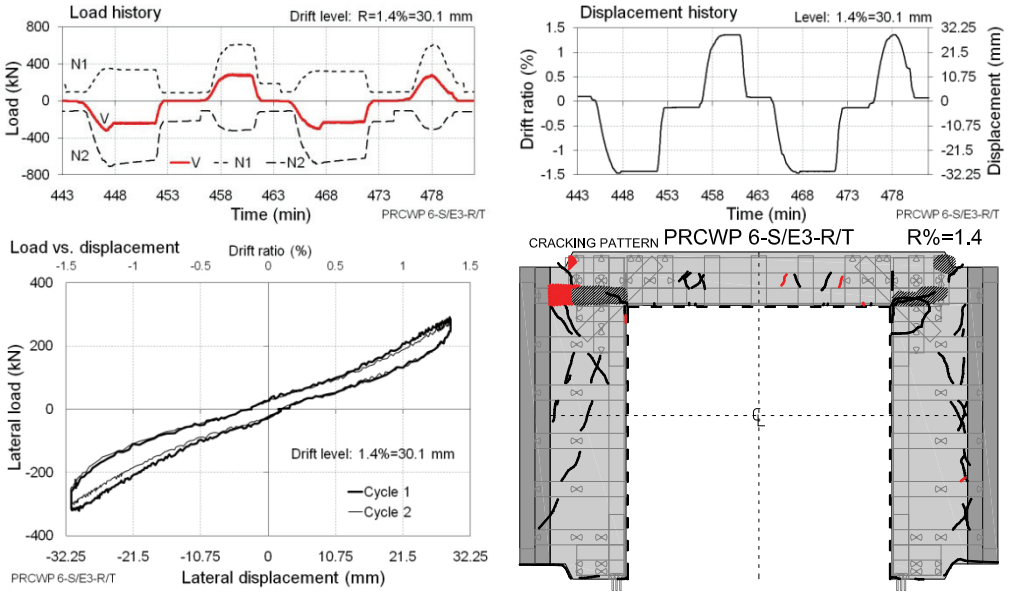

Commentary: Supplementary cycles were carried out to assess the post-failure response. The FRP debonding propagated toward the wing element along the horizontal strip at the pier#1-to-spandrel joint and the inclined cracking developed along the spandrel.

Figure E.140 Expanded cyclic response of PRCWP 6-S/E3-R/T at 1.4% drift ratio

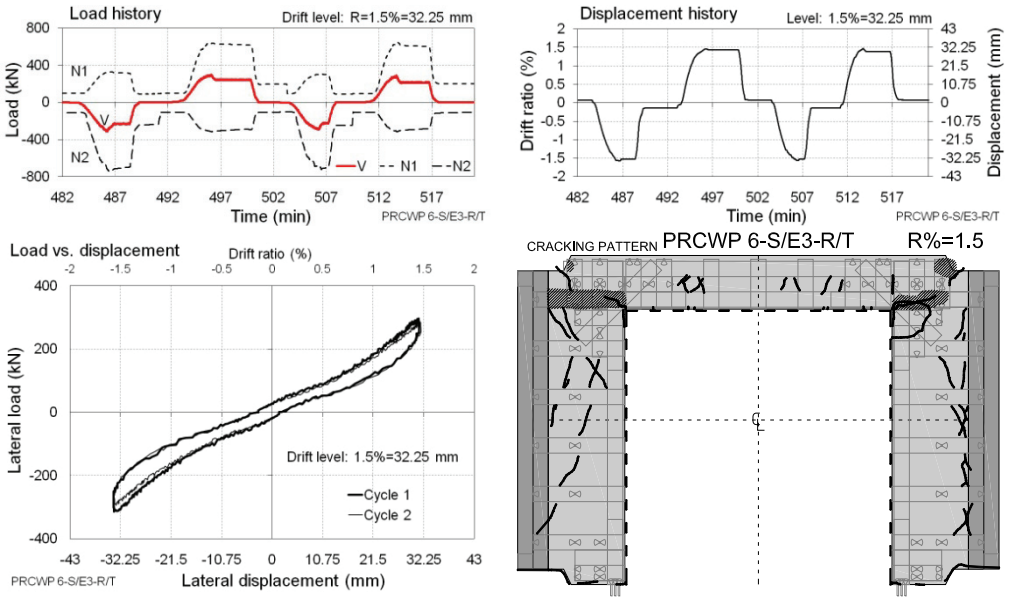

Commentary: Further concrete crushing occurred at the spandrel-to-pier connections. Concrete debris fell off from the pier#2-to-spandrel connection.

Figure E.141 Expanded cyclic response of PRCWP 6-S/E3-R/T at 1.5% drift ratio

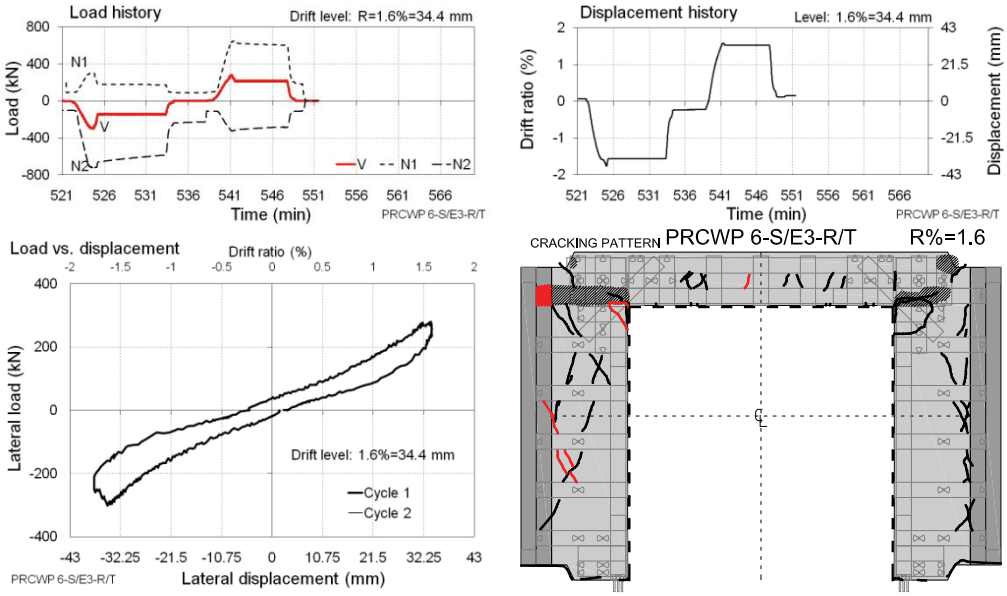

Commentary: Intense snapping sounds were heard denoting FRP rupture. In the positive loading direction the end-anchorage of the horizontal FRP strip atop the opening peeled off at the pier#1-to-wing joint. Concurrently inclined cracks developed across pier#1. At this point the test was stopped.

Figure E.142 Expanded cyclic response of PRCWP 6-S/E3-R/T at 1.6% drift ratio

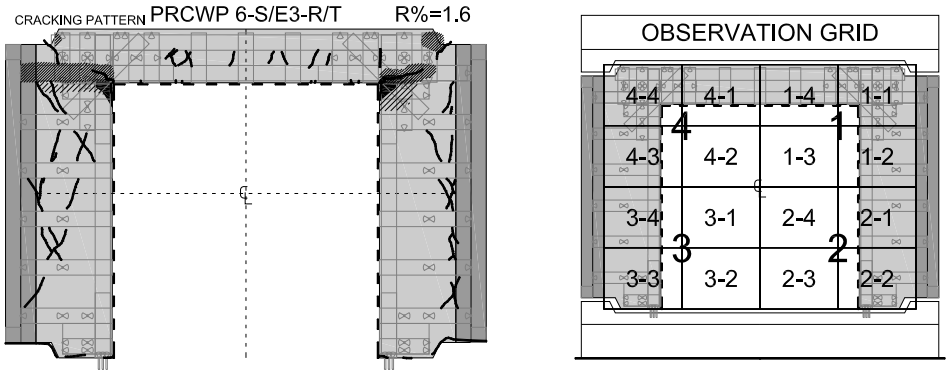

Figure E.143 Cracking pattern and observation grid PRCWP 6-S/E3-R/T

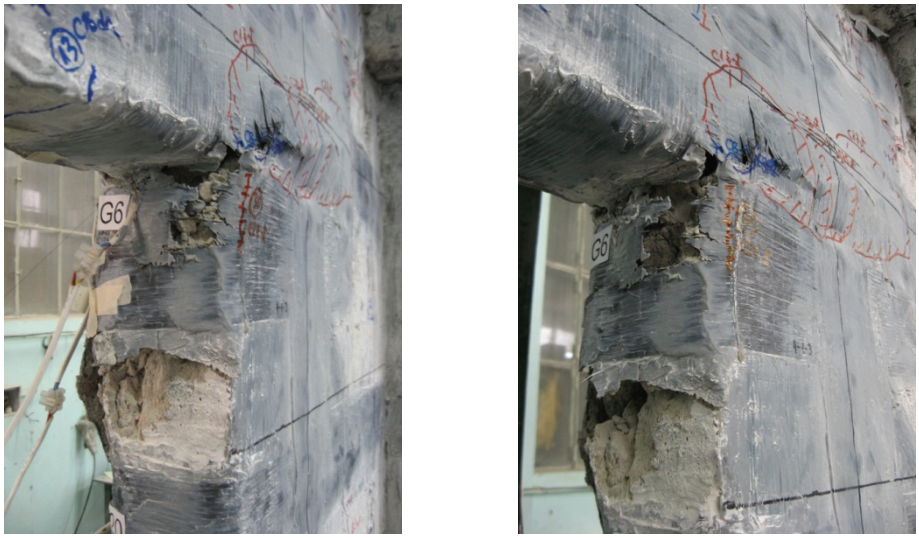

Figure E.144 Failure detail PRCWP 6-S/E3-R/T: FRP confinement fracture at the spandrel-to-pier#2 connection (obs. grid 1-1)

Figure E.145 Failure detail PRCWP 6-S/E3-R/T: FRP bulging and fracture at the spandrel to pier connections (obs. grids 4-4 and 1-1)

Appendix F Cyclic energy dissipation

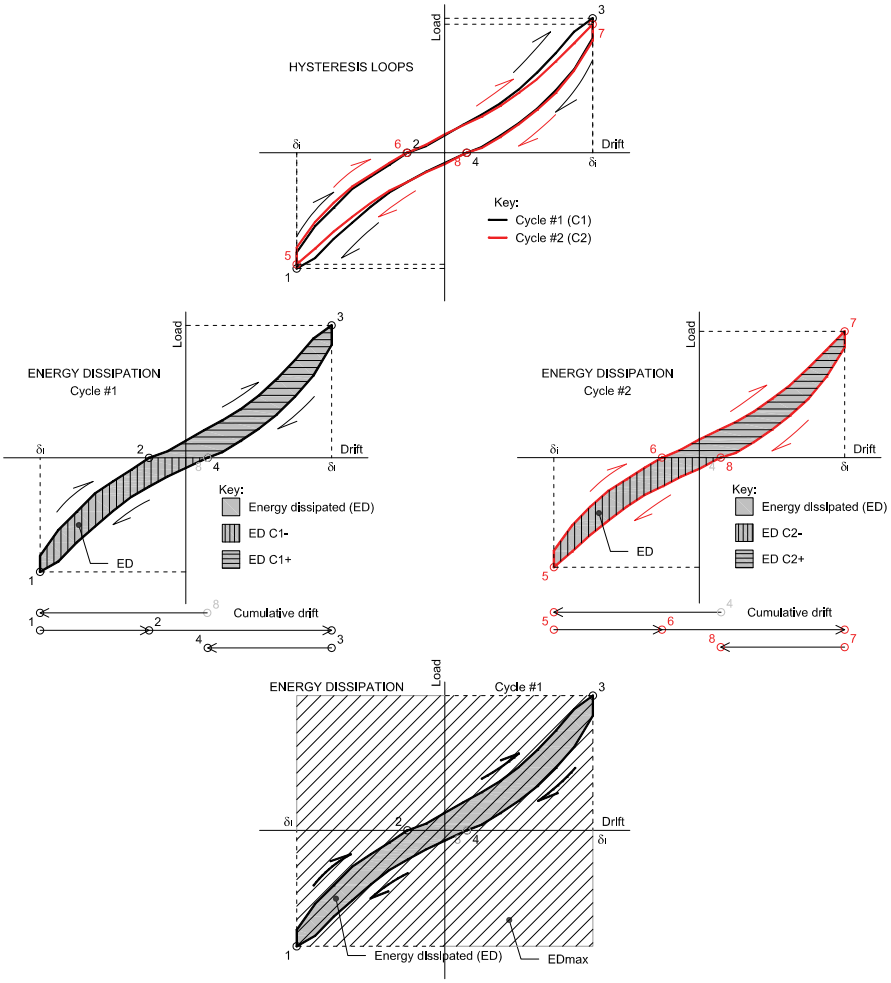

Figure F.1 Definitions related to the cyclic energy dissipation

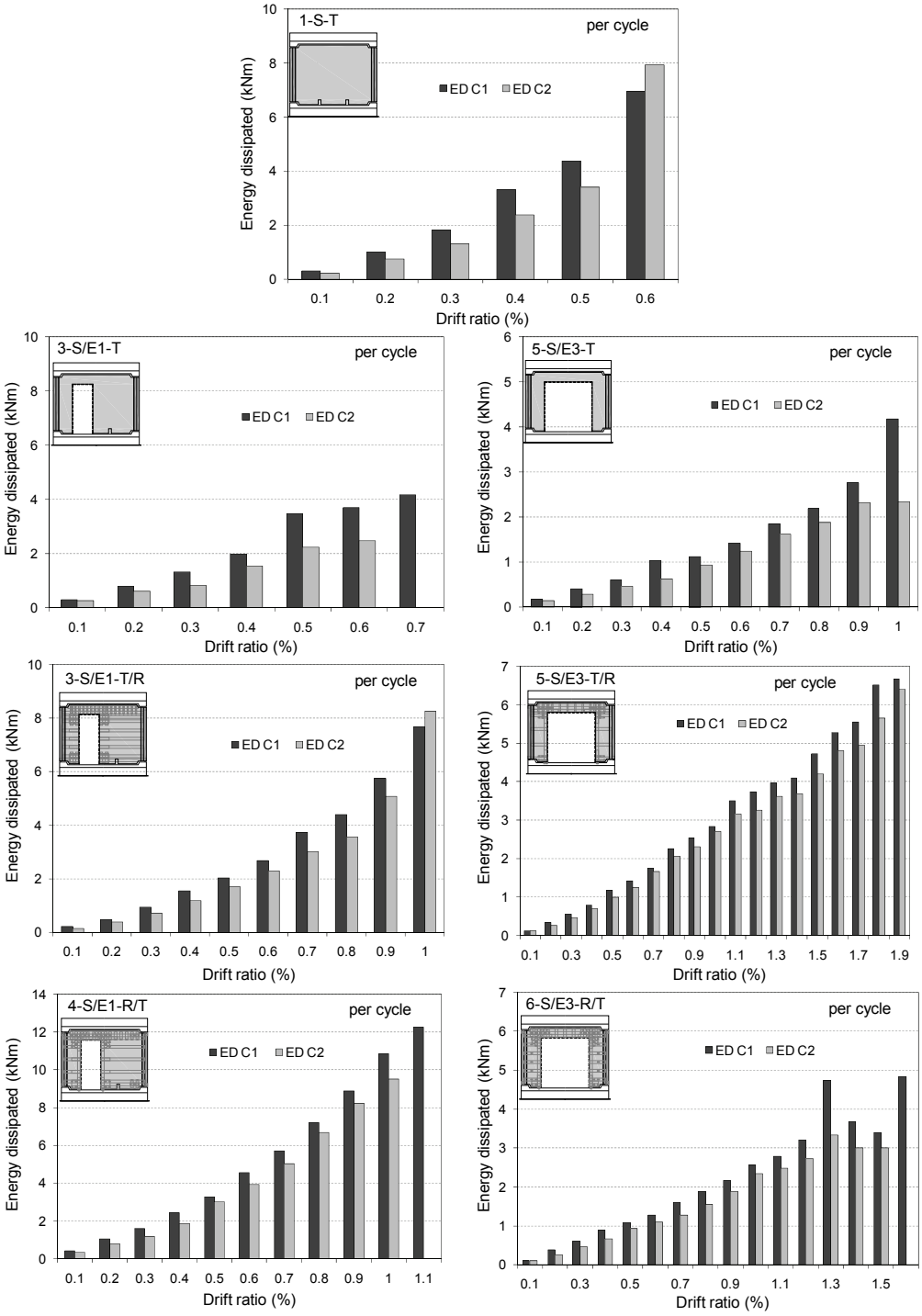

Figure F.2 Energy dissipation per cycle

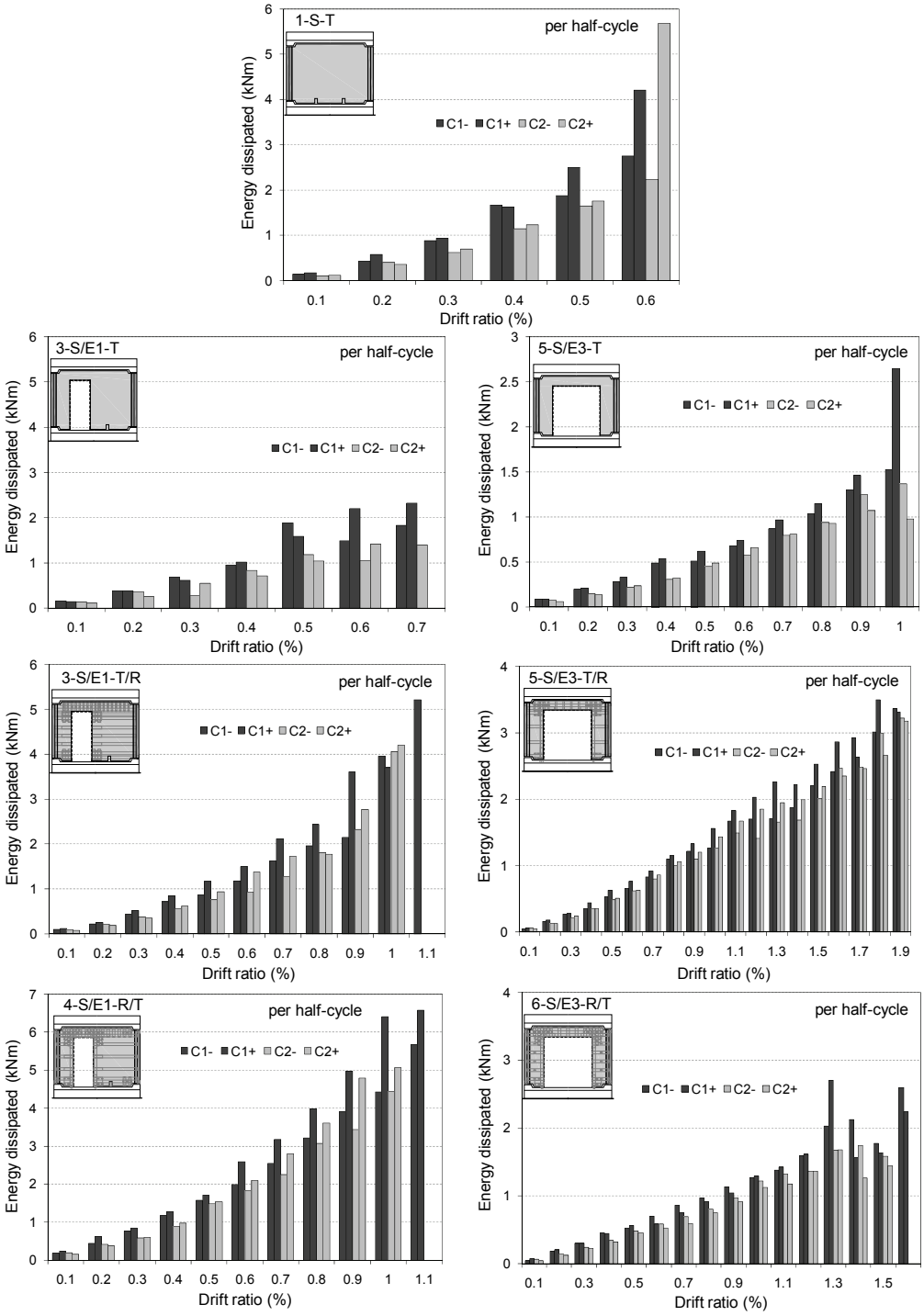

Figure F.3 Energy dissipation per half-cycle

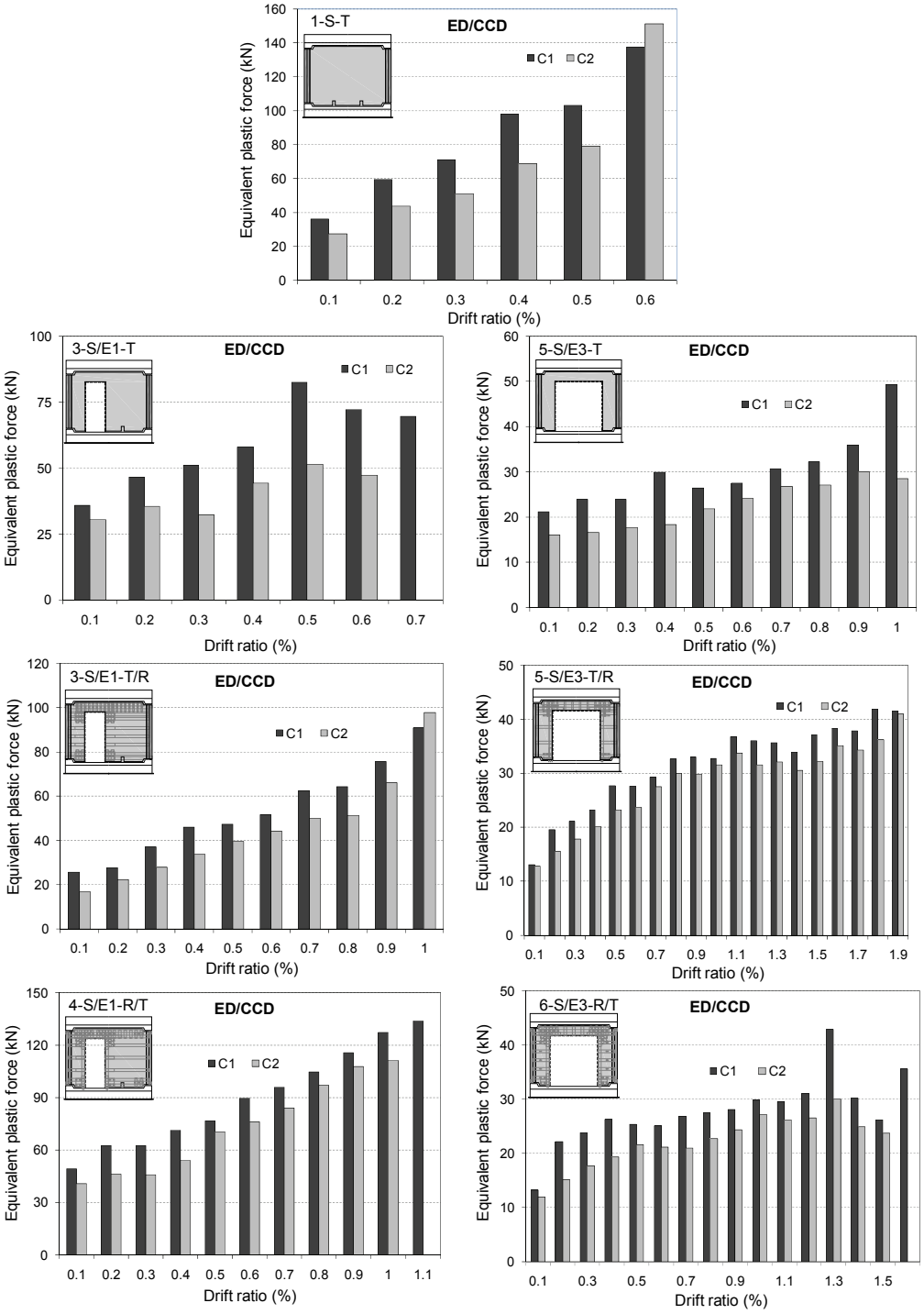

Figure F.4 Cyclic energy dissipation rate

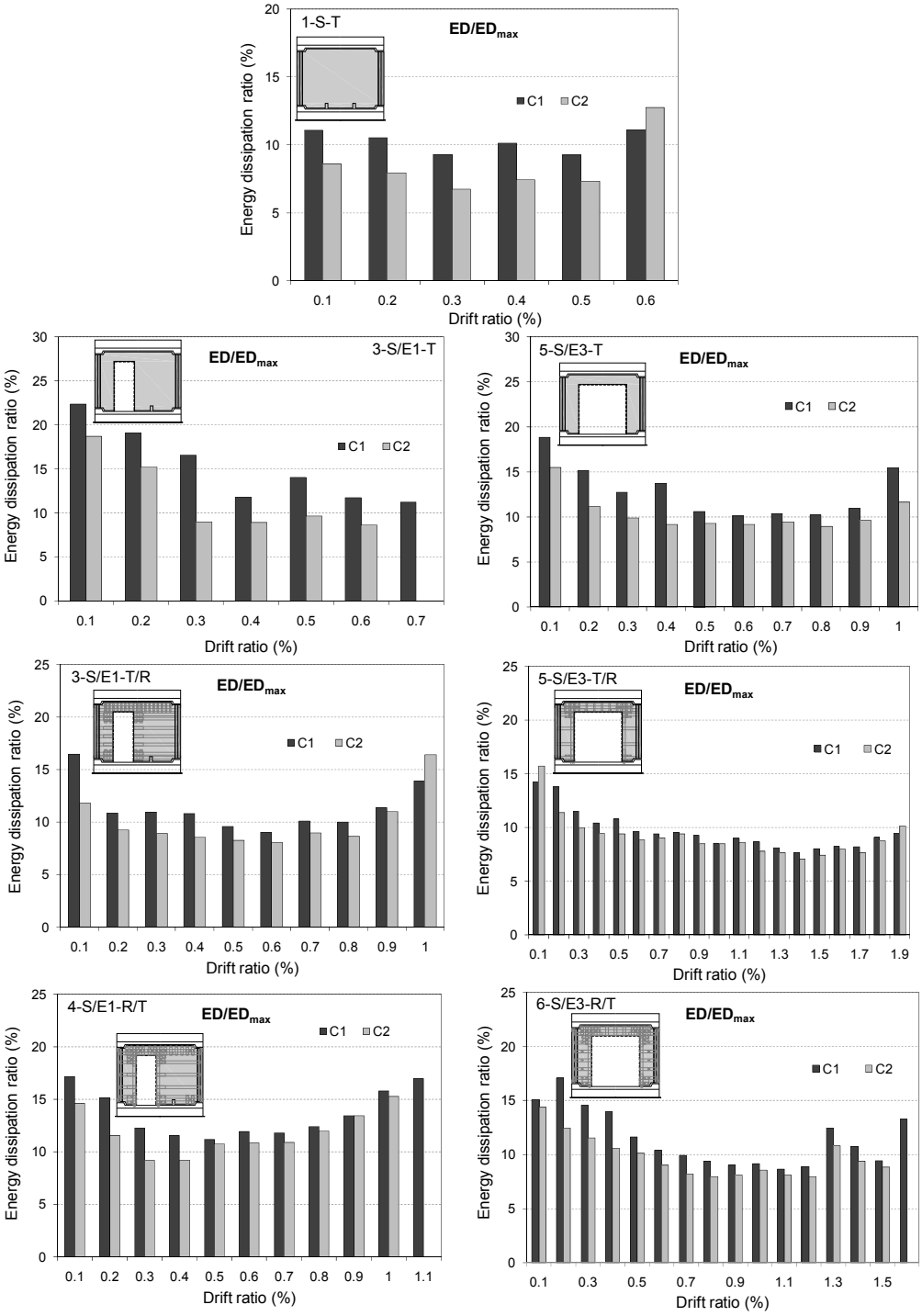

Figure F.5 Cyclic energy dissipation ratio